Doctoral Dissertation
Doctoral Program in Aerospace Enginering (33.rd cycle)

Theoretical, numerical, and experimental methodologies for structural analysis of polymeric aeronautical elements produced via additive manufacturing

Roberto Torre
* * * * * *

Supervisor
Prof. Salvatore Brischetto

Doctoral Examination Committee:
Prof. Alaimo Andrea, Università degli Studi di Enna - Referee
Prof. Giunta Gaetano, Luxembourg Institute of Science And Technology - Referee
Prof. Dimitri Rossana, Università del Salento
Prof. Kashtalyan Maria, University of Aberdeen
Prof. Zaccariotto Mirco, Università degli Studi di Padova

Politecnico di Torino
19th July, 2021

I hereby declare that, the contents and organisation of this dissertation constitute my own original work and does not compromise in any way the rights of third parties, including those relating to the security of personal data.

. . . . . .

Roberto Torre
Turin, 19th July, 2021

to my family

Mom and Dad, your example taught me how to fly, dream, and live. Without your love, none of this would matter; you are what I aspire to be.

Valerio and Mattia, you have never left my side; I will never leave yours. We are forged in eternal love.

Momo, you enriched my soul.

The only Heaven I'll be sent to
Is when I'm alone with you.

Acknowledgements

It is never too late to change careers to pursue true passions, but the context is everything. I have personally experienced and treasured this teaching. Several people guided me and gave me selfless support and insights.

Professor Salvatore Brischetto gave me the possibility to work by his side; he supported me with critical advice, continuous supervision, and guidance. Ours has always been a team effort, and I will always be grateful to him for this. I also thank Professor Paolo Maggiore; many professional and research achievements would have been further without his help.

Ufficio 28 has been a melting pot of ideas. The invaluable guidance and support of Andrea and Carlo in the early years, the effective collaboration with Sara, the company and the discussion with Pier Carlo are gifts that I carry in my heart.

Many people have kindly supported, endured with extraordinary patience, and directly helped me in these years. At the risk of doing someone wrong, I feel I have to explicitly thank those who were always there, in all circumstances: Alessandra, Alex, Alice, Elena, Federica, and Gioacchino, whom I consider like a brother. I cannot forget the fundamental contribution of Davide Mezzetta, my company tutor in my first work experience. Your dedication to family and work inspired me.

Summary

Additive Manufacturing (AM) technologies received increasing attention in these years. They differ from the conventional machining because they shape components by adding material instead of removing or deforming it. This aspect results in flexibility and efficiency; it allows simplifying manufacturing, especially with complex geometries, increasing production performance and efficiency. AM, 3D printing, rapid prototyping are all definitions commonly used, in parallel, to describe the same concept; however, they hide very different processes, tools, and technologies. Many common materials can be employed; this directs the specific technology and process. AM does not innovate in terms of materials but in terms of their processing. Fused Filament Fabrication (FFF) stands out among polymeric-processing technologies thanks to its ease of use and the accessibility of materials and technology. It also expanded beyond fabrication facilities to the consumer market. FFF is at the core of this dissertation, together with the application polymer, the Polylactic Acid (PLA).

Choosing a material directs towards mechanical properties of a particular order of magnitude; however, any process affects them. Any technology guarantees a shift towards functional components if compliance with the performance criteria of the item is verified; this means understanding its structural behavior. From the mechanical response perspective, this translates into the structural analysis, requiring (among the others) a constitutive model. The long-term goal of this research path is an ad-hoc tool dedicated to structural analysis and optimization of 3D-printed components. It is a very ambitious result: considering the thermal, hygrometric, and mechanical boundary conditions, the feedstock material properties, and the component geometry, the output would be an optimized printing strategy and the mechanical response even when the printing parameters have already been selected. This work traces this path by proposing and validating a simplified approach to this problem. The polymeric isotropy vanishes in the transition to a finished object; it is speculated that a specific printing strategy trace anisotropy to orthotropy, which is easier to evaluate and manage. In this context, the thesis draws a parallel (initially only geometric) with composite materials and derives some analysis methodologies. The main *goal* of the research activity is to open up the possibility of standardizing the characterization and analysis processes.

The dissertation is organized into three main areas: theoretical, numerical, and experimental. A necessary introduction on FFF precedes those three aspects to discuss its operating principles and main process parameters, together with the scientific background on the mechanical performance of 3D-printed components. This introduction also establishes a technical vocabulary related to the printing process.

From a theoretical perspective, the first part outlines the approach to FFF-components to determine a constitutive model. It discusses a parallel with unidirectional composite laminae, emphasizing the appropriate distinctions. This suggests that a single FFF layer may exhibit an orthotropic behavior; this *hypothesis* guides in defining mechanical characterization tests. This setup is not trivial, as none of them are standardized. An intermediate and simplifying step is introduced, speculating that this parallel allows extending the Classical Lamination Theory (CLT) to this context. The theory is presented, and its simplifying hypotheses discussed. From the perspective of an ad-hoc tool for structural assessment, the starting point is a reliable solution for stress analysis, and a layer-wise evaluation of the problem is crucial. To this end, the last part of the dissertation discusses a comprehensive formulation for hygrothermal mechanical analysis of multilayered structures exploiting the exponential matrix method to handle the differential equations.

From an experimental point of view, the *methodology* introduced in the dissertation aims to define new standardized approaches for mechanical characterization. The feedstock polymer is characterized to assess its datasheet and provide a benchmark. No standardized test methods exist; two set-ups are proposed for tensile strength and modulus quantification. Then, assuming an orthotropic behavior for finished parts and relying on the CLT approach, tensile and shear tests are designed, drawing inspiration from the standard test methods for composites. In standardized tensile and shear tests for composite materials, the load introduction into the specimen is facilitated by a set of bonded tabs. Their optimal shape for FFF specimens is determined through a Design of Experiment (DoE) approach. The 2D orthotropic mechanical properties are defined: the non-isotropy and the degradation over the transition from the filament to the finished part are confirmed. A speculative research on the compression behavior shows an asymmetric behavior between compression and tension along the same load application direction and allows an experimental approach to buckling. External strain monitoring is conducted through Digital Image Correlation (DIC), as in-contact instruments proved to affect the mechanical response of polymeric specimens.

The numerical perspective is introduced with a set of tests designed to validate the approach. A three-point bending, a simple bending, and a bending torsion test are simulated through finite element models tuned with a CLT constitutive model. Several set-ups accentuate the non-isotropic response of the FFF-processed PLA. The mechanical response prediction is excellent when the model considers the

orthotropic behavior hypothesis. Retaining the feedstock material properties leads to more significant discrepancies; this validates the approach. Buckling prediction is also reasonable, if the model considers the actual compressive behavior.

The dissertation discusses an aeronautical application example, considering an Unmanned Aerial Vehicle (UAV) with an FFF-printed frame. A structural validation is proposed, limiting the study to the mechanical response of some specific components.

Contents

List of Tables

List of Figures

Chapter 1

Introduction

This chapter is devoted to the description of Fused Filament Fabrication. After an in-depth explanation of the operating principles and the main process parameters, the chapter describes the set-up necessary to shift from a CAD model to an object. A specific focus is made on the material and printer used in the research work, PLA and Intamsys Funmat HT, respectively. The purpose of this chapter is also to establish a technical vocabulary related to the printing process. The last section discusses the scientific background related to studying the mechanical performance of 3D-printed components.

1.1 Additive manufacturing

Additive Manufacturing (AM) is a hypernym, which includes a particular category of production processes; it is sometimes referred to as *3D printing*. The term *additive* was introduced at the dawn of the new millennium to underline a substantial difference with classical machining processes based on material *removal*. In milling, drilling, and turning, the components are shaped from a block of a raw material from which the excess is removed through proper tools. AM processes distinguish from them, as the final object is produced adding up material, with a *layer by layer* scheme [1]. The terms used in AM technologies have been recently established in ISO/ASTM 52900 standard [2], to which this thesis strictly adheres. Three basic principles can be used to shape materials into components of the intended geometry [2], [3]: *formative shaping*, *subtracting shaping* and *additive shaping*. The latter involves a successive addition of material, and it is applied by AM technologies. The 3D shape of the component to be produced is sliced into a certain number of layers, which are physically reproduced one-by-one, adding the material. The techniques used for this addition, together with the materials compatible with them, differentiate the various processes. The concept of *adhesion* runs parallel to that of *addition*, as the added material needs to adhere to

the surrounding. Different principles of bonding characterize other processes and determine which materials can be used. The material needs to be in a particular state to adhere, which usually imply *fusion*, to be understood in a broad sense. Among addition, adhesion, and fusion, the first is the crucial concept behind any additive manufacturing process. As will be discussed in the next sections, this unique feature allows obtaining complex geometries without complex tools or complex molds, specifically designed and prepared before the machining. In parallel, it standardizes the production, allowing an almost direct shift from CAD modeling to the finished component, strongly reducing the overall production time that would be needed with some traditional processes. For these reasons, AM became widely used in the frame of rapid prototyping [4] but recently started to be used in several manufacturing fields [5]. Needless to say, it is not yet able, nor has this as a goal, to replace conventional production processes, which still represent the fastest and cheapest choice in many fields at least in the near future: large-production, large-size components, top-quality production. As discussed, AM processes rely on material deposition; it is intrinsic that the material is added up only where needed to build up the component, except for some support structures required for a specific situation. This makes those processes interesting in the perspective of production waste, which is cut to the bone. It is not the purpose of this thesis to provide a detailed digression on additive printing technologies or cataloging them in terms of characteristics or applicability. Interesting insights in this regard can be found in the work of Wong and Hernandez [1], where a classification of the processes is proposed considering the *state* of the raw material (liquid, solid, powder). An even more detailed catalog of AM processing is proposed in [2]; a preliminary grouping is made in terms of the materials (polymers, ceramics, metal). Right after, a more detailed overview is proposed in terms of *state of fusion*, *material feedstock* and *material distribution*.

Among the technologies capable of processing polymers, Fused Filament Fabrication (FFF) takes a relevant position. It relies on thermoplastic polymers in the form of continuous filament, which are heated and deposited in subsequent layers to create an object [6]. FFF is also known as Fused Deposition Modelling (FDM), as patented in 1989 by Stratasys [7]. The double name arises from the patent expiry in 2009, which allowed others to apply the technology. However, FDM is a trademark of Stratasys itself, so although the technology is essentially the same, it is referred to as FFF when a different company manufactures the printer. The list of the materials that can be processed via FFF/FDM includes well-known polymers, like ABS (Acrylonitrile butadiene styrene), PLA (Polylactic acid), PC (Polycarbonates), PET (Polyethylene terephthalate), PTU (Thermoplastic polyurethane), Nylon. Particular uses might require special requirements; in those cases, niche polymers are used, like PEEK (Polyether ether ketone), ULTEM (Polyetherimide), PEKK (Polyetherketoneketone). They are characterized by linear, non-crosslinked,

and poorly branched polymer chains; consequently, they have (relatively) low softening temperatures. Each polymer brings a set of characteristics that make it suitable/unsuitable in different operating scenarios. Some features essential to consider in the choice of a polymer are here listed:

- *Ease of printing*: measuring the issues arising during the print (adhesion, accuracy, thermal shrinkage, etc.)
- *Visual quality*: linked to surface finish and printing accuracy
- *Heat resistance*: maximum temperature that the object is capable of withstanding before softening
- *Mechanical resistance*: maximum load that the material is capable of withstanding
- *Impact resistance*: the ability of the material to withstand a sudden impact
- *Adhesion between layers*: the measure of the quality of the adhesion between different print layers

The reader will notice how none of those properties has been quantified; for some of them, a range of values can be expressed; for others, only a qualitative assessment can be done.

1.2 Principles of Fused Filament Fabrication

A detailed description of the printing process through FFF is discussed here. As anticipated, the raw material comes in the form of a filament wound around a plastic coil. Manufacturers provide those coils in a vacuum bag to avoid moisture absorption and aging of the polymer. Three standard diameters exist for the raw material; 1.75 mm is the most common, but 2.85 mm and 3.00 mm are also used [8]. Coils usually weight between 250 and 2000 g, representing the maximum weight of a continuous 3D print. An example of a FFF filament spool is reported in Figure 1.1.

Figure 1.2 gives a graphical representation of a 3D printer. The polymeric filament is dragged by a *gear wheel* and pushed towards a heated chamber, known as *hot end*, equipped with a metallic nozzle. With the hot end at the appropriate temperature, the filament liquefies inside the chamber; the action of the gear wheel continuously pushes the liquefied polymer out of the nozzle [9]. The exit hole has smaller dimensions than those of the raw filament; standard sizes are in the range $0.2-1.0$ mm [10]. Out of the nozzle, the polymer takes the form of a viscous and thin thread. This process takes place while the nozzle moves, keeping a constant distance from a flat surface. That distance is known as the *layer height* [11]; the surface as

Figure 1.1: Example of a black PLA spool, manufactured by Shenzhen Eryone Technology.

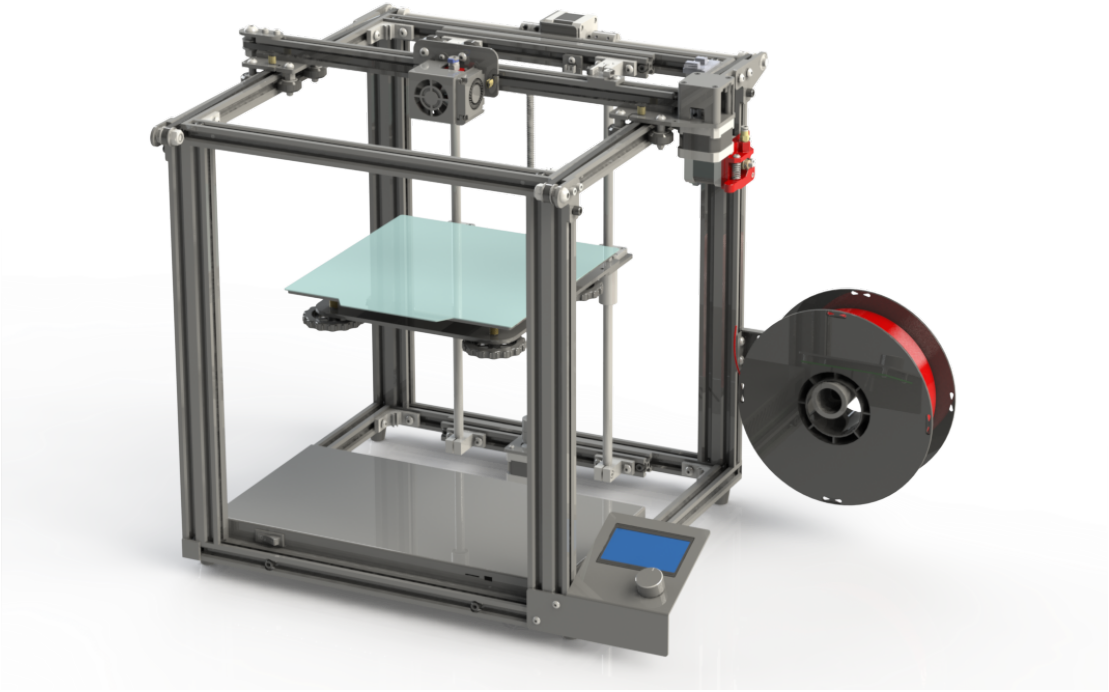

Figure 1.2: Render of a generic 3D printer.

the *printing bed*. Figure 1.3 shows the relation between the nozzle diameter $\varnothing_n$ and the layer height l_h.

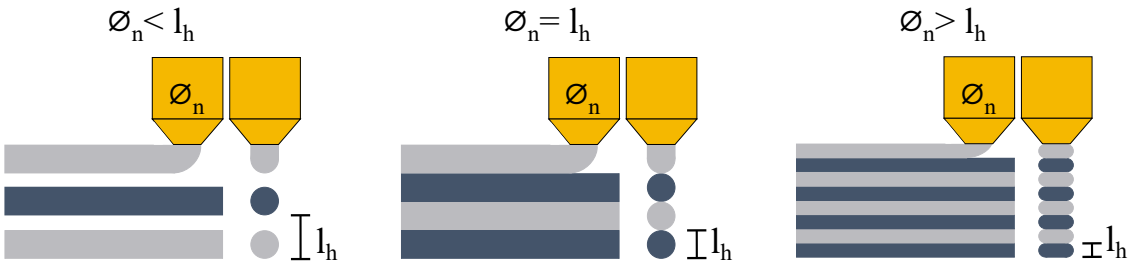

Figure 1.3: Relation between the nozzle diameter and the layer height.

Once outside the nozzle, the thread has a cylindrical shape, with a circular cross-section. If deposited in this shape, it would remain as a cylinder over a flat surface, leaned. The same would happen to the other threads; no bonding would happen, neither between threads nor between a thread and the underlying surface. The extruded filament needs to be flattened over the printing bed; consequently, the layer height needs to be smaller than the nozzle diameter [12]. As shown in Figure 1.3, the deposited and flattened thread takes the form of a filament with an oval eyelet cross-section; the simultaneous motion of the print head allows the filament to develop in length. The process continues with the nozzle depositing other filaments over the printing bed; any shape can be reproduced; consequently, the next filaments can be deposited in adjacent position(s) to the previous(es), or not. The polymer is deposited in a numerical controlled process in which the nozzle moves in two planar directions. Once a layer is done, the cycle repeats: the printing bed moves down to an amount of the layer height, and the nozzle deposits new filaments over the previous. Figure 1.4 focuses on a single layer of a generic component; during the printing process, the extruder follows a specific path, which can be customized by the operator. A certain number of peripheral filaments are shown; they closely follow the external and internal contour of the section. Consequently, they depend on the actual geometry of the component. Once the external and the internal contour(s) are done, the print head moves and fills the section. The *internal infill* can be customized; some examples are shown in Figure 1.4. When a

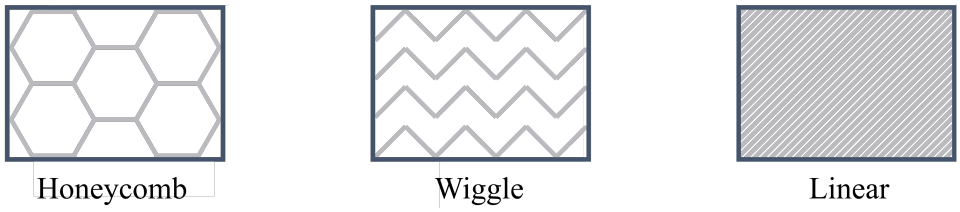

Figure 1.4: Examples of internal infill pattern.

solid component is needed, the so-called *linear infill* is chosen, as it allows to reach a 100% infill percentage; if that is the case, the extruder deposits a certain number

of parallel filaments adjacent to each other. When a solid component is not necessary, different infill patterns can be chosen, and the infill percentage customized as required.

Mechanics of a 3D printer

The gear wheel is the only mechanism that controls the material supplying and dispensing. The gear wheel can be positioned either just above the hot-end or at a distance (see Figure 1.5). The first set-up is known as *direct extrusion*, as the filament is directly pushed towards the nozzle. The latter set-up as *bowden extrusion*, as the filament runs into a bowden cable in the path between the wheel and the hot-end [13]. The choice between the two set-ups shall be weighted according

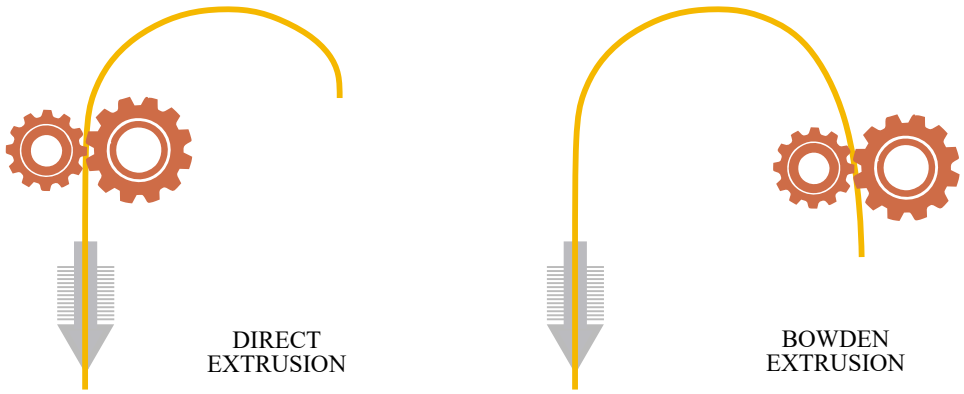

Figure 1.5: Direct vs. bowden extrusion systems.

to printing requirements. Fast prints take advantage of bowden extrusion as the moving mass is smaller, and the inertial effects are limited. The nozzle can achieve higher speeds (reads high accelerations) without affecting the printing quality. In bowden extrusion, the interaction between the filament and the inner surface of the bowden cable causes frictional effects. Consequently, higher torque is required to push the filament. Besides, there is a certain kind of delay between the actions of the motor, and the results live up to the nozzle. Consequently, direct extrusion leads to more precise extrusions at low/moderate speed. The contact between the filament and the cable is also an element of choice when abrasive filaments are used, as the frictional effects can be increased and the service life of the tube reduced. In both cases, the motor causes the filament to be first in traction, then in compression. The compression force for extrusion needs to overcome the pressure drop through the system, which depends on the viscous properties of the molten material and the geometry of the flow in the heating chamber and the nozzle. During the deposition, the filament is subjected to shear deformation, which causes shear-thinning: a pseudoplastic behavior in which the viscosity decreases. The mass flow rate through the print head depends on the pressure drop between the hot end

and the external environment, on the nozzle geometry, and on the viscosity of the material, which is, in turn, a function of the temperature. An electrical resistance heats the hot end; a thermocouple is also present for temperature monitoring. The system continuously turns the resistance on and off, using a thermocouple in a negative feedback circuit. In printers equipped with a Cartesian reference system, the print head is held in a suspended position by two cylindrical supports, respectively parallel to the main X and Y directions. At least two stepper motors guarantee the movement of the print head. They are placed externally to the printing area and drive the print head through connection belts supported by suitable transmissions. In a small number of devices, the print head is still, and the print bed bears the movement in those two directions. Another stepper motor transmits motion to the gear wheel that supplies material to the print head. Consequently, this assembly is generally known as a feeder. NEMA ICS 16-2001 [14] standard has spread among FFF devices. Within this category, the motors are distinguished by the torque rating and their size; the two quantities are closely related. Smaller motors (lighter and with lower torque rating) are commonly used in direct extrusion feeders.

Nozzles of 3D printers

The hot end is the terminal portion inside which the filament passes. It is an assembly made up of several elements; an example is provided by the exploded view shown in Figure 1.6.

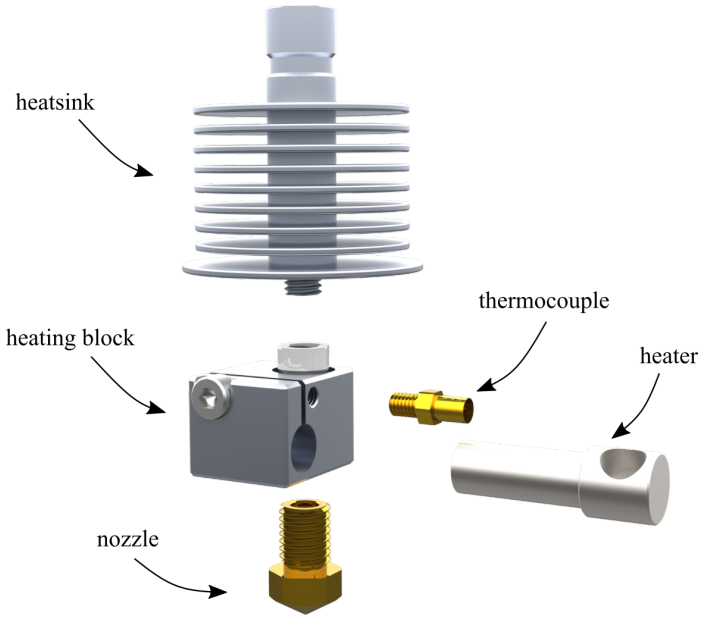

Figure 1.6: Exploded view of a standard hot end.

In the shape of a parallelepiped, the central part is known as the *heating block* or *heating cartridge*. It is made of metal and has several slots for the heater (the electrical resistance), the thermocouple, and the nozzle [15]. It is also vertically crossed by a hole, in which the filament flows towards the nozzle. It is subjected to stresses of a different nature. It is thermally stressed, as it directly houses the heater; it is mechanically stressed, as it undergoes compression of the filament on the nozzle by the gear wheel. Therefore, two characteristics must be considered to choose the right material:

- the thermal properties (especially conductivity),
- the mechanical properties at high temperatures.

The concept of high temperature is relative: different materials offer good performance, or not, depending on the extrusion temperature, therefore depending on the polymer. Most heating blocks are made of aluminum alloy or brass. Above the block, there is a *heatsink*, usually cylindrical. The heatsink mates a fan acting directly on its surfaces. Its aim is to dissipate heat, preventing it from flowing upwards. The primary purpose is to create a sort of clear boundary between the high-temperature zone (in which the filament is softened and then melted) and the zone in which the polymer is still solid; otherwise, the gearwheel would not be able to push the filament down. Secondly, it prevents damage to the components located in the upper part of the device. Below the block and screwed to it, there is the *nozzle*. It is the terminal part of the assembly and the last element with which the filament is in contact before its deposition. It has axial symmetry and, usually, an external conical shape. Internally the filament passes through an initial duct and reaches a chamber in which it rests once melted. The plastics exit the chamber through a conical hole whose final diameter is the so-called nozzle diameter. Brass is a widely used material in standard nozzles, especially with common polymers such as ABS and PLA. It has excellent thermal conductivity, which is advantageous as it efficiently and quickly conducts heat to the polymer. Furthermore, it is easily machined, which makes brass nozzles cheap. Polymers loaded with abrasive materials require harder materials, such as aluminum or steel. The nozzles can be classified according to the size of the outlet section. *Pointed nozzles* are those in which the wall surrounding the exit hole is tiny. On the other hand, *flat head nozzles* are those in which the wall surrounding the outlet hole is thicker (a sort of circular crown). Both are good solutions but in different situations. The first category reduces the heat transfer to the filaments already deposited, adjacent to the one being printed. However, they require much more attention in the position calibration phase. The second category is less demanding from the calibration point of view but heat (and possibly touch and melt again) the surrounding material [8].

Thermal environment in 3D printing

Most printers are equipped with an open chamber, which means that the print volume is open to the surrounding environment on one or more sides. On the other hand, higher quality printers are fitted with top and/or lateral panels, closing the print volume or possibly sealing it. Most polymers are susceptible to sudden changes in temperature, which can cause severe shrinking, causing cracks, or adhesion problems [16]; isolating the processing component limits air currents or temperature changes external to the process. Some specific polymers, generally those characterized by excellent thermal performance, require that the temperature be kept constant and at a value higher than the ambient one. Industrial printers are equipped with a heating system, completed by thermocouples that feed a feedback and control system [17]. For the same reason, almost all printers are equipped with a heatable printing bed. The temperature gradient between the nozzle and the surface can be very high, leading to poor adhesion of the first layer and, eventually, to process failure. The point of layer sticking is crucial. The whole process is based on a subsequent deposition of layers. If each layer did not adhere effectively to the previous one, the result would not be satisfactory. The adhesion between two polymeric layers of the same material is overall simple to be obtained. Adhesion to the print bed is more complicated as the two materials differ, and the thermal gradient is higher (the molten polymer is at a high temperature, while the bed is at room temperature). In those devices with a heatable printing surface, this gradient is reduced. However, the surface cannot be heated at will as temperature must be lower than the glass transition temperature of the polymer to facilitate its solidification.

Build plates in 3D printing

Build plates are ideally flat surfaces to which the part can temporarily bond during the process. Different solutions can achieve this purpose. The simplest and also the cheapest choice is borosilicate glass. Easy to find and manufacture, the glass has a low thermal conductivity, promoting a homogeneous heat diffusion on heated printing plates, provided for a longer heating time. However, the glass surfaces are incredibly smooth, making the adhesion of the first print layer difficult. Consequently, it is common to interpose a thin layer of an adhesive before printing; several solutions have been proposed in this respect [18]. Some manufacturers have developed ad-hoc products; even easier to find alternatives, such as PVA sticks and hair sprays, work very well for a wide range of polymers. Polyethylenimine (PEI) sheets are also used to improve adhesion, making them adhere to the glass surface. Others propose glass plates overlaid with special coatings (of a different kind) that promote adhesion. This solution retains the advantages of a glass surface but simplifies its use, as it allows printing without any prior surface treatment.

However, the coating naturally deteriorates over time; this process is further accelerated by the operator when removing the printed parts without special attention. Polypropylene sheets can be used in place of glass. Their main advantage is the improved adhesion, even without the use of particular products. However, they are susceptible to scratches and surface damage; they are also less rigid than glass. Therefore, they do not guarantee a perfectly flat surface (at least not over time). Several manufacturers have also proposed flexible sheets. Generally, these are thin metal sheets overlayed with an adhesive coating (including PEI). These sheets are then held in place on the printer frame through magnets, which, distributed all over the surface, ensure that the metal sheet is flat. The advantage of this solution comes from the fact that no tools are needed to remove the printed objects. A manual flexing of the metal sheet allows for pop prints off. This solution is not necessarily compatible with all printers, as the frame must have ferromagnetic properties to respond to the action of the magnets.

1.3 From CAD to a component

As discussed, FFF is a numerical control process. The 3D printer reads as an input a text-like file, which contains all the instructions. The next section will describe its formatting and programming language in detail. In short, the file contains instructions to position the nozzle and build plate and on how much plastic to extrude. The translation of a solid geometry into numerical control instructions requires several steps; a brief discussion follows:

- *3D CAD model.* A 3D Computer Assisted Design software is used to model the component.
- *Export into .stl.* Any CAD software might be used; the geometry of the native file format of the CAD is then translated into a universal file format, known as Standard Triangulation Language (STL), to standardize the next step.
- *Slicing and .gcode export.* The .stl file is processed by specific software, which slices the component into layers and generates the machine language.

The steps are few; this gives the idea of how simple it is to materialize a component after its conceptualization.

The design of the 3D geometry via CAD software is a typical phase among all the manufacturing processes; it does not involve any peculiarity from the perspective of Additive Manufacturing. The second phase requires attention, while the third one is undoubtedly the crucial one.

1.3.1 Export into .stl format

STL stands for Standard Triangulation Language. It is also known as Standard Triangle Language and as Standard Tassellation Language. It is a universal file format for 3D geometry. Its acronym is self-explanatory: only the surfaces of the components (whether internal or external) are described, discretized by a certain number of triangles [19]. Each triangle is saved through the space coordinates of its three vertices and the unit vector orthogonal to it, facing outwards. The order in which the coordinates of the three vertices are reported establishes a rotation direction; through the right-hand rule, it too provides the direction normal to the triangle pointing out of the body. It might seem like repeated information; however, it is necessary to verify that the file has been compiled correctly. The coordinates are expressed as numbers in absolute value, without any unit of measurement. Therefore, the latter must be specified when a .stl file is imported to scale its size correctly. The file can be binary or in ASCII code; the following code gives an example of how each triangle is defined.

```
solid name
    facet normal ni nj nk
        outer loop
            vertex v1x v1y v1z
            vertex v2x v2y v2z
            vertex v3x v3y v3z
        endloop
    endfacet
endsolid
```

For a .stl to describe a solid correctly, the (external) surface must be effectively closed and connected. The software used in the next step takes care of this preliminary check before proceeding. Triangles are two-dimensional elements, which are required to discretize any surfaces. When the surface is flat, and all edges are segments, the discretization is perfect, and the .stl surface is identical to the nominal one. However, in most cases, surfaces are curved or have curved edges/contours, so the tessellation results in an approximation. This point is fundamental as the next step (export in .gcode) will rely on the .stl, therefore on its coarseness. Two parameters can improve the approximation [20]. The first is the *(linear) tolerance*; with this parameter, the maximum admissible distance between the nominal surface and the discretized surface is set (see Figure 1.7). Lower values lead to a more detailed representation through more triangles (with smaller dimensions). The second parameter is the *angular tolerance*. It establishes the maximum angular difference between the normals of adjacent triangles. Lower values induce a denser tessellation in areas with a high radius of curvature. Case by case, it is necessary to compromise the accuracy of the representation and the file size.

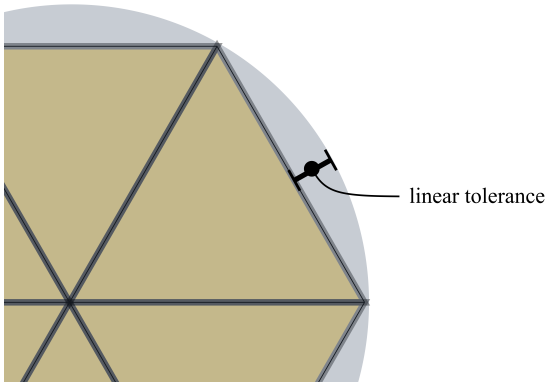

Figure 1.7: Representation of a the linear tolerance parameter for .stl discretization.

1.3.2 Slicing and .gcode export

It is the crucial phase, as at this stage the tool path and all the printing instructions are generated. A considerable number of processing parameters need to be evaluated and set. A detailed description is given here. In this work, the commercial slicing software Symplify3D [21] has been used; a set of screenshots will also be presented to facilitate the discussion.

Gcode programming language

Gcode means *Geometric Code*, its purpose is to instruct a machine on how to move its tool(s) in space and what to do while moving. In the case of 3D printing, the tool is the printhead. Consequently, the code lines instruct the printhead on

- where to move, and how fast;
- if to extrude, and how much.

There are also instructions not directly related to extrusion and deposition, such as the temperatures of the nozzle, print bed (and possibly print volume), and the on/off switching of the cooling fans. Below is a portion of a Gcode.

```
G90
M82
M106 S0
M140 S30
M190 S30
M104 S210 T0
M109 S210 T0
G28
G1 X106.674 Y123.072 F2000
```

```
G1 Z0.100 F1000
G1 E0.0000 F600
G92 E0
G1 X106.704 Y123.048 E0.0025 F2400
G1 X106.768 Y122.997 E0.0078
G1 X106.798 Y122.974 E0.0103
G1 X107.877 Y122.190 E0.0972
G1 X107.905 Y122.170 E0.0995
...
M104 S0 ; turn off extruder
M140 S0 ; turn off bed
M84
```

A quick observation of the code explains the name *numerical control*: the whole code is scattered with numbers, preceded by a letter [22]. The letters *X*, *Y*, and *Z*, indicate coordinates. Consequently, they reveal the position to be reached by the nozzle. *G1* precedes all the lines with coordinates; it means *linear movement*. In essence, each line starting with *G1* demands the nozzle to move to the designated position (from the previous) once the prior commands have been completed. In most cases, *G1* lines are completed by the letter *E*, which means *extrusion*. If present, it is followed by a number that indicates the amount of material to extrude while moving. This indication is provided by defining an extruder coordinate along the filament. The position of the filament is expressed in absolute or relative coordinates. *F* completes some of those lines; it stands for *feed-rate*. The value that follows indicates the maximum speed the nozzle can assume in that movement. That value also applies to all the following lines of code without reporting any. The lines marked with the letter *M* describe actions not directly related to the extrusion and the print head movement. The letter *S*, which always follows, gives a numeric setting to the command preceding it. *M106*, for example, turns on the cooling fans at speed following the letter *S*. *M140* sets the value following *S* as the target temperature for the print bed; *M190* stops printing, waiting for it to be reached. Similar reasoning applies to *M104* and *M109*; in this case, the temperature refers to the nozzle *T0* (tool 0). Knowing of the .gcode language allows adding customized code. At the beginning of each .gcode considered through this research work, the following code was added:

```
G0 F4200 X0 Y0
G1 Z15.0 F4200
G92 E0
G1 F200 E12
G92 E0
M83
G1 F400 X10 Z0.4
```

```
M221 T1 S300
G1 F200 X30 E+8
M221 T1 S100
M82
G92 E0
```

This code aims to extrude some sacrificial polymer before starting to free the nozzle from scraps of the previous process. The nozzle is brought into the home position (*X0 Y0*) but moved away from the print bed (*Z15.0*). 12 mm of the polymer are extruded in the air (*E12*). In the meantime, the print bed approaches the nozzle (*Z0.4*). In 20 mm of linear translation along the X direction (from *X10* to *X30*), another amount of polymer is extruded (*E+8*). This spot adheres to the print bed at an angle and does not interfere with the subsequent process. At the end of each .gcode the following code was added:

```
G92 E0
G1 Z260 E-7.50 F1000
```

This code quickly pulls the build plate away from the hot-end (*Z260*) while retracting a significant amount of filament to prevent clogging (*E-7.50*).

In the example, the *Z* coordinate is declared only once. Therefore, everything (movements and extrusions) that follows is characterized by the same pitch over the build plate. That is, it refers to the same layer. Once the instructions of this layer have been completed, the next *Z* coordinate will move the build plate downwards. New nozzle movements and actions will follow for the next layer. The code continues until the component has been completely described. The way to translate a solid component, described through its external surfaces, into layers and two-dimensional paths is discussed hereinafter.

A slicing software: Symplify3D

Gcode files are generated automatically by ad-hoc software, known as slicers, which effectively slice the component into a certain number of parallel layers, or cross-sections. Slicers are, therefore, the link between the 3D model and the finished object. They draw a complex set of geometric paths (the beads) for each layer and calculate how much material has to be extruded. The operation is automatic, but it is performed based on its algorithm, tuned by many parameters. Here follows a list and description of the main printing parameters:

- *Build Orientation*: it defines how the object is oriented in the 3D printing reference system. It depends on which surface is chosen by the operator as the bearing surface. As a general indication, it is good that the surface is flat and extended. However, this depends on the specific geometry of the component. Different orientations may or may not require support structures

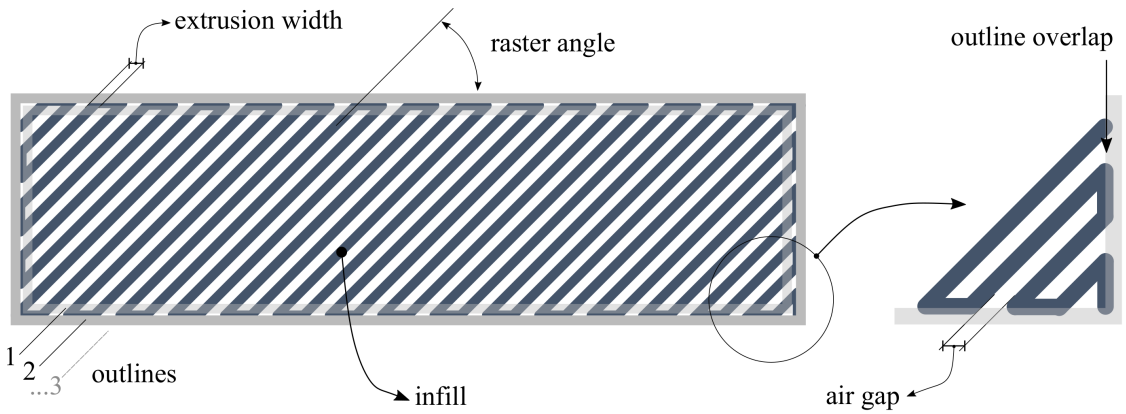

Figure 1.8: Representation of a single layer and its main printing parameters.

to be designed for the cantilevered surfaces. The topic of supports will be addressed in detail later.

- *Nozzle Diameter*: it is the actual diameter of the extrusion nozzle, to be set according to the dimensions of the nozzle carried by the 3D printer. The nozzle dimension sets an upper and a lower limit for both the extrusion width and the layer height by the above argument. Larger nozzles allow more material to be extruded per time unit; at the same time, smaller nozzles allows tighter tolerances.

- *Extrusion Multiplier*: the algorithm calculates how much material to extrude, per unit length, during the movement of the nozzle. Such an amount needs to be corrected when the user measures (or experiments) that the printer is extruding less or more material than it should be. This parameter allows this correction.

- *Extrusion Width*: it is the width of the extruded filament. By the above argument, its automatic value is calculated by the software algorithm; it can be customized, but it always takes values a bit higher than the Nozzle Diameter.

- *First Layer Width*: the extrusion width of the first layer can be customized; such value is usually modified when printing defect arises in the first layers, as it plays a role in first layer adhesion and the so-called *elephant foot* defect.

- *Primary Layer Height*: it is the nominal height of each layer. As discussed, its lower limit is an intrinsic characteristic of the machine in use; its upper limit depends on the Nozzle Diameter;

- *First Layer Height*: the height of the first layer can be customized; the operator might choose a thinner layer to increase the adhesion with the printing

bed or a thicker layer to overcome irregularities that may exist on its surface in contact with the object.

- *Outline / Perimeter Shells*: it is the number of the contour roads that follow the internal and external surfaces of the object, per layer; sometimes it is referred to as *vertical shells*.

- *Infill*: after the peripheral filaments have been deposited along the section contour, the nozzle fills the inside. The user can customize the filling strategy according to different needs. An example has been given in Figure 1.4.

- *Interior Fill Percentage*: it determines the volume fraction of the plastic over the overall volume of the part; it acts on the internal infill only.

- *Internal Infill Angle*: it is usually referred to as *raster angle*, and it is defined for *linear infill* only. It determines the deposition direction of the filaments with respect to the reference system of the printer. It can be freely set. The operator can specify a sequence of infill angles to alternate the deposition direction between one layer and another.

- *Air gap*: it defines the distance between adjacent filaments on the same layer from their respective midline. It may be positive (detached filaments), zero (in contact filaments), or negative (superposed filaments). It can be refined, customizing the *contour to contour air gap* and *perimeter to raster air gap*.

- *Outline Overlap*: it set the overlap between the peripheral filaments and the infill, in percentage or as an absolute value. As the perimeters follow the contours and the infill is customized, it is used to prevent the perimeters and the infill to detach.

- *Extruder Temperature*: it sets the nozzle temperature; it can be customized in the range provided by the filament manufacturer. For amorphous polymers, the nozzle temperature needs to exceed the glass transition temperature of the material; in semi-crystalline polymers, the melting point needs to be reached for the viscosity to be adequate for the extrusion. Furthermore, incorrect heating of the extruding filament would prevent chemical bonds from forming with the polymer chains of the underlying layer, thus reducing the mechanical properties in the vertical direction [23]. Usually, higher temperatures are used for aged plastics or to facilitate extrusion.

- *Bed Temperature*: it sets the temperature of the printing bed. It is used to reduce the thermal gradients, as they play a role in warping and in poor bed adhesion. It should be kept under the glass transition temperature of the polymer.

- *Chamber temperature*: it sets the temperature of the chamber. As discussed before, it can not be set in all the 3D printers, neither all the printable polymers require it.
- *Default Printing Speed*: it is the movement speed of the print head. Its upper value depends on the 3D printer in use. Higher speeds reduce the processing time but cause lower surface finish and quality due to inertial effects.
- *First Layer Speed*: the print speed of the first layer can be customized; it is usually lowered from the default value to increase bed adhesion.
- *X / Y Axis Movement Speed*: it defines the movement speed of the extruder while no extrusion is in progress.
- *Retraction Distance*: it defines the length of the filament to be retracted by the extruder, while it moves without extruding. Some plastic may come out anyway from the nozzle unintentionally during these movements due to the pressure built up inside it and due to gravity. Retraction reduces internal pressure; it is used to prevent leakages, thus defects.
- *Z Axis Movement Speed*: it defines the movement speed of the printing bed, between a layer and the subsequent.
- *Filament diameter*: it is the nominal diameter of the filament.
- *Skirts*: they are a certain number of peripheral beads that surround the object, keeping at a distance. Their purpose is to ensure a smooth extrusion once component printing begins. They also allow the operator to check that the area in which the component will be printed is calibrated correctly and, if necessary, to make last-time corrections. The number of skirts, their distance from the part, and their height can be customized.

In addition to these, lots of other parameters can be set. For some of them, a suggested range value is provided by the manufacturer of the polymer. Many of them have to be defined by the operator in light of experience and as a function of the object peculiarities and the polymer to be used. By the time a new polymer (and, sometimes, a new spool of the same polymer) is used, a certain percentage of the trial-and-error process must be carried out. It has been demonstrated that the properties of FFF/FDM 3D-printed components, including the mechanical ones, the dimensional accuracy, and the surface finish, are a function of the process parameters [11]. Once set, the parameters determine a so-called *printing profile*. The software shows a layer-by-layer preview of the printing process, in which all the steps are shown. An estimate of the printing time and the amount of material to be extruded is also given. The color scale highlights different printing speeds as some processing phases might have different printing speeds. Slicing software allows also to translate, rotate, and scale the model.

Supports for cantilevered surfaces

A separate discussion should be made on the so-called supports. Since the FFF is based on a continuous layers overlap, they need support on which to be deposited. If the element to be printed has cantilevered surfaces, some layers could not rely on support surfaces. This drawback can sometimes be solved by changing the orientation of the component in space. When this solution is not definitive, it is possible to prompt the software to generate sacrificial elements as temporary support to be printed together with the piece and subsequently removed. The design is almost automatic; however, some parameters can be customized.

1.4 Materials

As anticipated, the materials used with FDM/FFF are mainly amorphous thermoplastic polymers, given that a gradual decrease in viscosity takes place as the temperature increases. Assuming that no degradation occurs at a specific temperature, the polymer chains obtain enough thermal energy to move freely, leading the polymer to behave like a viscous liquid. The *glass transition temperature* is a characteristic of a polymer. It represents the temperature at which the material becomes rubbery and many of its properties, mechanical included, change abruptly; those changes are reversible. The glass transition temperature largely depends on the chemical nature of the polymer chains. By continuing to increase the temperature, the polymer achieves the behavior of a viscous liquid [24]. This peculiar characteristic of amorphous polymers allows the extrusion to be easier controlled, as a wide process range can be used. On the contrary, semi-crystalline polymers show a marked decline in mechanical properties in correspondence to the melting point; it is, therefore, harder to estimate their behavior as the temperature changes. A perfect crystallinity does not exist in polymers; one would find disordered regions and crystallites of different sizes. In the viscous liquid state, the chains are highly knotted, and a long time is required for diffusion, for a three-dimensional order to be set up, and for the formation of crystalline zones. Consequently, rapid cooling usually prevents the development of significant degrees of crystallinity [24].

A polymer printed via FFF/FDM undergoes different challenges. It is extruded with a specific flow rate, at constant pressure, through a nozzle with a defined diameter. While it cools down, it has to shape a structure with self-sustaining capabilities; sometimes, it has to allow bridging. Upon returning to room temperature, it has to be stable, without showing significant distortions and shrinking that could influence the geometrical shape of the designed item. The degree of "printability" of polymer is a topic of interest. A viscoelastic model has been developed in [25]. A large number of parameters are discussed; some of those do not directly depend on the polymer, but depend on the geometry of the component. This means

that with the same polymer, the success of a print may depend on the volumetric component dimensions: larger volumes amplify, for example, the effects linked to thermal restriction. Some parameters are those process parameters previously discussed. This means that the printability of a polymer depends on an careful selection of their values (usually a trial and error process):

- T_{ext}, extruder temperature
- h, layer height
- w, extrusion width
- t_l, the time between one layer and the next
- Q, volume flow rate through the nozzle
- P_{max}, maximum nozzle pressure

Some parameters are crosslinked between them. t_l and Q, for example, are directly linked to the default printing speed, to geometrical shape of the component and to some technical details of the device:

- D_n, nozzle diameter
- L_n, nozzle length

At the same time, further two temperatures might influence the degree of printability. In particular,

- T_{amb}, room ambient temperature, as it influences the thermal gradients
- T_{sub}, temperature of the previous layer, while the next is being printing

The intrinsic thermal and mechanical properties of the polymer itself obviously play a very important role.

- E, elastic modulus at room temperature
- σ_{yield}, yield strength
- ρ, density at room and at extruder temperature
- ν, viscosity at room and at extruder temperature
- α, thermal expansion coefficient
- $G_0^{'}$ - $G_0^{''}$, storage and dissipation modulus

1.4.1 Polylactic Acid

Bioplastics are polymers of natural origin, biodegradable, or both. When those materials have the same properties as those of conventional plastics, they offer additional benefits, such as reducing harmful emissions during production and the possibility of recycling/safe disposal. Three main categories of bioplastics exist:

- *Non-biodegradable, fully or partially bio-based*, (e.g. PE, PET, PA).
- *Biodegradable, bio-based*, (e.g. PLA, PHA, PBS).
- *Based on fossil and biodegradable resources*, (e.g. PBAT).

The Polylactic acid (PLA) is a bio-based polyester obtained from renewable sources. It is also biodegradable in a controlled environment; outside specific temperature and humidity range, it still decomposes, but at a slower speed. Despite this, it retains properties similar to other petroleum-based thermoplastics. Thus, it is considered an ecological alternative to traditional polymers. It is considered safe when in contact with food for human consumption; as it is non-toxic, it also has applications in the medical field. PLA is obtained through polymerization of lactic acid, its monomer. Lactic acid is a carboxylic acid; it can be obtained by chemical synthesis or by fermentation. Chemical synthesis is based on the hydrolysis of lactonitrile, which is obtained from acetaldehyde and hydrogen cyanide. Fermentation production, instead, is a cheaper and more widely used technique. It is based on natural resources fermentation, such as plants with starch (mostly corn, wheat, and sugar canes). Lactic acid can be found in two different enantiomers: L-lactic acid and D-lactic acid, as shown in Figure 1.9.

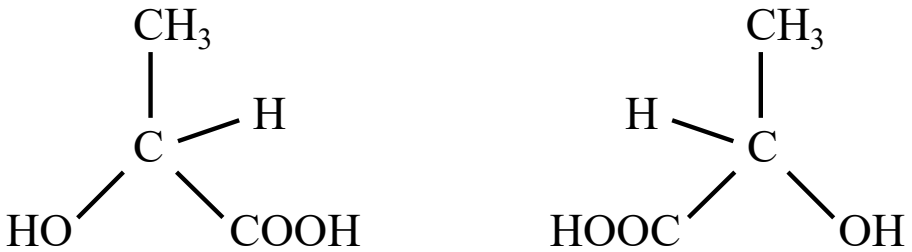

Figure 1.9: L-lactic acid on the left and D-lactic acid on the right.

Depending on the enantiomer used in the polymerization, PLA variants are possible, which differ in the spatial orientation of their atoms. Once the lactic acid is obtained, polymerization is carried out to obtain PLA; it consists of a chemical reaction that occurs by polycondensation or ring-opening. As semi-crystalline polymers, a glass transition temperature and a melting temperature can be defined. Their values are relatively low, which simplifies the printing process. This implies a rapid decay of the mechanical properties at temperatures slightly above ambient

temperature: it is not suitable for applications where the temperature exceeds 50 °C. It has a hygroscopic behavior: it has been demonstrated that this polymer is greatly influenced by the environmental conditions, especially by the humidity of the storage [26]. Therefore, it is necessary to be very careful in controlling the storage humidity of the PLA, as its excessive content can cause problems during processing. It is also essential to avoid exceeding the processing temperature to prevent degradation. PLA can be extruded, injected, casted, thermoformed, and 3D-printed. In this context, it spreads very rapidly for two main reasons. The first is undoubtedly the price: on the final consumer market, 1 kg spool of PLA is sold at around $20 - 30$ €. The second reason is the ease of printing. It is possible to obtain excellent results while maintaining different printing parameters in quite wide ranges. It also features limited warping, which significantly reduces the risk of delamination between layers and separation from the print bed. It also has excellent adhesion with unsophisticated build platforms (such as glass) treated with standard products (like hair spray). The filaments are produced starting from transparent PLA pellets, which are reduced to powder, mixed with additives (including pigments), dried at temperatures above the glass transition temperature, and finally extruded in the desired diameter between 185 and 200 °C [27]. The new filament is then cooled and wrapped around a spool. As in other polymers, the stretching of its chains can improve some mechanical properties, as the tensile modulus and the resistance to impact.

Throughout this research, a black PLA filament manufactured by Shenzhen Eryone Technology Co., Ltd. has been used. The data-sheet provided by the manufacturer is reported in Table 1.1 for convenience; as previously discussed, the mechanical properties there reported may be considered representative of the raw material only [28].

1.5 Intamsys FUNMAT HT

All the specimens and components discussed in this work have been printed using a professional, industrial-grade, FUNMAT HT 3D printer, manufactured by Intamsys Technology. It comes with a cubic printing volume of 260 mm per side and a ceramic build plate. This 3D printer covers all the printable polymers; the nozzle can reach 450 °C, and the build plate can be heated up to 160 °C. Furthermore, the printing volume may be sealed and kept at a constant temperature, up to 90 °C. This makes it appropriate for working with high-performance functional materials like PEEK (Polyether ether ketone), ULTEM (Polytherimide) and PPSU (Polyphenylsulfone). It has a positional accuracy of 12.5 μm in X and Y directions, and 50 μm in Z direction, which represents the minimum layer height. By default, it is equipped with a 0.4 mm diameter nozzle. An image of the printer is shown in Figure 1.10. The interface with the operator is managed by a touch display

Mechanical/Physical properties		
Density	1.24 g/cm^2	ASTM D792
Melt Flow Rate (MFR) at 210°C	15 g/10min	ASTM D1238
Tensile strength	65 MPa	ASTM D638
Tensile yield	60 MPa	ASTM D638
Young modulus	3950 MPa	ASTM D638
Impact strength	5.5 KJ/m^2	ASTM D256
Moisture absorption	$< 1\%$	ISO 61
Thermal properties		
Printing temperature	$195 - 215$ °C	-
Melting temperature	150 °C	ASTM D3418
Vicat softening temp.	55 °C	ASTM D3418
Glass transition temp.	55 °C	ASTM D3418

Table 1.1: Eryone black PLA data-sheet [29].

and a multi-function push-button. Through the display, the user can access all the functions to operate and maintain the device.

Figure 1.10: Intamsys Funmat HT 3D printer.

Filament loading

After the printer has been switched on, the filament needs to be loaded. Once the material has been specified, the function is (almost) automatic. The printer

pre-heats the nozzle to the optimum temperature; at this point, it moves the print head to a central position to facilitate handling by the operator and drives the gear wheel. The operator manually inserts the filament inside the hot end, waiting for it to be managed by the printer. A small amount of material is extruded to remove any residue of previous prints from the nozzle. The hot end moves to its home position and the heater and the gear wheel are turned off.

Pre-heating

If the polymer requires that the printing surface be heated (and eventually, that the entire printing chamber is brought up to temperature), proceed by modifying the temperatures of interest. It is good practice to carry out this pre-heating before the next phase (calibration of the printing bed) as the heating of the metal parts produces thermal deformations. If the calibration is performed with the printer cold, it may be necessary to repeat it, as it is not accurate with a warm printer.

Printing bed calibration

It is not necessary to perform this step before every print. It should be repeated at regular intervals (for example, once every two weeks) and whenever the printer is moved, or the nozzle replaced. The printing surface always needs to be at the same (and correct) distance from the nozzle for a successful process. The unit step in the vertical direction is tiny; 50 μm in this printer. Calibration is, therefore, a precise operation. The risks of a partial (or total) incorrect calibration are:

- If the build plate is too far from the nozzle, the first layer will partially stick to it or not stick at all. The process will fail due to a partial separation between object and plane or because subsequent layers will not have a support surface.
- If the print bed is too close to the nozzle, the extrusion will be incomplete. The pressure inside the nozzle increases due to the the non-extruded polymer. If the surface in contact with the printing surface is small, the excess polymer may be accidentally extruded at the beginning of the second layer or in correspondence with the printing bed surface defects. If the surface in contact with the printing bed is large, the filament stops advancing and begins to wear out under the continuous action of the gear wheel at the same point.

The Funmat HT features a three-point calibration system. The printing surface is supported by three threaded connections, equipped with an elastic spring; one is placed in the front, at the center, two in the rear corners. By acting on a screw, it is possible to raise the printing table (that is, to bring it closer to the nozzle) or to lower it. The action on each screw affects the spatial arrangement of the entire plane. There is an automatic setup for calibration; once selected, the printer will alternatively position the nozzle in correspondence with the three screws. Using

a thickness gauge and acting on each screw, it is possible to adjust the height. It is good to repeat these steps a second (and even a third) time to check that the calibration is satisfactory. The process involves the subsequent printing of a certain number of "concentric" rectangles of decreasing size in other printers. The process is long enough for the operator to observe the thickness of the deposited filaments and adjust the height accordingly where necessary. The next rectangles are to verify that the correction has been adequate.

Surface preparation

Before each print, it is necessary to clean the surface very carefully and deposit an adhesive substance on its surface to limit delamination risk. Cleaning the top is extremely important: any residue influences the success of the process as it alters the distance between the top and nozzle and affects adhesion. The discussion on defects can also be extended to intrinsic defects of the print bed; although visually perfect, it can be characterized by a random distribution of defects (generally crests and roots). These defects are inevitable unless their location is identified and avoided (where possible). A series of precautions allows to mitigate their effect: thicker layers, printed at a slower speed and at a higher temperature than the default values are usually less sensitive. Most polymers require the smooth surface of the print bed (borosilicate glass, in this case) to be treated to promote adhesion. In the case of PLA, this can be easily achieved with a simple hair spray.

Printing and final operations

Once the previous steps have been completed, the device is ready for printing. An SD memory card containing the .gcode file is inserted into its reader. The operator manually selects the file from the touch display, and printing begins. In this phase, it is possible to choose whether to have the printer read the print settings in the .gcode or use the manufacturer default values for the selected filament. At the end, the hot-end returns to a resting position, and the electrical resistances turn off. The component must be removed from the build plate close to the end of the process. Especially when the build plate has been heated during the process, it is possible that removing a cold piece will damage the plate due to the polymer shrinkage that occurred in the elapsed time.

1.5.1 First-time process parameters calibration

Whenever a new filament (or a new printer) is used, some previously discussed parameters need a preliminary test and quantification. Unique texts have been developed for their evaluation.

Quantification of the extrusion multiplier

As described, the filament may have a slightly different diameter than the nominal one. The printer acts as a mere executor. The amount of polymer to be extruded is calculated by the slicing software and communicated to the printer through the filament coordinate. If the filament diameter is larger than the nominal value, the nozzle will extrude more polymer; the reverse would occur in the opposite case. The extrusion multiplier corrects this effect. A first estimation can be obtained by measuring the effective diameter of the filament with a digital caliper. It is possible to determine the percentage difference in the cross-sectional area of the filament with respect to the expected nominal value from the diameter. Its inverse constitutes the first estimate of the parameter considered. For example, if the filament cross-section is 1% greater, 0.99 is the value to be considered. A more accurate verification can be achieved through a print test. A cube featuring a single perimeter and without any infill is printed (see Figure 1.11). The thickness of the cube wall should coincide with the extrusion width. The percentage difference can be calculated by measuring its thickness with a digital caliper. The inverse is the required extrusion multiplier. This test is known as *thin wall test*. The evaluation carried out on black Eryone PLA filament quantified this parameter at 1.05.

Figure 1.11: Thin wall test for extrusion multiplier quantification: the thickness of the wall should coincide with the bead width.

Quantification of the extruder and bed temperature

Filament manufacturers suggest a relatively wide range of printing temperatures; for Eryone black filament, $195 - 215\ ^{\circ}C$ was suggested as extrusion temperature. Within this range, it is possible to select the optimal temperature through a simple test. A "tower" consisting of several overlapping elements is printed (see Figure 1.12), each element at a different temperature, with steps of $5\ ^{\circ}C$. In this case,

the evaluation is qualitative: the element that does not show evidence of under extrusion (too low temperature) or excessive melting (too high temperature) has been printed with the right parameter. A temperature of 200 $°C$ was selected. As far as the build platform is concerned, its temperature was set to 30 $°C$. Several test prints revealed that with the platform at room temperature, adhesion was not difficult. That has been set to ensure uniformity in different environmental conditions (e.g. summer/winter).

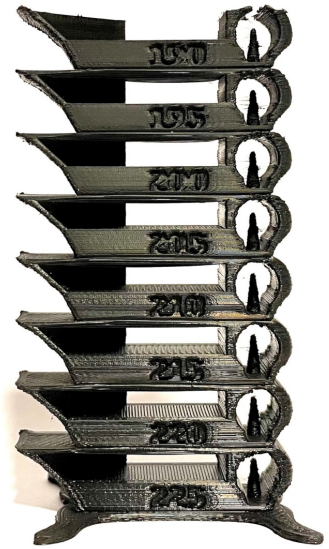

Figure 1.12: Temperature test for extrusion temperature quantification.

1.6 Shifting from prototyping to production

Shifting from a 3D model to a real object is very easy through FFF; this, joined with the small size of the 3D printers and the low cost of materials, justified the increase of interest developed around it. Those machines were thought of as rapid prototyping tools and used for a long time for non-functional items. How to shift from prototyping to manufacturing of a final component?
In all additive manufacturing processed parts, the mesostructure generally consists of overlapping layers; consequently, an overall directionality in the properties is present [2]. As the operator can (almost) freely orient the component into the printer reference system, the properties also depend on how the element is placed compared to the direction perpendicular to the layers. Furthermore, the part properties are strongly cross-linked with the production process itself, also understood

as the particular machine and the production parameters. A shift towards functional components can be achieved if the compliance with the performance criteria is verified. This requires the mechanical properties of the parts to be evaluated, and there is still much uncertainty in this regard [30]. This concept goes beyond the mere quantification and reflects the understanding of their structural performances and behavior. This topic is of growing interest in the literature, as numerous results are reported; two main threads/lines of investigation can be found:

- Linking some process parameters with the mechanical properties; in other terms determining the influence of some aspects of the process over the structural behavior of the items;
- Mechanical characterization with specific process parameters: once the process is set, some mechanical properties are estimated in such conditions.

On the fringe, attempts were made to predict properties of FFF fabricated components under analytical or numerical approximation. Less attention was paid to predict the mechanical behavior of printed components, using the mechanical properties so far determined (or predicted). Examples of research in which an attempt has been made to numerically evaluate the mechanical behavior of functional components exist but must be considered with caution. For example, assembled bolt and nut in 3D-printed ABS and PLA were analyzed using the Finite Elements Method in [31]. However, the mechanical properties of both have been assumed to be those of the base polymer, although several studies show that this is not the case [32].
The literature review of the state-of-art in this respect gives a good starting point for this research activity, as it shows some consolidated points but also reveals weaknesses and inspirations. Tension and compression tests are the most frequently performed and standard tests for mechanical characterization. The tests are similar; a generic beam is loaded along its longitudinal direction in tension or compression. The testing machine acts on the specimen through two grips, of which usually one moves at a constant speed. The specimen geometry is designed to highlight the mechanical response of the material in the load application direction; some details in the geometry are meant to allow gripping and facilitate the load transmission. The applied load and the measured strain are the data sampled during the test, through which a set of mechanical properties in the load application direction are determined [33]. The earliest investigations on tensile and compression mechanical properties of 3D-printed polymeric components can be traced back to Rodriguez et al. [34]. The authors evaluated the modulus of elasticity and the shear modulus of a single ABS filament and showed that they were higher than those resulting from tensile tests of printed specimens. In this evaluation, rectangular cross-section specimens were used following ASTM-D3039 [35]. The authors proved that the voids distribution characterizing the mesostructure did not fully justify this decrease. A linear infill

was used, and several raster angles were considered. The highest values of the considered properties belonged to specimens in which the filaments were aligned to the load application direction. The authors also considered the effect of aligned and skewed stacking sequences and that of the air gap. They found that a negative air gap (partial superposition among adjacent filaments) had a positive effect.

The anisotropic behavior of printed elements and the decrease of the bulk mechanical properties were also observed in [36] for tensile strength. Specimens with linear infill and different raster angles behaved differently; the highest strength was observed when the filaments were parallel to the load application direction, the lowest when they were normal to it. In this case, ASTM-D3039 was followed for tensile specimens design; the authors found that the classical dog-bone specimens required by ASTM-D638 produced unwanted stress concentrations that lead to premature failure. Besides, a decrease in the tensile strength was observed with respect to the bulk material. Similar results were also found with different polymers with respect to the anisotropy and the deterioration of the mechanical properties due to the printing process.

The influence of process parameters

In [37], ULTEM was considered, and dog-bone specimens were printed. The authors evaluated both the tensile strength and the tensile modulus, given that Digital Image Correlation was used as a non-contact strain measuring device. They found that both the mechanical properties depend on samples orientation relative to the printer reference system. In all configurations, a decline was observed with respect to injection molded ULTEM. The specimens with the filaments oriented in the load application direction had the closest values to the raw material ones. Durgun [38] observed similar results to Ahn [36] and Zaldivar [37]. The authors followed ISO 527 standard and tested several specimens varying their build orientation and their infill raster angles. FFF-printed components anisotropy was confirmed, as the mechanical properties significantly changed among the specimens built with a different orientation but the same infill. Simultaneously, the infill influenced the mechanical behavior, as the specimens build with different infill, but the same orientation, showed different mechanical properties. Higher values were measured as the filaments tended towards the load application direction. The tensile modulus and the tensile strength did not excessively differ from the values declared by the polymer manufacturer, except in the case of samples printed perpendicular to the printing surface when significant differences arose in terms of tensile strength. Similar results on different polymers confirmed that the raster angle for linear infills is crucial and induces a marked anisotropy. The filaments deposition direction showed the best mechanical performances under tensile tests, even for ULTEM [39].

Wittbrodt [40] studied a process parameter, the extrusion temperature, and an aesthetic parameter, the color of the filament, searching for their influence on the

tensile strength. As discussed in the previous section, PLA is naturally transparent; it takes different colors by adding additives. The measurements obtained through a diffractometer revealed that the additives induce a different percentage of crystallinity (in any case, higher than that found in virgin PLA). The tensile strength decreases as the percentage of crystallinity increases. The authors determined that extrusion temperature also affects tensile strength and percentage of crystallinity, however not in the same way. The tensile strength increases with increasing temperature, while there is a maximum percentage of crystallinity at an intermediate value of the temperature range considered. Tymrak [41] tried to validate the components printed in FFF from home-desktop devices for functional use. He has mechanically characterized both PLA and ABS, taking care to study how the layers thickness and two specific linear infills affected two mechanical properties in tension. As for ABS, the maximum tensile strength was found for thinner layers, the maximum elastic modulus for thicker layers. However, this relationship did not hold true for PLA, characterized by more significant variability in sets with constant parameters. The author concluded that within the limits of the mechanical properties of these polymers, their use for functional components is entirely admissible, as the determined properties are lower but similar to those of classical injection molding. The authors observed that the section planes of tested specimens appear homogeneous solid surfaces in correspondence with higher extrusion temperatures. They speculated that a significant thermal bonding developed inside each layer and outside it. This led to higher mechanical performances, especially in terms of strength. The possible application of FFF in the medical field led Carlier [42] to propose a Design of Experiment (DoE) to evaluate an extensive set of printing parameters systematically. The layer thickness was considered, together with the deposition rate and the extrusion temperature. ASTM D638 type IV specimens were printed and tested. Higher temperatures promoted higher tensile modulus and strength. Thicker layers induce lower values, instead. Those results were found for different printing directions; however, the extrusion temperature effect was not unique.

Uddin [43] also questioned the possibility of using FFF printed components as functional items. In this sense, these authors also evaluated the effects of the layer thickness on the mechanical performances, in a more general analysis that included how the specimens were arranged in the 3D printer volume. The analysis validated once again the anisotropic behavior of the printed objects. According to the authors, this limits the practical applications of objects in FFF. It was adopted as the reference standard. Surprisingly, the authors determined that the best mechanical performances arose in correspondence with thinner layers. The justification is that thinner layers induce a lower porosity and, therefore, a lower distribution of initiation failure points. The best mechanical performances are also those obtained when the load application direction is parallel to the XY printing plane. The influence of the same parameters was also assessed about the compression mechanical characterization tests, with comparable results. The layer height was also studied in [44],

together with the fill percentage, the specimen orientation in the print volume, and the number of peripheral filaments. Following a 4-parameter, two-level DoE, an experimental campaign was organized to determine their influence. Tensile strength and stiffness modulus were used as mechanical output parameters. The authors determined that the infill percentage and the number of perimeters are the most significant factors; the higher their value, the greater the output parameter. The infill percentage has a simple explanation: a solid part is always more rigid and resistant than a partially hollow one, produced with the same principle and the same material. Instead, the peripherals filaments increase the number of filaments parallel to the direction of application of the load, which is undoubtedly an interesting starting point. The effect induced by the layer height is limited; however, the mechanical properties worsen as it increases. The authors also considered printing times, energy consumption, and component weight, reporting guideline values on the optimal build parameters depending on the individual and desired output. The number of peripheral filaments has also been investigated in [45]. It was found that the more filaments are arranged along the perimeter of the specimen, the greater its mechanical response. However, since the specimens have an elongated shape, the perimeter is parallel to the load direction, at least in the narrowest section. As discussed in [46], this point must be taken into serious consideration: the contribution of the perimeters can be high, so much to hide the infill behavior. The lack of standardization is evident here. Simultaneously, the number of perimeters cannot be considered an absolute parameter: their beneficial action manifests when they are parallel to the load application. However, it is the shape of the objects that determines their geometric characteristics, which means that their (positive) effect depends solely on the component shape.

A similar analysis has been proposed in [47]. The significant variability of PLA mechanical properties already found in [41] has been confirmed. It has been verified that the layer height affects, but only slightly, the variability of the mechanical properties. For both ABS and PLA, it is confirmed that high internal infill percentages induce high mechanical properties. The authors also verified the single filament properties before its processing through FFF, and determined that a decline in mechanical properties occurs across the printing process. This effect was evident for ABS (-22%, in the best combination of process parameters), much less for PLA (-4%). A few years earlier, the same process parameters, with the addition of raster width and air gap, were studied in [48]. The output function was the compressive strength of FFF-printed ABS parts. The alignment of the polymeric macromolecules in the extrusion direction justified the anisotropy of the components. At the same time, a key role has been recognized for porosity, which develops mainly in specific preferential directions (between the layers, between the beads). It is known that porous defects play a large role in determining the mechanical performance of AM components. Their quantity and distribution depend on the process; however, they might be negatively influenced by how the process

parameters are tuned and the specifics of the component shape. Several authors confirmed that pores in AM manufactured components initiate the failure and that their position with respect to the external surfaces is of great importance. The role of porosity was further confirmed in [49]. The authors verified that negative air-gaps reduce porosity and, as a collateral effect, increase the mechanical performances of the parts, even in traction. Positive air-gaps have a similar effect to infill percentages below 100%. The effect of porosity was also considered in [50, 51]. The authors proposed an optical method that justified why specific parameters affected the mechanical properties. The work focused on the tensile properties of PolyCarbonate (PC); the parameter used as a measure of the output was the tensile strength. It confirmed that larger distributions and sizes of voids adversely affect mechanical properties. By focusing on the width of the deposited layer and the air gap, a tensile strength increase up to 30% was possible. It was noted that the lowest the air-gap and the highest the bead width, the highest the tensile strength. The returned value is significant: the printing parameters contribution to the mechanical properties was already known, but this quantification gave an idea of their percentage weight.

Plott et al. [52] also analyzed the effects of voids in silicone 3D-printed tensile specimens. The linear infill was studied; the author considered different tool-paths, differently combining the outlines and the infill angle. In this way, different void configurations were obtained, which confirmed they acted as stress-concentrating features, limiting the capabilities in terms of ultimate tensile strength; disseminated, large, and elongated voids significantly reduced it. Incidentally, the configurations having minimal void arrangement acted similarly to injection-molded specimens. Similar to voids, edge corners originated combining a specific infill configuration and the geometry acted as stress concentration factors.

The lack of standardization in mechanical properties determination of FFF-printed items has been highlighted by various researchers [53]. It will be clarified further that ASTM D638 is generically aimed at plastic materials and targets their tensile properties. It does not explicitly refer to components printed through FFF. Some authors questioned whether the proposed geometries were adequate for this production technology; others studied the influence of the different geometries proposed in the standard on the output results. Laureto [54], for example, considered the differences obtained in terms of tensile strength between type I and type IV specimens. The two geometries differ in size and the connection between the narrowest section and the terminal expansion. Differences in the results were observed. The authors explained this with the influence of the geometry on the mesostructure. Therefore, the authors recommended that the specimens have geometries equivalent to the real ones of the components in question, further reducing the possibility of standardizing the tests. Similar results and similar considerations were reported by Torrado [55] after an experimental campaign that involved all five types of specimens provided for by the ASTM standard.

A broader perspective reveals that many authors concentrated on reinforcing materials embedded in printable-polymers to improve the mechanical properties. For example, Ning [56] studied the characteristics of FFF specimens starting from an ABS filament to which carbon fibers of different lengths and amounts were added. A similar study was carried out by Justo [57], who used long fibers instead and Nylon as the base polymer. In parallel, PLA was also considered a printable matrix of carbon fiber composites in [58] and [59]. The contributions to this line of research are many, as reported in [60]. Recently, researchers began to extend research on the effect of printing parameters on such new composites [61]. Even in this the effect of porosity was studied. [62]. The discussion on this line of research is deliberately restricted: as already stated, this research work aims to validate the extension to the manufacture of Fused Filament fabricated components by discussing a constitutive model. It is understood that the mechanical properties in any way determined will be of the order of magnitude of those of the respective polymer. Polymers have naturally limited mechanical properties [63]. The applications in which these are not adequate require different materials or alter the mechanical characteristics and are not the purpose of this work.

Mechanical properties under specific process parameters

As already discussed, the mechanical properties of FFF components need to be evaluated as they differ from those (already known) of the reference polymer. Lay et al. [32] discussed an interesting example in this sense on three different polymers: ABS, PLA, and Nylon. Impact resistance, and two tensile properties, stiffness and strength, were considered. The reference values for all three polymers were quantified from specimens manufactured by injection molding. The reported differences are remarkable: the minor was found in the stiffness modulus of 3D-printed Nylon (-14%), while it settled at almost -50% for PLA. These results certainly provide design indications, but they were obtained (and they are therefore valid) through a single type of specimen, produced with the printing profile recommended by the device manufacturer for each filament. Raj et al. [64] aimed to compare PLA with ABS in the biomedical field. Some mechanical properties were determined, and the degradation of the same elements in different environments was studied. ASTM D638 type V specimens were probably printed in a flat position with respect to the building plane: no printing parameters were reported. Salim [65] carried out an experimental campaign involving both tensile and flexural tests, targeting ABS and PLA specimens printed in FFF. The author reported in detail the behavior of the two polymers. In particular, PLA appeared to be more resistant and rigid, both in traction and bending than ABS. However, the latter bears more significant deformations before rupture. The tests were performed according to the Type IV ASTM D638 standard. The production of the specimens, however, took place according to fixed printing parameters.

1.7 Estimating the mechanical response

The previous section clarified that the mechanical properties of the additively manufactured parts depend on the process and the characteristics of the polymer. This limits the use of FFF for producing functional parts [66], but it is still a problem that could be overcome if a campaign of mechanical tests is performed with the machine, polymer, and process parameters to be used. The most critical issue relates to anisotropy: even if specific process parameters are set, layered processing, raster angle, component orientation, and void distribution keep the major players in this context. Within the same component and in specific conditions, the degree of anisotropy can be as high as 50% [67].

Most of the research groups conducted tensile tests following the standard test method for polymeric materials, ASTM D638. Although this may seem an established point, some researchers questioned what specimen type was adequate among the dog-bone suggested geometries. It has been reported [36, 68] that those geometries produced premature failures in correspondence with specimen fillets due to stress-concentration. This issue does not always occur because it relates to the geometry-infill interaction, which is not the same with different printing parameters. In such cases, the researchers proposed the rectangular cross-section geometry required by ASTM D3039 for composite materials. By grouping the research works homogeneously, the heterogeneity of the results would still be wide. Leaving aside the process parameters linked to the single bead characteristics (dimensions, temperatures, speed), different mechanical properties would be found when:

- Different specimen geometries are considered, which suggests that a part-to-part variation may exist.
- Different infill strategies are used.
- The specimen is differently positioned and oriented in the build volume, which suggests that an intra-part variation may exist.

This variability limits the chances to exploit this technology for end-user functional parts: the mechanical properties to be used in a design phase are a question. A designer could choose all the technological parameters, such as height and width of the deposited bead, temperatures, speed, infill strategy. The row material and its manufacturer could be chosen once, and a characterization campaign could be run. However, the mechanical properties would still depend on the orientation of the specimens and their shape; the component would have an anisotropic behavior. The lower values recorded in the considered sample could be used. This would be conservative, but it would not allow the material to be fully exploited with a view to structural optimization. Knowledge of each printing parameter contribution is not sufficient; a different assessment is required. The next chapter will focus on the macrostructure observed in the objects printed with a linear infill strategy. In

this context, a constitutive model of the printed material will be asserted. Based on this hypothesis, a standardized procedure will be discussed and validated to fully characterize its mechanical behavior. This procedure will make the structural analysis of printed elements possible.

Chapter 2

Theoretical background of the research activity

This chapter discusses the theoretical background behind this research work. Understanding how to approach the components printed via Fused Filament Fabrication (FFF) to determine a constitutive model for structural verification is the goal. The possibility of describing the mechanical behavior through the Classical Lamination Theory (CLT) will be outlined for quasi-solid elements [1] with linear infill and fixed printing parameters. To this aim, the mesostructure of FFF layers will be discussed in-depth, drawing a parallel with uni-directional composite laminae highlighting the appropriate distinctions.

2.1 Introduction

The peculiarities of Fused Filament Fabrication have been described in Chapter 1; a specific focus has been made on the process and its main parameters. The possibilities of polymeric 3D printing already discussed raised the interest of researchers. The development of Additive Manufacturing technologies in general, and FFF in particular, is of intense interest in those application scenarios where a fast shift from design to product matters. This is even more true for components with complex machining. The material performance prediction is a challenge that prevents an intensive use of those techniques. Nowadays, the design of any component capable of sustaining a load is always complemented by a simulation of its mechanical performances; those simulations are usually needed to predict its behavior before production. They require a constitutive model for the material,

[1] Cuan-Urquizo [46] defines quasi-solid the FFF-printed elements with 100% infill; "quasi" comes from the unavoidable occurrence of voids owed to the process.

describing its mechanics, and a set of *coefficients*, quantifying it. To design components and select materials, a detailed quantification of the mechanical properties is required. The relevant standards are then identified as a function of the material itself and the inherent peculiarities of its intended use. After it has been processed through a generic technology, the mechanical properties of a material are not necessarily those of the raw material. The effects of processing methods on engineered materials are also a great interesting topic, as production technologies cannot be fully exploited if this step has not been thoroughly discussed. The importance of this theme is endorsed by the high number of published papers that were considered in Chapter 1. However, the literature review highlighted that a deeper understanding of the mechanical behavior of these components is needed, which is often problematic. Each print parameter has its individual influence; however, their combination leads to a result which is difficult to predict. With fixed parameters, however, the mechanical behavior is a function of the specific direction considered. The anisotropic behavior has been identified by several authors, who have discussed it explicitly or implicitly. However, few works in the literature deal with a predictive model of mechanical properties, which is useful for validating the structural behavior of printed objects and has been validated with actual boundary conditions.

2.2 Micromechanic and macromechanic approaches to FFF

At least two different approaches allow estimating the mechanical behavior of a structure printed via FFF. The micromechanical methods proposed in the literature focused on a single bead level and its interaction with the surrounding ones. These tools are handy in analyzing stress and strain fields at the local level but have found no application in more complex and larger structures. Therefore, a macromechanical approach at a global level is discussed; this will represent the present research foundation.

2.2.1 Micromechanics approaches for mechanical properties predictions

A micromechanical approach to the problem was proposed by Croccolo et al. [69], who developed an analytical model for tensile strength and stiffness prediction. This model considers as input the mechanical properties of the feedstock polymer; the mechanical characterization is made via injection-molded specimens in isotropic conditions. The authors studied the problem focusing on linear infill solid prints with a different number of perimeters, subjected to a load parallel to the build plate. In this context, a fundamental element was defined. It includes

inclined rasters (those of the infill), longitudinal rasters (those of the perimeters), or both. All rasters within the same element cooperate in handling the applied load. The axial stiffness of each raster is assumed to be equal to that found for the material feedstock. According to an experimentally calibrated constant, the adjacent beads exchange a tangential force proportional to the elongation gradient. The authors then printed dog-bone specimens according to ASTM D638, following all five proposed geometries; the first one calibrated the adhesion. The model was then used to predict the mechanical behavior of the remaining geometries. With four perimeters and a raster angle of $[+45°/-45°]$, predictions were excellent, with an error as low as 6.6%. Cuan-Urquizo et al. [70], on the other hand, proposed a solution that took porosity into account. The authors considered that infills below 100% induce a controlled porosity. By alternating the raster angle between 0° and 90°, the beads formed a lattice-like structure whose mechanical properties can be predicted by a simple finite element model. In this model, each bead is represented by many beam elements (Timoshenko formulation). The nodes of each element lie in the physical contact points between the beads. The mechanical properties of each element were obtained through a tensile test on a single printed bead, with a length of 10 mm, which required a dedicated instrument. This model was then validated through an analytical approach based on the rule of mixture. These methodologies are interesting because they highlight fundamental aspects in predicting local failures: both investigated the stress field at the local level. However, they are not conclusive when analyzing components with complex geometry in the context of generic boundary conditions; the macromechanical response appears to be more representative.

2.2.2 A macromechanical approach to FFF parts

The macromechanical approach leaves out the behavior of the structure at the local level to search for a constitutive model representing an homogeneous equivalent material. A critical consideration must be made as how to determine these properties. Standardized methods for measuring a wide range of mechanical properties of polymeric materials exist since a long time. Consequently, most authors applied the existing standards to measure those properties in FFF 3D-printed elements. A look at those standards allows to see how detailed are the descriptions of the scope and target of each of them. Taking as an example the Standard Test Method for Tensile Properties of Plastic, ASTM D638 [71], reference is made to Sheet, Plate, Molded Plastics, Rigid Tubes, and Rigid Rods. While describing the features of the specimens, several details are given to the surface finish, in a way related to specific machining technologies. In this respect, there are at least three comments that can be made [72]:

1. Are the existing standards appropriate for FFF processed parts?

2. If they are, what is the reason for the lack of uniformity in preexisting studies?

3. If they are not, how to design a process of standardization?

The differences between traditional polymer processing and FFF arose in the previous chapter. A sequence of polymeric layers deposition, coupled with a peculiar pattern for each of them, is unlikely to have the same mechanical behavior of a homogeneous melting. An appropriate standardized test should relate both the material properties and the particular mesostructure. A further challenge comes from the fact that the mesostructure itself is not unique and might depend on the part design and the process parameters. The previous chapter discussed that the user could customize several parameters that directly act on the mesostructure, and this customization is not restricted just to the infill pattern. Focusing on a simple linear infill, the raster angle can be customized (and it can vary through the layers), the bead width and height can be chosen, their in-plane superposition (or separation) may be set. It is evident that different parameter configurations yield differ mesostructures and, therefore, resulting in different mechanical behavior. Such configurations, such mesostructures, will have different degrees of anisotropy and therefore manifest different behaviors among them and with respect to a homogeneously melted mesostructure. The combinations of printing parameters are numerous, and an attempt to propose and validate a constitutive model for each of them is a daunting task. This work focuses on a specific infill, as it seemed to have specific characteristics that might simplify a constitutive model definition, implementation, and validation. While discussing the characteristics of FFF in Chapter 1, it was noted that the *linear infill* is undoubtedly the easiest path to be considered. Its graphical representation is shown in Figure 2.1. Considering for a moment a single layer, one can appreciate that each filament is deposited in parallel with the adjacent ones. A set of parallel filaments constitutes each layer, all oriented in the same direction. A look along the vertical direction allows to distinguish among two further configurations; the *aligned configuration*, in which each filament of the new layer is deposited above the corresponding one of the previous layer, and a *skewed configuration*, in which each filament of the new layer is deposited with a certain offset with respect to the corresponding one of the previous layer. The difference between the two is also clarified in Figure 2.2, where the two infills are represented through a cross-section view. Consider the *linear infill* with *aligned configuration*. Inside each layer, the filaments are all oriented along the same direction, thus parallel among them. This situation does not change while moving from layer to layer; symmetries exist. Simultaneously, if one considers a plane parallel to filaments and perpendicular to layers, the situation does not change. This kind of mesostructure seems to simultaneously manifest:

- a noticeable degree of inhomogeneity
- the presence of three planes of geometrical symmetry

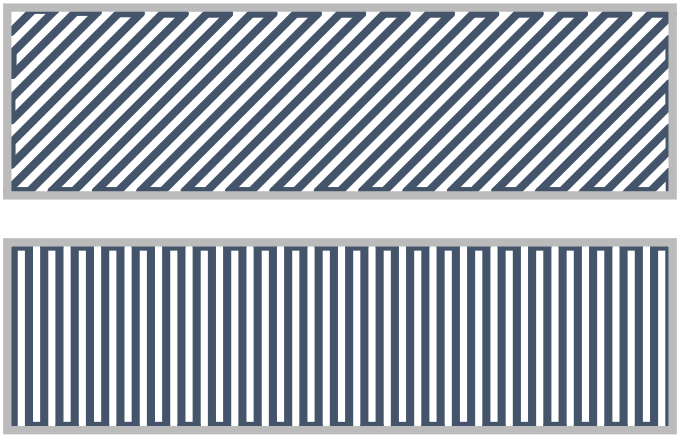

Figure 2.1: Example of two layers with linear infill and different raster angle.

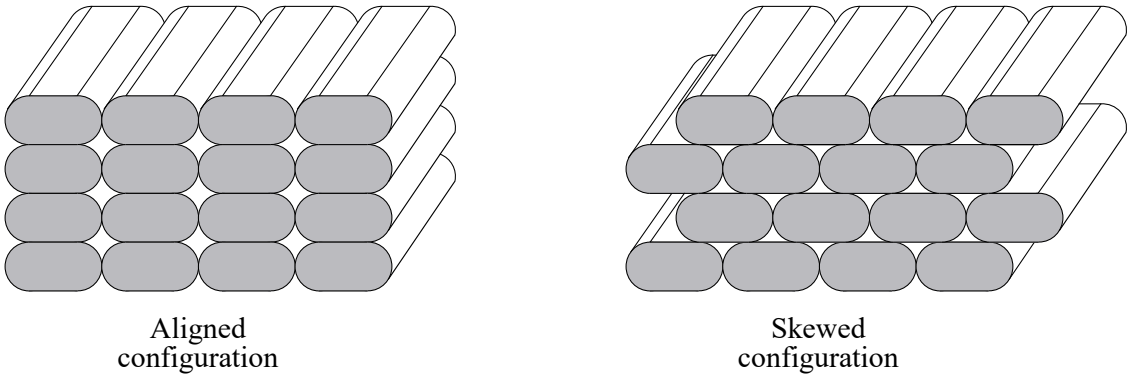

Figure 2.2: Cross-section of a FFF component with rectilinear infill; aligned configuration vs. skewed configuration.

Previously it was mentioned that the mechanical properties might differ from that of the raw material due to processing. This mesostructure leads one to suspect that, beyond a generic anisotropy, the mechanical properties might manifest some directionality. Some characteristics of such a mesostructure might be speculated.

First effect - molecular chain alignment

It is well known that during extrusion, chain alignment occurs [73]. Polymer molecules are naturally randomly coiled. However, the friction with the internal wall of the extruder aligns them with the flow direction, which is also the deposition direction. As linear polymer chains have a unidirectional nature, anisotropy arises when a common direction substitutes the random orientation. Along this direction, the elastic modulus and the strength increase while decrease along the perpendicular directions to it [74]. It might be assumed that something similar takes place in each filament extruded during a FFF process.

Second effect - time of deposition

In the deposition direction, a constant and continuous extrusion occurs as long as the requested length has not been completed. Instead, in the two directions perpendicular to it, a new filament is extruded next to the previous or above the corresponding filament of the last layer. The previous filament and the underneath filament were deposited at earlier stages: filaments at different drying stages surround each new filament.

Third effect - bead cross-section shape

As discussed in Chapter 1, each isolated bead has an oval-shaped transverse cross-section, with two symmetry axes. The vertical dimension is limited by the layer height, the horizontal one by the bead width. The flow rate induces a certain pressure over the new filament, which is pressed over the previous layer and spread sideways. This increases the contact area between filaments; however, two superposed filaments have a greater contact surface than those side by side [75].

Fourth effect - voids distribution

A key aspect is represented by the distribution of voids inside the part. By excluding tangency voids and localized defects, FFF produced components show a certain distribution of voids even with a 100% infill. This manifests itself as a series of lined up voids between adjacent extruded filaments. Due to their shape, their apparent cross-sections differ as a function of the direction of view. Some details are shown in Figure 2.3.

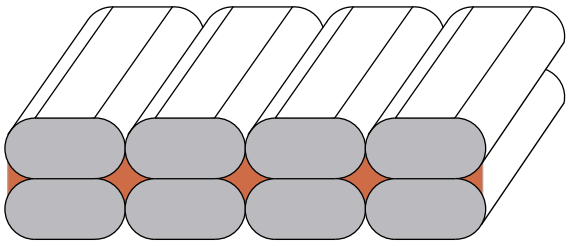

Figure 2.3: Voids in a cross-section of a FFF component with aligned linear infill. Voids are outlined in orange.

The considerations made up to now on the *linear infill* with *aligned configuration* show that some *special* features exist along with three specific and mutually orthogonal directions. Besides, those features are symmetric with respect to the three mutually orthogonal planes defined by those three directions. Evident geometrical symmetries also straighten those symmetries. If that symmetry was reflected

in the mechanical properties, an orthotropic behavior would result. As shown before, the mechanical properties might take higher values in a specific direction while deteriorating in the other two. This issue can also be found in composite laminae embedding unidirectional long fibers, which are characterized by an orthotropic behavior. In this respect, the mesostructure gives further confirmation: the pattern of a single FFF layer and a single Uni-Directional Composite (UDC) lamina are very similar. If such similarity would result in a similar mechanical behavior will be discussed in detail in the following.

2.3 The analogy between FFF and Uni-Directional Composites

An analogy between specific FFF components and Uni-Directional Composites (UDCs) laminates would allow deriving some analysis methodologies and open up the possibility of standardizing the characterization process. The main characteristics and properties of a laminate will be presented here as a reference to underline similarities and differences between the two categories.

2.3.1 Uni-Directional Composites

A Composite Material (CM) is a heterogeneous material made of two (or more) constituents. The physical, chemical, and mechanical properties of each of the constituents differ among them. Furthermore, the overall mechanical properties of the resulting CM differ, themselves, from those of the constituents. As a rule, they are a certain function of the mechanical properties of the constituents, their relative volume fraction in the composite, their chemical interaction, and their relative arrangement. Among CMs, Fibre Reinforced Composites (FRCs) distinguish themselves by the peculiar shape of a constituent. FRCs are made of two physical phases (that is, two different materials), the *fibers* and the *matrix*, plus a third component, the *interface region* among them. FRCs can be classified following several criteria, which include (but are not limited to) the characteristics of the fibers (discontinuous/continuous, short/long, aligned/random, etc.) and the nature of the matrix (metal, ceramic, polymeric), etc. This introduction is not meant to describe FRCs comprehensively. A detailed description will be given only for a specific subcategory. Among Fibre Reinforced Polymers (FRPs), featuring a polymer-based resin as a matrix, one can distinguish the Uni-Directional Composites, a special class of FRCs in which the fibers are oriented along the same direction. For further reference, this direction is commonly referred to as the *direction 1* in the material reference system as detailed in Figure 2.4. The same image allows going into the details of the two phases of a UDC, described below:

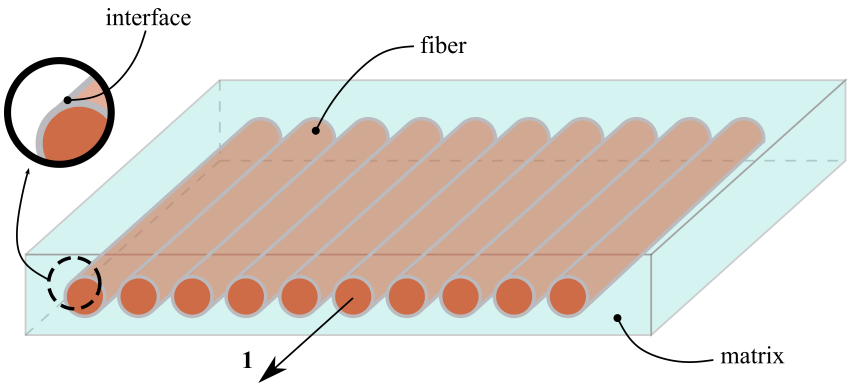

Figure 2.4: Phases and components of a unidirectional lamina.

- *Fibers*: they are in the form of cylindrical bars. Those employed in composite materials have high mechanical properties (elastic modulus and tensile strength) compared to those of the matrix. However, an isolated fiber can only sustain tensile loads along its length. A typical range of diameters is $1 - 10\,\mu$m. Between the two components the fibers are the stiffer phase.
- *Matrix*: the role of the matrix is fundamental, although its mechanical properties would not appear to be significant if compared to those of the fibers. As the overall concept, the matrix holds together the fibers and gives the form to the component. Furthermore, the matrix allows the load to be transferred among the fibers. The mechanical properties of the matrix are those of the bulk material.

As anticipated, the mechanical properties of fibers and matrices are quite different: the firsts are much stiffer and stronger. Once they are combined into a CM, their interaction influences the overall properties, which are a function of:

- The mechanical properties of the fibers.
- The mechanical properties of the matrix.
- The fibre Volume Ratio (VR).
- The orientation of the fibers into the composite.
- The interface between fibers and matrix.

The way the applied load is transferred between fibers and matrix can be explained by analyzing a single fiber surrounded by the matrix. Assume the load is applied to this body along the longitudinal axis of the fiber. Two different patterns may come out. When the body is *under tension*, the load is exchanged between the matrix and the external surface of the fiber through shear stresses. To one end of the

fiber, the shear stress takes its maximum value. As it decreases up to zero moving along the fiber, tensile stress develops inside it, with an opposite trend. The load is, then, balanced by the two stresses together. We would not find an isolated fiber inside a body made of unidirectional composite in a much more general situation. Instead, we would find that further ones surround each fiber. The external load is, therefore, distributed among the fibers. Tensile stress develops inside each of those cooperating in load balancing. If a fiber is discontinued or breaks, a reversed balance between normal and shear stresses occurs in the end section. The normal stress decreases up to zero, and the shear stress increases up to a maximum value. The matrix transfers the load to those fibers nearby through shear stresses. When the body is *under compression*, the load transfer between the matrix and the fiber takes place with the same mechanism. However, compressive stress develops inside the fiber, which would lead it to buckle. In contrast with this, the matrix provides lateral restraint, lowering this tendency.

The fundamental building block of composite materials is the *lamina*, a sheet of many fibers embedded into a matrix. A *unidirectional lamina* is a lamina in which all the fibers are oriented along the same *direction*. As the lamina has a two-dimensional nature, another key direction arises. For further reference, the direction that is normal to the fibers and lies in the lamina plane will be referred to as *direction 2* in the material reference system. The mechanical behavior in the two directions is different. In direction 1, laminae show the highest strength and stiffness, while those properties are lower in direction 2. The direction normal to the fibers and normal to the lamina will be referred to as *direction 3*. Directions 1, 2 and 3 constitute the so called *Material Reference System*, whose definition is detailed in Figure 2.5. A single lamina is insufficient; several laminae need to be piled along direction 3 up to obtain the necessary thickness and strength. A *laminate* is a set of laminae stacked up. The laminae may be arranged with different fiber orientations inside each laminate to obtain the desired stiffness and strength. A *unidirectional laminate* is a laminate in which only unidirectional laminae are stacked up, all with the same fiber orientation. Such a unidirectional laminate behaves as an orthotropic material; the material reference systems of each lamina are aligned. For this reason a single material reference system can be defined, in which three material symmetry planes can be highlighted:

- The plane $1-2$, parallel to the fibers and the laminae.
- The plane $1-3$, parallel to the fibers and orthogonal to the laminae.
- The plane $2-3$, orthogonal to both the fibers and the laminae.

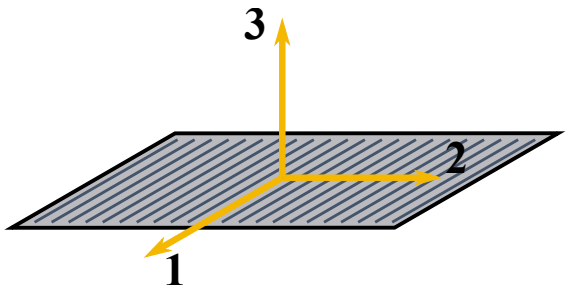

Figure 2.5: Material reference system of a unidirectional lamina.

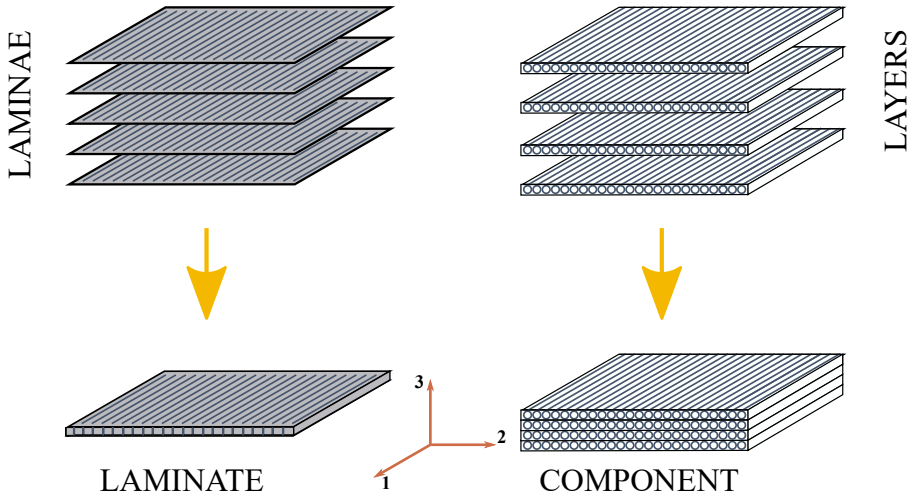

Figure 2.6: A unidirectional laminate compared to a FFF component with linear infill.

2.3.2 Peculiarities of FFF with respect to UDC

Figure 2.6 compares a set of UDC laminae with a set of linear infill FFF layers in the upper part; a UDC laminate with a linear infill FFF component in the lower part. The geometric similarity is indisputable: in both cases, elongated elements are arranged in a preferential direction: the fibers and the beads, respectively. Similarly, in FFF configurations, three prevailing directions can be identified. *Direction 1*, as in unidirectional composites, runs parallel to the beads; *direction 2* is orthogonal to the beads but parallel to the layers; *direction 3* is orthogonal to both the beads and the layers. These three mutually orthogonal directions originate three planes of geometric symmetry:

- The plane $1-2$, parallel to the beads and the layers.
- The plane $1-3$, parallel to the beads and orthogonal to the layers.
- The plane $2-3$, orthogonal to both the beads and the layers.

In analogy, the mechanical properties are different when evaluated in these three directions, as reported in [76], [77], [78] and discussed in Chapter 1. The best mechanical performances occur in direction 1, while the other two show lower values. In analogy with the fibers of the UDCs, it can be assumed that the beads are responsible for supporting the applied load. The first difference arises here. In 3D-printed components, no matrix is present between the beads. There is no phase responsible for transmitting the load between adjacent beads other than the beads themselves. The beads are in contact with each other and transmit the load directly among them. The second difference is in the shape of the single bead cross-section: unlike the fibers, well represented by a circular section (even if not perfect) it has an oval shape, flattened along direction 3. At the same time, FFF allows better control over the degree of alignment of the beads than UD fibers, as deposition occurs individually. These three points are of fundamental importance.

In FFF, the deposition strategy induces two types of bonds: *intra-layer bonds* are generated between adjacent filaments within the same layer; *inter-layer bonds* instead arise between two superposed beads of different layers (see Figure 2.7). During the deposition of a bead, a combination of molecular diffusion and cross-

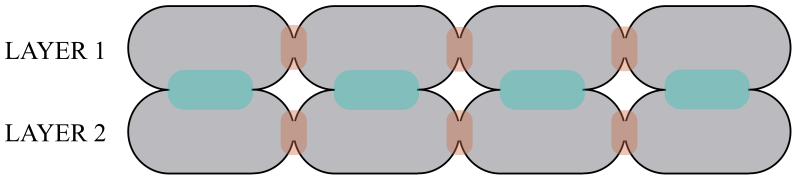

Figure 2.7: Cross-section of a FFF component: intra-layer bonds (orange) and inter-layer bonds (light-blue).

linking occurs between the polymer chains. Some authors describe this phenomenon as viscous sintering [79]. Frenkel [80] had already discussed it; with the supply of a sufficient amount of heat during a given time interval, two adjacent polymeric filaments tend to coalesce to reduce the free energy available and the overall surface area. Coalescence is never complete between FFF beads, as the elapsed time before complete solidification is limited. Each of them is not completely in contact with the surrounding ones; due to the cross-section shape of the beads, the intra-layer and the inter-layer contact surfaces differ. Consequently, the bond strength depends on the size of the contact surfaces between adjacent beads. The characteristics of these two types of bonds are different, as the time in which they develop and the available heat are different. Inside the same layer, it is possible to assume that the time elapsed from the deposition of a bead and the one next to it is not sufficient for the first to cool down completely. The new bead, therefore, comes into contact with a polymer at a still moderate temperature. For the beads deposited on top of a previous layer, a longer time may have elapsed. However, different cooling rates can also occur locally [79], which further affects the coalescence between the beads.

Quantifying the degree of coalescence between adjacent beads is complicated from the parallel occurrence of mass transfer and transient heat phenomena [81].

Given these differences, the micromechanical behavior between FFF and UDC will undoubtedly be different. This is also demonstrated by the attempt reported in [34] to extend the *rule of mixtures* to FFF. For unidirectional composite materials, this rule allows predicting the mechanical properties of composite material through an average of the properties of the constituents, weighted as a function of their respective volumetric fraction [82]. In the case of Fused Filament fabricated parts, this rule could be applied considering the stiffness modulus of the feedstock filament and its volumetric fraction in the component; the last obtained taking into account the porosity. The estimates, however, do not provide satisfactory results unless they are corrected by an empirical factor taking into account the bond strength [83]. Despite this, at the macromechanical level, the analogy may still hold.

Macromechanics studies composite materials behavior through the apparent properties of equivalent homogeneous material. After considering the microstructure and defining the elements of primary importance, it deals with average mechanical properties that neglect the microstructure but directly result from how its effects were considered [84]. Such a study could also be conducted on Fused Filament fabricated components: ignoring the local interaction between adjacent fibers and working with the apparent properties of equivalent homogeneous material.

2.4 3D constitutive equations

The fundamentals of the stress-strain relations are proposed in this section; these concepts and their notation will be used in the next chapters. Consider an infinitesimal cube made of a linear-elastic material. The cube is located in an orthogonal coordinate system $1-2-3$, with its faces aligned with the reference system planes. Nine components need to be specified to define the stress state at a point completely. Each stress component depends not only on its direction but also on the surface upon which it is applied. Each surface of the infinitesimal cube can be uniquely defined through its normal direction. This way, each stress component σ_{ij} needs two indices to be defined; i indicates the direction in which the stress is applied, j the surface upon which. σ_{ij}, therefore, represents the i^{th} component of the stress tensor, acting on the j^{th} direction. Figure 2.8 completely shows the 9 components of the stress tensor. The Cauchy stress tensor groups all the components that define entirely the stress state at a point; it can be expressed by a 3×3 matrix:

$$\boldsymbol{\sigma} = \sigma_{ij} = \begin{bmatrix} \sigma_{11} & \sigma_{12} & \sigma_{13} \\ \sigma_{21} & \sigma_{22} & \sigma_{23} \\ \sigma_{31} & \sigma_{32} & \sigma_{33} \end{bmatrix} = \begin{bmatrix} \sigma_{11} & \tau_{12} & \tau_{13} \\ \tau_{21} & \sigma_{22} & \tau_{23} \\ \tau_{31} & \tau_{32} & \sigma_{33} \end{bmatrix} \tag{2.1}$$

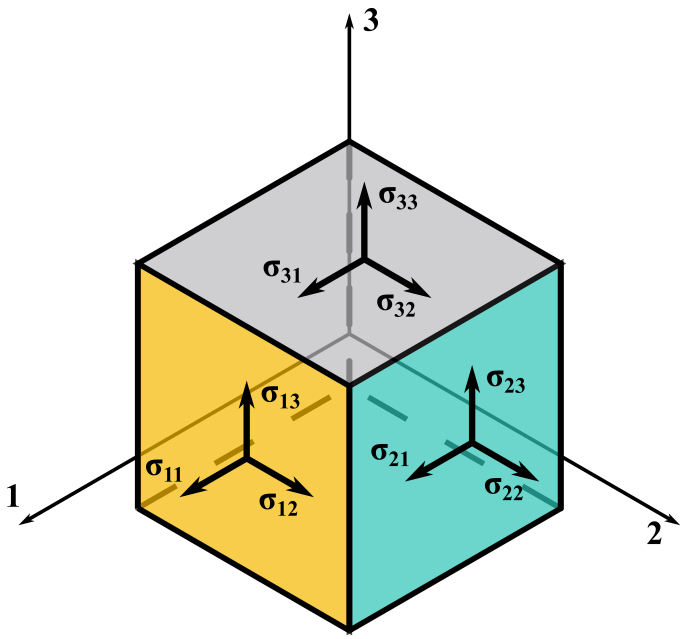

Figure 2.8: Stress tensor cube: 3D stress component notations.

The *normal stresses* σ_{ii} are the diagonal therms; they act normally to the surfaces, and their effect is to change the volume of the infinitesimal cube. The off-diagonal terms $\sigma_{ij} = \tau_{ij}$, with $i \neq j$, are the *shear stresses*, which tend to deform the infinitesimal cube without changing its volume. It can be proved that the stress tensor is symmetric, meaning that $\sigma_{ij} = \sigma_{ji}$, with $i \neq j$, by imposing the conservation of momentum. The Voigt notation takes advantage of this property and allows to compact the stress tensor in a 6-component stress vector:

$$\boldsymbol{\sigma} = \begin{bmatrix} \sigma_{11} & \sigma_{22} & \sigma_{33} & \sigma_{23} & \sigma_{13} & \sigma_{12} \end{bmatrix}^T = \begin{bmatrix} \sigma_{11} & \sigma_{22} & \sigma_{33} & \tau_{23} & \tau_{13} & \tau_{12} \end{bmatrix}^T \tag{2.2}$$

In case the cube is subjected to a certain stress field, a generic point would manifest some displacements. u is the displacement in direction 1, v the displacement in direction 2, and w the displacement in direction 3. The description of the strain tensor as a 3×3 tensor is in analogy with the stress one; its elements can be obtained by deriving the three displacements, as described by the Equation 2.3.

$$\epsilon_{ij} = \begin{bmatrix} \epsilon_{11} & \epsilon_{12} & \epsilon_{13} \\ \epsilon_{21} & \epsilon_{22} & \epsilon_{23} \\ \epsilon_{31} & \epsilon_{32} & \epsilon_{33} \end{bmatrix} = \begin{bmatrix} \frac{\partial u}{\partial x} & \frac{1}{2}(\frac{\partial u}{\partial y} + \frac{\partial v}{\partial x}) & \frac{1}{2}(\frac{\partial u}{\partial z} + \frac{\partial w}{\partial x}) \\ \frac{1}{2}(\frac{\partial v}{\partial x} + \frac{\partial u}{\partial y}) & \frac{\partial v}{\partial y} & \frac{1}{2}(\frac{\partial v}{\partial z} + \frac{\partial w}{\partial y}) \\ \frac{1}{2}(\frac{\partial w}{\partial x} + \frac{\partial u}{\partial z}) & \frac{1}{2}(\frac{\partial w}{\partial y} + \frac{\partial v}{\partial z}) & \frac{\partial w}{\partial z} \end{bmatrix} \tag{2.3}$$

By definition, the strain tensor also is symmetric, meaning that $\epsilon_{ij} = \epsilon_{ji}$, with $i \neq j$. The Voigt notation takes advantage of this property and allows to compact the strain tensor in a 6-component strain vector:

$$\boldsymbol{\epsilon} = \begin{bmatrix} \epsilon_{11} & \epsilon_{22} & \epsilon_{33} & 2\epsilon_{23} & 2\epsilon_{13} & 2\epsilon_{12} \end{bmatrix}^T = \begin{bmatrix} \epsilon_{11} & \epsilon_{22} & \epsilon_{33} & \gamma_{23} & \gamma_{13} & \gamma_{12} \end{bmatrix}^T \tag{2.4}$$

With the stress and the strain vectors defined, the linear material law linking strain to stress can be expressed by Equation 2.5.

$$\boldsymbol{\sigma} = \boldsymbol{C}\boldsymbol{\epsilon} \tag{2.5}$$

It holds for linear elastic materials or in the neighborhood of an equilibrium point when $\boldsymbol{C}$ is the tangent value. $\boldsymbol{C}$ is the so-called *matrix of elastic coefficients* and it is fourth-order tensor. In principle, it has $3^4 = 81$ coefficients; because of the minors symmetries it reduces to 36 elastic coefficients. However, similar reasoning of the one made with respect to the stress and the strain tensor leads to a reduction of the number of the independent elastic coefficients to 21. The stress-strain relation for the most general case of an *anisotropic material* is, therefore:

$$\begin{bmatrix} \sigma_{11} \\ \sigma_{22} \\ \sigma_{33} \\ \tau_{23} \\ \tau_{13} \\ \tau_{12} \end{bmatrix} = \begin{bmatrix} C_{11} & C_{12} & C_{13} & C_{14} & C_{15} & C_{16} \\ C_{12} & C_{22} & C_{23} & C_{24} & C_{25} & C_{26} \\ C_{13} & C_{23} & C_{33} & C_{34} & C_{35} & C_{36} \\ C_{14} & C_{24} & C_{34} & C_{44} & C_{45} & C_{46} \\ C_{15} & C_{25} & C_{35} & C_{45} & C_{55} & C_{56} \\ C_{16} & C_{26} & C_{36} & C_{46} & C_{56} & C_{66} \end{bmatrix} \begin{bmatrix} \epsilon_{11} \\ \epsilon_{22} \\ \epsilon_{33} \\ \gamma_{23} \\ \gamma_{13} \\ \gamma_{12} \end{bmatrix} \tag{2.6}$$

Such a relation, expressed by Equation 2.6 holds when no symmetry plane exists for the material properties. There are categories of materials for which the number of independent elastic constants may be further reduced. *Monoclinic materials* are those in which a single plane of material properties symmetry exist. Assuming $1-2$ as the plane of symmetry, the number of independent elastic constants reduces to 13, and Equation 2.6 becomes:

$$\begin{bmatrix} \sigma_{11} \\ \sigma_{22} \\ \sigma_{33} \\ \tau_{23} \\ \tau_{13} \\ \tau_{12} \end{bmatrix} = \begin{bmatrix} C_{11} & C_{12} & C_{13} & 0 & 0 & C_{16} \\ C_{12} & C_{22} & C_{23} & 0 & 0 & C_{26} \\ C_{13} & C_{23} & C_{33} & 0 & 0 & C_{36} \\ 0 & 0 & 0 & C_{44} & C_{45} & 0 \\ 0 & 0 & 0 & C_{45} & C_{55} & 0 \\ C_{16} & C_{26} & C_{36} & 0 & 0 & C_{66} \end{bmatrix} \begin{bmatrix} \epsilon_{11} \\ \epsilon_{22} \\ \epsilon_{33} \\ \gamma_{23} \\ \gamma_{13} \\ \gamma_{12} \end{bmatrix} \tag{2.7}$$

A particular class of monoclinic material is that of *orthotropic materials*, for which three orthogonal planes of material symmetry exist. The intersections of those three planes produce three orthogonal directions, known as the principal material directions. If the reference system $1-2-3$ and principal material directions coincide, the independent constants of the stiffness matrix further reduce to 9, and Equation 2.7 becomes:

$$\begin{bmatrix} \sigma_{11} \\ \sigma_{22} \\ \sigma_{33} \\ \tau_{23} \\ \tau_{13} \\ \tau_{12} \end{bmatrix} = \begin{bmatrix} C_{11} & C_{12} & C_{13} & 0 & 0 & 0 \\ C_{12} & C_{22} & C_{23} & 0 & 0 & 0 \\ C_{13} & C_{23} & C_{33} & 0 & 0 & 0 \\ 0 & 0 & 0 & C_{44} & 0 & 0 \\ 0 & 0 & 0 & 0 & C_{55} & 0 \\ 0 & 0 & 0 & 0 & 0 & C_{66} \end{bmatrix} \begin{bmatrix} \epsilon_{11} \\ \epsilon_{22} \\ \epsilon_{33} \\ \gamma_{23} \\ \gamma_{13} \\ \gamma_{12} \end{bmatrix} \tag{2.8}$$

For orthotropic materials, a particular relation holds between stresses and strains. Unlike anisotropic and monoclinic materials, no cross-relation exists between normal and shear stresses in the material principal reference system. In some orthotropic materials, it might exist a plane in which the mechanical properties are the same in all directions. This plane is defined as the plane of isotropy, and it allows to further reduce the independent constants to 5. Those material take the name of *trasversely isotropic*; the stress-strain relation takes the following form:

$$\begin{bmatrix}\sigma_{11}\\ \sigma_{22}\\ \sigma_{33}\\ \tau_{23}\\ \tau_{13}\\ \tau_{12}\end{bmatrix} = \begin{bmatrix}C_{11} & C_{12} & C_{13} & 0 & 0 & 0\\ C_{12} & C_{11} & C_{13} & 0 & 0 & 0\\ C_{13} & C_{13} & C_{33} & 0 & 0 & 0\\ 0 & 0 & 0 & C_{44} & 0 & 0\\ 0 & 0 & 0 & 0 & C_{44} & 0\\ 0 & 0 & 0 & 0 & 0 & (C_{11}-C_{12})/2\end{bmatrix} \begin{bmatrix}\epsilon_{11}\\ \epsilon_{22}\\ \epsilon_{33}\\ \gamma_{23}\\ \gamma_{13}\\ \gamma_{12}\end{bmatrix} \tag{2.9}$$

A significant number of materials exhibit an infinite number of symmetry planes, these are the so called *isotropic materials*. In such a case, only two independent constants are needed to build-up the stress-strain relation:

$$\begin{bmatrix}\sigma_{11}\\ \sigma_{22}\\ \sigma_{33}\\ \tau_{23}\\ \tau_{13}\\ \tau_{12}\end{bmatrix} = \begin{bmatrix}C_{11} & C_{12} & C_{12} & 0 & 0 & 0\\ C_{12} & C_{11} & C_{12} & 0 & 0 & 0\\ C_{12} & C_{12} & C_{11} & 0 & 0 & 0\\ 0 & 0 & 0 & \frac{1}{2}(C_{11}-C_{12}) & 0 & 0\\ 0 & 0 & 0 & 0 & \frac{1}{2}(C_{11}-C_{12}) & 0\\ 0 & 0 & 0 & 0 & 0 & \frac{1}{2}(C_{11}-C_{12})\end{bmatrix} \begin{bmatrix}\epsilon_{11}\\ \epsilon_{22}\\ \epsilon_{33}\\ \gamma_{23}\\ \gamma_{13}\\ \gamma_{12}\end{bmatrix} \tag{2.10}$$

2.4.1 A focus on orthotropic materials

In the previous paragraph, it was stated that, in the principal material directions, the relationship between stress and strains is that expressed in Equation 2.8, and that the number of independent elastic constants reduces to 9. However, the laboratory tests for the mechanical characterization of materials do not directly derive the stiffness matrix values. These tests allow measuring the so-called *engineering constants*; in the case of orthotropic materials, there are three types[2]:

- *Longitudinal moduli / Young moduli*: given a specific direction of loading, they correlate axial strain and stress.
- *Poisson ratios*: given a specific direction, they correlate the axial deformation with the corresponding deformation in a perpendicular direction.

[2]In the more general case of an anisotropic material, this list is supplemented by the *Chentsov coefficients* and the *coefficients of mutual influence* [85].

- *Shear moduli*: given a plane of shear loading, they correlate the shear strain to the shear stress.

The strains components can be obtained through those coefficients, imagining to apply one stress component individually at a time; in a three-dimensional stress state, they take the following expression:

$$\epsilon_{11} = \frac{1}{E_1}\sigma_1 - \frac{\nu_{12}}{E_1}\sigma_2 - \frac{\nu_{13}}{E_1}\sigma_3 \tag{2.11}$$

$$\epsilon_{22} = -\frac{\nu_{21}}{E_2}\sigma_1 + \frac{1}{E_2}\sigma_2 - \frac{\nu_{23}}{E_2}\sigma_3 \tag{2.12}$$

$$\epsilon_{33} = -\frac{\nu_{31}}{E_3}\sigma_1 - \frac{\nu_{32}}{E_3}\sigma_2 + \frac{1}{E_3}\sigma_3 \tag{2.13}$$

$$\gamma_{23} = \frac{1}{G_{23}}\tau_{23} \tag{2.14}$$

$$\gamma_{13} = \frac{1}{G_{13}}\tau_{13} \tag{2.15}$$

$$\gamma_{12} = \frac{1}{G_{12}}\tau_{12} \tag{2.16}$$

Equations 2.11-2.13 show that axial stresses and strain are linked, even if referred to different directions; Equations 2.14-2.16 show that as for the shear stresses and strains, there is no coupling between different components. Hooke law inverse form is obtained regrouping Equations 2.11-2.16 similarly to 2.8; the coefficient matrix takes the name of *compliance matrix*.

$$\begin{bmatrix} \epsilon_{11} \\ \epsilon_{22} \\ \epsilon_{33} \\ \gamma_{23} \\ \gamma_{13} \\ \gamma_{12} \end{bmatrix} = \begin{bmatrix} S_{11} & S_{12} & S_{13} & 0 & 0 & 0 \\ S_{12} & S_{22} & S_{23} & 0 & 0 & 0 \\ S_{13} & S_{23} & S_{33} & 0 & 0 & 0 \\ 0 & 0 & 0 & S_{44} & 0 & 0 \\ 0 & 0 & 0 & 0 & S_{55} & 0 \\ 0 & 0 & 0 & 0 & 0 & S_{66} \end{bmatrix} \begin{bmatrix} \sigma_{11} \\ \sigma_{22} \\ \sigma_{33} \\ \tau_{23} \\ \tau_{13} \\ \tau_{12} \end{bmatrix} \tag{2.17}$$

$$= \begin{bmatrix} \frac{1}{E_1} & -\frac{\nu_{21}}{E_2} & -\frac{\nu_{31}}{E_3} & 0 & 0 & 0 \\ -\frac{\nu_{12}}{E_1} & \frac{1}{E_2} & -\frac{\nu_{32}}{E_3} & 0 & 0 & 0 \\ -\frac{\nu_{13}}{E_1} & -\frac{\nu_{23}}{E_2} & \frac{1}{E_3} & 0 & 0 & 0 \\ 0 & 0 & 0 & \frac{1}{G_{23}} & 0 & 0 \\ 0 & 0 & 0 & 0 & \frac{1}{G_{31}} & 0 \\ 0 & 0 & 0 & 0 & 0 & \frac{1}{G_{12}} \end{bmatrix} \begin{bmatrix} \sigma_{11} \\ \sigma_{22} \\ \sigma_{33} \\ \tau_{23} \\ \tau_{13} \\ \tau_{12} \end{bmatrix} \tag{2.18}$$

The compliance matrix would seem to consider 12 independent coefficients; however, since the inverse of a symmetric matrix is also symmetric, it follows from the off-diagonal terms that:

$$\frac{\nu_{ij}}{E_i} = \frac{\nu_{ji}}{E_j} \tag{2.19}$$

Consequently, three Young moduli, three Poisson ratios, and three shear moduli fully define the orthotropic mechanical behavior. Therefore, an orthotropic material is characterized in its mechanical behavior when these 9 coefficients are known.

Material coefficients transformation

The constitutive relations discussed up to this point refer to the $1-2-3$ coordinate system. As already discussed, they are considerably simplified in orthotropic materials when this coordinate system coincides with the principal material coordinate system. This is not always the case; a classic example is that of composite laminates. It is common for lamination to follow a particular pattern, which implies that each layer, with its material coordination system, is oriented differently from the others. Define $x-y-z$ as the structure reference system; in the most general case, this does not coincide with $1-2-3$ but is rotated counterclockwise by an angle θ around the z-axis (see Figure 2.9). The relationship that binds the two

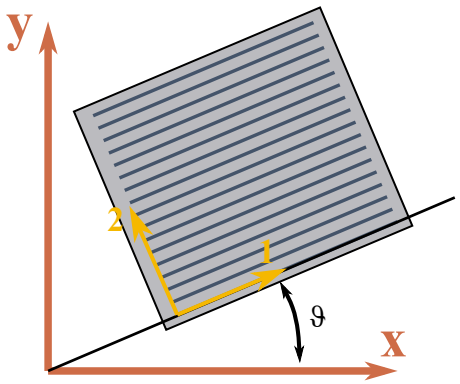

Figure 2.9: Material reference system rotated of an angle θ with respect to structure reference system.

reference systems is:

$$\begin{bmatrix} x_1 \\ x_2 \\ x_3 \end{bmatrix} = \begin{bmatrix} cos\theta & sin\theta & 0 \\ -sin\theta & cos\theta & 0 \\ 0 & 0 & 1 \end{bmatrix} \begin{bmatrix} x \\ y \\ z \end{bmatrix} = [L] \begin{bmatrix} x \\ y \\ z \end{bmatrix} \tag{2.20}$$

The matrix $[L]$ allows the transformation of the stress tensor from the material reference system (subscript m) to the structure reference system (subscript s); T is the transpose operator.

$$[\sigma]_m = [L][\sigma]_s[L]^T \tag{2.21}$$

$$[\sigma]_s = [L]^T[\sigma]_m[L] \tag{2.22}$$

Turning to Voight notation, this means:

$$\begin{bmatrix}\sigma_{xx}\\ \sigma_{yy}\\ \sigma_{zz}\\ \sigma_{yz}\\ \sigma_{xz}\\ \sigma_{xy}\end{bmatrix} = \begin{bmatrix} cos^2\theta & sin^2\theta & 0 & 0 & 0 & -sin2\theta \\ sin^2\theta & cos^2\theta & 0 & 0 & 0 & sin2\theta \\ 0 & 0 & 1 & 0 & 0 & 0 \\ 0 & 0 & 0 & cos\theta & sin\theta & 0 \\ 0 & 0 & 0 & -sin\theta & cos\theta & 0 \\ sin\theta cos\theta & -sin\theta cos\theta & 0 & 0 & 0 & cos^2\theta - sin^2\theta \end{bmatrix} \begin{bmatrix}\sigma_{11}\\ \sigma_{22}\\ \sigma_{33}\\ \sigma_{23}\\ \sigma_{13}\\ \sigma_{12}\end{bmatrix} \tag{2.23}$$

The transformation matrix is called [T]. The reasoning is analogous for the strain tensor,

$$[\epsilon]_m = [L][\epsilon]_s[L]^T \tag{2.24}$$

$$[\epsilon]_s = [L]^T[\epsilon]_m[L] \tag{2.25}$$

However, switching to Voight notation involves a different definition for shear components. The result is, therefore:

$$[\sigma]_s = [T][\sigma]_m \tag{2.26}$$

$$[\epsilon]_m = [T]^T[\epsilon]_s \tag{2.27}$$

The last two relations allow the transformation of the elastic coefficients C_{ij} from the material reference system to the structure reference system. Indeed,

$$[\sigma]_s = [T][\sigma]_m = [T][C]_m[\epsilon]_m = [T][C]_m[T]^T[\epsilon]_s \tag{2.28}$$

In the structure reference system, the matrix of elastic coefficients, therefore, takes the following form:

$$[C]_s = [T][C]_m[T]^T = \begin{bmatrix} \bar{C}_{11} & \bar{C}_{12} & \bar{C}_{13} & 0 & 0 & \bar{C}_{16} \\ \bar{C}_{12} & \bar{C}_{22} & \bar{C}_{23} & 0 & 0 & \bar{C}_{26} \\ \bar{C}_{13} & \bar{C}_{23} & \bar{C}_{33} & 0 & 0 & \bar{C}_{36} \\ 0 & 0 & 0 & \bar{C}_{44} & \bar{C}_{45} & 0 \\ 0 & 0 & 0 & \bar{C}_{45} & \bar{C}_{55} & 0 \\ \bar{C}_{16} & \bar{C}_{26} & \bar{C}_{36} & 0 & 0 & \bar{C}_{66} \end{bmatrix} \tag{2.29}$$

Plane stress in a unidirectional laminate

The peculiarities of unidirectional laminae allow further simplifications. The highest mechanical properties of a unidirectional laminate develop along the fibers, *direction 1*. The mechanical properties are lower in *direction 2* and *3*, both orthogonal to the previous. *Direction 3* is the *lamination direction*, which is the direction in which all the laminae are layered. Then, the single lamina is predominantly a two-dimensional element, which develops in the $1-2$ plane. These mechanical

and geometrical peculiarities determine that each lamina can withstand significant loads only within the $1-2$ plane. Any outside load would be an unnatural load for these elements.

Laminae are usually studied under the assumption of *plane stress* state. Plane stress is particular stress state in which all the stresses outside the plane $1-2$ are zero:

$$\sigma_3 = 0, \quad \tau_{23} = 0, \quad \tau_{31} = 0 \tag{2.30}$$

Under this assumptions, Equation 2.17 reduces to

$$\begin{bmatrix} \epsilon_{11} \\ \epsilon_{22} \\ \epsilon_{33} \\ \gamma_{12} \end{bmatrix} = \begin{bmatrix} S_{11} & S_{12} & S_{13} & 0 \\ S_{12} & S_{22} & S_{23} & 0 \\ S_{13} & S_{23} & S_{33} & 0 \\ 0 & 0 & 0 & S_{66} \end{bmatrix} \begin{bmatrix} \sigma_{11} \\ \sigma_{22} \\ 0 \\ \tau_{12} \end{bmatrix} \tag{2.31}$$

For orthotropic materials each shear strain is linked to the corresponding shear stress; under the assumption of plane stress, the two lines of out-of-plane shear are simplified. The third line of Equation 2.17 cannot be simplified as the strain ϵ_{33} is not only a function of σ_{33}, but it is a function of σ_{11} and σ_{22} also. Another way to express the same relation is to express 2.31 as a 3×3 system, supplemented by an additional equation:

$$\begin{bmatrix} \epsilon_{11} \\ \epsilon_{22} \\ \gamma_{12} \end{bmatrix} = \begin{bmatrix} S_{11} & S_{12} & 0 \\ S_{12} & S_{22} & 0 \\ 0 & 0 & S_{66} \end{bmatrix} \begin{bmatrix} \sigma_{11} \\ \sigma_{22} \\ \tau_{12} \end{bmatrix} \tag{2.32}$$

$$\epsilon_{33} = S_{13}\sigma_{11} + S_{23}\sigma_{22} \tag{2.33}$$

Last equations may be rewritten in terms of engineering constants as follows:

$$\begin{bmatrix} \epsilon_{11} \\ \epsilon_{22} \\ \gamma_{12} \end{bmatrix} = \begin{bmatrix} \frac{1}{E_1} & -\frac{\nu_{21}}{E_2} & 0 \\ -\frac{\nu_{12}}{E_1} & \frac{1}{E_1} & 0 \\ 0 & 0 & 1/G_{12} \end{bmatrix} \begin{bmatrix} \sigma_{11} \\ \sigma_{22} \\ \tau_{12} \end{bmatrix} \tag{2.34}$$

$$\epsilon_{33} = -\frac{\nu_{13}}{E_1}\sigma_{11} - \frac{\nu_{23}}{E_2}\sigma_{22} \tag{2.35}$$

In terms of stiffness matrix, Equation 2.34 reads:

$$\begin{bmatrix} \sigma_{11} \\ \sigma_{22} \\ \tau_{12} \end{bmatrix} = \begin{bmatrix} Q_{11} & Q_{12} & 0 \\ Q_{12} & Q_{22} & 0 \\ 0 & 0 & Q_{66} \end{bmatrix} \begin{bmatrix} \epsilon_{11} \\ \epsilon_{22} \\ \gamma_{12} \end{bmatrix} \tag{2.36}$$

where

$$Q_{ij} = C_{ij} - \frac{C_{i3}C_{j3}}{C_{33}} \quad \text{where} \quad i,j = 1,2,6 \tag{2.37}$$

Recalling Equation 2.19, only 3 engineering constants are needed to determine the in-plane strains:

- Two Young moduli, E_1 and E_2.
- One Poisson ratio, ν_{12}.
- One shear modulus, G_{12}.

Moreover, two more Poisson ratios are needed to calculate ϵ_{33}, ν_{13} and ν_{23}.

Equation 2.36 is written in the material coordinate system. Each lamina is not used individually, but laminae are layered on each other to form the so-called laminate. The number of layers contributes to the thickness of the laminate, together with its mechanical properties. Lamination allows each lamina to be oriented differently, depending on stiffness and strength requirements or other parameters that were the main design target. Recalling Equation 2.29, Equation 2.36 in structure coordinate system reads:

$$\begin{bmatrix} \sigma_{xx} \\ \sigma_{yy} \\ \tau_{xy} \end{bmatrix} = \begin{bmatrix} \bar{Q}_{11} & \bar{Q}_{12} & \bar{Q}_{16} \\ \bar{Q}_{12} & \bar{Q}_{22} & \bar{Q}_{26} \\ \bar{Q}_{16} & \bar{Q}_{26} & \bar{Q}_{66} \end{bmatrix} \begin{bmatrix} \epsilon_{xx} \\ \epsilon_{yy} \\ \gamma_{xy} \end{bmatrix} \tag{2.38}$$

Is it possible to quantify both the mechanical properties and the behavior of a laminate from its laminae? This question was answered by Reissner and Stavksy in [86] and is commonly known as Classical Lamination Theory.

2.5 Classical Lamination Theory

The Classical Lamination Theory (CLT) studies the mechanical behavior of a laminate, starting from the mechanical properties of each lamina, its thickness, and its orientation in a global reference system $x - y - z$ (see Figure 2.10). All the laminae are parallel to each other; their respective direction 3 is parallel with the laminate thickness direction z. The orientation of the material reference system is therefore described by the angle θ_k only, of the $k - th$ lamina (see Figure 2.9). The theory relies on five simplifying hypotheses [87], whose compliance is to be assessed:

- Each lamina is thin when compared to its in-plane extension.
- Macroscopically, each lamina is made up of a linear-elastic, orthotropic and homogeneous material.
- A two-dimensional plane stress features both the laminate and each lamina.
- An ideal bond exists between laminae.
- The laminate fulfills Kirchhoff hypothesis.

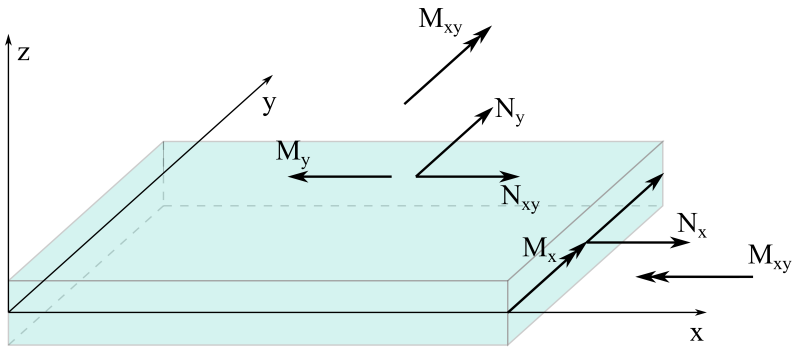

Figure 2.10: Global reference system, forces, and moments definition.

The Kirchhoff hypothesis implies that in addition to the normal components of shear strain, also the normal component of axial strain is zero, which contradicts Equation 2.35. In a general situation, the laminate is made up of n laminae, as shown in Figure 2.6. In each lamina, the stress field is described by Equation 2.35. However, it is more convenient to think about the forces and moments resultants with a view to the laminate. In the global reference system, forces and moments can be calculated by integrating the stresses into the thickness. By defining h as the overall thickness of laminate, the integral can be solved by adding together the contributions of the single integrals of each lamina.

$$\boldsymbol{N} = \begin{bmatrix} N_x \\ N_y \\ N_{xy} \end{bmatrix} = \int_{-h/2}^{h/2} \begin{bmatrix} \sigma_x \\ \sigma_y \\ \tau_{xy} \end{bmatrix} dz = \sum_{k=1}^{n} \int_{h_k-1}^{h_k} \begin{bmatrix} \sigma_x \\ \sigma_y \\ \tau_{xy} \end{bmatrix} dz \tag{2.39}$$

$$\boldsymbol{M} = \begin{bmatrix} M_x \\ M_y \\ M_{xy} \end{bmatrix} = \int_{-h/2}^{h/2} z \begin{bmatrix} \sigma_x \\ \sigma_y \\ \tau_{xy} \end{bmatrix} dz = \sum_{k=1}^{n} \int_{h_k-1}^{h_k} z \begin{bmatrix} \sigma_x \\ \sigma_y \\ \tau_{xy} \end{bmatrix} dz \tag{2.40}$$

CLT introduces into Equations 2.39-2.40 the stress-strain relations of Equation 2.35. The deformation field is rewritten under Kirchhoff hypothesis; the three components vary linearly in thickness. Each component is the sum of a constant term in the thickness (the normal and shear deformations of the average plane, $\boldsymbol{\epsilon}^\circ$) and a term linked to the section curvature and twist ($\boldsymbol{\kappa}$), linear with the z-coordinate.

$$\begin{bmatrix} \epsilon_1 \\ \epsilon_2 \\ \epsilon_6 \end{bmatrix} = \begin{bmatrix} \epsilon_1^\circ \\ \epsilon_2^\circ \\ \epsilon_6^\circ \end{bmatrix} + z \begin{bmatrix} \kappa_1 \\ \kappa_2 \\ \kappa_6 \end{bmatrix} \tag{2.41}$$

With this mathematical step, the integrals of Equations 2.39-2.40 are simple to solve, as the elastic coefficients in each lamina are constant. Once the terms of each lamina have been added, equations Equations 2.39-2.40 can be grouped into:

$$\begin{bmatrix} \boldsymbol{N} \\ \boldsymbol{M} \end{bmatrix} = \begin{bmatrix} \boldsymbol{A} & \boldsymbol{B} \\ \boldsymbol{B} & \boldsymbol{D} \end{bmatrix} \begin{bmatrix} \boldsymbol{\epsilon}^\circ \\ \boldsymbol{\kappa} \end{bmatrix} \tag{2.42}$$

$\boldsymbol{A}$, $\boldsymbol{B}$ and $\boldsymbol{D}$ are 3×3 matrices. $\boldsymbol{A}$ contains the membrane stiffness coefficients, $\boldsymbol{D}$ the flexural-torsional stiffness coefficients, and $\boldsymbol{B}$ the coupling coefficients between the two phenomena.

Introducing CLT into FEM

The CLT has been introduced to simulate the mechanical behavior of some simple elements. As will be detailed in the following chapters, to study real applications in terms of geometry and boundary conditions, the predictions will be performed via a commercial code based on Finite Elements and not analytically.

Finite Element models embed a 2D orthotropic constitutive model based on a 5×5 matrix of elastic coefficients. The reason lies in the kinematic model, which does not meet the stringent requirements of the CLT but those of the First-order Shear Deformation Theory (FSDT). In this context, the constitutive equations of each lamina gain a further contribution, which is added to Equation 2.35:

$$\begin{bmatrix} \sigma_{yz} \\ \sigma_{xz} \end{bmatrix} = \begin{bmatrix} Q_{44} & Q_{45} \\ Q_{45} & Q_{55} \end{bmatrix} \begin{bmatrix} \gamma_{yz} \\ \gamma_{xz} \end{bmatrix} \tag{2.43}$$

These additional quantities affect the resultants, as they introduce the transverse force resultants Q_x and Q_y:

$$\begin{bmatrix} Q_y \\ Q_x \end{bmatrix} = K \sum_{k=1}^{n} \int_{h_k-1}^{h_k} \begin{bmatrix} \sigma_{yz} \\ \sigma_{xz} \end{bmatrix} dz \tag{2.44}$$

In Equation 2.44, K is the shear correction factor. It is used to modify the plate transverse shear stiffness, and it is based on energy considerations. The idea behind the K factor can be practically exploited to turn the FSDT Kinematics into the CLT by penalizing the transverse force resultants. In practice, by introducing sufficiently high stiffness coefficients in the constitutive model to make the material infinitely rigid for transverse effects.

2.5.1 CLT applied to FFF

The geometric similarities with a UDC lamina and the results reported by different researchers have suggested that a single FFF layer, produced with linear infill, may exhibit orthotropic behavior. Consequently, if this were true, the superposition of several layers with this feature and the same raster angle should result in an orthotropic behavior element. This hypothesis, if verified, would represent a considerable simplification in the mechanical behavior prediction. As discussed extensively in Section 2.4.1, the matrix of elastic coefficients of an orthotropic material contains only nine linearly independent coefficients in the material reference system:

1. three tensile moduli of elasticity, E_{11}, E_{22}, E_{33};
2. three Poisson ratios, $\nu_{12}, \nu_{13}, \nu_{23}$;
3. three shear moduli of elasticity, G_{12}, G_{23}, G_{13};

To handle this kind of matrix is simpler than dealing with a full matrix, mainly due to reducing the elastic coefficients to be determined. This advantage is restricted to a particular type of infill, linear and with 100% filling. By varying these two parameters, FFF components get different mesostructures, necessarily characterized by other mechanical behavior. Nothing suggests that alternative mesostructures allow similar reasoning. However, as already seen in Chapter 1:

- The mechanical properties deteriorate if compared to the feedstock material when the infill percentage is less than 100%.
- Linear infill is the only one that allows printing a quasi-solid component.

As a result, this is the particular combination that is likely to be used for functional components. Furthermore, the linear infill facilitates standardizing the characterization process, which would be much more complicated otherwise. An example is given by the definition of the material reference system. With any infill, defining a material reference system to conduct a defined set of tests might be ambiguous. Such ambiguities disappear with a linear infill, as the material reference system follows the mesostructure. Once the stiffness matrix has been determined following this approach, structural analyses could also be performed on components with the same linear infill but a different raster angle. At the same time, analyses could also be carried out on components in which the raster angle varies along the thickness direction. It could also be possible to optimize the raster angle sequence following the design requirements. The stiffness matrix can be rotated in the structure reference system as seen in Equation 2.20, starting from the elastic coefficients determined in the material reference system.

The stiffness matrix of an orthotropic material can be determined entirely through six mechanical characterization tests. Three tensile tests allow quantifying the three Young moduli and the three Poisson ratios simultaneously. In other words, three tensile tests allow filling the first 3×3 block of the stiffness matrix. Three shear tests can then complete the diagonal of the matrix. The setup of these tests is not trivial, as none of them are standardized for components produced via FFF and with the mesostructure previously discussed. Therefore, each test must need to undergo a design phase. For this reason, in the initial phase of the research, the question arose whether the parallel with the FRCs could allow extending the CLT.

In Section 2.5 the simplifying hypotheses of CLT have been discussed. Modifying lamina in layer and laminate in structure, the hypotheses read:

- Each layer is thin enough.
- Macroscopically, each layer is made up of a linear-elastic, orthotropic and homogeneous material.
- A two-dimensional plane stress features both the layer and each structure.
- An ideal bond exists between layers.
- The structure fulfills Kirchhoff hypothesis.

The layer thickness is in the same order of magnitude as a UDC lamina. The possible orthotropic behavior of the single layer, at a macroscopic level, will be the subject of the next chapters.

The assumptions made in this chapter are not entirely new. Although significantly different from each other, the results obtained by other researchers seem to confirm these hypotheses. However, in no case, with the matrix obtained, has the mechanical behavior predicted by CLT been validated on structures with realistic loading conditions. Furthermore, in the absence of standardized tests or consolidated approaches, different researchers followed other paths. Rodriguez et al [34]. first studied FFF ABS with linear infill and assumed that the mesostructure could have an orthotropic response. Consequently, the authors performed a set of tensile tests on $1-2$ plane, through which they determined the two Young moduli E_1 and E_2, the Poisson ratio ν_{12}, and the shear modulus G_{12}. The tests relied on constant and rectangular cross-section specimens, according to ASTM D3039; the geometry of the specimens was derived directly from the standard developed for fiber composite materials, without any adjustment or rethinking. No further information was made available about the actual polymer deposition strategy; the presence of a certain number of peripheral beads was not specified. The mechanical properties confirmed the anisotropy and their decay with respect to the reference values of the feedstock material. Li et al. [83] reconsidered Rodriguez's work, reproduced the set of tests in $1-2$ plane with the same geometry, and defined a stiffness matrix 3×3 assuming that the mechanical behavior was orthotropic. Thus, the stiffness matrix allowed the authors to effectively predict the behavior of further tensile specimens printed with different raster angles. Casavola et al. [88] proposed a similar study, based, however, on dog-bone samples, according to ASTM D638, without any rethinking even in this case. All specimens were printed with two perimeters. Through a set of tensile tests in the plane, the 3×3 matrix of the elastic coefficients was defined, both of a PLA and an ABS. CLT was then tested on an additional tensile specimen with a symmetric and balanced sequence of layers. The results were excellent, with less than 1.5% errors for ABS and 6% for PLA.

Those insights will be considered in the new standard characterization procedure described in the next chapter. Once the characterization is complete, the 3×3 matrix obtained through the CLT approach will be used to predict the mechanical

behavior of structural elements subjected to more complex load and constraint conditions. Introducing CLT, and a 3×3 reduced stiffness matrix, limits the application field to mainly two-dimensional structures; however, it will be a strong starting point for extending to the full 6×6 matrix when validated.

Chapter 3

Experimental setup

This chapter is dedicated to the mechanical characterization of 3D PLA, processed via Fused Filament Fabrication (FFF). A specific reference standard for the mechanical properties determination of 3D-printed components does not exist yet. Assuming that the 3D-printed samples may have an orthotropic behavior under certain circumstances and their mechanical response can be described by the Classical Lamination Theory (CLT), it is necessary to define a new standard method. The starting points are the test methods for polymers. A preliminary discussion on tensile tests, however, will show their unsuitability. Therefore, the discussion will continue taking inspiration from the standard test methods for composites, exploiting the arguments discussed in the previous chapter. The geometry and set-up will, however, require a specific design, especially related to the tabs. At the end of the chapter, the mechanical properties necessary to define the 3×3 reduced stiffness matrix from the CLT perspective will be determined.

3.1 Introduction

Chapter 2 focused on FFF 3D-printed component with a linear infill. In this context, the discussion of the theoretical aspects focused on the mesostructure of these components. Three orthogonal planes of geometric symmetry have been identified within linear infill components at a constant raster angle. These symmetries also exist within unidirectional composite laminates. In the latter, these geometric symmetries also characterize the mechanical properties, which implies that UDCs have an orthotropic behavior. Together with other mechanical considerations, a possible analogy between the two materials has been inferred. If this were confirmed, the mechanical behavior of FFF 3D-printed components might be orthotropic under specific circumstances. The first step to test this hypothesis requires a tailored mechanical characterization campaign: the tests must necessarily fit the orthotropy hypothesis and the mesostructure characteristics. To this end, Chapter 2 went into

detail on the elastic coefficients necessary to describe the mechanical behavior of an orthotropic material. Given the material reference system $(1-2-3)$, where 1 is the bead direction, 2 the in-plane direction normal to the bead, and 3 the out-of-plane direction orthogonal to the bead, those coefficients can be summarized as follows:

- three Young moduli, E_{11}, E_{22}, E_{33};
- three Poisson ratios, $\nu_{12}, \nu_{13}, \nu_{23}$;
- three shear moduli, G_{12}, G_{13}, G_{23}.

The Young moduli and the Poisson ratios can be determined through tensile tests; the shear moduli can be quantified through shear tests. This chapter will discuss the characteristics of the required specimens in terms of geometry and mesostructure. The whole discussion will take advantage of the further simplification introduced by the CLT; consequently, after the experimental tests have been designed, only the properties to determine the 3×3 reduced stiffness matrix will be quantified:

- two Young moduli, E_{11}, E_{22};
- one Poisson ratio, ν_{12};
- one shear modulus, G_{12}.

Before determining the values of the four coefficients, a preliminary experimental campaign has been conducted to design the tests. Those preliminary tests have been performed using sacrificial PLA spools; this to preserve a single and dedicated spool for the actual characterization and validation tests and keep consistency between them. As discussed in Appendix A, differences in the mechanical properties might arise between different PLA filaments and even between different spools from the same manufacturer.

This chapter will deepen the mesostructural characteristics of tensile and shear specimens, which are required to determine the mechanical properties under the CLT assumptions; this means answering the questions:

1. how should the specimen and its beads be oriented with respect to the load application direction in tensile tests?
2. how should the specimen and its beads be oriented with respect to the load application direction in shear tests?

It is vital to answer those questions before going into testing procedures and geometries of the specimens. Their geometry, their shape, is not a standalone feature. Regardless of the test, the specimens are designed to provide a well defined stress state such that the desired material properties can be obtained and avoid unwanted

side effects. For this reason, the material itself, its microstructure, and the manufacturing process contribute to determining these characteristics.

In the following, a large number of tensile and shear specimens will be considered. Figure 3.1 illustrates the nomenclature used for their identification to facilitate the reading and referring to the results.

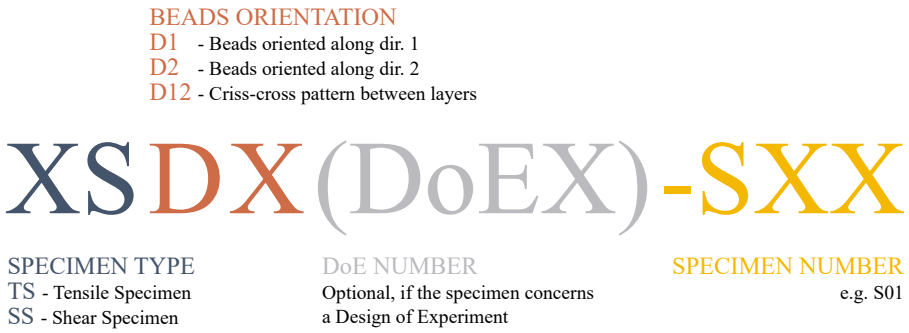

Figure 3.1: Nomenclature definition for all the tensile and shear specimens.

3.2 Tensile properties determination

Among the mechanical characterization tests, tensile tests play a major role. As the word itself suggests, they allow determining the tensile properties of a material in the load application direction. A specimen is subjected to tension; its geometry is designed to make a uniform tensile stress state develop inside it. Several set-ups have been developed over time, each of which is characterized by many peculiarities. Those peculiarities depend on material microstructure (e.g., ceramic, glasses, metals, polymers), its larger structures, its classification by use, and on several and specific subcategories. Nevertheless, in all tensile test specimens, one can find several constants. In a generic tensile test, one would expect that the tensile coupon is longer in the load application direction and keeps a constant section at least in a *region of interest*. This region is where the mechanical properties under investigation are quantified. The rest of the geometry is functional to ensure that the tensile stress is as uniform as possible in this region. The coupon is expected to be loaded through two symmetric grips, which act on two *gripping regions*. Usually, polymers are tested with flat *dog-bone* shaped specimens with a rectangular cross-section. The cross-section dimensions increase in the gripping area, where specimens are provided with expansions. Metals use either similar flat dog-bone specimens or cylindrical specimens, for which those expansions are obtained through a radius increase. Composite materials use flat rectangular specimens with a constant cross-section. When needed, the expansions in the gripping regions are obtained through a set of customized *tabs* and a different material bonded to the specimen. The

characteristics of the gripping areas and their connection to the region of interest are essential for the load transmission, and for mechanical properties quantification.

The response of the material is studied in terms of tensile stress and tensile strain. The first is quantified through the applied load, measured by the load cell of the testing machine; the second is measured through contact or non-contact transducers (e.g., strain gauges, extensometers, Digital Image Correlation). The list of properties that can be quantified include:

- The *modulus of elasticity*: the slope of the stress-strain curve of a material, under the proportional limit.
- The *proportional limit*: the highest stress sustained by a material during a tension test at which the linear relation between stress and strain is still verified.
- The *elastic limit*: the highest tensile stress sustained by a material for which no permanent deformations exist once the specimen is released.
- The *tensile strength*: the maximum tensile stress a material is capable of sustaining.

When a second transducer monitors the transverse strain, the tensile test also provides:

- The *Poisson ratio*: the ratio between transverse to longitudinal strain under the proportional limit.

Overview on tensile tests

In tensile tests, the top and bottom endpoints of the specimen are positioned into the grips of the testing machine. The tests are usually performed in displacement control, which means that the test machine constantly adapts the applied load to ensure the imposed displacement. During the test, it samples the displacement of the upper cross-beam and the load imposed on the specimen through the load cell, which can be replaced according to the maximum expected load and the required sensitivity in the measure. The data is sampled at regular time intervals and saved in a text file. The raw data, the applied load and the imposed displacement, do not lead to the classic stress vs. strain relation and derive the most important mechanical properties of a material. The transition from the applied load to stress is simple; as the load application direction is parallel to the longitudinal axis of the specimen, therefore perpendicular to its cross-section, the stress is calculated by means of Equation 3.1.

$$\sigma = \frac{P}{A_0} \tag{3.1}$$

Where P is the applied load, and A_0 is the minimum initial cross-section of the specimen (i.e., the undeformed section of the region of interest). Finding the longitudinal deformation of the specimen is more complicated. A classic relation, written in analogy to Equation 3.2, reads,

$$\epsilon = \frac{\Delta L}{L_0} \tag{3.2}$$

Defining ΔL and L_0 is more complex: the first is the imposed displacement, the second is the initial length. As anticipated, usually the cross-section is not constant along the whole longitudinal direction. Consequently, the deformation is not constant along the axis of the specimen, which means that ΔL is not homogeneously distributed along L_0. Different instruments can be used to measure the effective strain, distinguished between contact instruments and non-contact instruments. Digital Image Correlation has been considered through this research, discussed in depth in Appendix B; consequently, the front surface of each specimen has been prepared with a random distribution of white/gray marks. Contact instruments such as strain gauges have been discarded as discussed in Appendix B.

Specimen alignment and load transmission

The tensile test are extremely influenced by the correct alignment of the specimen with the load application direction. This warning is present in any standard test method. When alignment is not guaranteed, the load is applied eccentrically, which can cause lateral-lateral bending of the specimen. This takes for granted that the jaws of the testing machine have been aligned before the test; otherwise, the load would again be eccentric and cause anteroposterior bending. The universal testing machine MTS QTest10 has been used in all tests; its gripping system is shown in Figure 3.2. Through a pair of cranks, two metal plates are pushed against

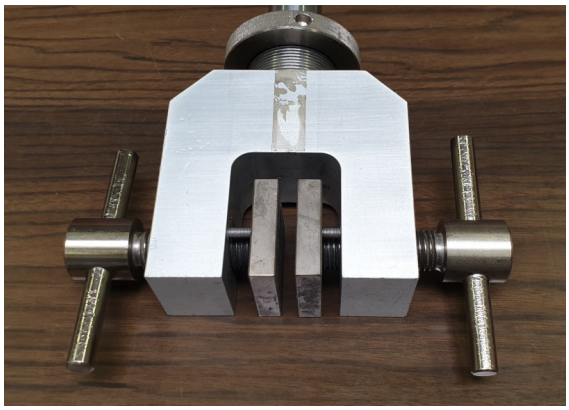

Figure 3.2: Gripping system of the universal testing machine MTS QTest10.

the surfaces of the specimen, which are tightened manually by acting on external

handles. From the machine frame to the specimen, the axial load transmission is through static friction, whose maximum value depends on the friction coefficient and the normal force. The resulting friction force has to be higher than the maximum load that can be sustained by the specimen during the test to ensure that the specimen does not slip. A set of preliminary tests revealed that ensuring proper alignment with this manual system is complex. The specimen has to be manually held in place while tightening the bottom grip. However, the rotating handles can cause the two plates to rotate slightly, and this rotation might affect the specimen orientation. Furthermore, manual positioning prevents the operator from ensuring consistency in the relative position between specimen and plates. An adapter has been designed to overcome this problem. A graphic render of the adapter and the MTS grip is shown in Figure 3.3; the installation phases are shown in Figure 3.4, the 2D drawing of the adapter is available in Appendix D. At the bottom, the shape

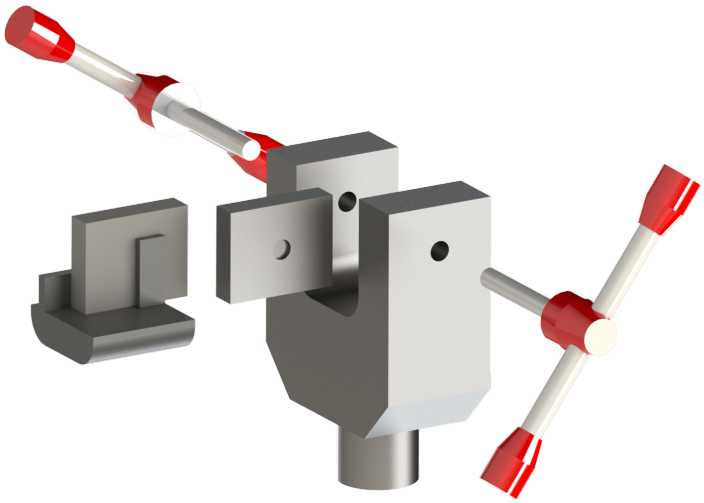

Figure 3.3: Graphic render of the assembly between the MTS grips and the designed adapter for specimen alignment.

of the device faithfully reproduces that of the seat between the steel frame and the plates, flush with their bottom surface. In this way, once installed, it acts as a support base for the plates, preventing their rotation but allowing their translation. It also provides a support base for the specimen, which ensures that all samples are positioned equally. A vertical tooth ensures the alignment with the load application direction once the specimen is in contact with it. An identical device has been installed inside the upper grip.

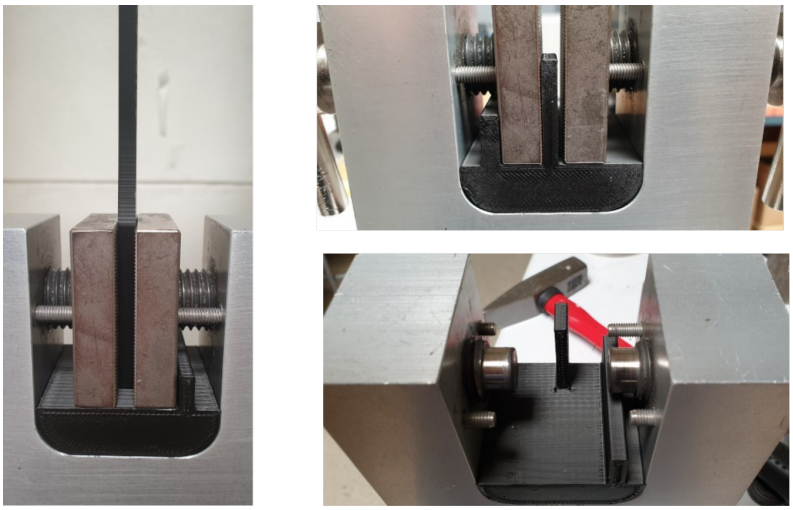

Figure 3.4: MTS grips and adapter for specimen alignment: installation phases.

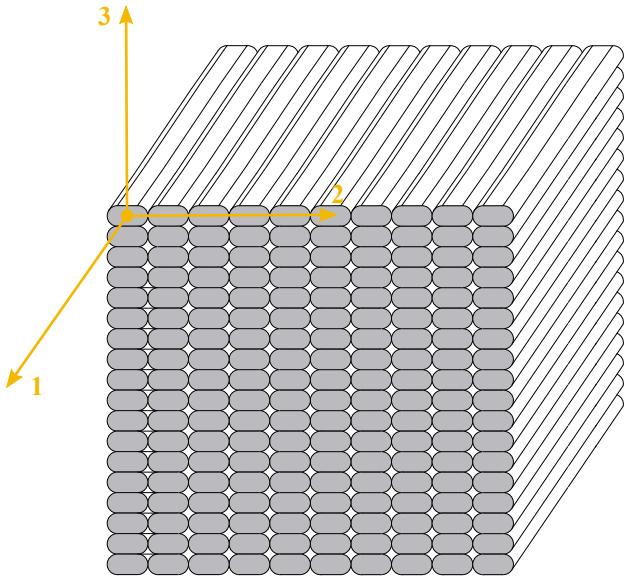

Figure 3.5: Mesostructure of a generic unidirectional FFF cube.

Mesostructure of tensile specimens

Despite the specific geometry, each tensile specimen has a *region of interest* in which the mechanical properties are evaluated. To obtain a specific set of Young moduli and Poisson ratios, the mesostructure arrangement with respect to the load application direction should be determined. Figure 3.5 exposes the mesostructure of a unidirectional FFF cubic element. Following the comments of Chapter 2 the raster angle is the same for all the layers. The three principal material directions are also underlined. Since each tensile test detects mechanical properties in the load

application direction, the load will need to be aligned with direction 1, direction 2, and direction 3 to determine the properties along each one. To do so, it is necessary to visualize and extract from the cube of Figure 3.5 the specimens, or at least their region of interest.

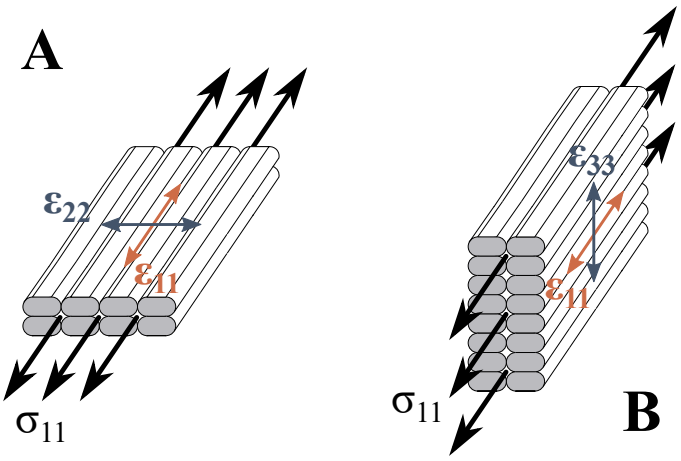

Figure 3.6: Tensile properties evaluation along direction 1: mesostructure of a generic specimen. In A the specimen lies flatwise, in B sidewise.

Figure 3.6 shows two alternatives for the tensile properties evaluation along direction *1*. The load is applied into the direction defined by the black arrows, which is parallel to direction *1* in the material reference system. The Young modulus E_{11} can be easily determined monitoring the stress σ_{11} and the strain ϵ_{11} along direction *1*. However, the main surface of the specimen could lie on plane *1-2*, or plane *1-3*. In the first case the contraction in direction *2* would also be measurable. Matching the transverse strain ϵ_{22} with the longitudinal one, ϵ_{11}, the Poisson ratio ν_{12} can be obtained. The second case allows instead to measure contractions in direction *3*; through ϵ_{33} this which leads to determine the Poisson ratio ν_{13}.

In Figure 3.7 two alternatives are proposed for the tensile properties evaluation along direction *2*. Also in this case, the black arrows define the load application direction, which is aligned to direction *2* in the material reference system. The Young modulus E_{22} can be easily determined monitoring the stress σ_{22} and the strain ϵ_{22}. However, the main surface of the specimen could lie on plane *1-2*, or plane *2-3*. In the first case, given the load application direction, the measurable contraction is that of direction *1*. Matching the transverse strains ϵ_{11} with the longitudinal ones ϵ_{22}, the Poisson ratio ν_{21} can be obtained. The second case allows to measure contractions in direction *3*; through ϵ_{33} this leads to determine the Poisson ratio ν_{23}.

For completeness, Figure 3.8 proposes two alternatives for the tensile properties evaluation along direction *3*. The black arrows defining the load application direction align with direction *3* in the material reference system. The Young modulus

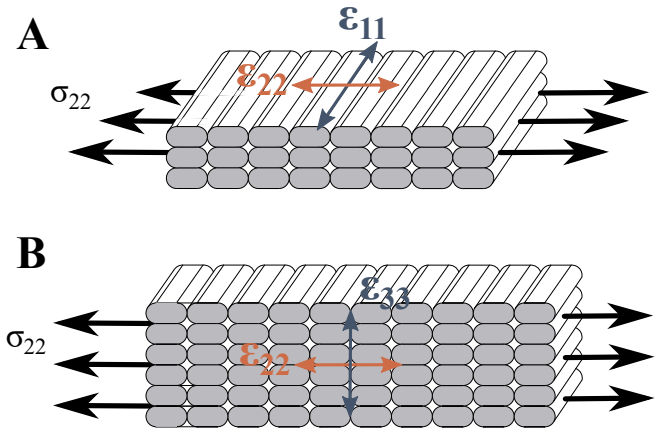

Figure 3.7: Tensile properties evaluation along direction 2: mesostructure of a generic specimen. In A the specimen lies flatwise, in B sidewise.

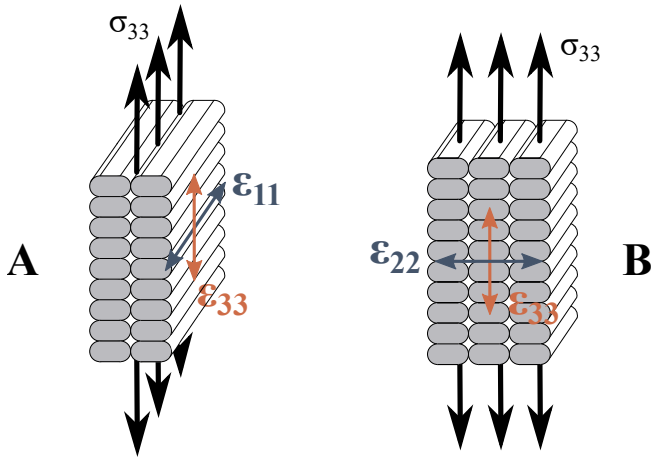

Figure 3.8: Tensile properties evaluation along direction 3: mesostructure of a generic specimen. In A the beads are parallel to the front surface of the specimen, in B they are perpendicular to it.

E_{33} can be easily determined monitoring the stress σ_{33} and the strain ϵ_{33}. However, the main surface of the specimen could lie on plane *1-3*, or plane *2-3*. In the first case, given the load application direction, the measurable contraction is that of direction *1*. Matching the transverse strain ϵ_{11} with the longitudinal one ϵ_{33}, the Poisson ratio ν_{31} can be obtained. The second case allows instead to measure contractions in direction *2*; through ϵ_{22} this leads to determine the Poisson ratio ν_{23}.

This analysis highlighted that two alternatives exist from the point of view of the stiffness modulus for each direction. However, a reasoned and specific choice must drive the research. To determine all the Poisson ratios, together with the stiffness

modulus through a set of three tensile tests, the choice of each configuration is not independent of that made for the others. For example, beginning with direction *1*, configuration A results in E_{11} and ν_{12}. Consequently, configuration A of direction *2* should be discarded because it results in ν_{21}, together with E_{22}, and ν_{12} and ν_{21} are not linearly independent, as seen in Equation 2.19. This reasoning could be extended with different examples, starting from a different configuration and direction of reference. For simplicity, Table 3.1 shows the chosen configurations and the resulting properties.

TSD1		TSD2		TSD3	
Conf. A		Conf. B		Conf. A	
E_{11}	ν_{12}	E_{22}	ν_{23}	E_{33}	ν_{31}

Table 3.1: Configurations for the tensile specimens mesostructures.

Specimens design

A benchmark to assess if a tensile test is acceptable or not is the failure mode/location. The geometries in tensile coupons are designed to produce an (almost) uniform tensile stress distribution inside the region of interest and, in any case, higher in magnitude than any other specimen region. A direct consequence is that the geometry is designed to produce a failure within the region of interest. A failure in any other position suggests a stress concentration, which is due to an incorrect introduction of the uni-axial load into the specimen. Tensile tests are usually considered unacceptable when the coupon fails outside the region of interest. Under these circumstances, the tensile behavior might not be correctly evaluated, and the specimen might fail prematurely. The gripping region turns out to be characterized by a complex stress field due to the coexistence of the gripping pressure and the axial load. Higher cross-section are usually designed in the regions where a complex stress field exists, to prevent the specimen from failing prematurely in those areas. This can be achieved through width-tapering (see Section 3.3) or thickness-tapering (see Section 3.4). However the end regions can not be simply expanded, but the expansions need to be connected to the narrow section with an appropriate transition region. This transition region should be smooth enough; sharp edges or sudden transitions may lead to stress concentrations, thus premature failure of the specimens. This discussion is of fundamental importance and, as anticipated, no standardized guidelines are available for 3D-printed plastics. In a first instance, reference will be made to standardized tests for properties determination in polymers. The failure mode of those specimens will lead to propose and discuss modified UDC specimens-like.

3.3 Tensile tests according to ASTM D638

The American Society for Testing and Material issued the standard describing the test method for tensile properties determination of Plastics under the designation ASTM D638 [71]. It covers plastics, whether reinforced or not. Some geometric and mechanical considerations, however, restrict its application field. In fact, it is suitable for elements with a thickness up to 14 mm; however, under 1 mm in thickness, ASTM D882 is more appropriate. Furthermore, it is discouraged for reinforced plastics with a tensile modulus higher than 20 GPa. In this case, test method D3039 [35] is suggested; the substantial difference between the two standards stands in specimens geometry, thus in the way the load is transferred to the *region of interest*, as this chapter will discuss later. The Standard lists the preferred geometries, as a function of the machining process and the geometrical features of the material to be tested. A first distinction is made between rigid tubes, rigid rods, and *sheets, plates, and molded plastics*. The latter three compose a single category, for which *dog-bone specimens* are suggested, also referred to *dumbbell-shaped specimen*. Under this category, the thickness of the material drives the shape and the dimensions of the specimens. Reinforced composites and highly orthotropic laminate require instead a single and unique design. The standard describes 5 types specimens whose shapes are discussed in Figure 3.9. TYPE I, II, III & V specimens share the same shape, which is slightly modified in TYPE IV. The two shapes are similar; both are characterized by a constant rectangular cross-section in the middle of the specimen (the *region of interest*, *reduced section* or *narrow section*) and by two same-thickness expansions at the ends. The difference between the two lies in the transition region, which modifies how the load is transmitted. The standard provides some more points of reflection while defining them:

1. TYPE I: it is the preferential specimen for rigid plastics, to be used when the material is as thick as 7 mm; it is the only design for reinforced composites studied under the frame of this test method.

2. TYPE II: it is an alternative to specimens TYPE I when the failure does not occur in the narrow section.

3. TYPE III: to be used over 7 mm in thickness but under 14 mm, which is the upper limit of the standard.

4. TYPE IV: to be used to compare the same material in various rigidity conditions.

5. TYPE V: to be used below 4 mm in thickness.

The main discriminating factor among the five specimen types is thickness. This consideration arises from the machining process, which in turn reflects the thickness

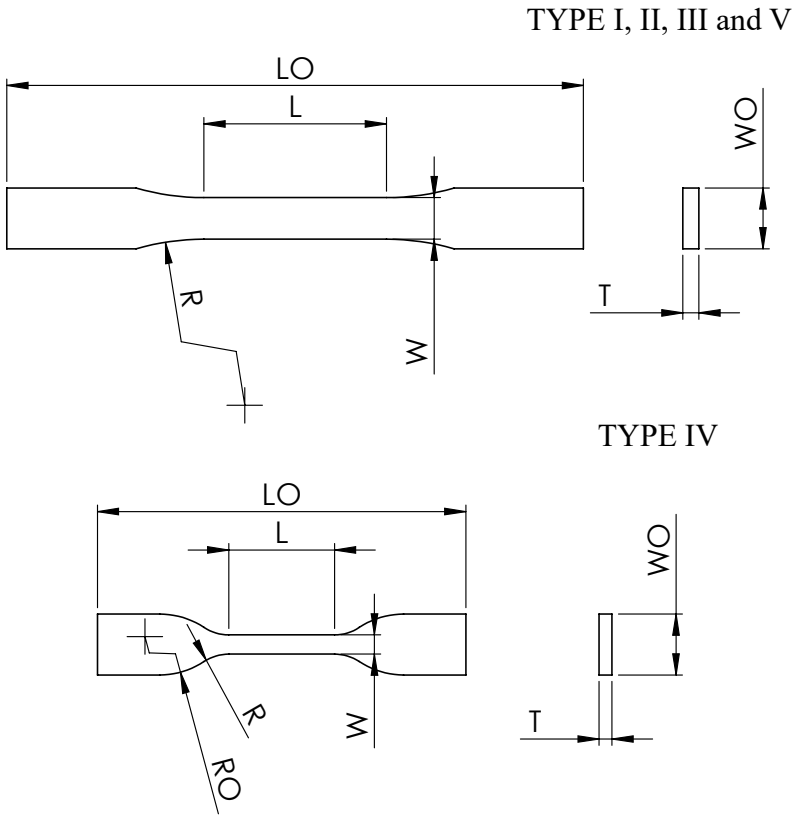

Figure 3.9: ASTM D638 [71]. TYPE I, II, III & V specimens on the top; TYPE IV specimen below.

of the material. However, in the frame of FFF there is no specific thickness to be considered as any value in the range *layer height* − *Z build dimension* can be accomplished.

The goal of all five geometries is to obtain a uniform distribution of stresses in the narrow section. TYPE I specimens are of common use; in traditional machining, those specimens are produced by injecting the melted polymer into an appropriate mold (for injection molding components) or cutting it from a plastic sheet (for extruded parts). However,

- great care should be taken during manufacture to avoid inner or outer defects;
- the surface finish plays a crucial role; consequently, any mark, sign, or imperfection shall be removed from all the surfaces of the specimen;
- different tensile properties might be found with varying technologies of manufacturing due to possible induced inner orientation of the polymeric macromolecules.

TYPE I shape does not own any particular challenge for FFF production if the only target is to build the object without any specific requirement. The following will establish whether the combination of these geometries with the mesostructures discussed in Section 3.2 is satisfactory trough a set of preliminary tensile tests.

3.3.1 Preliminary tests

ASTM D638 TYPE I specimens were produced, following the geometry reported in Figure 3.9. Table 3.2 sums the recommended dimensions and the actual ones up. The *length overall* was increased from the recommended minimum value, 165 mm to 180 mm. In this way the length of the griping area was increased to (slightly more than) 40 mm and a greater contact surface between specimen and the gripping plates was obtained. The 3D CAD model of a single specimen was

Dimensions	Recommended		Actual	
W - width of narrow section	13	mm	13	mm
L - length of narrow section	57	mm	57	mm
WO - width overall, min	19	mm	19	mm
LO - length overall, min	165	mm	180	mm
G - gage length	50	mm	50	mm
D - distance between grips	115	mm	115	mm
R - radius of fillet	76	mm	76	mm

Table 3.2: ASTM D638 TYPE I recommended and actual dimensions for preliminary specimens.

designed with SolidWorks, and then converted into an .stl file. The same .stl file was differently oriented into the 3D printing reference system, and it was given different printing parameters to obtain the different configurations. The .gcode file instructions were prepared with Simplify3D. Each print was configured to result in five identical specimens sequentially; this means that the 3D printer completed each sample at once before printing the other(s). Table 3.3 shows the common printing parameters among the several prints. Each specimen was carefully positioned into the grips, aligned with the load application direction, and tightened. The tests were conducted in displacement control; the machine adapts the applied load to maintain the custom testing speed. ASTM D638 suggests three values for TYPE I specimens, choosing the lowest producing failure in 30 s to 5 min. The lowest speed value was considered in the early stage, 5 mm/min. The results will be discussed later; however, it can be anticipated that this speed was compliant with the requirements, despite specimen configuration.

The following preliminary tests are devoted to highlighting if the set-ups are acceptable or not. The key points will be the failure location, the failure mode,

1st layer height	0.20	mm
Gen. layer height	0.10	mm
Nozzle diameter	0.40	mm
Extrusion width	0.50	mm
Infill percentage	100%	-
1st layer extrusion temp.	190	°C
Extrusion temperature	200	°C
Bed temperature	30	°C
Extrusion multiplier	1.05	-
Default speed	3000	mm/min
Retraction distance	3	mm

Table 3.3: Printing parameters used in ASTM D638 TYPE I specimens production for preliminary tests.

and the maximum sustained load. No stress-strain correlations were made; consequently, no mechanical properties were derived at this stage.

Direction 1

As discussed in Section I, the beads should be oriented in the specimen longitudinal direction to determine the tensile properties along direction 1 in the material reference system. With the longitudinal direction of the specimen aligned with direction X in the 3D printer reference system, the linear infill should have a raster angle equal to 0°. The previous considerations on the Poisson ratio also require that the specimen be placed flat on the build plate. Once the specimen orientation in the 3D printer reference system and the characteristics of the infill have been determined, the characteristics of the possible perimeter(s) have to be evaluated. Fig. 3.10 shows a preview of two possible configurations. The top configuration considers a specimen printed with a single peripheral filament; in the bottom configuration, instead, the specimen is produced with no peripheral filaments. Both the two cast doubts on their adequacy.

- The infill beads do not develop all in the longitudinal direction in both configurations; some go through the entire length while others end on the filleted surface. The continuous beads cooperate in load transmission along their length; however, high shear stresses might develop in the width-tapering region, especially on the contact surfaces between the last discontinued beads and the first continuous beads (moving from outside to inside).
- The slicing software algorithm produces an asymmetric distribution of discontinued beads.

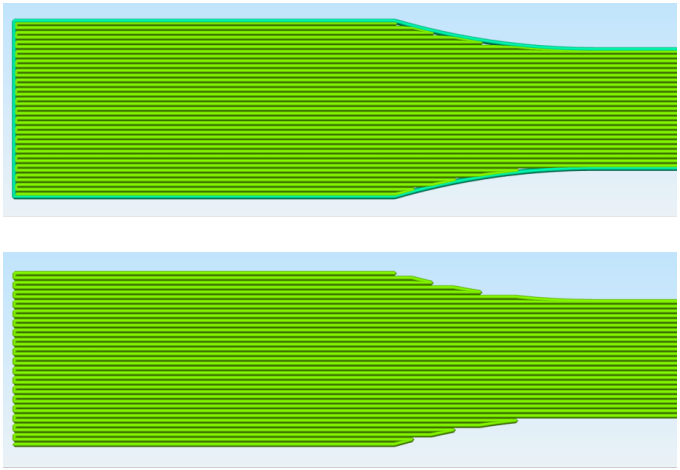

Figure 3.10: Alternative printing configurations for preliminary dog-bone specimens: tensile properties determination in direction 1.

- At each end of the discontinued filaments, an edge corner appears (see Figure 3.11).

Edge corners usually have two explanations:

- Once the nozzle reaches the endpoint of a filament in linear infill patterns, it makes a U-turn to get back and deposit the adjacent one. This operation makes the nozzle stay an additional time in the almost-same position: to reverse its direction, the nozzle is subjected to different accelerations. A small but finite amount of time is required, and a small amount of polymer leak out from the nozzle.

- There is a small overlap between adjacent filaments; where a discontinued filament ends, it is like this overlap involves three filaments, the two mutually parallel and the third orthogonal to both.

A peripheral filament could alleviate some issues, delivering continuous external surfaces. However, it brings along with other concerns. The perimeter may be introduced with superposition or juxtaposition, with respect to the infill filaments. In the first case, this would likely worsen the edge corners distribution. In the latter scenario, it would induce a distribution of voids. In both the case studies, there is the risk of a stress concentration in the transition region, which instead is meant to reduce it incidentally.

A set of five specimens was printed and then tested to evaluate their mechanical response in a tensile test. The printing followed the parameters shown in Table 3.3; the test reflected the ASTM D638 standard, as previously discussed. Figure 3.12 shows the print preview; Figure 3.13 shows the specimens after the tensile test.

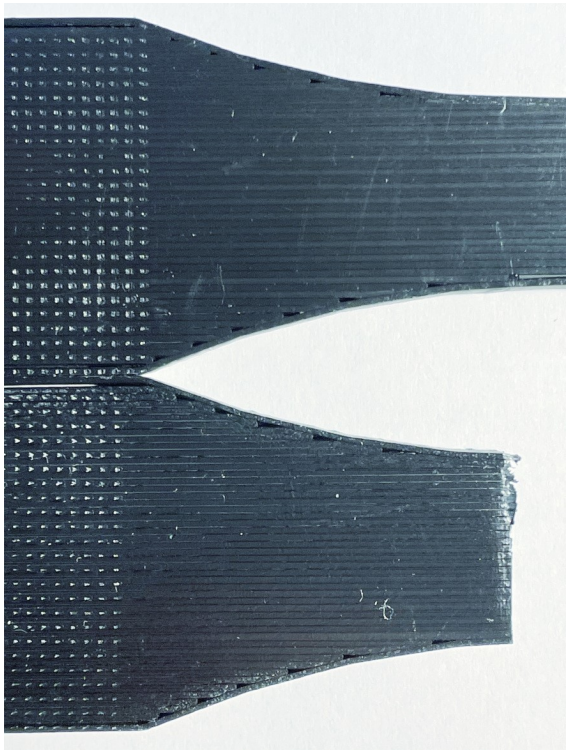

Figure 3.11: Magnified view of printing defects in a dog-bone specimen for direction 1.

Two transverse lines were drawn to locate the failure with respect to the transition region of the specimens. The failure took place in unacceptable positions: within the gripping region or in the transition zone. Besides, the failure occurred at tensile stress in the range $30-40$ MPa, much lower than the feedstock values determined in Appendix A. There is no hint of plastic deformation; all specimens failed with a clear fracture line. All these observations suggest that some stress concentration source prematurely induced failures. Their location points to the conjunction between specimen geometry and mesostructure.

Direction 2

As discussed in Section I, the beads should be oriented along the specimen transverse direction to determine the tensile properties along direction 2 in the material reference system. With the longitudinal direction of the specimen aligned with direction X in the 3D printer reference system, the linear infill should have a raster angle set equal to 90° to comply with this requirement. The previous considerations on the Poisson ratio also require that the specimen be placed on-edge over the build plate. In this case, also, the specimens could be printed with peripheral filament(s)

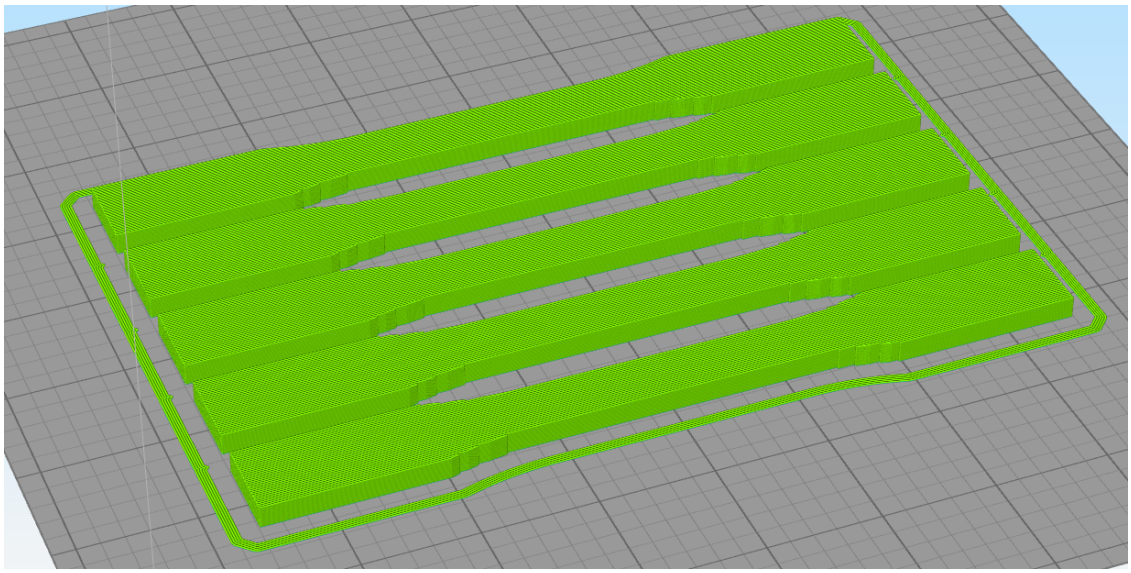

Figure 3.12: 3D printing preview: dog-bone specimens for tensile properties determination along direction 1.

Figure 3.13: Failed dog-bone specimens for mechanical properties evaluation in direction 1 after the preliminary tests.

or without (see Figure 3.14). However, as the perimeters follow the external specimen contour in each layer, they would be deposited along the principal longitudinal direction in the region of interest. This would be in contradiction with the required mesostructure; consequently, this configuration was rejected. In both cases the specimens stick to the building plate just in correspondence to the lateral surfaces of the expansion regions. Therefore, the narrow section would not be in contact

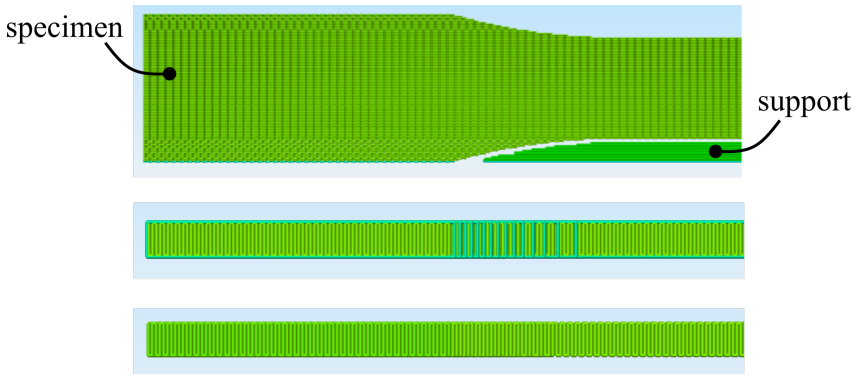

Figure 3.14: Alternative printing configurations for preliminary dog-bone specimens: tensile properties determination in direction 2.

with the building plate, thus featuring highly cantilevered forms. Some supports would be needed to succeed in printing such configurations, distributed below the cantilevered sections. However, Chapter 1 showed that the bottom surface would not be perfectly flat and smooth, with an uneven distribution of partially isolated filaments in the first layers. Moreover, the filleted surface profiles develop along the Z direction in the 3D printer reference system. Due to the layer-by-layer nature of FFF, the external surface of the fillets would have a stair-stepper aspect, inducing stress concentrations (see Figure 3.15).

Figure 3.15: Magnified view of the printing defects in a dog-bone specimen for direction 2.

A set of five specimens was printed and then tested to evaluate their mechanical response in a tensile test. The printing followed the parameters shown in Table 3.3; the test reflected the ASTM D638 standard, as previously discussed. Figure 3.16 shows the print preview; Figure 3.17 shows the specimens after the tensile test. Two transverse lines were drawn to locate the failure with respect to the transition

region of the specimens. The result is similar to that described for the tensile tests

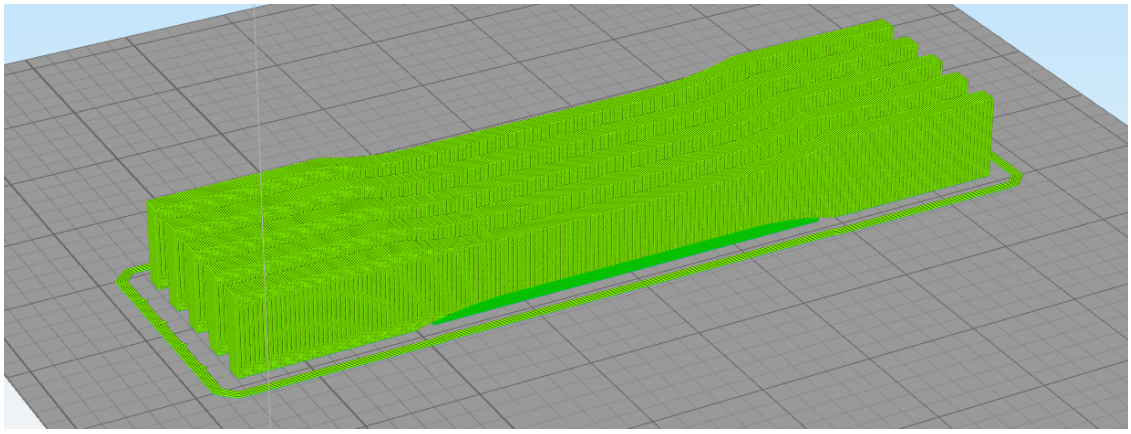

Figure 3.16: 3D printing preview: dog-bone specimens for tensile properties determination along direction 2.

Figure 3.17: Failed dog-bone specimens for mechanical properties evaluation in direction 2 after the preliminary tests.

along direction 1. All the specimens manifested unacceptable failures; they were located within the gripping region or in the transition zone. Besides, the failure

occurred at tensile stress in the range $20 - 30$ MPa, which is further lower than the feedstock values determined in Appendix A. All specimens failed with a clear fracture line, between adjacent beads. All these observations suggest that some stress concentration source prematurely induced failures. Their location points to the conjunction between specimen geometry and mesostructure.

3.4 Tensile tests according to ASTM D3039

The tensile tests performed with the geometry provided for the polymeric materials did not lead to satisfactory results. As discussed, tensile tests along with directions 1 and 2 in the material reference system showed premature failures. Those failures have been justified with the conjunction between the specimen geometry and the two mesostructures. A distribution of defects has been identified across the transition zone, in which all failures occurred. Such geometry is therefore not suitable in this context. In the transition zones, the cross-section of the specimen changes. An alternative solution could be to test specimens characterized by a constant section along the longitudinal axis not to induce any discontinuity. This guided the research activity towards the standard test method to determine tensile properties in composite materials. The ASTM issued the reference standard under the designation D3039 [35].

The standard requires that a coupon is in the shape of a constant rectangular cross-section. The minimum length should equal the sum of the gripping region, the gage length and two times the specimen width. There is no other specific requirement in terms of dimensions, except for some recommended values. The geometry is required to ensure a sufficient number of fibers within the cross-section to be statistically representative of the feedstock material behavior [35]. Consequently, the thickness and width of the specimens were increased with respect to the suggested values. This took into account the macroscopic difference between fiber and bead and included a more significant number of beads into the cross-section. As for the length, it was reduced to a value compatible with the printing volume of most of the printers on the market, always with a view to standardization. Figure 3.18 shows a 2D drawing of the specimen with quotes definition; the dimensions are reported in Table 3.4.

Dimensions		Recommended		Actual	
		0° unid.	90° unid.	TSD1	TSD2
LO - length overall	[mm]	250	175	190	190
W - width	[mm]	15	25	25	25
T - thickness	[mm]	1	2	3	4

Table 3.4: ASTM D3039 recommended and actual dimensions for tensile specimens.

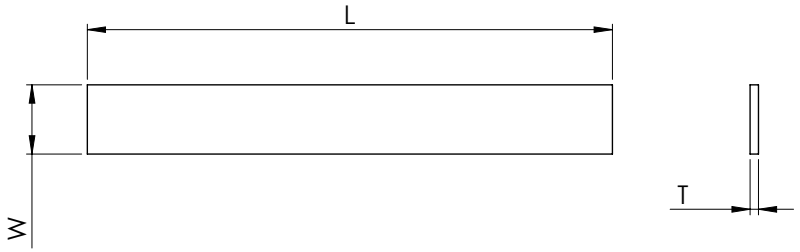

Figure 3.18: ASTM D3039 [35] reference geometry for tensile specimens.

Like other tensile tests, the load is introduced into the specimen by two plates, which transfer the tensile load by friction. The surfaces in contact with the specimen are generally non-smooth; this increases the adhesion coefficient and allows a higher load transmission. However, this can cause surface indentation and therefore be responsible for a premature failure. As anticipated, the specimens required by this standard method have a constant and rectangular section. The D3039 standard suggests but does not require a set of 4 tabs for each specimen, two per each end, one per side. In short, they are interposed elements between the specimen and the gripping system. They have three main features:

- They prevent specimen indentation.
- They reduce the stress concentrations at the cross-section where the specimen exits the grips.
- They can result in a thickness-tampering system; with a suitable geometry, they make the cross-section in the region of interest smaller than the cross-section of any other region.

The dog-bone geometry for metals and polymers relies on the same consideration: the specimen cross-section is increased everywhere, outside the region of interest. In that case, the end expansions produce a width-tapering of the specimen. This solution is often not feasible for composite materials due to their low resistance to shear stresses. Here it is assumed that the same reasoning may hold for FFF components but that the reason lies in the localized concentration of defects that the dob-bone geometry presents.

Tab design parameters

If tabs are required, their geometry must be carefully defined; failing this, the tab itself can induce additional stress concentrations. The advantage relative to the superficial damage of the gripping regions is always guaranteed, as tabs physically shield the specimen. However, when improperly designed, they can cause premature failures in the regions they are applied to. Literature describes the key factors for an

effective behavior of the tabs for composite materials applications; obviously, this literature is not present about components manufactured via FFF. This section is aimed to determine the appropriate characteristics of the geometry experimentally. This analysis may start from the discussion reported for composite materials in [89]. The factors that have been considered are discussed hereinafter.

The material of the tab. The choice depends on needs of a different nature; in the first place, it must ensure that the load is transferred adequately to the specimen without yielding in advance. Other requirements can be thermal or economic. A widely accepted solution is to use glass fiber composites. In specific cases, carbon/epoxy composites or metals are also used. In the particular case of this work, it was decided not to consider this parameter as a variable. Tabs printed in PLA have been used, following some preliminary considerations:

- Ease of customization: printing the tabs via FFF allows customizing their geometric and dimensional features freely.
- Mechanical behavior affinity: tab and specimen are made of the same polymer; therefore, it can be speculated that their mechanical behavior does not differ significantly.
- Ease of gluing: the fundamental role of the adhesive will be addressed in the following; gluing together two elements of the same constituent is undoubtedly an advantage because the behavior of the adhesive towards the two elements is known once assessed the polymer-glue affinity.

The adhesive. It allows the load transmission due to shear stresses between the tabs and the specimen. The investigation has been restricted to cyanoacrylate adhesives compatible with PLA. The adhesive strength assessed by the manufacturer has been considered as the key parameter. The choice fell on UHU Bostik two-component epoxy adhesive D2870, which reported an adhesive strength of 170 km/cm^2.

The geometry. Among all the design variables, the geometric shape and dimensions of the tab take fundamental importance. Figure 3.19 shows two alternative configurations for a tabbed specimen. Apart from the geometric dimensions, the two ones are identical in the gripping region. The termination region can be of two types: untapered or tapered. In the second case, the transition between the grasping region and the region of interest occurs gradually, while in the first one, it occurs suddenly. Three parameters can be taken into consideration for the tapered configuration:

- Tab thickness, t_{tab}
- Tab taper angle, α_{tab}

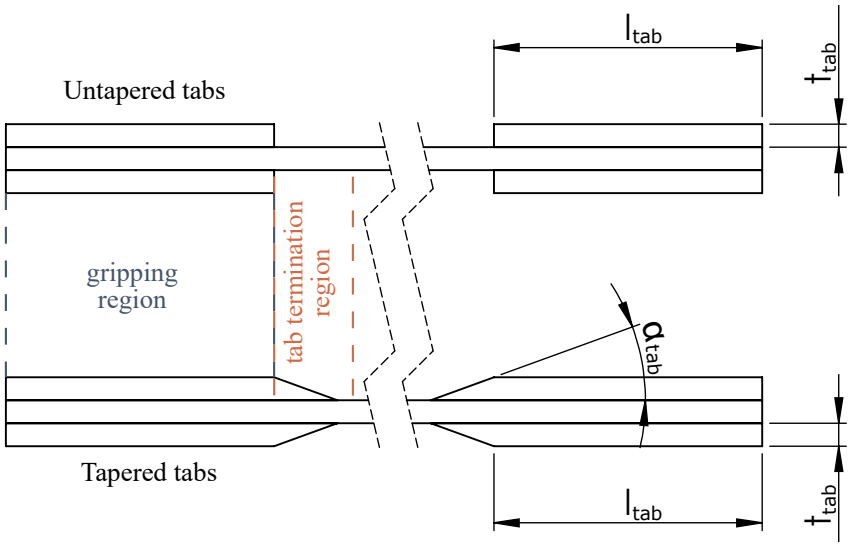

Figure 3.19: Tab design: tapered and untapered configuration for ASTM D3039 tensile specimens.

- Tab length, l_{tab}

The untapered configuration degenerates into the other one when the angle equals 90. From the geometric point of view, they can be considered as a single configuration, which can be described parametrically through the three variables.

Adams [89] reports that for composite materials, the longer the tab, the lower the stress concentrations in the exit section. However, with all other parameters being fixed, this decrease is negligible in the range $25 - 150$ mm. Taking into account that the longitudinal dimension of the gripping plates is 50 mm, this value has been chosen. Smaller taper angles reduce the geometric discontinuity between the transition region and the region of interest. Adams, therefore, reports that the optimal configuration would be the one in which the angle is as small as possible. However, it cannot tend to 0, both for production and for mechanical considerations. The transition region is not subjected to the grip pressure; as the angle decreases, this region increases in size, and the transverse and shear stresses might induce delamination between the tab and the component. The range between 5° and 90° has been considered as design range; however, more importance has been given to the lower corners. For what concerns the thickness, Adams suggested $1 - 2$ mm for general use; in fact, the author found little dependence on this parameter. To verify this point, the range under investigation has been extended, including thicknesses of 0.5 mm.

3.4.1 Tabbing set-up

The set-up to assemble specimens and tabs is described here. It is valid for both the coupons intended for the design variables validation and the definitive specimens for mechanical characterization. The tabs were printed through FFF with sacrificial PLA; they have always been produced with their large flat surface in contact with the building plate. This surface is intended to be welded with that of the specimens; however, it resulted extremely smooth. As indicated by the manufacturer, those surfaces have been roughened using sandpaper; this facilitated adhesion. The surfaces were then cleaned. Right after, the regions of the specimen not to be glued were masked with adhesive tape. The UHU Bostik D2870 adhesive comes in a double-syringe blister; one contains the resin, the other the hardening agent. An equal amount of both components is squeezed into the mixing glass. The two parts are then mixed with a synthetic spatula. The obtained mixture is then applied to the surfaces of the sample, where the tabs must adhere. This operation must be quickly performed as the adhesive remains processable for about 5 minutes after mixing. The tabs are then put into position; the spatula is then used to remove excessive glue and level the residues in the termination region. Some preliminary tests verified that this operation is essential to avoid delamination between specimen and tabs, especially in the tapered configuration. A clamp system is used to hold components in place. Immediately after putting it in place, the masking tape is removed. The manufacturer recommends a time of 20 minutes. To ensure complete cure of the adhesive, there was an hour before removing the vices.

3.4.2 Validation of tab design

The tab and adhesive materials have been selected, and the tab length has been set; the remaining parameters to consider are the thickness and the taper angle. The tab design has been investigated in the literature with respect to composite materials. How to set the choice in the FFF context? To adequately assess those parameters, a Design of Experiment (DoE) has been used with two factors and four levels. The Taguchi method has been considered; it allows to study and quantify in terms of mean and variance how different factors influence a key output of a process. The method is well suited to discrete-valued factors, which can only assume specific values, or levels. The factors and their respective levels are shown in Table 3.5; both the thickness and the taper angle are continuous variables, but the problem has been simplified considering only four possible levels. The DoE has been used for both types of specimens; nothing indicated that the effect of the tabs could be the same. Two runs have been completed to verify that the results of the first DoE were consistent. Only in the first DoE of direction 1 was the test speed added as a third parameter to verify FFF PLA behavior at different load application speeds. The second DoE in direction 1 verified that the tab geometry

Factors		Levels			
t_{tab} - Thickness	[mm]	0.5	1	1.5	2
α_{tab} - Taper angle	[deg]	5°	10°	20°	90°
v - Test speed	[mm/min]	0.5	2	3.5	5

Table 3.5: DoEs for tab design: factors and levels.

and the testing speed had distinct and independent influences. Consequently, from the second DoE onwards, the testing speed has been kept constant and equal to the value suggested for polymeric materials in [71]. An L16 design has been considered in each test; 16 tensile tests were then performed for each DoE. Two different output variables could be discussed:

- *The maximum load sustained by the specimen*, σ^{max}. If the tab geometry is not adequate and induces a stress concentration, it can be speculated that the specimen would yield prematurely, at lower loads.
- *The failure location*, y^{fail}. The specimen should fail in the region of interest, positioned symmetrically with respect to the midsection. The closer the failure location to the tab (possibly coinciding), the more likely the tab has negatively influenced the stress field. Specimens with tabs of different thickness and tapering angles have different lengths of interest. The failure has been located by measuring its distance from the closest tab with respect to the overall length of the region of interest.

DoEs: specimens loaded in direction 1

The parameters discussed in Section 3.4, combined into an L16 design, gave 16 different combinations of tab thickness, tab bevel angle, and test speed. The machine control system reported the load vs. displacement relation for each specimen as a direct output. All individual plots are given in Appendix C for convenience; Figure 3.20 summarizes the mechanical behavior of the whole run. All curves have an initial linear trend, which is followed by a more or less pronounced plastic region. There is a considerable variability in the maximum sustained load and fair variability in their slope. The sample is not uniform: in addition to different testing speeds, the specimens featured other tabs, meaning different geometry in the region between the two grips. Figure 3.21 shows the specimens at the end of the tensile tests; each of them features an identification label. There is considerable variability in the failure modes; using the failure codes reported in [35], they can be grouped as follows:

- *LAB/T (Lateral - At tab - Bottom/Top)*: specimens 1, 2, 5, 6, 7, 10, 11, 13, 15, 16.

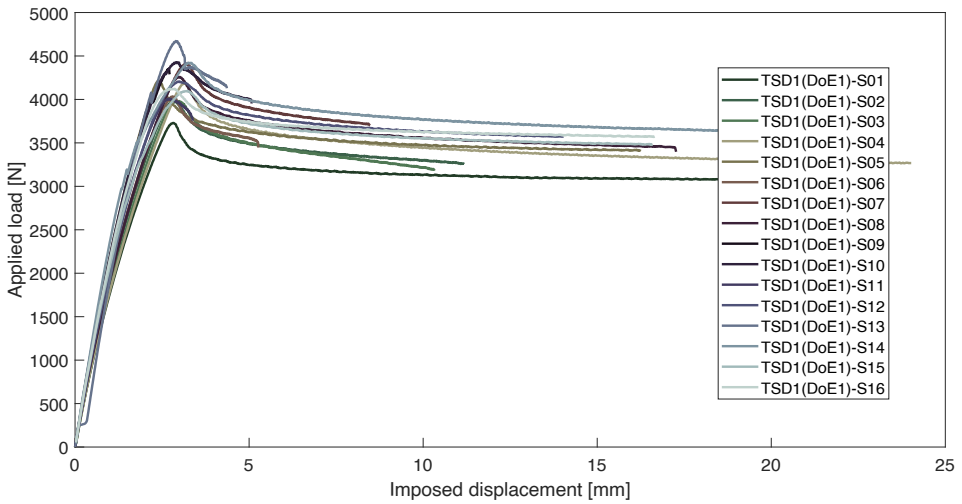

Figure 3.20: First DoE, tensile specimens loaded in direction 1: applied load vs. imposed displacement curves of the whole sample.

Figure 3.21: First DoE, tensile specimens loaded in direction 1 after the tests.

- *LIB/T (Lateral - Inside tab - Bottom/Top)*: specimen 9.
- *LWB/T (Lateral - <W from tab - Bottom/Top)*: specimens 3, 12.
- *LGM (Lateral - Gage - Middle)*: specimens 4, 8, 14.

Acceptable failure modes occurred three out of sixteen times (LGM); two further specimens failed at the limits of acceptability (LWB/T). The maximum sustained

stress σ^{max} has been used to evaluate the proper load introduction into the specimen; the failure location y^{fail} has not been considered as DoE output parameter due to the different residual deformation of the specimens. σ^{max} has been calculated using Equation 3.1, through the highest load recorded by the testing machine and the actual dimensions of each specimen. The results of the first DoE for specimens loaded into direction 1 are shown in Figure 3.22. The mean of means shows that

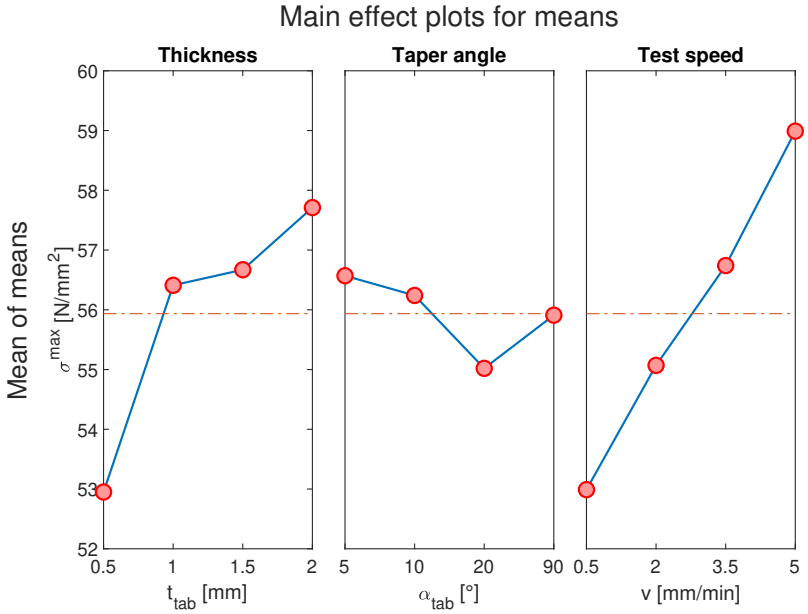

Figure 3.22: First DoE, tensile specimens loaded in direction 1: Taguchi analysis, σ^{max} vs. t_{tab}, α_{tab}, and v.

both geometrical parameters have influenced the output magnitude. σ^{max} increases with the tab thickness and as the taper angle decreases. Consequently, this DoE identified $t = 2$ mm and $\alpha = 5°$ as the best combination of geometric tab parameters for a proper load introduction into tensile specimens. It also confirmed that PLA behaves differently at different testing speeds.

A second DoE has been used to confirm those indications and exclude that the different testing speeds could have tainted the results. The geometric parameters discussed in Section 3.4 combined into an L16 design, gave 16 different combinations. All individual plots of the load vs. displacement relation appear in Appendix C for convenience; Figure 3.23 summarizes the mechanical behavior of the whole run. The variability of their slopes and the maximum sustained load are analogous with the previous DoE. Tested specimens are shown in Figure 3.24; each of them features an identification label. It is interesting to note that some specimens manifested necking; in those cases, they have been not brought to rupture as it

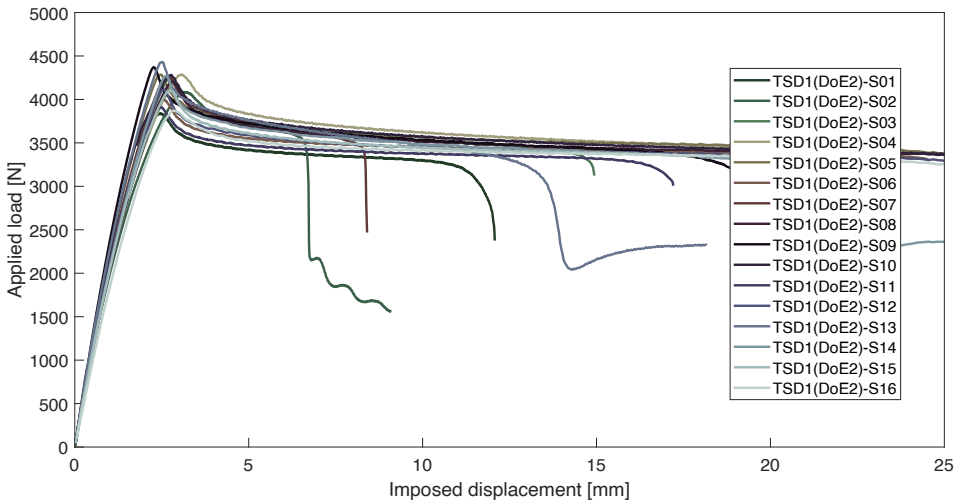

Figure 3.23: Second DoE, tensile specimens loaded in direction 1: applied load vs. imposed displacement curves of the whole sample.

Figure 3.24: Second DoE, tensile specimens loaded in direction 1 after the test.

would have been a lengthy process. This indicates that the typical plastic behavior of polymers can probably be excited along the direction 1 of the material only by acceptably introducing the load. The failure codes can group the samples as follows:

- *LAB/T (Lateral - At tab - Bottom/Top)*: specimens 1, 3, 6, 7, 8, 11, 12, 15.
- *LIB/T (Lateral - Inside tab - Bottom/Top)*: specimen 2.

- *LWB/T (Lateral - <W from tab - Bottom/Top)*: specimens 4, 16.
- *LGM (Lateral - Gage - Middle)*: specimens 5, 9, 10, 13, 14.

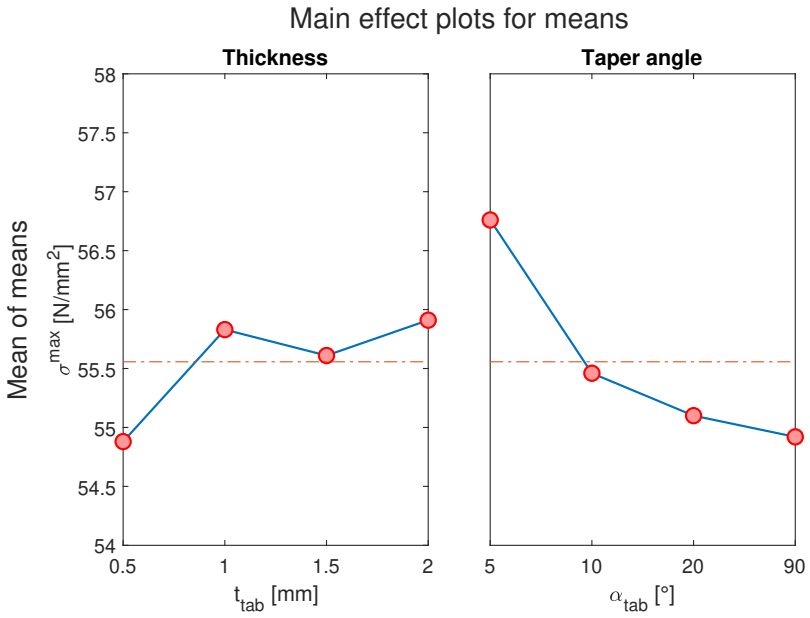

Figure 3.25: Second DoE, tensile specimens loaded in direction 1: Taguchi analysis, σ_{max} vs. t_{tab} and α_{tab}.

Acceptable failure modes occurred five out of sixteen times (LGM); two further specimens failed at the limits of acceptability (LWB/T). Using the maximum stress σ^{max} as an indicator of proper load introduction, this DoE confirmed the previous outcome. Also in this case, the failure location y^{fail} could not be used as DoE output parameter due to the different residual deformation of the specimens, much more pronounced due to the necking of some specimens. The results of the second DoE for specimen loaded in direction 1 are shown in Figure 3.25. By excluding the testing speed from the parameters, the mean of means shows that both the geometrical ones have influenced the output magnitude in the same way as in the previous evaluation.

DoEs: specimens loaded in direction 2

The DoEs for specimens loaded in direction 2 had the same scheme; the geometric parameters discussed in Section 3.4 have been combined in an L16 design. Again, all individual plots are available in Appendix C; Figure 3.26 summarizes the overall behavior of the first run. All the specimens behaved linearly initially, with similar variability in the slopes to that seen previously; the maximum load is

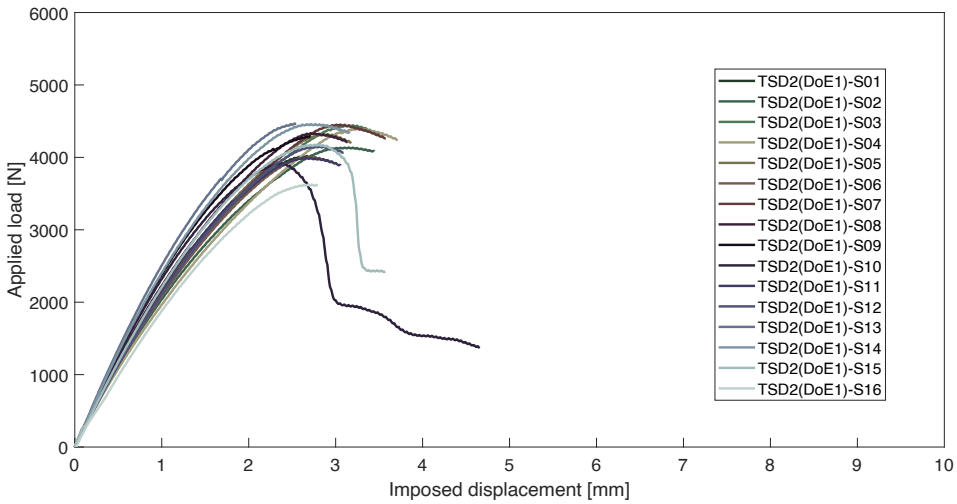

Figure 3.26: First DoE, tensile specimens loaded in direction 2: applied load vs. imposed displacement curves of the whole sample.

Figure 3.27: First DoE, tensile specimens loaded in direction 2 after the test.

much less scattered. However, all the specimens failed immediately after reaching the maximum sustained stress σ^{max}. Figure 3.27 shows the entire sample at the end of the experimental campaign. Unlike the previous specimens, the variability in terms of failure mode is very low; all the coupons broke abruptly, with a flat failure section. Using the failure codes reported in [35], they can be grouped as follows:

- *LAB/T (Lateral - At tab - Bottom/Top)*: specimens 13, 15.

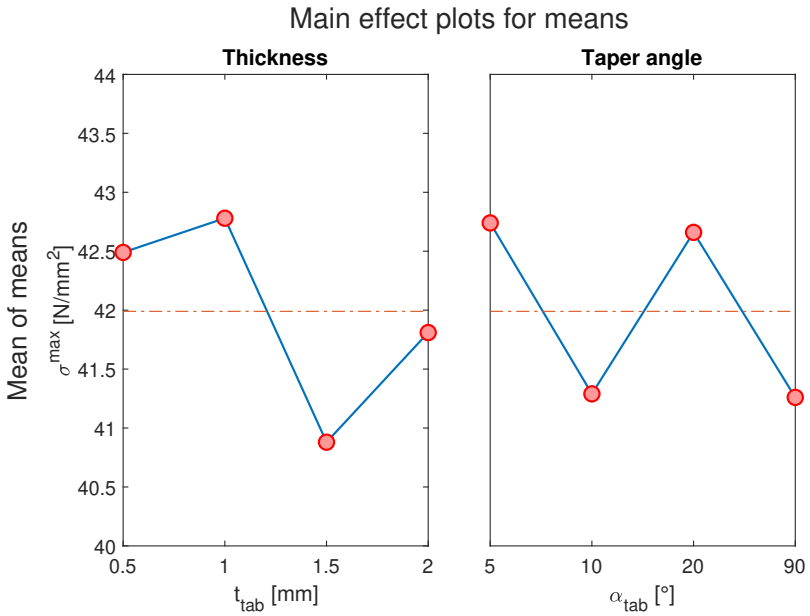

Figure 3.28: First DoE, tensile specimens loaded in direction 2: Taguchi analysis, σ^{max} vs. t_{tab} and α_{tab}.

- *LIB/T (Lateral - Inside tab - Bottom/Top)*: specimen 9, 10, 16.
- *LWB/T (Lateral - <W from tab - Bottom/Top)*: specimens 1, 2, 14.
- *LGM (Lateral - Gage - Middle)*: specimens 3, 4, 5, 6, 7, 8, 11, 12.

Unacceptable failure modes occurred five out of sixteen times; most of the specimens failed in the gage section (LGM + LWB/T), although some near the termination region (LWB/T). Using the maximum sustained stress σ^{max} as the output variable, the results of the DoE for specimen two are shown in Figure 3.28. It is interesting to note that in this case, the indications provided by the DoE were not as straightforward as in the previous cases. A partial hint is present for the thickness, as 1 mm seems to drive higher sustained stress. Regarding the taper angle, the graph fluctuates; 5° and 20° drove the maximum values, 10° and 90° the minimum ones. For this reason, the analysis has been repeated using the failure location y^{fail} as an output parameter. The results are expressed in Figure 3.29; as anticipated, the position is measured from the nearest tab and indicated as a percentage to the length of the region of interest. This was to compensate for the fact this length varied among the different specimens. The mid-section of each sample is located at 50%; the closer the failure location, the better the output. Figure 3.29 clarified the influence of the two parameters; the failure location is driven towards the middle of the specimen by a tab thickness of 1 mm and a taper angle of 20°.

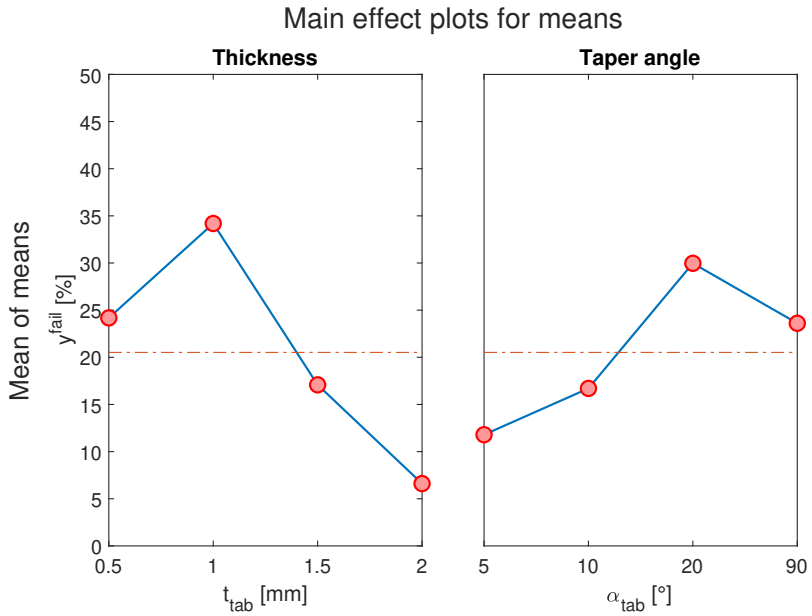

Figure 3.29: First DoE, tensile specimens loaded in direction 2: Taguchi analysis, y^{fail} vs. t_{tab} and α_{tab}.

As previously done, the DoE has been repeated a second time. The results in terms of failure location y^{fail} are shown in Figure 3.30. This second DoE confirms the first indications, as it shows that the thickness of 1 mm and the taper angle of 20° lead to a failure location away from the tabs. For completeness, Figure 3.31 shows the specimens at the end of the experimental campaign; Figure 3.32 groups the load vs. displacement relations of the sample. The individual curves are available in Appendix C. The failure classification allows grouping the specimens into:

- *LAB/T (Lateral - At tab - Bottom/Top)*: specimens 4, 5, 12, 15, 16.
- *LWB/T (Lateral - <W from tab - Bottom/Top)*: specimens 1, 2, 3, 9, 10, 13, 14.
- *LGM (Lateral - Gage - Middle)*: specimens 6, 7, 8, 11.

Therefore, this second DoE confirms the positive trend of the previous; most of the specimens, 11 out of 16, showed an acceptable failure mode, even if most at boundaries (LWB/T).

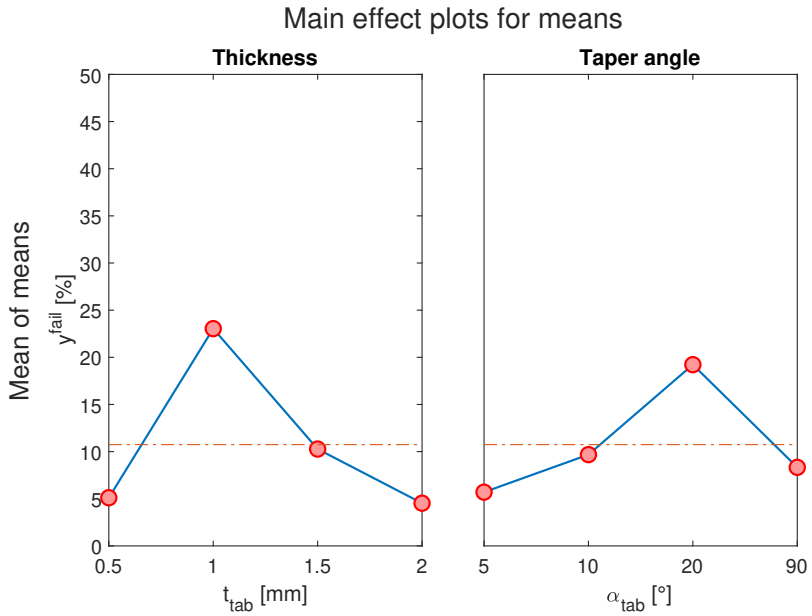

Figure 3.30: Second DoE, tensile specimens loaded in direction 2: Taguchi analysis, y^{fail} vs. t_{tab} and α_{tab}.

Figure 3.31: Second DoE, tensile specimens loaded in direction 2 after the test.

3.4.3 Tensile tests for mechanical characterization

As discussed in the introduction, a single PLA spool has been used to print the actual specimens for mechanical characterization and the specimens for the validation tests. This limited the dimensions of the specimen sample to 9 which is consistent with the minimum number of specimens, 5, required by ASTM D3039. On the other hand, this sample size preserves a margin for reprinting (and retesting)

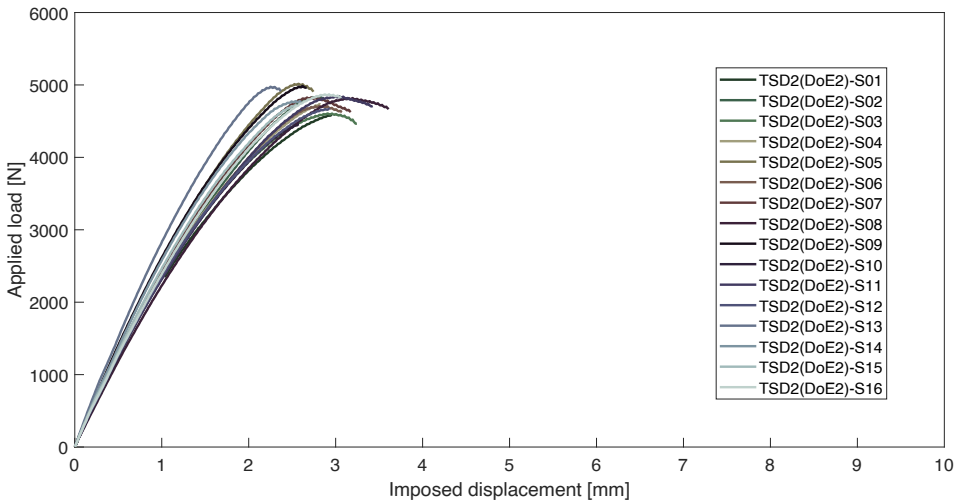

Figure 3.32: Second DoE, tensile specimens loaded in direction 2: applied load vs. imposed displacement curves of the whole sample.

specimens that have failed unacceptably. As for the DoEs, the tests have all been performed under displacement control. 5 mm/min is the lowest cross-head speed for polymeric materials discussed in ASTM D638, to be used if specimens fail within $0.5 - 5$ minutes. This is different with respect to the required testing speed discussed in ASTM D3039 (2 mm/min, with failure within $1 - 10$ min); however, the first one has been used to keep consistency with the pratices generally used with polymeric materials. Before the tests, the cross-section of each specimen has been measured with a digital caliper. The measurement of both thickness and width has been repeated five times; the values have been averaged to obtain a representative number. Since preliminary DoE tests shown loads up to 5 kN, a 10 kN load cell was installed on-board the MTS QTest. To avoid any eccentricities in the load application direction with respect to the specimen longitudinal axis, the alignment of the jaws was checked before the experimental campaign. The adapters discussed in Section 3.2, and presented in Figure 3.4, have been installed in both jaws as done in the preliminary tests. Specimens have been placed first in the lower grip and then in the upper one. The longitudinal and transverse strain have been monitored through DIC, following the algorithm discussed in Appendix B. The tests have been recorded with a Canon D3500 DSLR Camera. As discussed in Appendix B, the optical zoom has been set to 35 mm to avoid focal distortions. The tensile stress has been calculated through the applied load and the initial cross-section dimension (see Equation 3.1). The testing machine sampled the applied load, thus the tensile stress, at 5 Hz. The frame rate of the DSLR camera videos has been reduced to 5 fps while importing the frames to the correlation software to match this. After each test, the operator counted on a stress vs. time relation, a longitudinal strain

vs. time relation, and a transverse strain vs. time relation. The video of the test necessarily starts before the test beginning, as the camera is operated manually. The first data of the stress vs. time relation represents the *first* instant of the test as the testing machine starts sampling as the test begins. The strains and the stress have been synced over time through the following criterion: a random strain distribution map with close to zero values (positive and negative) due to image noise characterizes the frames preceding the test; the first instant of the test is that in which the longitudinal displacements map is fully concordant with the load application direction.

Direction 1

Following the terminology in Figure 3.1, the specimens have all the prefix *TSD1*. The geometrical dimensions of their cross-section are shown in Table 3.6; the mean values and the standard deviations of the sample are also reported. The individual

SPECIMEN	Cross-section W [mm]	Cross-section L [mm]
TSD1-S01	24.91	2.96
TSD1-S02	24.99	3.04
TSD1-S03	24.99	3.02
TSD1-S04	25.00	3.04
TSD1-S05	25.00	3.01
TSD1-S06	24.92	2.97
TSD1-S07	24.94	2.98
TSD1-S08	24.91	2.97
TSD1-S09	24.92	2.99
TSD1 Sample		
mean	24.95	3.00
st.dev	0.041	0.031

Table 3.6: Geometrical dimensions of TSD1 sample specimens.

tensile stress vs. longitudinal strain curves are given in Appendix C; Figure 3.33 shows the behaviour of the whole sample. Figure 3.34 shows the specimens loaded into direction 1 at the end of the tests. All specimens exhibited necking; note how this happened in the gage section. The coupons were not brought to failure as the plastic deformation in the necking region deformed the gray/white pattern, preventing the strain correlation at the late stages of the tests. Nevertheless, specimens 1, 4, and 5 show how failure would have occurred within the necking region. Using the failure codes reported in [35], all specimen failures can therefore be classified as *LGM - Lateral Gage Middle*.

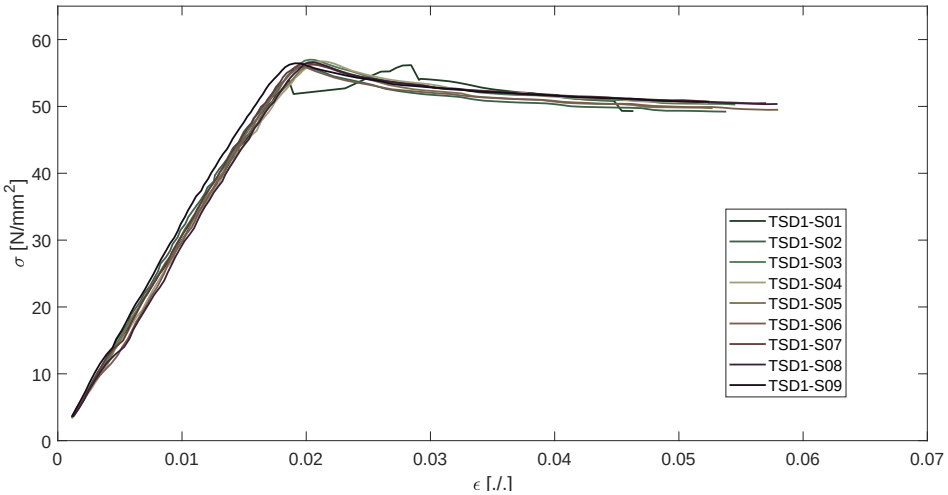

Figure 3.33: Tensile tests in direction 1: stress vs. strain curves of the whole sample.

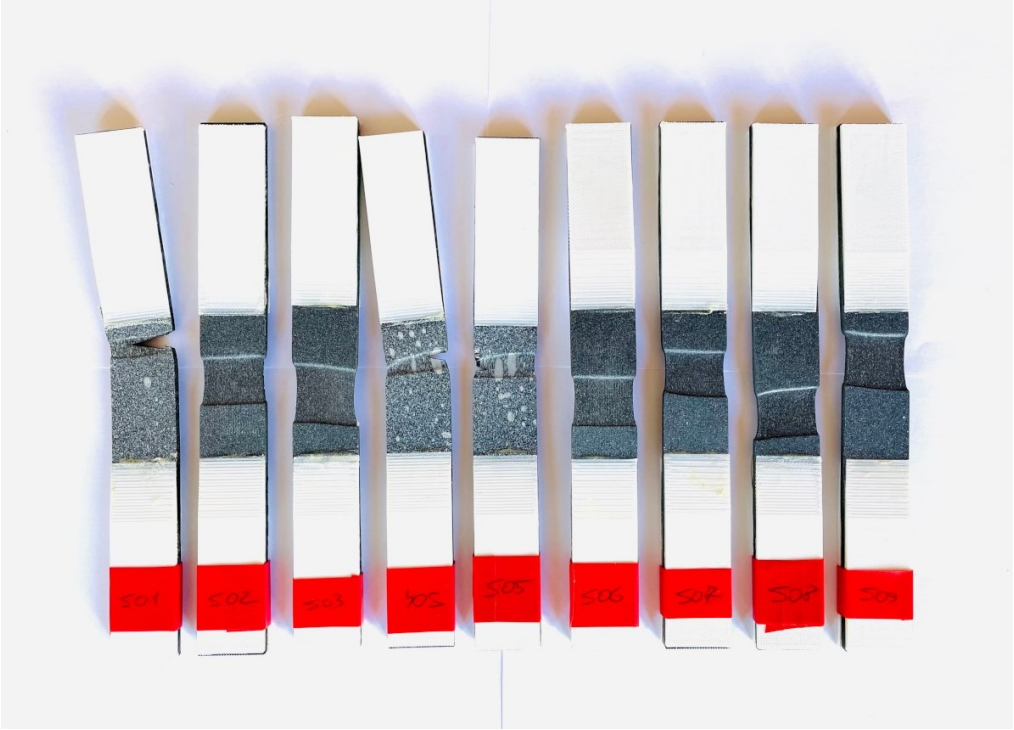

Figure 3.34: Specimens for tensile properties determination in direction 1 at the end of the tests.

All the curves have an almost linear trend; their maximum is preceded by a slight deviation from linearity, and followed by a wide plastic region at an almost

constant load. To be thorough, these tests allowed to calculate:

- the modulus of elasticity, E_{11}, through a set of linear regressions on intervals of gradually increasing size. The iterations stop when the new linear regression coefficient differs from the mean of the previously calculated values by more than 5%;
- the tensile proportional limit, σ_{11}^{pro}, identified with the stress value at which the iterations for E_{11} calculation stopped;
- the tensile strength, σ_{11}^{max}, using the maximum load reported by the testing machine;
- the Poisson ratio, ν_{12}, evaluating the average of the transverse strain vs. longitudinal strain ratio in the linear section of the curve.

Table 3.7 reports the individual values obtained through this experimental campaign, together with the mean and the standard deviation values. The data shown

SPECIMEN	Mechanical analysis			
	E_{11} [MPa]	σ_{11}^{max} [MPa]	σ_{11}^{pro} [MPa]	ν_{12} [-]
TSD1-S01	3007	56.18	53.36	0.288
TSD1-S02	3094	55.83	51.72	0.303
TSD1-S03	3029	56.99	54.33	0.269
TSD1-S04	2920	56.75	55.39	0.274
TSD1-S05	2987	56.26	51.81	0.277
TSD1-S06	2944	56.00	54.31	0.275
TSD1-S07	3037	56.41	56.41	0.297
TSD1-S08	2867	56.64	54.30	0.269
TSD1-S09	3183	56.44	54.31	0.321
TSD1 Sample				
mean	**3008**	**56.39**	**53.99**	**0.286**
st.dev	94.51	0.368	1.522	0.018

Table 3.7: Tensile tests in direction 1: results of the experimental campaign.

in bold, ie $E_{11} = 3008$ MPa, $\sigma_{11}^{max} = 56.39$ MPa, $\sigma_{11}^{pro} = 59.33$ MPa, and $\nu_{12} = 0.286$ are the output of this characterization campaign. Note how the values obtained for E_{11} and σ_{11}^{max} are lower than those obtained on the feedstock material but still in the same order of magnitude.

Direction 2

Following the terminology of Figure 3.1, all specimens have the prefix *TSD2*. With respect to the dimensions of their cross-section, the mean values and the standard deviations of the sample are discussed in Table 3.8 together with the individual values. The behaviour of the whole sample is described by Figure 3.35;

SPECIMEN	Cross-section W [mm]	L [mm]
TSD2-S01	24.84	4.12
TSD2-S02	24.83	4.13
TSD2-S03	24.82	4.14
TSD2-S04	24.85	4.14
TSD2-S05	24.83	4.12
TSD2-S06	24.82	4.15
TSD2-S07	24.83	4.13
TSD2-S08	24.83	4.16
TSD2-S09	24.78	4.13
TSD2-S10	24.81	4.16
TSD2 Sample		
mean	24.82	4.14
st.dev	0.019	0.015

Table 3.8: Geometrical dimensions of TSD2 sample specimens.

Appendix C reports all the individual tensile stress vs. longitudinal strain curves. The tested specimens are shown in Figure 3.36. All specimens failed abruptly within the gage section; the failure line coincides with the interface between adjacent beads. No necking manifested, nor a macroscopic plastic deformation. All specimen failures can therefore be classified as *LGM - Lateral Gage Middle*, through the failure codes reported in [35]. The curves have an almost linear trend. The maximum is preceded by a slight deviation from linearity, and all the specimens failed after it. The considerations relating to how each mechanical property has been determined are similar to those reported for the previous sample. To be thorough, these tests allowed to calculate:

- the modulus of elasticity, E_{22};
- the tensile proportional limit, σ_{22}^{pro};
- the tensile strength, σ_{22}^{max};
- the Poisson ratio, ν_{23}.

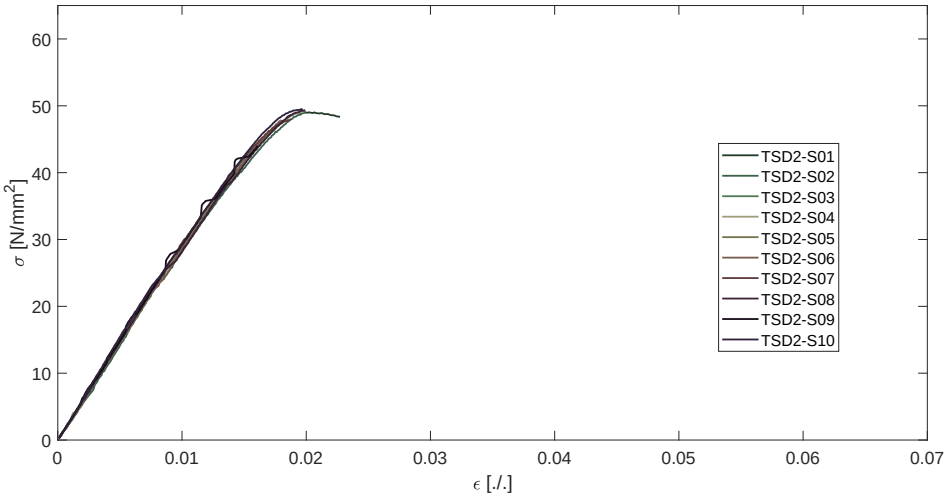

Figure 3.35: Tensile tests in direction 2: stress vs. strain curves of the whole sample.

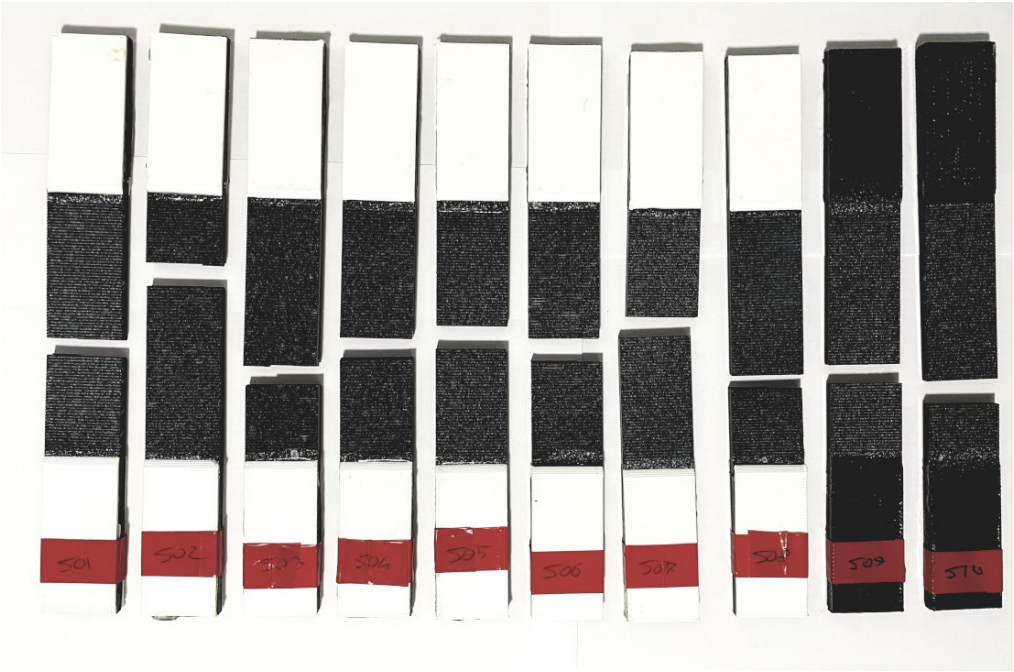

Figure 3.36: Specimens for tensile properties determination in direction 2 at the end of the tests.

The individual values obtained through this experimental campaign are reported in Table 3.9, together with the mean and the standard deviation values. The output of the second characterization campaign are data shown in bold, ie $E_{22} =$

SPECIMEN	Mechanical analysis			
	E_{11} [MPa]	σ_{11}^{max} [MPa]	σ_{11}^{pro} [MPa]	ν_{12} [-]
TSD2-S01	2863	49.03	47.74	0.282
TSD2-S02	2783	49.03	46.24	0.233
TSD2-S03	2902	46.79	46.60	0.265
TSD2-S04	2905	49.10	46.22	0.289
TSD2-S05	2866	47.66	47.16	0.252
TSD2-S06	2840	47.90	47.31	0.249
TSD2-S07	2902	48.01	43.88	0.286
TSD2-S08	2821	49.36	46.47	0.262
TSD2-S09	2950	44.03	43.54	0.259
TSD2-S10	2926	49.50	47.00	0.292
TSD2 Sample				
mean	**2876**	**48.04**	**46.22**	**0.267**
st.dev	50.97	1.659	1.409	0.020

Table 3.9: Tensile tests in direction 2: results of the experimental campaign.

2876 MPa, $\sigma_{22}^{max} = 48.04$ MPa, $\sigma_{22}^{pro} = 46.22$ MPa, and $\nu_{23} = 0.267$. Note how the values obtained for E_{22} and σ_2^{max} differ from those obtained in the previous characterization campaign and are even lower than those obtained on the feedstock material. This confirms the anisotropy of the material.

3.5 Shear properties determination

Like tensile tests, to determine the shear response of a material, it is necessary to induce an adequate stress field. The standard procedure for isotropic materials considers a cylindrical specimen subjected to torsion. For this category, the shear modulus would be directly related to the Young modulus and the Poisson ratio according to Equation 3.3:

$$G = \frac{E}{2(1+\nu)} \tag{3.3}$$

A difference between the experimental value and that predicted by the classical relationship leads to suspect that the material may have a generically anisotropic behavior [90]. At the same time, the relationship could not be considered as the previous results on E_{11} and E_{22} confirms that the material is not isotropic. To fully characterize an orthotropic material, three shear modules and three shear strengths need to be quantified. Reducing the application field to composite materials makes it possible to distinguish between in-plane shear behavior and interlaminar shear

behavior. Various tests have been developed and investigated over time, each characterized by specific indications according to the properties to be determined. In the most general case, a commonly accepted test is the V-notched shear test, also known as the Iosipescu shear test, which allows determining both interlaminar and in-plane properties. It considers rectangular and flat specimens, with two symmetrical v-notches causing a reduction of the cross-section where a shear stress state develops due to a load applied on two opposite edges of the sample, along the same line but opposite. Several other tests have been developed to overcome some limitations. The rail shear test is an alternative that guarantees a more significant gage section and allows a higher load to be transmitted; it considers a rectangular and flat specimen with constant cross-section dimensions. The load is here applied to the faces of the sample. The V-notched rail method combines the advantages of the two tests; the specimen is characterized by two symmetrical v-notches, as the Iosipescu test, but it is loaded through its faces, as the rail test. A complex set-up characterizes all these tests, but they are indispensable for determining the interlaminar behavior. In the specific case of the in-plane shear modulus of composite materials, an alternative is offered by tensile test on ± 45 specimens, following ASTM D3518 [91]. Recalling the parallel speculated between UDC and FFF components and the CLT hypotheses, a single shear stiffness coefficient would be required to complete the elastic coefficients matrix, the one that in Chapter 2 has been called G_{12}.

The response of the material is studied in terms of shear stress and shear strain. As in the case of tensile tests, the first one is quantified through the applied load, measured by the load cell of the testing machine; the second one is measured through contact or non-contact transducers (e.g., strain gauges, extensometers, Digital Image Correlation). The list of properties that can be quantified includes:

- The *shear modulus of elasticity*, which represents the slope of the shear stress vs. shear strain curve of a material, in the linear region;
- The *shear strength*, which is maximum shear stress a material is capable of sustaining.

Mesostructure of shear specimens

As the tensile tests have determined that the behavior of the material is not isotropic, it is necessary to determine the specimen mesostructures for the load application scheme. Despite the specific geometry, each shear specimen has a region of interest in which the mechanical properties are evaluated. Recalling the mesostructure of a cubic and unidirectional FFF element, it is necessary to imagine and extract the regions of interest. This discussion is simplified here because it takes advantage of the previous reasoning on tensile properties and follows it.

Since introducing the shear load in a specimen is more complicated than introducing the tensile load, the idea is to fully exploit the coupling between geometry and mesostructure already established for composite materials.

3.6 Shear tests according to ASTM D3518

ASTM issues the standard test method for the in-plane shear response of composite materials under the designation D3518 [91]. The standard is dedicated to fiber-reinforced polymers with a high stiffness modulus. This standard is simpler to apply than the others briefly introduced; it allows to determine the in-plane shear properties through a tensile test. The shear response of the material is excited due to the particular lamination of the component: with respect to the load application direction, the reinforcements are not arranged at 0° or 90° but off-axis, with an angle of ±45°, alternated from lamina to lamina. The geometry description is very simple, as it completely refers to that provided by ASTM D3039. A rectangular tensile coupon is considered, with constant cross-section; the load is introduced into the specimen by two plates, which transfer the tensile load by friction. The tests have to be performed under displacement control. ASTM D3518 requires a test speed producing the specimen failure in $1 - 10$ minutes and suggests an attempt value of 2 mm/min. Since ASTM D3039 and ASTM D3518 are intended for composites, much stiffer than PLA, the ASTM D638 indication of 5 mm/min has been considered to keep consistency with the practices generally used with polymeric materials. Before the tests, each specimen has been measured with a digital caliper. Particular attention has been paid to the cross-section dimensions. For both thickness and width, the measurement has been repeated five times; the values have been averaged to obtain a representative number.

Thanks to the particular stacking sequence, the in-plane shear stress can be calculated through the laminate plate theory as:

$$\tau_{12} = \frac{P}{2A_0} \tag{3.4}$$

where P is the tensile load applied to the specimen, and A_0 is its initial cross-section. Similarly, the laminate plate theory calculates the in-plane share strain from the longitudinal and transverse strains of the coupon. In particular, having defined a global reference system $X - Y$, with X arranged along the longitudinal axis of the specimen and Y along the transverse direction, the in-plane shear strain can be calculated as

$$\gamma_{12} = \epsilon_x - \epsilon_y \tag{3.5}$$

where ϵ_x is the longitudinal strain, in the X direction, while ϵ_y is the transverse strain, in the Y direction. Consequently, as far as geometry is concerned, the description in Figure 3.18 applies. The standard requires a $[+45/-45]_{ns}$ stacking

sequence, with n included in the range $4-6$. This implies that the thickness is obtained through 16, 20, or 24 laminae. For the same reasoning on the macroscopic difference in fibers and beads dimensions, the requirement $[+45/-45]$ was fulfilled; however, the thickness was increased to count 30 layers, reaching a value of 3 mm. For what concerns the length, the same reasoning on the printing volume of most of the printers on the market discussed for tensile specimens applies. The width was kept as suggested in [91]. The recommended and the actual dimensions are therefore presented in Table 3.10. All the other specificities of the tensile

Dimensions		Recommended $\pm 45°$ unid.	Actual SSD12
LO - length overall	[mm]	$200-300$	190
W - width	[mm]	25	25
T - thickness		$16-20-24$ laminae	3 mm

Table 3.10: ASTM D3518 recommended and actual dimensions for shear specimens.

tests are also valid in this case: the test is performed under displacement control until the specimen breaks; however, the test has to be suspended if the specimen does not fail within the strain limit of 5%. This limitation takes into account that at high deformations, the required lamination at $\pm 45°$ is violated due to fiber scissoring. The standard reports that tabs are usually not required; however, taking into account that the test is, in essence, a tensile test, the acceptable failure modes should drive the assessment. The need for a set of tabs, and their characteristics, have been considered following the literature indications already discussed.

3.6.1 Validation of tab design

Since the reference geometry is the same, the same reasoning followed for the tensile tests still holds. Once the tab and adhesive materials, and the tab length have been set, the thickness and the taper angle were assessed through a Design of Experiment, following the Taguchi method. The parameters and their respective levels are shown in Table 3.5; combined into an L16 design, they gave 16 different combinations of tab thickness, tab bevel angle. Two runs have been completed to verify that the results of the first DoE were consistent. The same output variables of tensile tests have been considered; however, some considerations suggested the maximum load sustained by the specimen, τ^{max}. All individual plots are given in Appendix C for convenience; Figure 3.37 summarizes the mechanical behavior of the whole run. All curves have an initial linear trend and stop shortly after the maximum load. There is a considerable variability in the maximum sustained load and fair variability in their slope. As for tensile specimens, the sample is not uniform due to different lengths in the region or interest. Figure 3.38 shows the

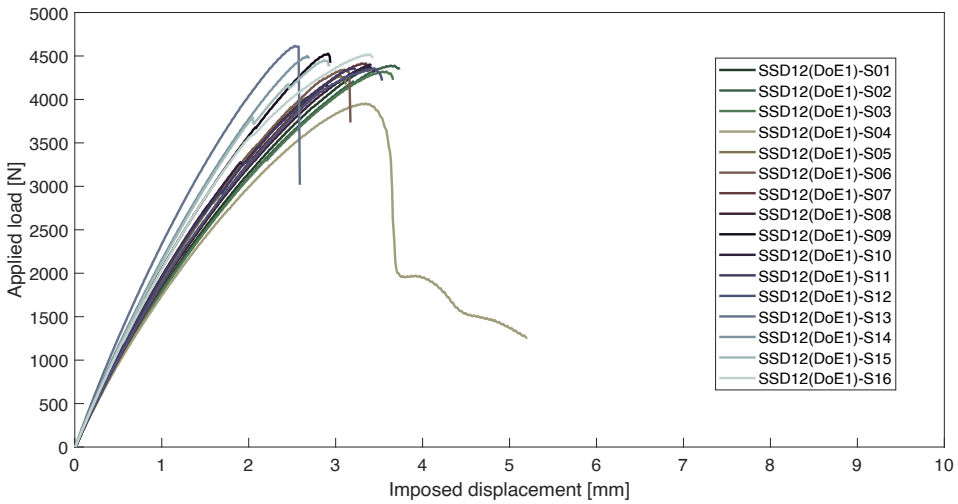

Figure 3.37: First DoE, ±45° shear specimens: applied load vs. imposed displacement of the whole sample.

specimens at the end of the tensile tests; each of them features an identification label. As for the failure modes, almost all the specimens failed at 45°, which

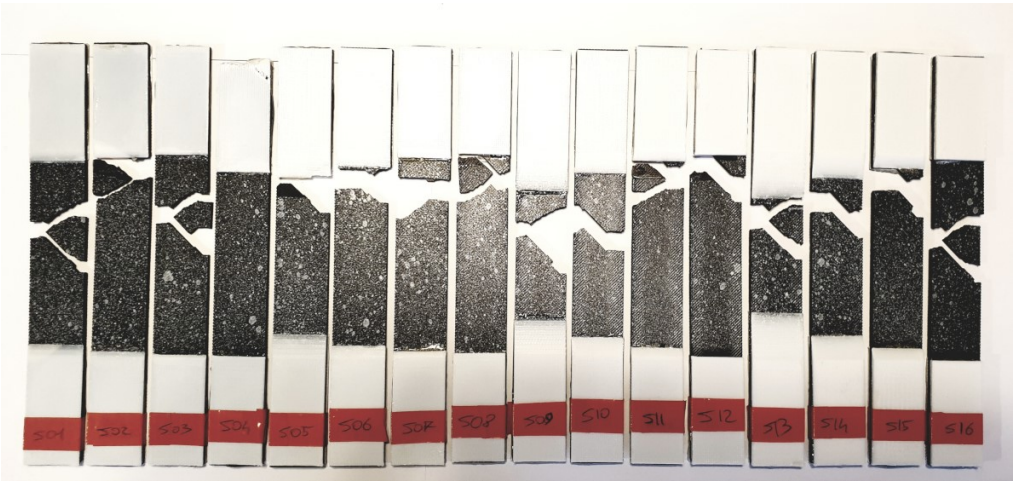

Figure 3.38: First DoE, ±45° shear specimens after the tests.

consolidates the hypothesis of near pure shear condition. Since the crack is also distributed longitudinally, it is difficult to associate a coordinate; associating a failure code is difficult for the same reason. However, few specimens failed outside the gage section, which suggests that the tabs facilitate the load introduction in all the configurations. Consequently, the maximum sustained stress τ^{max} has been used to evaluate the proper load introduction into the specimen. τ^{max} has been

calculated using Equation 3.4, through the highest load recorded by the testing machine and the actual dimensions of each specimen. The results of the first DoE for specimen one are shown in Figure 3.39. The mean of means shows that both

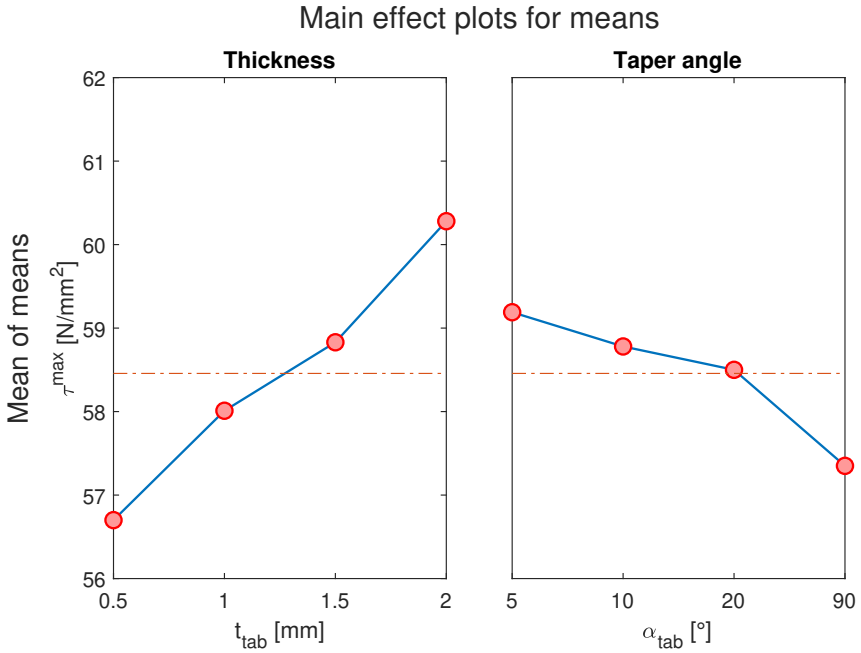

Figure 3.39: First DoE, ±45° shear specimens: Taguchi analysis, τ^{max} vs. t_{tab} and α_{tab}.

parameters have influenced the output magnitude, similarly to what happened for tensile specimens loaded in direction 1. τ^{max} increases with the tab thickness and as the taper angle decreases. Consequently, this DoE identified $t = 2$ mm and $\alpha = 5°$ as the best combination of geometric tab parameters for a proper load introduction into the specimens. A second DoE has been used to confirm those indications. All individual plots of the load vs. displacement relation appear in Appendix C for convenience; Figure 3.40 summarizes the mechanical behavior of the whole run. The variability of their slopes and the maximum sustained load are analogous with the previous DoE. Tested specimens are shown in Figure 3.41; each of them features an identification label. As in the previous case, almost all the specimens failed at 45°. Using the maximum sustained stress τ^{max} as an indicator of proper load introduction (see Figure 3.42), this DoE confirmed the previous outcome; both the geometrical ones have influenced the output magnitude in the same way as in the previous evaluation. Both DoEs validated the tab geometry; the maximum sustained stress indexed the correct load introduction into the specimen. Therefore, considering the geometry of Figure 3.19, a tab bevel angle of 5° and

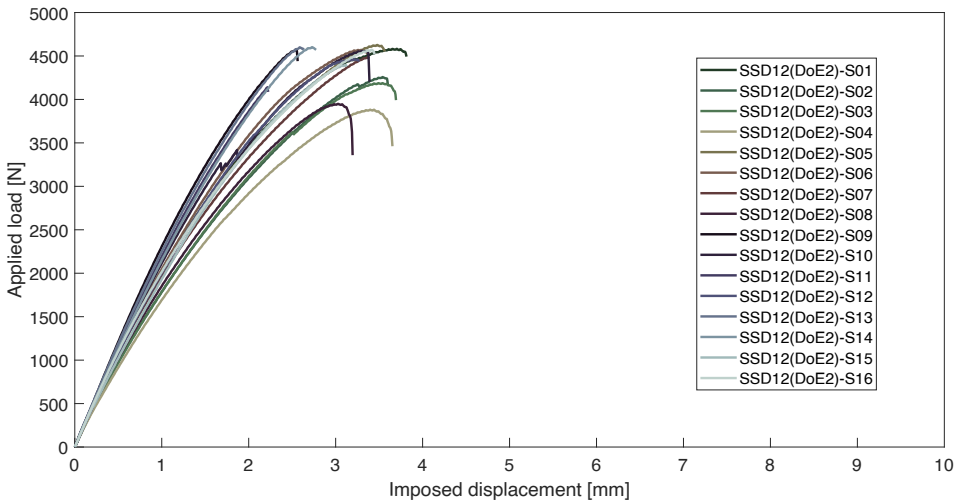

Figure 3.40: Second DoE, ±45° shear specimens: applied load vs. imposed displacement curves of the whole sample.

Figure 3.41: Second DoE, ±45° shear specimens after the tests.

a tab thickness of 2 mm have been identified for in-plane shear specimens. The following characterization campaign followed these requirements.

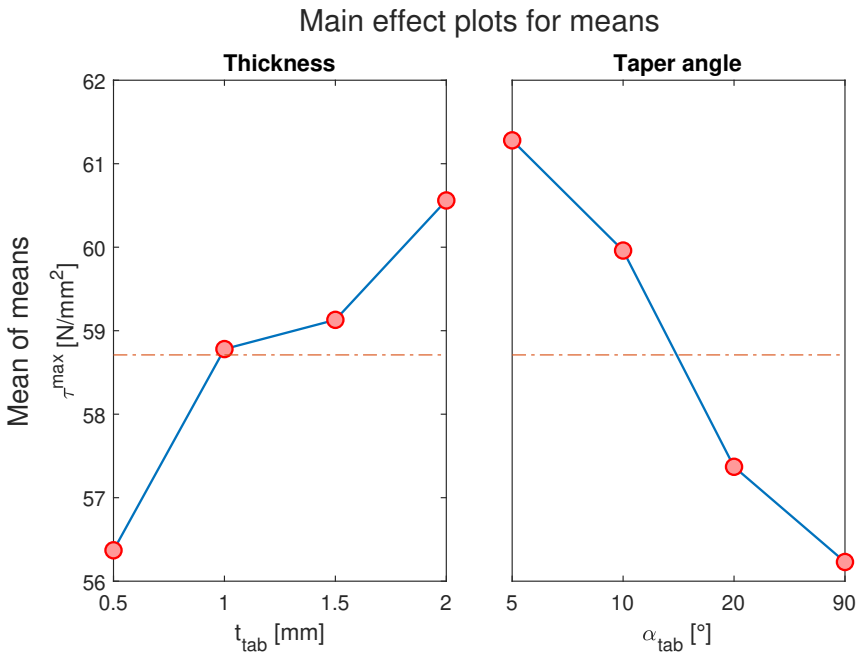

Figure 3.42: Second DoE, ±45° shear specimens: Taguchi analysis, τ^{max} vs. t_{tab} and α_{tab}.

3.6.2 Actual tests

As anticipated, to keep consistency between the actual characterization tests and the validation tests, a single PLA spool has been entirely dedicated to them. As a result, a reduced specimen sample has been considered. In analogy with the tensile tests performed in directions 1 and 2, a sample of 7 specimens has been considered. The numerical value may seem limited; however, it is consistent with the minimum number of specimens, 5, required by ASTM D3039, on which the test method described by ASTM D3518 relies. Furthermore, the identified PLA amount allowed excluding from the analysis and possibly reprinting those specimens that behaved inconsistently with the sample or shown unacceptable failure modes. Following the terminology in Figure 3.1, all specimens have the prefix SSD12. The geometrical dimensions of their cross-section are shown in Table 3.11; the mean values and the standard deviations of the sample are also reported. Before the experimental campaign, and after installing a 10 kN load cell, the alignment of the MTS QTest jaws has been checked to avoid eccentricity in the application of the load. For the same reason, the adapters discussed in Section 3.2, and represented in Figure 3.4, have been installed in both jaws. Each specimen has been then placed first in the lower grip and then in the upper one. The longitudinal and axial deformations have been monitored through DIC, following the algorithm discussed

SPECIMEN	Cross-section W [mm]	T [mm]
SSD12-S01	24.92	2.96
SSD12-S02	24.93	2.94
SSD12-S03	24.84	2.96
SSD12-S04	24.89	2.94
SSD12-S05	24.90	2.96
SSD12-S06	24.89	2.96
SSD12-S07	24.84	2.96
SSD12-S08	24.89	2.96
SSD12-S09	24.83	2.95
SSD12-S10	24.86	2.95
SSD12 Sample		
mean	24.88	2.95
st.dev	0.038	0.008

Table 3.11: Geometrical dimensions of SSD12 sample specimens.

in Appendix B. The tests have been recorded with a Canon D3500 DSLR Camera, with the optical zoom set to 35 mm to avoid focal distortions and at a suitable distance to shoot the entire region of interest. The longitudinal and the transverse strain have been combined as described by Equation 3.5 to obtain the shear strain. The applied load, measured by the testing machine, and the initial cross-section dimension have been combined as required by Equation 3.4 to obtain the shear stress. Stresses and strains have been sampled at 5 Hz. The videos frequency was lowered from 30 fps to match the test machine and allow the association of the data. After each test, the operator counted on stress vs. time relation and strain vs. time relation. The sync over the time has been performed in analogy with what discussed for tensile tests, considering as the first instant of the test the one in which the longitudinal displacements map showed a concordant displacement in direction.

The individual shear stress vs. shear strain curves are given in Appendix C; the behavior of the whole sample is shown in Figure 3.43. Figure 3.44 shows the specimens at the end of the tests. All the samples failed within the gage section. All the failure sections are at ± 45, suggesting that every specimen failed by shear stresses. The failure codes reported in [35] allows to classify all the specimen failures as *LGM - Lateral Gage Middle*. No necking manifested, nor a macroscopic plastic deformation. The curves have an almost linear trend. The specimens failed briefly after the maximum load, preceded by a slight deviation from linearity. All specimens failed within the 5% strain limit, as required by [91]. The same script

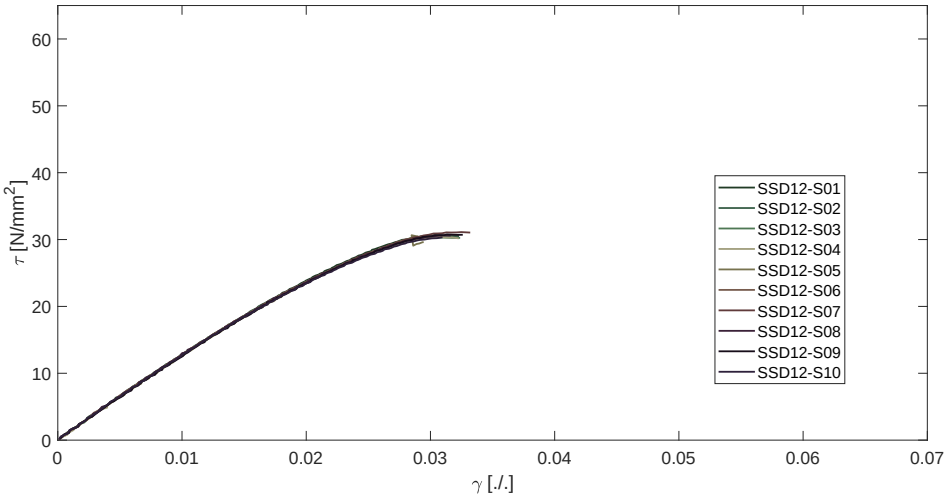

Figure 3.43: Shear tests: stress vs. strain curves of the whole sample.

Figure 3.44: Specimens for shear properties determination at the end of the tests.

used to post-process the tensile specimen was used; however the stiffness modulus has been calculated in a simplified way. The chord shear modulus was quantified in a 4000 $\mu\epsilon$ range, starting from 4000 $\mu\epsilon$ epsilon, as requested by [91]. These tests allowed to calculate:

- the chord shear modulus of elasticity, G_{12};
- the shear strength, τ_{12}.

SPECIMEN	Mechanical analysis G_{12} [MPa]	τ_{12}^{max} [MPa]
SSD12-S01	1232	30.63
SSD12-S02	1228	30.63
SSD12-S03	1240	30.30
SSD12-S04	1233	30.40
SSD12-S05	1213	30.65
SSD12-S06	1237	30.61
SSD12-S07	1230	31.12
SSD12-S08	1232	30.63
SSD12-S09	1206	30.77
SSD12-S10	1220	30.34
SSD12 Sample		
mean	**1227**	**30.61**
st.dev	10.81	0.236

Table 3.12: Shear tests: results of the experimental campaign.

Table 3.12 shows the individual values, the means and standard deviations quantified through this esperimental campaign. The output of the shear characterization campaign are shown in bold, ie $G_{12} = 1227$ MPa, $\tau_{12}^{max} = 30.61$ MPa.

3.7 Discussion of the results

This section briefly discusses the results. Appendix A showed a tensile strength of 58.49 MPa and a stiffness modulus of 3093 MPa for the feedstock material. Through the typical Poisson ratio of 0.3 for PLA, the shear modulus estimate returned 1190 MPa. The boxplot in Figure 3.45 summarizes the comparison between the results in terms of tensile strengths. The printed PLA behaves differently than the feedstock material as a function of the load application direction. The difference is minimal if the load is applied in direction 1, but clearer for direction 2. The boxplot in Figure 3.46 summarizes the comparison between the results in terms of tensile moduli. It is confirmed that the behavior of feedstock PLA differs from that of 3D-printed material. The difference is more evident when considering the latter solicited along the 2 direction, confirming that the mesostructure induces at least anisotropic behavior.

The boxplot in Figure 3.47 summarizes the comparison between the results in terms of shear modulus. A slight difference is also present from this point of view. However, 3D-printed PLA appears to behave slightly more rigidly in the face of this stress.

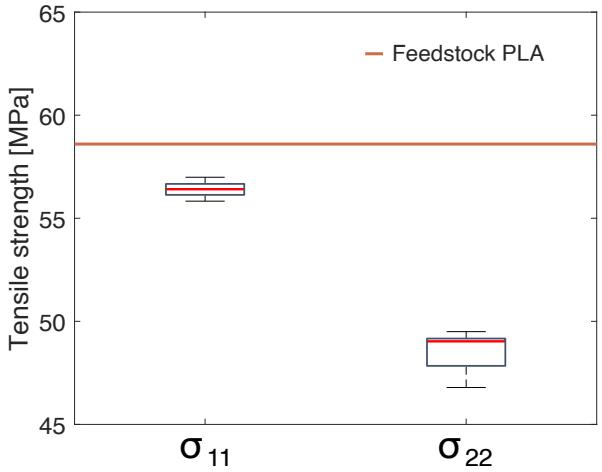

Figure 3.45: Comparison between the tensile strengths of the feedstock PLA with σ_{11}^{max} and σ_{22}^{max}.

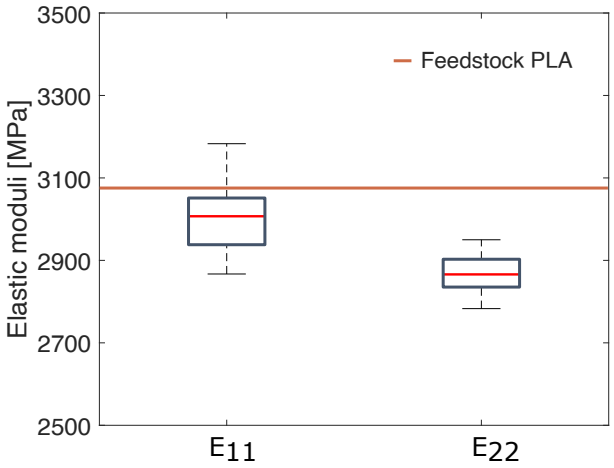

Figure 3.46: Comparison between the elastic modulus of the feedstock PLA with E_{11} and E_{22}.

All these results are important because they show how the preliminary values of raw PLA cannot be used with confidence in the mechanical design of printed parts. In the next chapter, these properties will be used to compute the 3×3 reduced stiffness matrix. A set of validation tests will assess the predictability of the mechanical behavior of the printed elements, through the properties determined here and the assumptions discussed in Chapter 2.

The experimental campaign aimed to describe the mechanical behavior from a mesostructure perspective. This approach is not detached from the microstructure

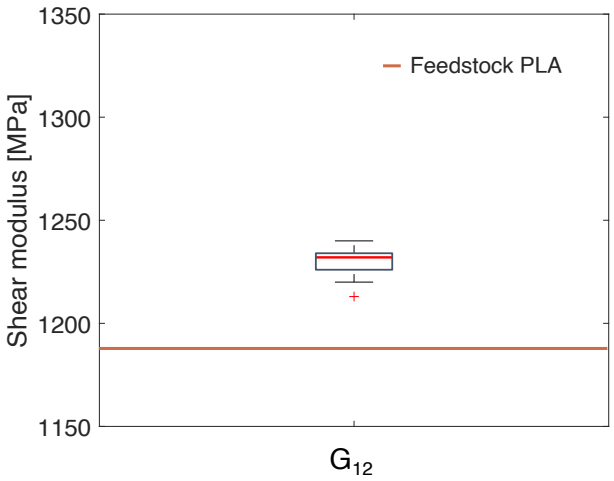

Figure 3.47: Comparison between the shear modulus of the feedstock PLA with G_{12}.

but a result of how it was considered. The output is a equivalent material, which does not investigate the complex interactions present at the microstructure level. A detailed study on the actual microstructure of the components should first consider the bonding between the beads, i.e., how the interaction between adjacent and overlapping filaments evolves. This approach can rely on mathematical models of neck growth between polymeric filaments, some of which have already been discussed [79]. However, the influence of the process (printing) parameters should be modeled, evaluating their impact on the phenomenon to have an image of the actual microstructure of a 3D print. At the same time, it would be necessary to find a way to describe how the microstructure changes in the presence of a different printing strategy (e.g., different raster angles between overlapping layers). Obviously, two beads superimposed in parallel or with a right angle (or any angle) will manifest other interactions due to the different morphology of the generated neck.

Chapter 4

CLT validation tests

This chapter is dedicated to validate the approach proposed in the experimental campaign. Three different tests have been considered to have a heterogeneous sample of load cases: a three-point bending test, a simple bending, and a bending-torsion test. For each of them, specimens with different raster angles have been considered to accentuate the anisotropic response of the FFF-processed PLA. Each test and lamination (adopting here the UDC terminology) has been combined with three finite element models. The results show that the mechanical response prediction is excellent when the model is tuned with the mechanical properties determined in the hypothesis of orthotropic behavior. Assuming that FFF-processed elements retain the isotropic behavior of feedstock PLA leads to larger discrepancies.

4.1 Introduction

The mechanical characterization campaign conducted in Chapter 3 followed the assumption that the anisotropy of 3D-printed PLA can be lead back to orthotropy under specific circumstances. In this context, the mechanical properties have been derived, assuming that the Classical Lamination Theory might describe its mechanical behavior. This chapter is intended to verify this last point. Two validation tests have been conducted experimentally and simulated through the Finite Element Method. The constitutive model of the material is based on the CLT formulation, tuned with the mechanical properties discussed in Chapter 3. The chapter will discuss a three-point bending test and bending/bending-torsion tests on a cantilever beam with a point load at the tip. For each test, three specimen configurations have been considered to:

- validate the non-isotropic behavior of 3D-printed PLA, accentuating any difference;
- verify that CLT can predict the mechanical behavior of 3D-printed PLA components in different configurations.

Three lamination schemes have been tested, deriving the vocabulary from composites:

- [0°]. Specimens are printed with a raster angle of 0°; the beads are oriented in the longitudinal direction of the specimen, which coincides with the material direction 1. Direction 2 lies in the mid-plane of the coupon.
- [90°]. Specimens are printed with a raster angle of 90°; the beads are oriented in the transverse direction of the specimen, which coincides with the material direction 2. Direction 1 lies in the mid-plane of the coupon.
- $[+45°/-45°]$. Specimens are printed with an alternated raster angle of $+45°/-45°$, alternatively layer by layer. Material directions 1 and 2 always lie in the mid-plane of the coupon.

In the following, a large number of validation test samples will be considered. Figure 4.1 illustrates the nomenclature used for their identification to facilitate the reading and referring to the results; the classification also refers to the tests that will be presented in the next Section.

Figure 4.1: Nomenclature definition for all the validation test specimens.

For each test, and for each configuration, three models have been considered defining three different constitutive models for the coupon material to have a term of comparison.

- **CLT(ISO)_RAW**: this constitutive model considers the mechanical properties provided by the manufacturer. As already discussed in Chapter 1, the manufacturer supplies only one elastic modulus, assuming that 3D-printed PLA also has isotropic behavior. With a view to mechanical behavior prediction, this property is the only value available to an end-user who does not conduct a characterization campaign, together with the Poisson ratio, whose value for a solid-PLA is consolidated in the literature and equal to 0.3.

- **CLT(ISO)_FIL**: this constitutive model considers the mechanical properties determined from the PLA filament (e.g., its modulus of elasticity) in Appendix A, assuming that 3D-printed PLA preserves the isotropic behavior of the filament. This property is the only value available to an end-user who characterizes the feedstock material, together with the Poisson ratio, whose value for a solid-PLA is consolidated in the literature and equal to 0.3.

- **CLT(ORT)**: this model considers the outputs of the previous chapter to define a 2D orthotropic constitutive model for a single layer. As discussed in Chapter 2, the Reissner-Mindlin kinematic model underlies 2D Finite Elements with orthotropic material properties, driven by a 5×5 stiffness matrix. However, it can be traced back to the Kirchhoff model with appropriate penalties over the shear moduli G_{23} and G_{13}. The different configurations in terms of raster angle have been taken into account, defining a laminated composite. The actual number of FFF layers is considered, each with its corresponding orientation angle and thickness.

Notice how the CLT prefix characterizes all three models. Even in isotropic cases, the material properties have been defined through a 2D orthotropic constitutive model, appropriately tuned. This detail made it possible to compare homogeneous models considering different mechanical properties but keeping the kinematics unaltered. The mechanical properties considered in the three models are summarized in Table 4.1 for convenience. In CLT(ISO)_RAW and CLT(ISO)_FIL, the shear modulus G_{12} has been calculated through its relationships with the Young modulus and the Poisson ratio for isotropic materials. In all three models, the shear moduli G_{23} and G_{31} have been set to a magnitude order higher than all the other elastic coefficients to penalize them and trace the constitutive model back to Kirchhoff kinematic model. As will be seen below, shell elements in a commercial FE software will be used. They are based upon FSDT, which allows retrieving CLT by shear penalization.

CLT(ISO)_RAW			CLT(ISO)_FIL			CLT(ORT)		
E_{11}	3950	MPa	E_{11}	3093	MPa	E_{11}	3008	MPa
E_{22}	3950	MPa	E_{22}	3093	MPa	E_{22}	2876	MPa
ν_{12}	0.3	-	ν_{12}	0.3	-	ν_{12}	0.286	-
G_{12}	1519	MPa	G_{12}	1190	MPa	G_{12}	1227	MPa
G_{23}	10^3	GPa	G_{23}	10^3	GPa	G_{23}	10^3	GPa
G_{31}	10^3	GPa	G_{31}	10^3	GPa	G_{31}	10^3	GPa

Table 4.1: Mechanical properties for FE constitutive models.

4.2 Three-point bending test

The three-point[1] bending test is here presented and discussed as first test bench. It is a standardized test, used to determine the flexural properties of the materials; consequently, its set-up is facilitated by the presence of dedicated supports. It is also simple to perform and monitor. Guidance for such an experimental procedure is provided by the *Standard Test Methods for Flexural Properties of Unreinforced and Reinforced Plastics and Electrical Insulating Materials*, issued by ASTM under the designation D790 [92].

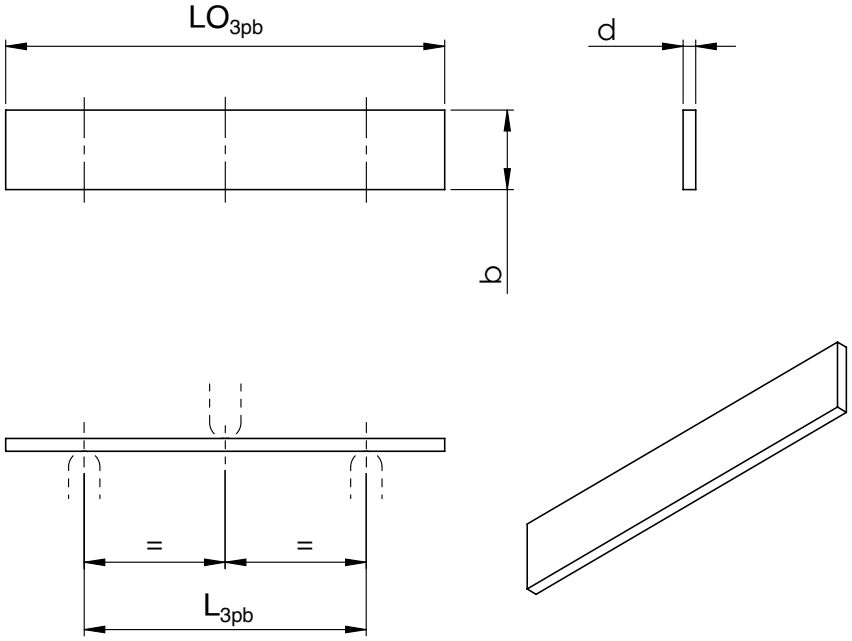

Figure 4.2: 2D drawing of a 3-point bending test specimen.

The specimen takes the form of a constant rectangular cross-section plate. It rests on two cylindrical supports; a third cylinder symmetrically loads it. Figure 4.2 shows a 2D CAD drawing of the specimen. The front view also shows the supports on which the specimen lies, represented with dashed lines. This representation also allows the distance between them to be reported. The standard does not impose specific dimensions but suggests geometric relationships between them. As for the standard tensile test for plastics, this handbook distinguishes between materials of different nature in manufacturing and mechanical behavior. There is no mention

[1] Although the four-point bending test would be preferable to ensure a part of the specimen under a constant bending moment along its longitudinal axis, available laboratory instrumentation forced choosing the three-point bending test.

of detail regarding the FFF processed polymers. However, there is a hint to orthotropic materials. The standard suggests using a span-to-dept ratio greater than 16 : 1 when the shear strength is lower than the tensile strength in the longitudinal direction of the specimen. Recalling the results seen in Chapter 3 in terms of tensile and shear strength, the dimensions shown in Table 4.2 have been selected. Notice how the overall length of the specimen guarantees a sufficient overhang to avoid slipping during the test [92].

Dimensions		
LO_{3pb} - length overall	140	mm
L_{3pb} - supports span	90	mm
b - width	25	mm
d - depth	4	mm

Table 4.2: Geometrical dimensions of 3-point bending test specimens.

The test is conducted in displacement control; a constant translation speed is set for the upper cylinder. The lower cylinders support the specimen. As the upper one moves downwards, it makes the specimen bend. Similar to tensile testing, the testing machine adapts the applied load keeping the translation speed constant. The machine control system then samples the applied load and the imposed deflection in the center-line at a custom frequency. Since the dimensions of the specimen are not fixed, the tests are not homogenized by means of the deflection speed, as is the case for tensile tests, but rather through the *rate of deformation of the external fibers*. ASTM D790 requires this rate Z to equals 0.01 mm/mm·min. Equation 4.1 is given to calculate the mobile cross-head speed (also known as *rate of cross-head motion*), as a function of the geometrical dimensions of the specimen:

$$R = \frac{ZL_{3pb}^2}{6d} \tag{4.1}$$

Given the nominal dimensions of the specimen presented in Table 4.2, a speed equals $R = 3.375$ mm/min has been considered.

$$\sigma_f = \frac{3PL_{3pb}}{2bd^2} \tag{4.2}$$

where P is the applied load, in N. The flexural strain can be obtained from the deflection D through Equation 4.3:

$$\epsilon_f = \frac{6Dd}{L_{3pb}^2} \tag{4.3}$$

Usually the flexural stress vs. flexural strain relation shows a linear dependence in the first part of the curve, similar to the corresponding tensile quantities. Through

Equations 4.2-4.3, the modulus of elasticity in bending E_B can be expressed as the ratio between σ_f and ϵ_f, in the region of the curve where the linear dependence still holds. Its analytical expression is given in Equation 4.4.

$$E_B = \frac{L_{3pb}^3 m}{4bd^3} \tag{4.4}$$

where m is the slope of the tangent to linear region of the load vs. deflection curve.

Equation 4.4 shows how the normalization with respect to the geometrical dimensions of the specimen strongly depends on L_{3pb} and d. Of the two quantities, the support span raises more concern and needs to be carefully determined, together with the position of the upper cylinder. As E_B is proportional to the cube of L_{3pb}, any dimensional error in its evaluation would be amplified. As suggested in [92],

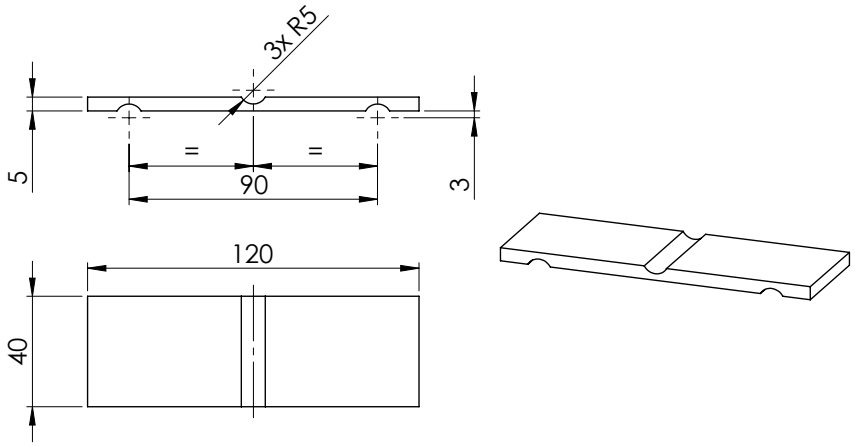

Figure 4.3: Alignment device for supports and nose spacing in bending tests.

an alignment device has been designed and printed. Figure 4.3 shows the 2D CAD drawing of the device; on the bottom, it is characterized by two semi-cylindrical sockets spaced $L_{3pb} = 90$ mm, whose longitudinal axes are parallel. On the top, a third semi-cylindrical socket is present: its longitudinal axis is parallel to those of the bottom ones and is positioned midway. The radii of the cylindrical sockets are the same of the metallic cylinders available on the fixture for flexural tests. In this way, the operator can simultaneously check that:

- the distance between the two lower cylindrical supports is the intended one;
- the upper cylinder is correctly located midway between the lower ones;
- all the three cylinders are all aligned.

4.2.1 Test samples and preliminary results

Following the definitions in Figure 4.1, the specimens discussed in this section will be all identified by the prefix *3PB*; the second part of the prefix differs following the deposition direction of the beads. A total number of 6 specimens has been printed, per configuration, achieving a total number of 18 components. Prior to each test, the geometrical dimensions have been measured with a digital caliper. The measurements are reported in Tables 4.3-4.5.

SPECIMEN	LO_{3pb} [mm]	d [mm]	b [mm]
3PBD1-S01	139.66	3.94	23.93
3PBD1-S02	139.57	3.95	23.86
3PBD1-S03	139.52	3.97	23.80
3PBD1-S04	139.46	3.98	23.80
3PBD1-S05	139.48	3.97	23.81
3PBD1-S06	139.82	3.96	23.88
3PBD1 Sample			
mean	139.58	3.96	23.85
st.dev	0.14	0.02	0.05

Table 4.3: Geometrical dimensions of 3PBD1 sample specimens.

SPECIMEN	LO_{3pb} [mm]	d [mm]	b [mm]
3PBD2-S01	138.81	3.93	23.92
3PBD2-S02	138.88	3.93	23.97
3PBD2-S03	138.92	3.94	24.18
3PBD2-S04	138.93	3.95	24.12
3PBD2-S05	139.36	3.94	24.31
3PBD2-S06	138.87	3.92	23.99
3PBD2 Sample			
mean	138.96	3.94	24.08
st.dev	0.20	0.01	0.15

Table 4.4: Geometrical dimensions of 3PBD2 sample specimens.

All the tests have been executed with an Instron 8801 servo-hydraulic machine, equipped with a 1 kN load cell. Figure 4.4 shows the test set-up. As previously discussed, the machine control system recorded the applied load P and the imposed

SPECIMEN	LO_{3pb} [mm]	d [mm]	b [mm]
3PBD12-S01	139.71	3.97	24.69
3PBD12-S02	139.67	3.96	24.69
3PBD12-S03	139.77	3.96	24.64
3PBD12-S04	139.64	3.95	24.53
3PBD12-S05	139.55	3.93	24.47
3PBD12-S06	139.67	3.96	24.66
3PBD12 Sample			
mean	139.67	3.95	24.61
st.dev	0.07	0.01	0.09

Table 4.5: Geometrical dimensions of 3PBD12 sample specimens.

Figure 4.4: Three-point bending validation tests: experimental set-up.

deflection D in the middle during the tests. Figure 4.5-4.7 reports the applied load vs. imposed deflection curves for the whole sample of configurations 3PBD1, 3PBD2, and 3PBD12. Over 5% strain, this bending test is no longer applicable [92] due to the changed geometric configuration between the specimen and supports. Considering the relation that links the flexural strain to the deflection in the centerline expressed by Equation 4.3, and recalling the nominal dimensions of the

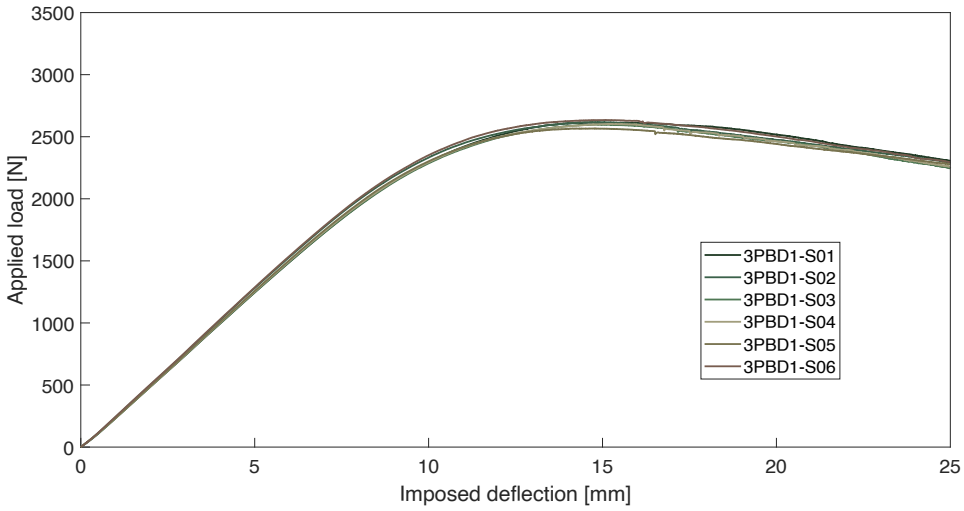

Figure 4.5: Three-point bending validation tests: applied load vs. imposed deflection curves of the 3PBD1 sample.

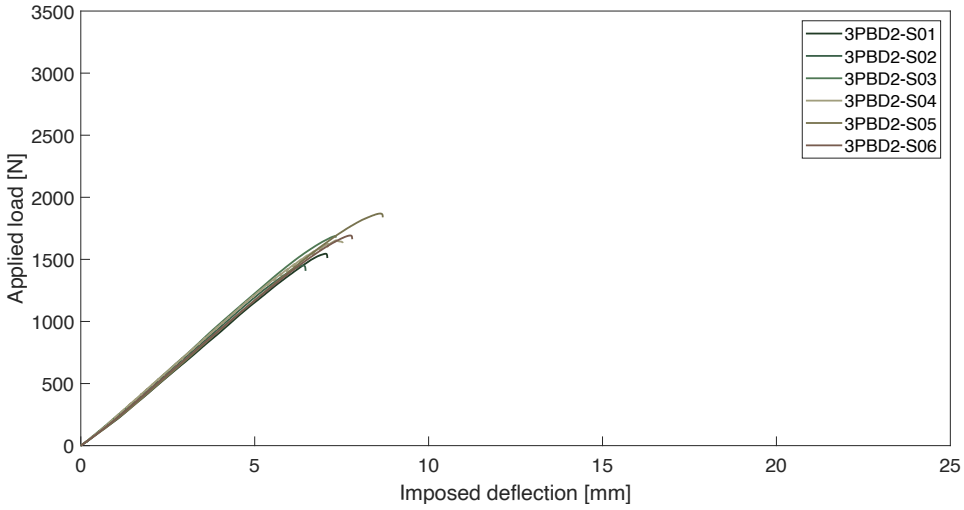

Figure 4.6: Three-point bending validation tests: applied load vs. imposed deflection curves of the 3PBD2 sample.

flexural specimens presented in Table 4.2, the limit deflection equals to 16.875 mm. Therefore, all the graphs are truncated at a slightly higher deflection. Note that the maximum point of each curve occurs before the maximum permissible deflection occurs. Those graphs are not strictly representative of the mechanical behavior of the 3D-printed PLA, as they still depend on the actual geometrical dimensions of each specimen, as the similar graphs presented in the previous chapter for other

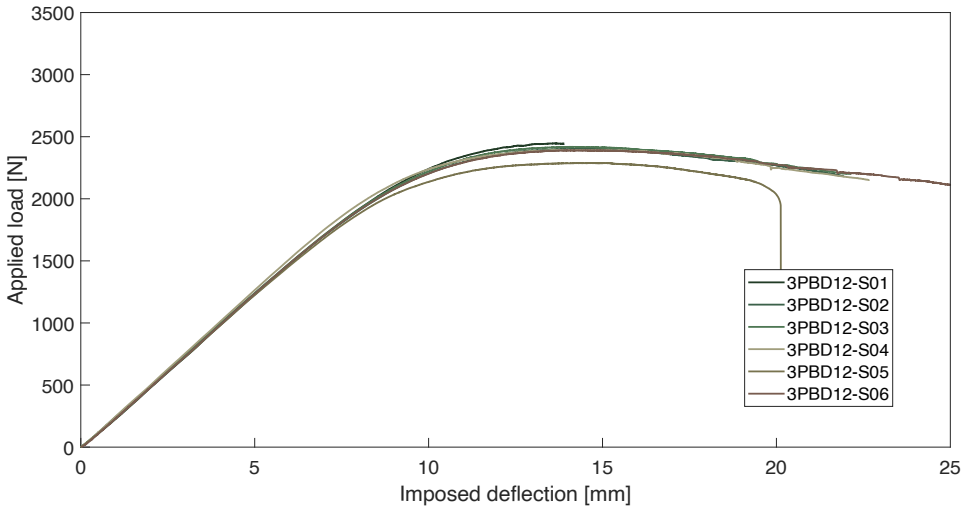

Figure 4.7: Three-point bending validation tests: applied load vs. imposed deflection curves of the 3PBD12 sample.

mechanical tests. However, they allow some preliminary considerations. All the samples, in all the configurations, showed an initial linear behavior, preceded by a *toe region* and followed by a more or less accentuated non-linear part. Within the graphs of a single configuration, the initial linear behavior slopes are similar, which indicates a low scatter in the data. Some offsets were initially present, which were due to the actual time zero of the test determination. The machine control system starts sampling data as soon as it is operated; however, the loading nose needed not to touch the specimen in the first moments of the test. A certain gap was necessary to avoid undesirable preloading of the coupons. The data pairs below 5 N have been discarded to compensate for this offset, and the load and the displacement zeroed.

4.2.2 Discussion of experimental results

The flexural stress vs. flexural strain relations can be derived through Equations 4.2-4.3 considering the actual geometrical dimensions of each specimen. As usual, the mechanical behavior of each configuration is summarized here in Figures 4.8, 4.9, and 4.10 for 3PBD1, 3PBD2, and 3PBD12 samples respectively. The individual curves are given in Appendix C. The quantification of the flexural modulus of elasticity followed the algorithm considered for tensile tests. In parallel, the flexural strength has been derived through the maximum sustained load. For each specimen, this took place before the 5% strain limit in every configuration. Tables 4.6-4.8 report the individual values obtained through this experimental campaign, together with the mean and the standard deviation values.

3PBD1 specimens: experimental results

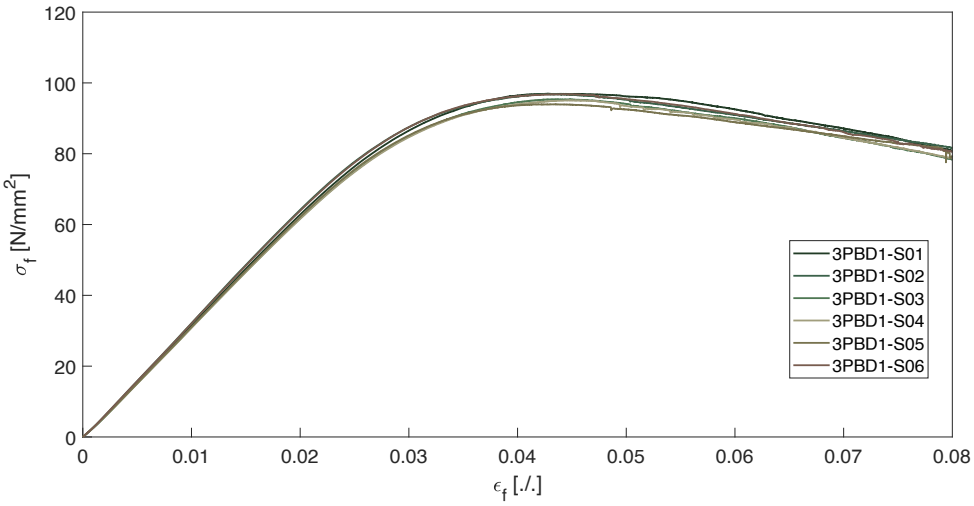

Figure 4.8: Three-point bending validation tests: flexural stress vs. flexural strain curves of the 3PBD1 sample.

SPECIMEN	Mechanical analysis E_B [MPa]	σ_f^{max} [MPa]
3PBD1-S01	3077	97.0
3PBD1-S02	3150	96.8
3PBD1-S03	3027	95.4
3PBD1-S04	3019	95.1
3PBD1-S05	3044	94.0
3PBD1-S06	3145	96.8
3PBD1 Sample		
mean	**3077**	**95.84**
st.dev	53.00	1.114

Table 4.6: Three-point bending tests for 3PBD1 specimens: results of the experimental campaign.

3PBD2 specimens: experimental results

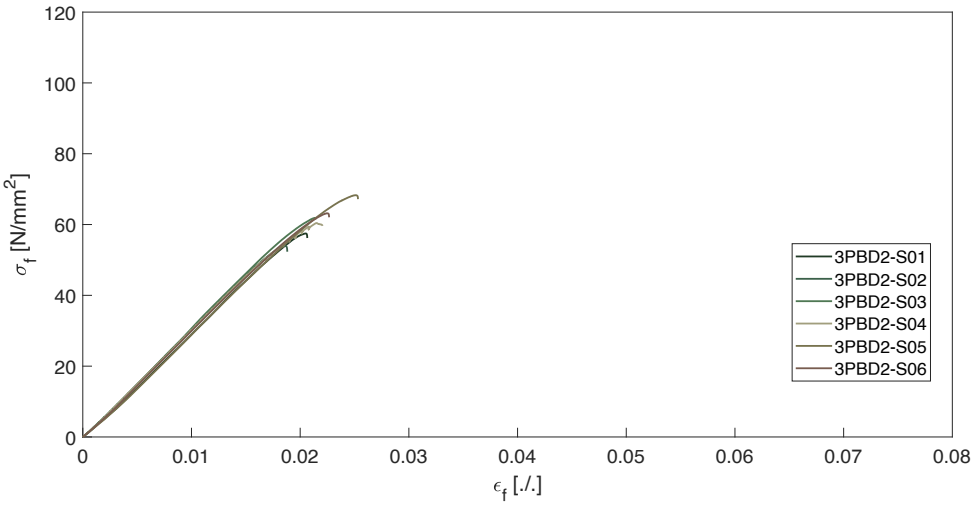

Figure 4.9: Three-point bending validation tests: flexural stress vs. flexural strain curves of the 3PBD2 sample.

SPECIMEN	Mechanical analysis	
	E_B [MPa]	σ_f^{max} [MPa]
3PBD2-S01	2857	57.5
3PBD2-S02	3014	54.0
3PBD2-S03	3040	61.9
3PBD2-S04	2993	60.4
3PBD2-S05	2860	68.3
3PBD2-S06	2954	63.2
3PBD2 Sample		
mean	**2953**	**60.87**
st.dev	71.55	4.483

Table 4.7: Three-point bending tests for 3PBD2 specimens: results of the experimental campaign.

3PBD12 specimens: experimental results

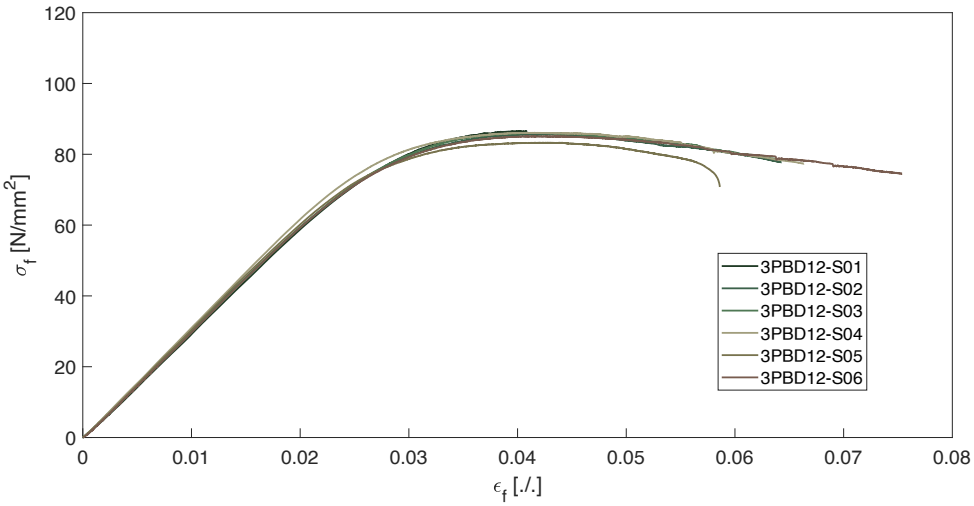

Figure 4.10: Three-point bending validation tests: flexural stress vs. flexural strain curves of the 3PBD12 sample.

SPECIMEN	Mechanical analysis	
	E_B [MPa]	σ_f^{max} [MPa]
3PBD12-S01	2873	86.5
3PBD12-S01	2946	85.7
3PBD12-S01	2930	86.1
3PBD12-S01	3049	86.1
3PBD12-S01	2988	83.3
3PBD12-S01	2928	85.1
3PBD12 Sample		
mean	**2952**	**85.46**
st.dev	54.85	1.063

Table 4.8: Three-point bending tests for 3PBD12 specimens: results of the experimental campaign.

The overall mechanical properties determined for each configuration are reported in Table 4.9 for comparison. The anisotropy of 3D-printed PLA is confirmed: the three specimen configurations behaved differently depending on their mesostructure. The results of the first configuration are taken as a reference to allow a percentage comparison. The bending modulus of 3PBD1 specimens is the

highest; 3PBD2 and 3PBD12 configurations proved to be less stiff than the previous of about 4%. However, they showed similar results. Differences also exist for the bending strengths; the highest value has been found for [0°] specimens. [+45°/ − 45°] and [90°] coupons behaved differently, showing a −11% and −38% with respect to the first configuration. In addition to the results, differences are

	3PBD1	3PBD2		3PBD12	
E_B	**3077** MPa	2953 MPa	−4.03%	2952 MPa	−4.06%
σ_f^{max}	**95.84** MPa	60.87 MPa	−36.49%	85.46 MPa	−10.83%

Table 4.9: Overall results of three-point bending tests.

also present in mechanical behavior. All specimens exhibited an extensive linear part in the flexural stress vs. flexural strain. However, a sudden failure occurred for 3PBD2 coupons at the maximum flexural load supported by the specimen; as observed in the tensile tests the behaviour along the direction 2 is brittle (due to the microstructure and the way the beads are connected). Both 3PBD1 and 3PBD12 instead maintained linear behavior up to a certain load level, deviated from it before reaching the maximum load, and exhibited an extensive region of plastic deformation. These differences certify the predominantly directional behavior but can be directly related to bending only up to the strain limit of 5%, for the reasoning discussed above. It is interesting to note how this behavior reflects that found for the tensile tests. This is justified by the load case: taking the mean surface of the specimens as a reference, a compression stress state develops in the upper layers, while a tensile stress state develops in the lower ones. However, this load case results in an out-of-plane deformation. The next section will be devoted to verifying if this behavior can be predicted by a FE model.

4.2.3 FE model of the test

This section describes in detail the finite element model proposed to simulate the validation tests. The specimen, the three cylinders, and their kinematics have been recreated in MSC Patran; MSC Nastran then processed the model. As in the experimental tests, in the FE model a displacement is imposed to the upper cylinder; the lower two act as constraints. The reaction forces are then evaluated and related to the imposed displacement. The FE model has a fixed geometry; the dimensions of the specimen and those of the cylinders are the nominal ones, already discussed in Table 4.2. The mechanical response strongly depends on the actual dimensions of the specimens, as already seen in the previous section. Consequently, it has been evaluated in terms of the equivalent modulus of elasticity in bending. E_B has been calculated starting from the reaction force in the vertical direction (i.e., the applied load) and from the deflection imposed by the upper cylinder through

Equation 4.4, similarly to what has been done in the experimental tests. This allowed disregarding the geometry.

The cylinders are three-dimensional components; their geometry has been easily recreated directly in MSC Patran and meshed with HEX elements. They ideally represent rigid and non-deformable bodies; being made of steel, they certainly are compared to PLA and considering the maximum loads reached during the tests. An isotropic material has been defined with a linear elastic constitutive model, which considered $E^{steel} = 210$ GPa and $\nu^{steel} = 0.3$ as property values. The specimen has been represented as a two-dimensional element with a rectangular shape and meshed with CQUAD8 elements.

The models required careful tuning in mesh convergence, friction, and contact analysis in addition to the mechanical properties. To be thorough, all assessments are discussed below.

Contact analysis

The three cylinders and the specimen are different bodies. At rest, they are in contact like an ideal cylinder and a plane are, by a segment parallel to the longitudinal axis of the cylinder. Once the loading cylinder moves down, such configuration evolves. Figure 4.11 shows the reaction forces that develop in the contact area between the specimen and the upper cylinder.

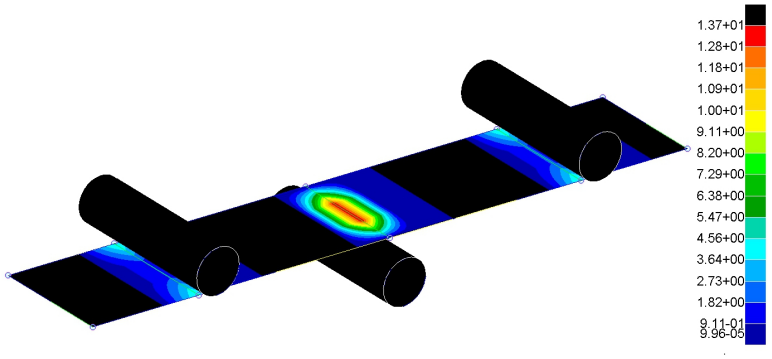

Figure 4.11: Three-point bending validation tests: contact analysis for FE model tuning. The normal contact forces under 1 mm deflection are shown, expressed in N.

Considering the normal forces, they are not uniformly distributed in the region close to the ideal contact segment. Over the upper surface, they concentrate in the middle of the specimen. Reversely, the highest reaction forces over the lower surface concentrate along the edges. Plotting the displacements in the thickness direction vs. the transverse direction helps to clear the matter (see Figure 4.12).

The upper cylinder imposes 1 mm deflection. A compression state develops in the upper layers in such a bending test and a tensile state in the lower ones. Due to the Poisson effect, lower layers experiment contraction, while the upper expansion. Consequently, the specimen bends also in the width-thickness plane. This bending is minimal but still sufficient to manifest itself in this inhomogeneity in normal forces distribution.

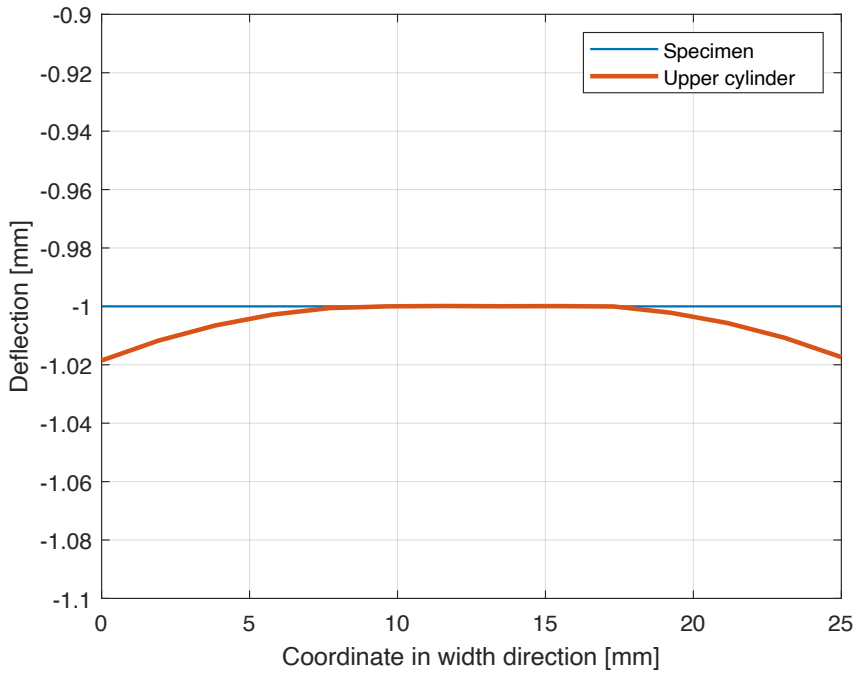

Figure 4.12: Deflection vs. transverse direction in correspondence to the upper cylinder.

Friction analysis

For a successful analysis, the FE solver prompts a non-zero friction coefficient between the cylinders and the specimen. Otherwise, the coupon would slip through the cylinders. The friction coefficient could not be experimentally measured; its value has been estimated. A preliminary analysis verified the influence of this parameter on the model to exclude it could taint the results. Literature research suggested a static coefficient of $\mu = 0.16 \pm 0.02$ in contact between un-reinforced PLA and metals. However, this coefficient is not unique, being a function of several factors:

- the temperature;
- the normal force exchanged between the two surfaces;

- the surface finish.

Friction Coefficient	Reaction Force
0.005	27.094 N
0.01	27.099 N
0.05	27.102 N
0.1	27.102 N
0.15	27.102 N
0.16	27.102 N
0.3	27.102 N
0.4	27.102 N
0.7	27.102 N

Table 4.10: Friction coefficient assessment: the results show its influence over the reaction force for a 3PBD1 specimen under 1 mm deflection.

This preliminary study has aimed to evaluate if the over/underestimation of the static coefficient would have affected the results, revealing its relative weight in the analysis. Several FEMs have been arranged; each of them had an imposed deflection of 1 mm. Table 4.10 shows that the friction coefficient varied between $\mu = 0.005$ and $\mu = 0.7$; its effect has been observed through the reaction force. Figure 4.13 shows the reaction force vs. the friction coefficient relation; the reaction force keeps constant within the range under investigation. Just meaningless fluctuations arise at very low friction coefficients. Analogous results have been obtained regardless of the constitutive model of the PLA. Consequently, the value $\mu = 0.16$ suggested in the literature has been used with confidence.

Mesh analysis and convergence

Section 4.2.3 introduced that the specimen has been described through its mean reference surface and meshed via IsoMesh CQUAD8 elements. This subsection is devoted to mesh analysis and convergence, checked before the final model. It is well known that FE models are usually stiffer than the corresponding components due to discretization and that the denser the mesh is, the more this gap reduces. However, with finer meshes, the computational time increases; a convergence study balances the two effects. Such analysis also allows to detect and avoid any singularities in the results which might derive from the mesh size and distribution. In analogy to previous background checks, the models had an imposed deflection of 1 mm; the constraint force and the total strain energy acted as output inspection parameters. The friction coefficient has been tuned considering the results exposed in the previous paragraph. Patran *Global Edge Length* (GEL) has been used as an indicator of mesh refinement; the lower the GEL, the finer the mesh. It indicates

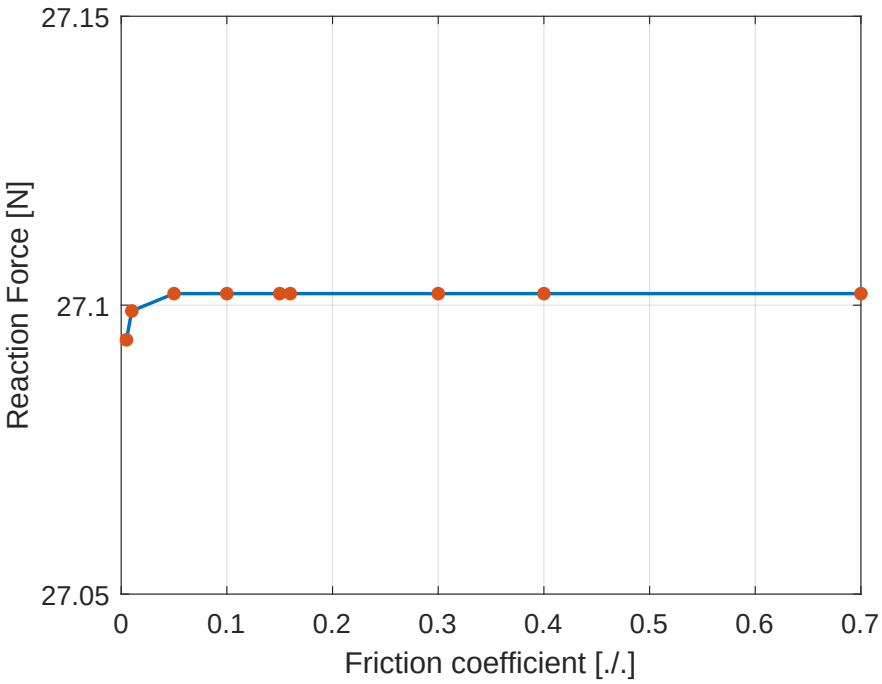

Figure 4.13: Friction coefficient vs. reaction force relation for a 3PBD1 specimen under 1 mm deflection.

the average linear dimension of the elements. Once set, MSC Patran automatically adapts the dimensions of every single element, trying not to warp them excessively. In this case the geometry of the simulated specimen is a rectangle, so the risk of the warped elements does not arise. The sparser mesh features a single element in the width direction; it can be obtained setting $GEL = 25$ mm. The lowest GEL index value has been driven to 0.5 mm, which means a total number of 14000 elements, 280 in the longitudinal, and 50 in the transverse directions. This measure the considered refinement range. Table 4.11 shows the relation between the GEL, the resulting reaction force and total strain energy. Their trend can be appreciated in Figure 4.14. The analysis has been carried out for CLT(ORT) model with a [0°] lamination sequences. The gap between the larger values of the GEL is due to the geometry of the problem and the dimensions of the specimen. With $GEL = 25$ mm only one element is present in the transverse direction of the specimen; with $GEL = 12.5$ mm two. The CQUAD8 element-based model proves very rapid convergence; note that there is no practical difference between the results driven by GELs included in the range $0.5 - 8$ mm. Accordingly, $GEL = 8$ mm has been considered. MSC Patran auto-mesh has been used for the cylinders; no preliminary assessment has been performed as they do not act as analysis elements but as constraints. The mesh details are summarized in Table 4.12.

3PBD1		
GEL [mm]	Reaction Force [N]	Total strain energy [10^{-3} J]
0.5	27.077	13.523
1	27.077	13.523
2	27.077	13.523
3	27.076	13.523
4	27.075	13.522
5	27.075	13.522
6	27.071	13.520
8	27.072	13.521
12.5	27.126	13.547
25	27.040	13.485

Table 4.11: Mesh analysis and convergence: the analysis shows the influence of the mesh size over the reaction force for a 3PBD1 and a 3PBD2 specimens under 1 mm deflection.

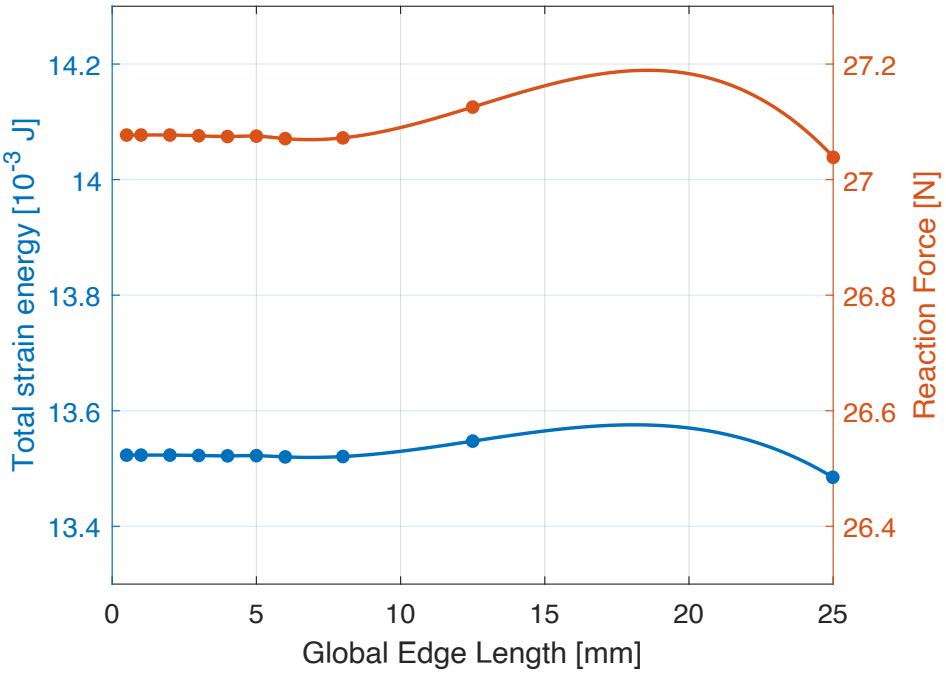

Figure 4.14: Mesh analysis and convergence, 3PBD1 sample: reaction force and total strain energy vs. global edge length.

	Specimen	Cylinders
Geometry	2D	3D
Mesh	CQUAD8	HEX8
Element type	Shell	Solid
GEL	8 mm	10.8 mm
Elements no.	54	327

Table 4.12: Mesh details for the three-point bending test FE model.

Displacement amplitude analysis

As anticipated, in a 3-point bending test, the flexural strain shall not exceed 5% [92]; this is due to geometrical nonlinearities arising when the specimen significantly differs from a flat element. Therefore, the influence of the imposed deflection has been studied to quantify its optimal value, not inducing nonlinearities in the response. In this analysis, the mesh size and the friction coefficient have been set following the previous reasoning. The specimen is subjected to different deflections in the range $0.5 \div 30$ mm, and the reaction force is evaluated. The ratio between the two is the output inspection parameter. The effects on both the [0°] and the [90°] lamination have been considered to generalize the investigation. The results are shown in Table 4.13. This analysis is free from any material and geometrical

3PBD1			3PBD2		
D [mm]	F [N]	F/D [N/mm]	D [mm]	F [N]	F/D [N/mm]
0.5	13.5	27.0	0.5	12.9	25.8
1	27.1	27.1	1	25.9	25.9
2	54.5	27.3	2	52.0	26.0
3	82.0	27.3	3	78.3	26.1
5	137.7	27.5	5	131.5	26.3
6	165.9	27.7	6	158.3	26.4
7	209.8	30.0	7	199.7	28.5
10	308.6	30.9	10	293.3	29.3
15	478.5	31.9	15	454.5	30.3
20	704.4	35.2	20	666.5	33.3
30	1094.8	36.5	30	1039.1	34.6

Table 4.13: Displacement analysis for the three-point bending test FE model.

non-linearity, as the constitutive model is a linear elastic one and the solver is SOL 101. An increase in the required load per unit displacement appears as the deflection increases when the small displacement assumptions of the governing equations in a linear analysis are invalidated. To better appreciate this trend, refer to Figure

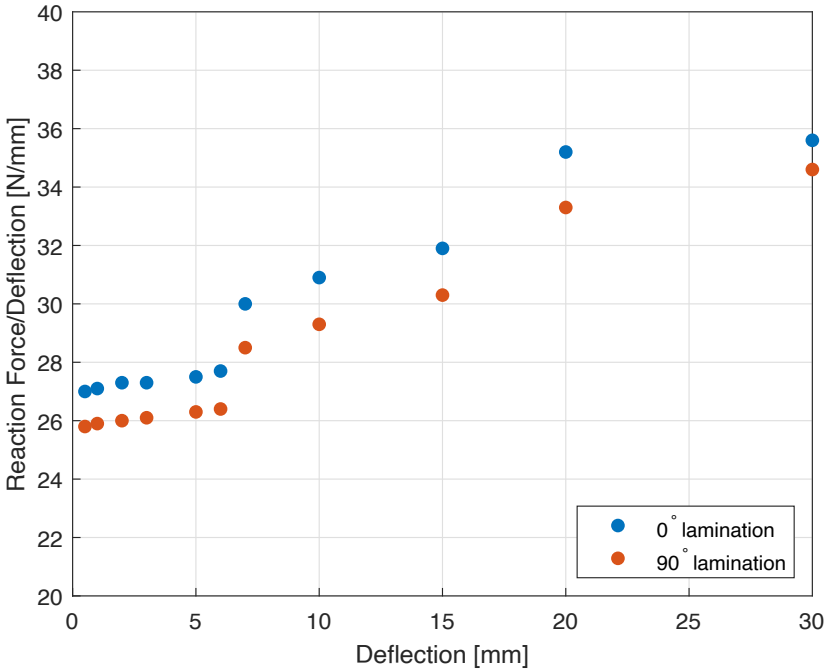

Figure 4.15: Reaction force per unit deflection trend for the three-point bending test FE model.

4.15. The trend is increasing as the deflection imposed increases due to geometric nonlinearities. For this reason, a deflection of 1 mm has been considered in the final model. Note that there are no appreciable load variations per unit displacement at the lower deflections.

4.2.4 Experimental and numerical results comparison

This section compares the experimental results with the numerical simulation, following the FE model tuning that has been previously discussed. To summarize, the analysis considered three configurations, as specimens with [0°], [90°] and [±45°] raster angles have been printed and tested. Three FE models simulated those tests:

- **CLT(ISO)_RAW**, tuned with the mechanical properties declared by the manufacturer, under the assumption that 3D-printed PLA behaves isotropically and keeps the same mechanical properties of the raw PLA after the FFF process. This model cannot take into account the different configurations and therefore provides a single output.
- **CLT(ISO)_FIL**, tuned with the mechanical properties determined from the tensile tests of the filament, under the assumption that 3D-printed PLA

behaves isotropically and keeps the same mechanical properties of the filament after the FFF process. This model also cannot take into account the different configurations and therefore provides a single output.

- **CLT(ORT)**, tuned with the 2D orthotropic mechanical properties discussed in the previous chapter, with the appropriate angle of orientation.

The equivalent bending modulus has been calculated following Equation 4.4 and has been used as a benchmark between the three simulations and the experimental results. The comparison is shown in Table 4.14. The closest results to the experiments have been highlighted in bold. It is immediately clear that the PLA feedstock raw data are inadequate to describe its mechanical behavior once FFF-processed as the percentage errors are in the order of 30%, which confirms the observations following from the results of the tensile tests. It can be speculated that those characteristics refer to the PLA pellets used to manufacture the filament; due to the production process and specific additives, they might vary. The model obtained using the mechanical properties experimentally obtained from the filament allows a good prediction of the mechanical behavior. Percentage errors are less than 10%. This model assumes that the specimen has isotropic behavior, so the results are unique regardless of the actual lamination of the coupons. The minimum percentage error occurs in correspondence with the 3PBD1 specimen. This pairs with the similarity in the stiffness modules between filament and direction 1, suggesting that mechanical properties remain unchanged to those of the filament, but only in the extrusion direction. On the other hand, the orthotropic model precisely simulates the behavior of the three laminations. The error is practically zero in the 3PBD1 and 3PBD2 configurations, and the FEM results coincide with the experimental one. The error is higher but still contained, for criss-cross lamination, indicating a probable difficulty for non-unidirectional laminations.

Experimental	3PBD1 $E_B = 3077$ MPa		3PBD2 $E_B = 2953$ MPa		3PBD12 $E_B = 2952$ MPa	
CLT(ISO)_RAW	3995	+29.8%	3995	+35.3%	3995	+35.4%
CLT(ISO)_FIL	3196	+3.9%	3196	+8.2%	3196	+8.3%
CLT(ORT)	**3087**	**+0.3%**	**2949**	**−0.1%**	**3143**	**+6.5%**

Table 4.14: Comparison between experimental results and numerical simulations for three-point bending test.

4.3 Bending/torsion and bending tests

The three-point bending test verified the predictive performances of a FE model tuned with the 2D orthotropic mechanical properties. However, it could be argued

that the boundary conditions of the previous test are elementary, still far from real operating conditions. This section discusses a second validation set-up: a different experimental test has been performed and then simulated by three FE models, embedding the three different constitutive models. The test discussed below does not rely on any standardized test method. Figure 4.16 shows a graphic render of the setup in two different configurations. Consider a coupon with a rectangular and constant cross-section; a rigid support constrains the rear end of the specimen. The front end is equipped with a H-beam, acting as a slide. Sliding support allows loading the coupon with a metal weight. The position occupied by the support modifies the load case: when positioned in the middle, the specimen is subjected to simple bending; otherwise, the load induces torsion and bending. The geometry

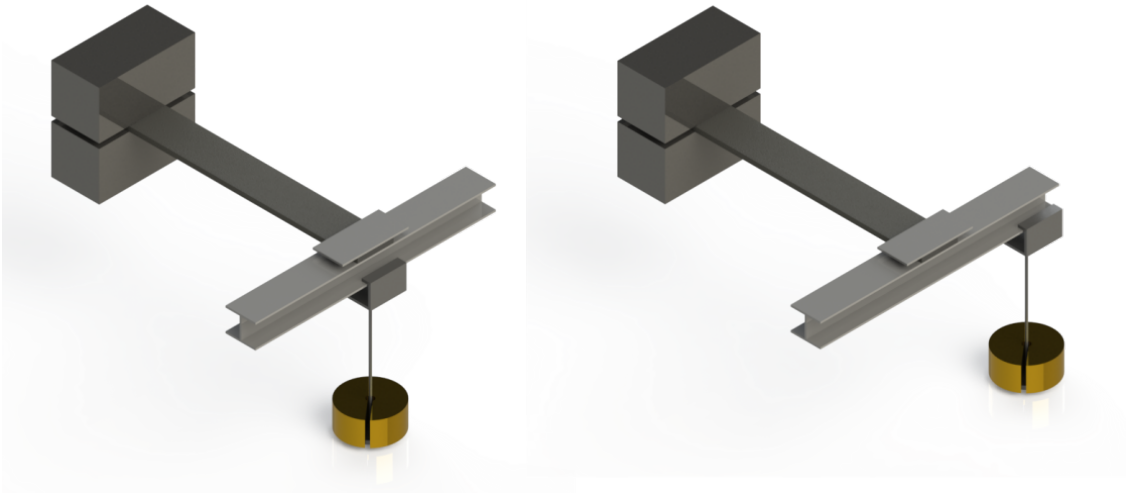

Figure 4.16: Graphic render of the simple bending/torsion and bending validation tests.

of the specimen is the same in the two configurations and shown in Figure 4.17. Three specimens have been printed, one for lamination, and used for both the simple bending and the torsion bending test.

The Digital Image Correlation system (see Appendix B) monitored the front surface of the specimen remotely to quantify the transverse displacements. The expected output is that the transverse displacement over the cross-section is almost constant in the case of simple bending tests; a gradient is expected in the transverse direction in torsion and bending tests due to the rotation imposed by the eccentric load.

4.3.1 Test set-up

The final set-up of the test required a large number of preliminary analyzes and evaluations.

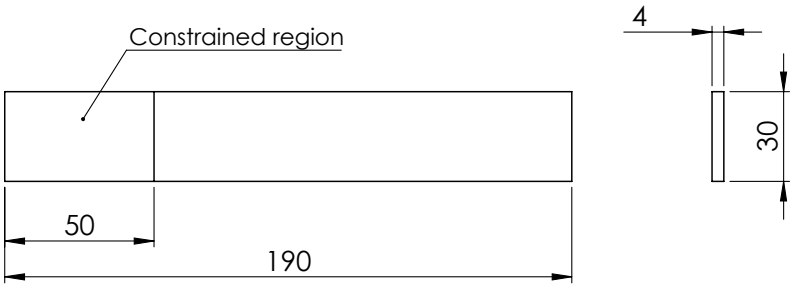

Figure 4.17: 2D drawing and geometrical dimensions of simple bending/torsion and bending test specimens.

- The finite element simulation of the phenomenon is of a static type; however, the manual loading of the weight is an intrinsically dynamic action. How to manage this aspect? The load is not applied gradually; how long does it take after the weight has been loaded to measure the static deflection? How long does it take to see the oscillations dissipate?

- What weight to apply to the support? This aspect has a close relationship with the DIC monitoring. Once loaded, the front surface does not keep coplanar to itself; it rotates, even if by a small amount. This rotation reflects into displacements perpendicular to the original surface. The DSLR camera is fixed in space, and its focal plane is parallel to the original surface. A single-camera constitutes the system, meaning that the only measurable displacements are those of a plane parallel to the focal. Consequently, an excessive specimen deflection could taint the DIC measurements, modifying the relative distance between the focal and the surface.

Specimen rest time for static measurements

As anticipated, the action of manually loading the weight is intrinsically dynamic: it occurs in a specific time interval, cannot be standardized or automated, and induces vibrations. Even with extreme care in the weight positioning, it is impossible to visually ensure the time necessary to completely dissipate the vibrations and provide that the coupon has found its equilibrium position. This is a problem, as the DIC records the displacements in each frame. A method must be established to identify the time interval to determine the deflection under static conditions. A preliminary test considered this point, using the simple bending set-up for simplicity. The weight applied is 500 g; the DIC monitored the front surface[2]

[2]Monitoring the lateral surface of the specimen (axial-thickness plane) would have required moving the DSLR camera away from it to grant a full picture. The ROI would have been very thin and stretched with a high number of pixels near the edges, generally subject to more noise.

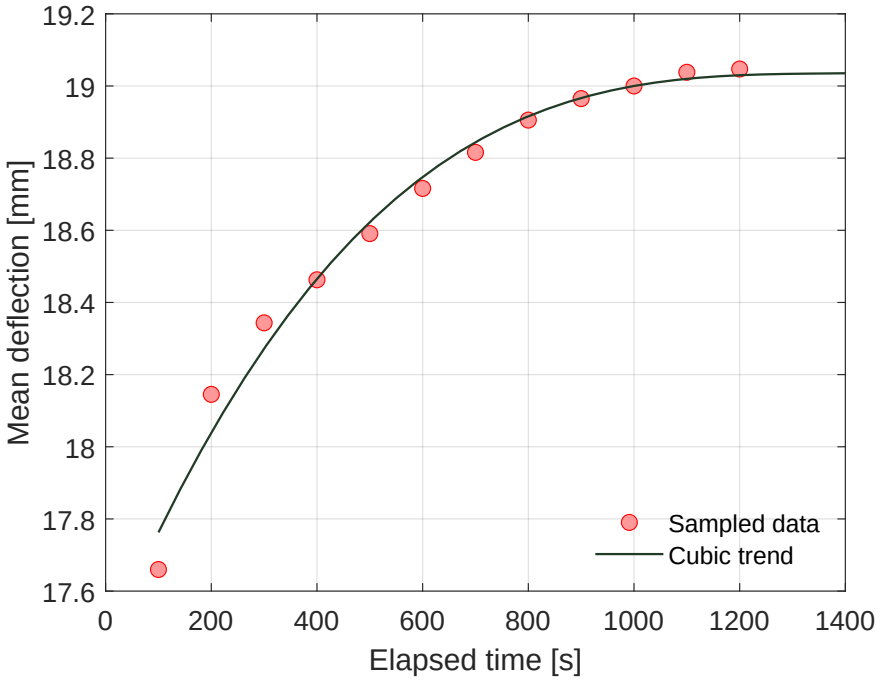

Figure 4.18: Deflection vs. time in a simple bending test.

of the specimen to quantify the mean displacement in the vertical direction. The test lasted up to the maximum video length of the DSLR camera, i.e., 20 minutes. The correlation has been performed at discrete intervals of 100 s, selecting the corresponding frames; this choice led to 12 sampling points during the test. Figure 4.18 shows the experimental trend; the solid line represents the cubic fit of the experimental values. Note how the deflection increases over time; however, the curve flattens out for a sufficiently high loading time and appears to show an asymptotic pattern starting from 1000 s. It can be speculated that manual loading of the specimen induces a more rigid response in the first phase of the test. Over time, the coupon adapts and reaches a definitive position of equilibrium. Consequently, the static displacement has been identified in the one recorded in the last moments of the test, i.e., after about 20 minutes from the load application, to have a benchmark between the experimental and static FE analyses.

Load amplitude definition

The second point of the set-up is related to the displacement monitoring via DIC. As discussed in Appendix B, in all the tests that required external monitoring of displacements and deformations, contact systems have been disregarded due to their possible influence on low modulus elements. Non-contact systems have been

preferred. A 2D DIC system allows monitoring the in-plane displacements of a flat surface, aligning the focal plane of the camera with it.

Due to bending, the front section rotates from the initial configuration. This rotation induces normal displacements with respect to the focal plane, which changes its position relative to the monitored surface. It is of fundamental importance to limit this rotation to prevent it from taint DIC measurements. A simple preliminary estimate of the front section rotation can be made analytically, following the Euler-Bernoulli assumptions and studying a fixed section beam with a point load at the tip. For the sole purpose of a preliminary estimate of the front section rotation ad deflection, assume that the material is homogeneous, isotropic, and has a linear elastic behavior. The cantilever beam problem can be easily solved by taking that Euler Bernoulli theory kinematic requirements are satisfied. The cross-sections of the specimen are flat and normal to the longitudinal axis, initially. Their thickness is also minimal compared to the actual bending length. Therefore, it is possible to speculate that the cross-sections remain flat and normal to the deflected axis once the load is applied. The theory is well known in the literature; only the results are discussed here. Equations 4.5 allow calculating the deflection and the rotation of the end section.

$$\begin{aligned} d_{end} &= \frac{PL^3}{3EI} \\ \theta_{end} &= \frac{PL^2}{2EI} \end{aligned} \tag{4.5}$$

P is the applied load, L the bending length, I the moment of inertia, and E the Young modulus. Consider $E = 3000$ MPa, and the geometric dimensions of the specimen shown in Figure 4.17. The first estimate of rotation and deflection in the front end is provided in Figure 4.19. For convenience, the load is expressed in kg, the deflection in mm, and the rotation in degrees. Due to the limited stiffness of the PLA, the characteristics of the cross-section, and the bending length, considerable deflections are obtained even by applying little loads. Consistently, very small loads have been considered, choosing between laboratory instruments. The overall weight of the support elements is 100 g; a further 100 g brass block has been considered to load the coupon with 200 g overall. This choice kept the front surface deflection lower than 4 mm and the rotation lower than 4°. As before, the reasoning considered the simple bending test for simplicity. However, the results have been considered for the bending torsion test also.

4.3.2 Discussion of the experimental results

Figure 4.20 shows the set-up common to simple bending/torsion and bending tests. The coupon is at rest: the rear end is tightened inside a metal block; the front end features the metallic slide. A white opaque spry has been used to prepare

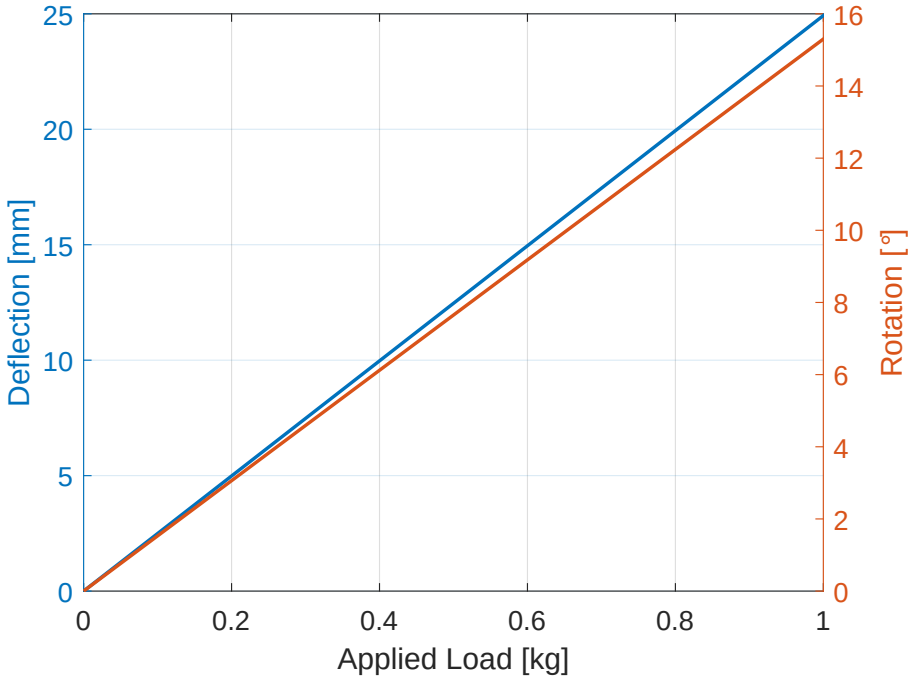

Figure 4.19: Deflection and rotation vs. applied load of the end section of a cantilever beam with point load.

the specimen front surface for displacement correlation. The DSLR camera has been positioned frontally to frame the prepared surface; the optical zoom has been set to 35 mm, to avoid image distortions, as discussed in Appendix B. An analog level helped in checking the specimen and camera alignment. The camera has been operated to record the rest position of the beam after waiting for a sufficient time interval to dissipate the installation-related vibrations. Consider that the specimen is already slightly bent in this configuration due to the metal slide weight, which acts in both the configuration as a 55 g weight in the middle.

Simple bending test results

Following the definitions of Figure 4.1, all the specimens discussed in this section will be identified by the prefix *CSB*; the second part of the prefix differs following the deposition direction of the beads. The 100 g brass block has been then placed on its support plate and loaded in the middle to induce a simple bending. Considering its supporting elements, the further applied load is 145 g. The transverse displacements have been measured by correlating the last frame of the video, approximately 20 minutes after applying the load. Although the cross-section is limited in size, it houses several DIC seeds. Each of them corresponds to a transverse displacement

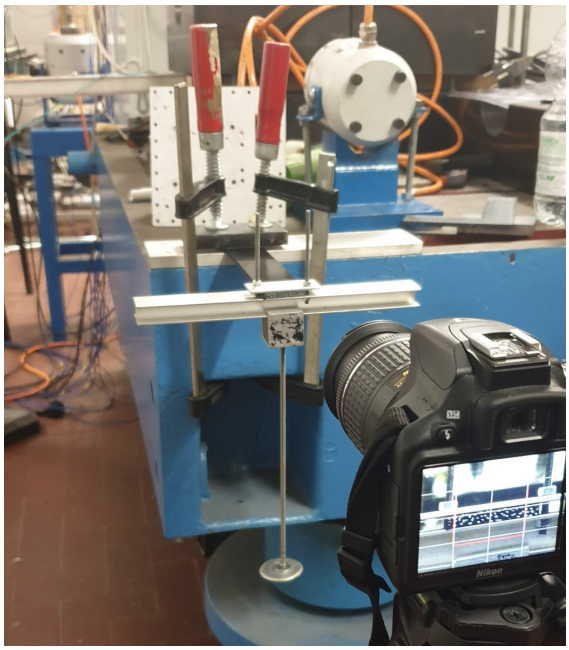

Figure 4.20: Simple bending and bending torsion tests set-up.

measure; the average value has been considered a representative measurement. The test has been repeated with three specimens featuring different laminations; Figures 4.21-4.23 compare the rest vs. deformed configurations and show the DIC transverse displacements maps. The results in terms of end deflection d_{end} are discussed in Table 4.15.

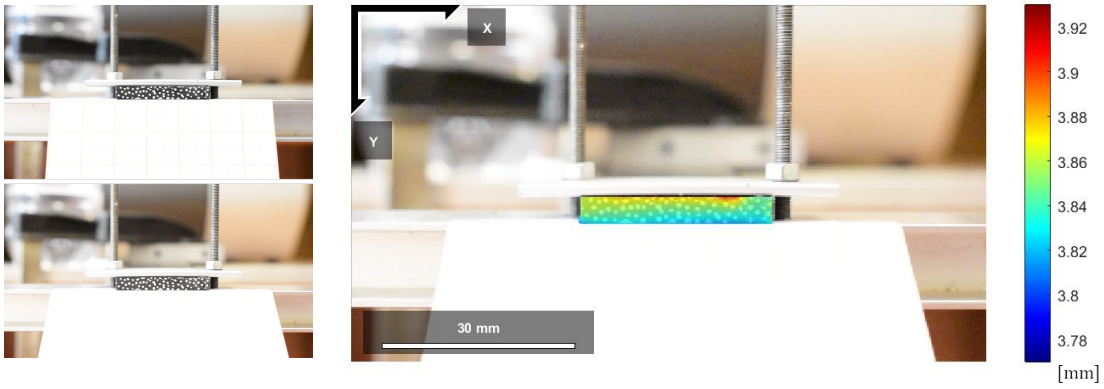

Figure 4.21: CSBD1: simple bending test, specimen build with 0° raster angle. Figures on the left compare the rest vs. deformed configurations, Figure on the right shows the DIC transverse displacements map.

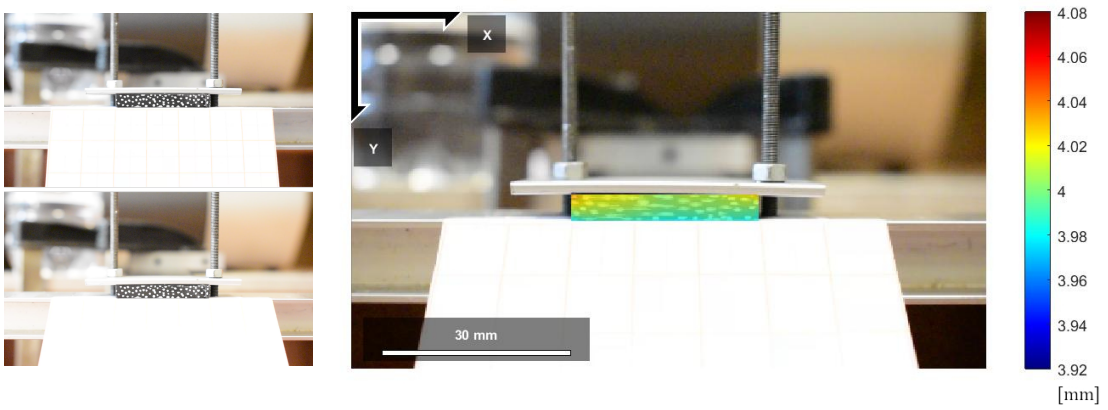

Figure 4.22: CSBD2: simple bending test, specimen build with 90° raster angle. Figures on the left compare the rest vs. deformed configurations, Figure on the right shows the DIC transverse displacements map.

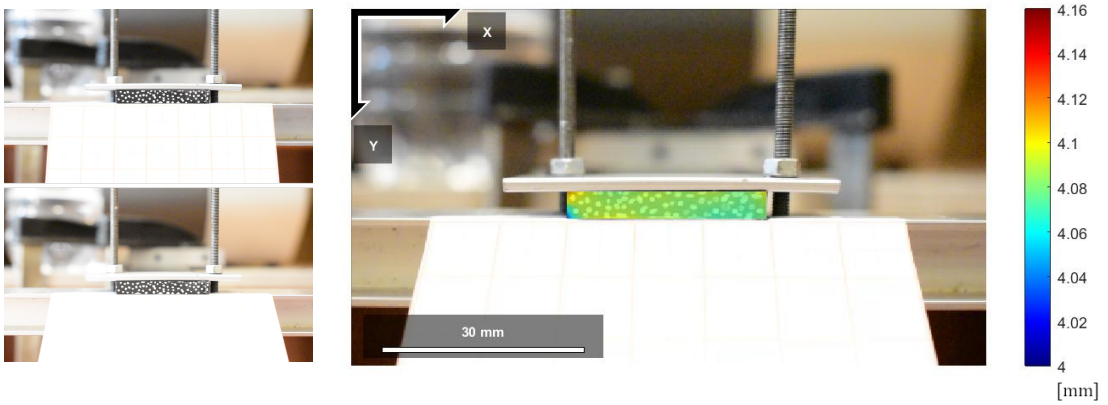

Figure 4.23: CSBD12: simple bending test, specimen build with ±45° raster angle. Figures on the left compare the rest vs. deformed configurations, Figure on the right shows the DIC transverse displacements map.

Simple bending test - 145 g load			
	CSBD1	CSBD2	CSBD12
d_{end}	3.85 mm	3.99 mm	4.08 mm

Table 4.15: Simple bending tests: results in terms of end deflection for the three configurations.

Bending and torsion test results

Following the definitions of Figure 4.1, all the specimens discussed in this section will be identified by the prefix *CTB*; the second part of the prefix differs following the deposition direction of the beads. The 100 g brass block has been then placed on its support plate and loaded in the right endpoint to induce bending and torsion. Considering its supporting elements, the further applied load is 145 g. The transverse displacements have been measured by correlating the last frame of the video, approximately 20 minutes after applying the load. Although the cross-section is limited in size, it houses several DIC seeds. Due to torsion, there is a gradient in the transverse displacements. The transverse displacements at the right and left ends of the section have been evaluated to consider the coupled effect of bending and torsion. Although the cross-section thickness is limited in size, it houses at least four seeds; each of them corresponds to a transverse displacement measure. For both the left and the right end, the end seeds displacements have been averaged to get a representative measurement. The test has been repeated with three specimens featuring different laminations; Figures 4.24-4.26 compare the rest vs. deformed configurations and show the DIC transverse displacements maps. The results in terms of end deflection at the left end d_{end}^{LX}, and at the right end d_{end}^{RX}, are discussed in Table 4.16.

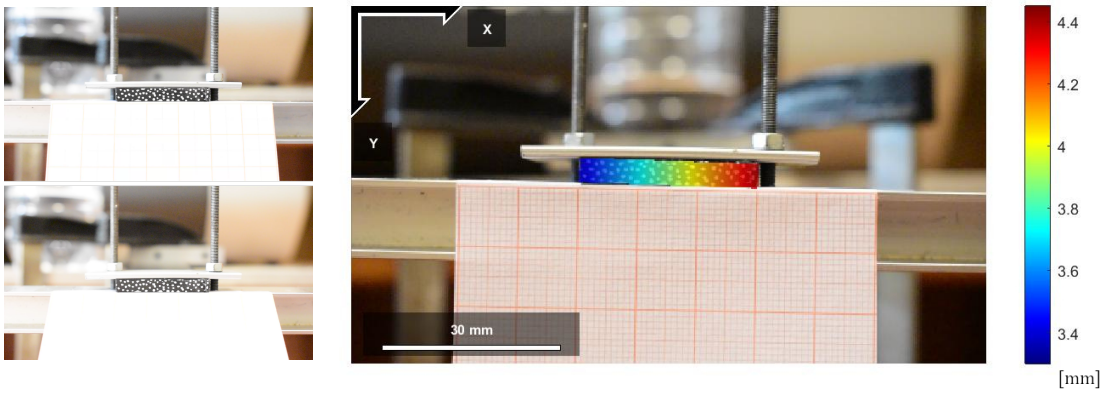

Figure 4.24: CTBD1: torsion and bending test, specimen build with 0° raster angle. Figures on the left compare the rest vs. deformed configurations, Figure on the right shows the DIC transverse displacements map.

4.3.3 FE model of the test

The FEM model is designed to replicate the experimental tests faithfully. It is essentially a two-dimensional model: the specimen is described through its mean surface; similarly, the H-beam slide is described in terms of the mean surfaces of its

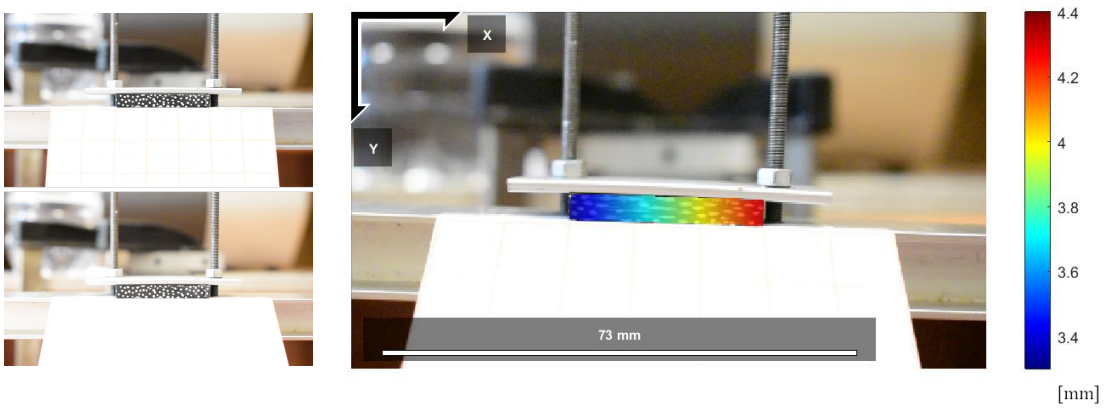

Figure 4.25: CTBD2: torsion and bending test, specimen build with 90° raster angle. Figures on the left compare the rest vs. deformed configurations, Figure on the right shows the DIC transverse displacements map.

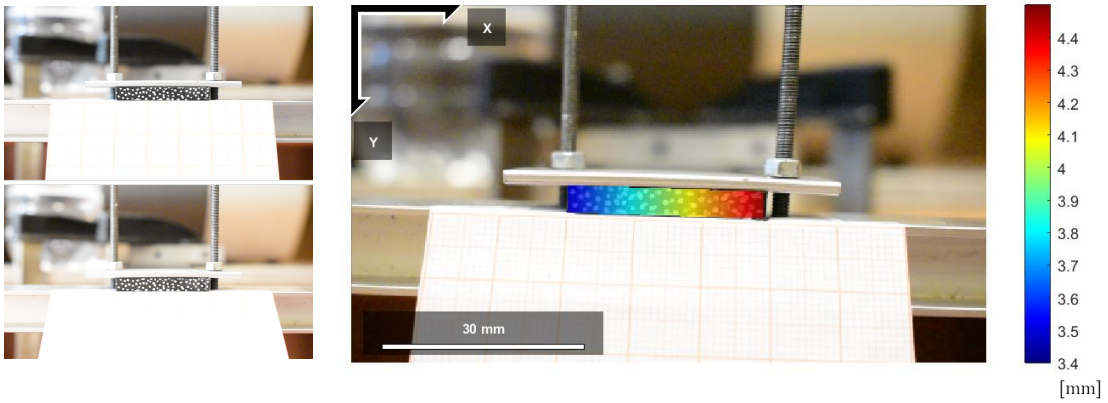

Figure 4.26: CTBD12: torsion and bending test, specimen build with ±45° raster angle. Figures on the left compare the rest vs. deformed configurations, Figure on the right shows the DIC transverse displacements map.

flanges and web. The upper flange has been offset from the specimen so that the two bodies are in contact once the thicknesses are set. A perfect bonding between the two elements is speculated, selecting Glued (G) in the FEs contact table.

The H-beam slide ideally represents a rigid and non-deformable body; it is aluminum made, so it certainly is compared to PLA and considering the loads involved in the tests. An isotropic material has been defined with a linear elastic constitutive model, which considered $E^{alu} = 73$ GPa and $\nu^{alu} = 0.3$ as property values. CQUAD4 shell elements meshed both the specimen and the H-beam slide. This model is simpler than that of the three-point bending test as the contact surface between the two components is defined from the beginning and remains the

Torsion and bending test - 145 g load			
	CTBD1	CTBD2	CTBD12
d_{end}^{LX}	3.38 mm	3.37 mm	3.49 mm
d_{end}^{RX}	4.38 mm	4.31 mm	4.47 mm

Table 4.16: Bending and torsion tests: results in terms of end deflection for the three configurations.

same. Consequently, MSC Patran auto-mesh has been used.

In the constrained region of Figure 4.17, all the translation degrees of freedom are cleared to describe the boundary condition. The model considers two different loads. The first describes the H-beam slide weight; it is fixed despite the load case. It is applied in the center of gravity of the H-beam slide. Since the latter is symmetric with respect to the specimen, the load is orthogonal to the longitudinal axis of the specimen, with no arm. The second load represents the weight of the brass block and its supporting elements. It is a point load, too; however, its application region depends on the load case. It coincides with the first load in simple bending: both act in the shear center of the cross-section. The second load is positioned at the end of the H-beam slide in the bending and torsion test; as out of the shear center, the second load induces a rotation of the section.

4.3.4 Experimental and numerical results comparison

The experimental results of Section 4.3.2 are here compared with the FE model described above. Both the simple bending test and the torsion and bending test considered three configurations, as specimens with [0°], [90°] and [±45°] raster angles have been printed and tested. As per the three-point bending test, three FE models have been considered, **CLT(ISO)_RAW**, **CLT(ISO)_FIL**, and **CLT(ORT)** for which the same arguments of Section 4.2.4 apply. The comparison is shown in Table 4.17, for the simple bending test; Table 4.18 compares the results for torsion and bending test.

In this case, also, the FE results highlighted in bold are the closest to the experiments. Both tests confirm the deductions of the three-point bending tests. PLA feedstock raw data do not describe the mechanical behavior of FFF-processed PLA. They cannot be used to predict its mechanical response, even if the components are quasi-solid. Once the actual mechanical properties of the polymeric filament are experimentally quantified, an isotropic model gives a good prediction in terms of displacements. The results are unique regardless of the actual lamination of the coupons; however, the errors are small. The simple bending test features a simple load case in terms of boundary conditions and load application. The output of the orthotropic model behaves as in the previous validation test: the error is practically

Simple bending - CSBD1			
Experimental	CLT(ISO)_RAW	CLT(ISO)_FIL	CLT(ORT)
$d_{end} = 3.85$ mm	$d_{end} = 2.83$ mm	$d_{end} = 3.77$ mm	$d_{end} =$ **3.83** mm
–	-26.5%	-2.1%	**-0.5%**

Simple bending - CSBD2			
Experimental	CLT(ISO)_RAW	CLT(ISO)_FIL	CLT(ORT)
$d_{end} = 3.99$ mm	$d_{end} = 2.83$ mm	$d_{end} = 3.77$ mm	$d_{end} =$ **4.01** mm
–	-29.1%	-5.5%	**$+0.5\%$**

Simple bending - CSBD12			
Experimental	CLT(ISO)_RAW	CLT(ISO)_FIL	CLT(ORT)
$d_{end} = 4.08$ mm	$d_{end} = 2.83$ mm	$d_{end} =$ **3.77** mm	$d_{end} =$ **3.77** mm
–	-30.6%	**-7.6%**	**-7.6%**

Table 4.17: Simple bending tests: comparison between experimental results and numerical simulations.

Bending and torsion - CBTD1				
Experimental	CLT(ISO)_RAW		CLT(ISO)_FIL	CLT(ORT)
$d_{end}^{LX} = 3.38$ mm	2.57 mm	-24%	3.21 mm -5.0%	**3.41** mm **$+0.9\%$**
$d_{end}^{RX} = 4.38$ mm	3.26 mm	-26%	4.07 mm -7.1%	**4.25** mm **-3.0%**

Bending and torsion - CBTD2				
Experimental	CLT(ISO)_RAW		CLT(ISO)_FIL	CLT(ORT)
$d_{end}^{LX} = 3.37$ mm	2.57 mm	-24%	**3.21** mm **-4.7%**	3.59 mm $+6.5\%$
$d_{end}^{RX} = 4.31$ mm	3.26 mm	-24%	4.07 mm -5.6%	**4.43** mm **$+2.8\%$**

Bending and torsion - CBTD12				
Experimental	CLT(ISO)_RAW		CLT(ISO)_FIL	CLT(ORT)
$d_{end}^{LX} = 3.49$ mm	2.57 mm	-26%	3.21 mm -8.0%	**3.32** mm **-4.9%**
$d_{end}^{RX} = 4.47$ mm	3.26 mm	-27%	4.07 mm -8.9%	**4.21** mm **-5.8%**

Table 4.18: Bending and torsion tests: comparison between experimental results and numerical simulations.

zero in the CSBD1 and CSBD2 configurations, and the FEM results coincide with the experimental one. The error is higher but still contained for criss-cross lamination. In the bending and torsion tests, the load case stresses the structure more complexly, reflecting on higher percentage errors. However, the absolute values are very small and generally lower than those offered by the two isotropic models,

which confirms the efficacy of the approach. However, the diagonal load case, combined with bigger errors for criss-cross laminations, gives rise to the suspicion that the layer interaction might not be directly comparable to what happens between composite laminae but requires further investigation.

Chapter 5

Compression properties investigation

This chapter[1] proposes a research on the compression behavior of FFF-printed parts. It relies on a specifically designed experimental campaign. Extending the geometry of simple compression specimens to a broader length range allows studying the buckling phenomenon. It is the first approach to this issue in association with the FFF. The study focuses on direction normal to the building plate. A small set of tensile tests complements the experimental campaign, thus providing a yardstick for evaluating the compression behavior. The experimental evidence shows that the FFF-processed polymer features an asymmetric behavior between compression and tension along the same load application direction. Consequently, numerical and analytical models provide a reasonable estimate of the critical loads only when tuned with the compressive properties.

5.1 Introduction

The topic of quantifying the mechanical properties of FFF-printed components has interested many authors. Chapter 2 has demonstrated how the matter is of considerable interest, and essential literature is present. Once clarified the anisotropy of a component and the dependence of its mechanical properties on the printing parameters, a literature review highlights the absence of an approach that allows exploiting the determined properties to carry out structural analyzes and optimizations, and therefore validate the functional behavior of a component. Thus, the following chapters have proposed and validated a particular approach that brings anisotropy back to simpler orthotropy. This approach defined some mechanical

[1]Part of the work described in this chapter has been previously published in [93], [94]

properties with a standardized set-up derived from unidirectional composites application; it received an initial validation by defining a 2D orthotropic constitutive model, following the CLT guidelines.

However, this sequence highlights the absence of studies and evaluations relating to the compressive behavior of FFF-printed parts. Filling this lack is essential to obtain a complete and exhaustive understanding. In analogy to the tensile properties, it is likely that:

- the mechanical properties in compression might depend on the evaluation direction;
- different printing strategies lead to different mechanical properties.

At the same time, nothing suggests a symmetry between tensile and compression properties; actually, the microstructure suggests the contrary in analogy with UDCs. The only results on this research line have shown that 3D-printed ABS and PET offer similar properties to injection molded parts when the printing process is tuned with a particular set of printing parameters [95]. In analogy to what has been discussed on tensile properties, Abbas et al. determined the influence of some process parameters on compressive strength [96]. The result is that this grows as the infill percentage increases, which shows consistency with [95].

Compression behavior is of fundamental importance also because of its link to the buckling phenomenon. Numerical and analytical approaches study this event for conventional materials and estimate the critical loads. As well as for mechanical compression performances, buckling also did not receive any interest in the field of FFF-printed parts. Consequently, it is unknown whether these conventional tools for its study are applicable or not. The experimental evaluation of the compression behavior and buckling study go together because any experimental research on buckling relies on compression tests. From a compression test, Kotsmid underlined three methodologies [97], which exploit:

- the maximum value of the longitudinal load, usually referred to as *Load Maximum* (LM),
- the maximum horizontal tangent point of the load vs. longitudinal displacement curve, usually referred to as *Load Axial Displacement* (LAD),
- the maximum horizontal tangent point of the load vs. transverse displacement relation, usually referred to as *Load Lateral Displacement* (LLD).

Those three different approaches provide an estimate of the critical load, with some variability. LM is frequently the method returning the highest value; LAD and LLD are similar, except when there is a linear relationship between the transverse and axial displacements. However, LM is often used, as it is easy to apply. Despite the

method, all authors used lateral displacement to monitor the evidence and assess the phenomenon onset. A case is reported in [98], aimed to evaluate the buckling of bamboo poles under compression. The authors monitored the transverse displacements using six transducers, arranged at different heights and in two directions perpendicular to each other to compensate for the cross-section symmetry. Once the phenomenon onset is determined, the maximum load has been identified as a critical value. Other similar applications have been reported for steel [99] and aluminum specimens [100].

5.2 Discussion of the experimental set-up

5.2.1 Compression tests

ASTM issued under the designation D695 the *Standard Test Method for Compressive Properties of Rigid Plastics* [101]. In analogy with the other standardized tests, there is no reference to Fused Filament Fabrication; however, this test method can be considered a starting point. It requires prismatic or cylindrical specimens with a constant cross-section, square or circular, respectively. The cross-section reference dimension is 12.7 mm, coinciding with the square side or with the circumference diameter. There is no univocal length for the specimen, as it depends on the mechanical characteristic to be determined. For compressive strength, the test method requires the specimen to be twice the length of the reference cross-sectional dimension, resulting in 25.4 mm. For compressive elastic modulus, the length is defined through the slenderness ratio S.

$$S = \frac{L}{\rho} \tag{5.1}$$

In the Equation, L defines the overall sample length while ρ the minor radius of gyration. S must be between 11 and 16; this results in a length in the range $40.4 - 58.7$ mm.

However, from a buckling perspective, the slenderness ratio plays a crucial role in defining the critical load; studying the phenomenon also means evaluating the relationship linking these two parameters. While remaining in the context of short coupons, an extension of the experimental campaign to the $20 - 65$ mm length range allowed a preliminary study. 10 runs of variable length have been considered, consisting of 10 coupons each to ensure statistical consistency in the results. The cross-section shape choice is not trivial: the specimen shows a sudden transverse deflection at the critical load. It is necessary to monitor this deflection to have an image of the phenomenon and establish its onset. As in the previous cases of tensile and bending tests, this experimental campaign requires evaluating a displacement measuring device, taking into account the specific features of the problem. A

cylindrical specimen could deflect in any direction due to the symmetry of its cross-section. In a different section, the coupon would follow the direction with the lowest moment of inertia [102]. Therefore, the square-based prism has an advantage, as it limits the possible buckling directions to four. Moreover, in this second scenario, the specimen offers a flat surface, which is well suited to be monitored by a remote system such as the DIC (see Appendix B). Figure 5.1 defines the 2D drawing of a generic coupon; Table 5.1 discusses the nominal dimensions of the actual coupons and defines the different runs. The Table also reports the slenderness ratio of each

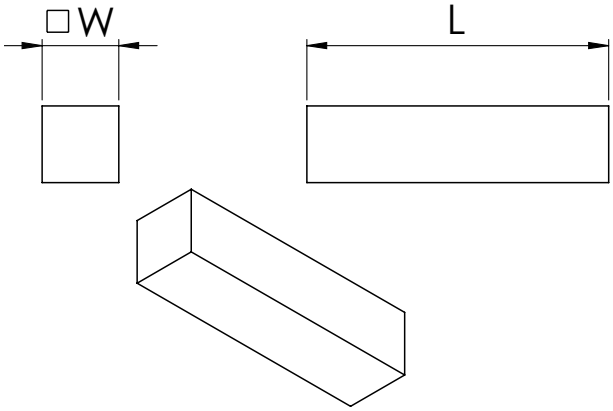

Figure 5.1: 2D drawing of a compression coupon.

	Nominal		
Run	W $[mm]$	L $[mm]$	S $[-]$
I	12.7	20	5.45
II	12.7	25	6.81
III	12.7	30	8.17
IV	12.7	35	9.54
V	12.7	40	10.90
VI	12.7	45	12.26
VII	12.7	50	13.62
VIII	12.7	55	14.99
IX	12.7	60	16.35
X	12.7	65	17.71

Table 5.1: Definition of the geometrical dimensions of compressive coupons.

run; this is useful as the buckling curves are generally expressed as a function of this parameter. Run II and Run VII fall within the definitions previously discussed for the determination of mechanical properties. The first almost coincides with the compressive strength requirements; the second features a slenderness ratio falling midway the range required for the compressive elastic modulus.

Specimens production

This preliminary study limited to direction 3 in the material reference system (the reader can refer to Figure 3.5 in Chapter 3). For this purpose, the load application direction was necessary parallel to direction 3; consequently, the specimens were arranged in the 3D printing volume with the longitudinal axis perpendicular to the build plate. The coupons are consistent with the whole experimental campaign discussed in this dissertation. Therefore they are made with the same compound, through the same printer, using the same printing parameters.

Test set-up

Compression tests have been performed on a multi-purpose Instron 8800 servo-hydraulic machine. It might seem an inconsistency, given that all the experimental campaigns of this dissertation relied on the MTS QTest Elite. However, preliminary tests on the shortest specimens showed ultimate loads higher than 10 kN, its maximum load capacity. The gripping system is very simple: the sample lies between two plates. The load application direction is parallel with its longitudinal axis: the lower plate moves in this direction, while the upper one is motionless. Consistent with the test method requirements, the lower plate moved at 1.3 mm/min. This translates into a displacement control test: the machine control system adapts the applied load to guarantee the imposed longitudinal displacement. The testing machine records the applied load and the imposed displacement at 5 Hz. They can be converted into compressive stress and strain using Equations 5.2-5.3:

$$\sigma = \frac{F}{A_0} \tag{5.2}$$

$$\epsilon = \frac{\Delta L}{L_0} \tag{5.3}$$

F is the applied load and ΔL the imposed displacement; A_0 and L_0 the original cross-section dimension and length, respectively.

To allow the external monitoring via DIC, the outer surfaces of each specimen have been prepared with a spray to obtain a random distribution of grays. The tests have been recorded with a Canon D3500 DSLR Camera positioned in front of a lateral surface of the specimen. As discussed in Appendix B, the optical zoom has been set to 35 mm to avoid focal distortions. The frame rate of the DSLR camera videos has been reduced to 5 fps to match the sample rate of the testing machine.

5.2.2 Tensile tests

A parallel set of tensile tests is here introduced to point out any asymmetries in tensile and compressive behavior. For consistency with the compression tests,

this quantification was required to be carried out along direction 3 in the material reference system.

A design process similar to that described in Chapter 3 has not yet been implemented for this direction. By analogy with tensile specimens for mechanical properties determination in directions 1 and 2, these tests kept their geometry and typology. Since direction 3 is orthogonal to the deposited beads, like direction 2, it has been speculated that the tabs designed in Chapter 3 for this last direction were adequate. Consequently, the tensile specimens follows the geometry already discussed in Figures 3.18-3.19. Table 5.2 recalls both the coupon and the tabs nominal dimensions. The test sample consists of a total number of 5 specimens,

Tensile specimen		
LO - length overall	[mm]	190
W - width	[mm]	25
T - thickness	[mm]	4
Tabs		
l_{tab} - tab length	[mm]	50
t_{tab} - tab thickness	[mm]	1
α_{tab} - tab taper angle	[deg]	20°

Table 5.2: Geometrical dimensions of tensile specimens and tabs for mechanical properties determination in direction 3.

with a rectangular and constant cross-section printed with the longitudinal axis directed perpendicular to the building plate. The coupons are consistent with the whole experimental campaign discussed in this dissertation. Therefore they are made with the same compound, through the same printer, using the same printing parameters. A set of tabs has been printed separately and subsequently glued with bi-component epoxy glue to each specimen.

Test set-up

In analogy with the tensile tests discussed in Chapter 3, the experimental campaign was conducted with the universal MTS QTest10 testing machine. The adapters discussed in Section 3.2, and presented in Figure 3.4, have been installed in both the tensile jaws. Specimens have been placed first in the lower grip and then in the upper one. The longitudinal and transverse strain have been monitored through DIC, following the algorithm discussed in Appendix B. The tests were performed in displacement control at 5 mm/min. They have been recorded with a Canon D3500 DSLR Camera with the optical zoom set to 35 mm to avoid focal distortions. The tensile stress has been calculated through the applied load and the initial cross-section dimension (see Equation 3.1). The testing machine control

system sampled the applied load and the imposed displacement at a frame rate of 5 Hz; the frame rate of the DSLR camera videos has been lowered to this value to match the acquisition frequency of the testing machine.

5.3 Analytical and numerical models

The experimental evidence will show that longer specimens have been globally affected by buckling. Several approaches can help predict this phenomenon, both on the analytical and on the numerical front. This chapter also aims to verify if these models are adequate in the context of FFF-printed components.

The underlying assumptions of analytical models that will be considered are here listed:

- The constitutive model of the material is isotropic and homogeneous. However, the previous chapters of this dissertation have shown that this is not true for 3D-printed PLA; with a 100% linear infill, there is a slight orthotropy.
- The cross-section of the specimen is uniform and constant. Its longitudinal direction perfectly coincides with the load application direction; it is perfectly straight. The compressive fixtures are undeformable; the interface surfaces induce no friction.
- The specimen is free from initial stresses; its weight is neglectable.

5.3.1 Analytical models

Two analytical models rely on the same formula, the Euler model and the tangent modulus theory [102]:

$$\sigma_{cr} = \frac{\pi^2 \tilde{E}}{S^2} \tag{5.4}$$

S is the slenderness ratio, calculated with Equation 5.4; however, it considers the so-called effective length instead of the overall length. It is obtained by multiplying the latter by a coefficient considering the boundary conditions. $\tilde{E}$ takes a different meaning as a function of the considered model. In the Euler model, $\tilde{E}$ is the linear modulus of elasticity, E, and this implies two more assumptions:

- the sample features high slenderness ratios;
- the proportional limit is not exceeded.

With the Euler model, the critical stress has a parabolic trend, and it increases as the slenderness ratio decreases. Above the proportional limit σ_p, the linear relationship between stresses and strains no longer holds, and the predictions are

inaccurate. The limit slenderness ratio within which the Euler model still holds is calculated by reversing the equation and introducing σ_p.

$$S_{lim} = \pi\sqrt{\frac{E}{\sigma_p}} \tag{5.5}$$

The tangent modulus theory extends Equation 5.4 beyond the elastic limit, introducing the tangent modulus E_t in place of the linear modulus. This model is better suited to describe the inelastic buckling; consequently, it does not rely on the additional two assumptions described before. Johnson's formula is the third analytical model; it is specifically designed for low slenderness ratio coupons. It relies on the following expression:

$$\sigma_{cr}^{J} = \sigma_y - \frac{\sigma_y^2 S^2}{4\pi^2 E} \tag{5.6}$$

It defines a new failure region by considering the yield stress of the material; the transition point between the Euler model and Johnson's formula derives from their equivalence, which returns:

$$S_{tra} = \pi\sqrt{\frac{2E}{\sigma_y}} \tag{5.7}$$

5.3.2 Numerical models

Finite element models can effectively simulate the buckling behavior of conventional materials. By disregarding the post-buckling, two solvers help handle this. As the name implies, the linear static solver, SOL101, defines the material properties through a linear elastic constitutive model. For isotropic materials, this translates into the elastic modulus and the Poisson ratio. It solves an eigenvalue problem: its amplitude returns the critical load as a multiplying factor to the applied load; the eigenvector gives the deformed shape of the coupon. The non-linear static solver, SOL106, defines the material properties through the actual stress vs. strain relation of the material. This solution also solves an eigenvalue problem, but gives the entire equilibrium path. From the input data perspective, SOL101 goes in parallel with the Euler model; SOL106 with the tangent modulus theory. The coupons are unidirectional elements, and the compressive load is applied along with its longitudinal direction. A set of FE models has been set-up, with the same boundary conditions and mechanical properties but varying lengths. A segment defines the geometry, meshed through 1D beam elements with BAR2 topology, describing both the mechanical and the inertial properties of the cross-section. The mesh keeps a constant element number, despite the actual length. The bottom end node is fully constrained; the lower only partial to allow defining the compressive force. The experimental evidence shows that all the specimens buckled with the first buckling mode; a unit transversal force has been included in the model to excite it.

5.4 Experimental results and discussion

This section presents the post processing of compression and tensile tests. In analogy with the procedure implemented in the tensile tests discussed in Chapter 3, in all tests DIC and machine sampling have been synced over time, considering that the first instant of the test is when the longitudinal displacements map showed a concordant displacement in direction. A random displacement distribution map with close to zero values due to image noise characterizes the frames that precede the test.

The compressive stress vs. longitudinal strain curves for a representative coupon per run is presented in Figures 5.2a-5.2j. Given that a total number of 100 specimens undergo compressive test, the plots are limited in number. The compressive stress derives from the applied load sampled by the testing machine (see Equation 5.2); the compressive strain is the DIC averaged longitudinal strain. The linear elastic region is present for all the slenderness ratios; shortly after all the curves show a (possibly local) maximum. Following the ASTM D695 definition, at this point the compressive yield stress of the specimen can be evaluated as the strain increases with a constant stress. The subsequent behavior at this point seems to depend on the slenderness ratio of the specimen. In shorter specimens (see Figures 5.2a-5.2c) the stress keeps constant for a large strains domain, then grows again. In longer specimens (see Figures 5.2e - 5.2j) the stress decreases as the test continues. Run IV specimen seem to be a watershed (see Figure 5.2d) as the compressive stress does not show significant changes for a wide range of strains. These feature follows the failure modes: shorter specimens undergo barreling compression mode, while buckling appeared for longer specimens. The watershed in terms of failure mode is represented by Run III specimen, as it showed double barreling.

The tensile stress vs. longitudinal strain curves for a representative coupon per run is presented in Figure 5.3. The tensile stress derives from the applied load sampled by the testing machine; the tensile strain is the DIC averaged longitudinal strain. The tensile behavior is noticeably different from the compressive one: all the specimens failed soon after the linear elastic region and at a very limited load.

5.4.1 Mechanical properties determination

The compressive and tensile mechanical properties determination is described section. Remember that compression tests consist of ten runs whose specimens have the same cross-section but a different slenderness ratio. The criteria that will be described below can be applied to each specimen. Reference will always be made to the single-run mechanical properties because the standard test method requirements provide specific geometries for the resistance and the modulus of compressive stiffness. As anticipated, these requirements are met by two specific runs only. The compression curves were post-processed in the same way as described in Chapter

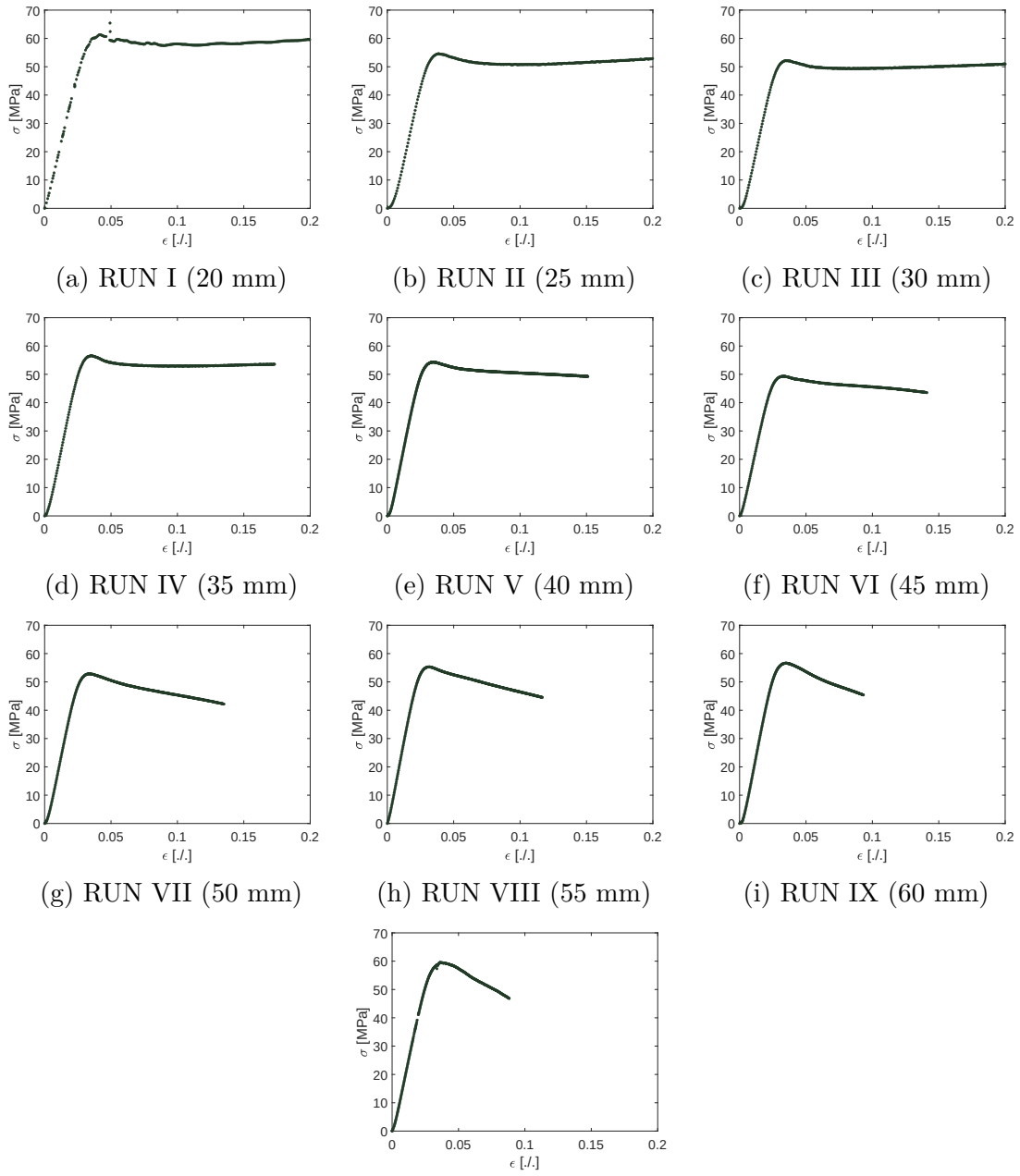

(a) RUN I (20 mm) (b) RUN II (25 mm) (c) RUN III (30 mm)

(d) RUN IV (35 mm) (e) RUN V (40 mm) (f) RUN VI (45 mm)

(g) RUN VII (50 mm) (h) RUN VIII (55 mm) (i) RUN IX (60 mm)

(j) RUN X (65 mm)

Figure 5.2: Compression tests along with direction 3: stress vs. strain relations.

3.

- The compressive modulus of elasticity, E_{33C}, has been calculated through a set of linear regressions on intervals of gradually increasing size. The iterations stop when the new linear regression coefficient differs from the mean of the

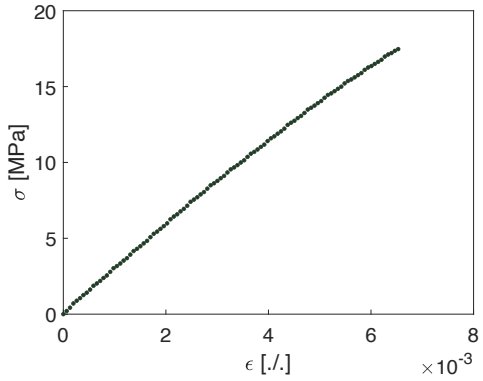

Figure 5.3: Tensile tests along with direction 3: stress vs. strain relations.

previously calculated values by more than 5%;

- the compressive proportional limit, σ^{pro}_{33C}, has been identified with the stress value at which the iterations for E_{33C} calculation stopped;
- the compressive yield stress, σ^{y}_{33C}, has been identified with the stress values at which an increase of strain occurred at a constant load.

The individual values have been averaged among the respective run; Table 5.3 reports the results. The compressive mechanical properties representative of the

RUN	Length [mm]	E_{33C} [MPa]	σ^{pro}_{33C} [MPa]	σ^{y}_{33C} [MPa]
I	20	1951	49.98	59.89
II	25	1997	45.97	52.95
III	30	2151	43.62	52.18
IV	35	2262	46.64	55.17
V	40	2283	43.90	52.69
VI	45	2226	43.19	50.83
VII	50	2301	45.06	53.08
VIII	55	2312	46.56	53.01
IX	60	2313	46.39	53.58
X	65	2210	45.89	58.04

Table 5.3: Compressive mechanical properties of each run.

3D-printed PLA can be obtained from the runs meeting the requirements described in the introduction. RUN II (25 mm-long) is the closest to the compressive yield requirements; its value can be considered representative. Excluding the last specimen, an increasing trend is observed for the compressive elastic modulus as the

slenderness ratio increases. It remains substantially constant in the range between RUN V and RUN IX, which confirms the requirements for determining the compressive modulus of elasticity. It is assumed that the intermediate run recorded value (RUN VII) can be considered representative.

The tensile curves have also been post-processed in the same way as described in Chapter 3; this allowed to determine the tensile modulus of elasticity E_{33}, the tensile proportional limit σ_{33}^{pro}, and the tensile strength σ_{33}^{max}. Table 5.4 compares the FFF 3D-printed PLA mechanical properties in compression and in tension along direction 3. Note that there is a substantial asymmetry between the reported values. The specimens behaved stiffer in traction by about the 25%; however, they failed at very low loads.

Mechanical analysis	
Compression	
E_{33C}	2301 MPa
σ_{33C}^{pro}	45.97 MPa
σ_{33C}^{y}	52.95 MPa
Tension	
E_{33}	2894 MPa
σ_{33}^{pro}	13.06 MPa
σ_{33}^{y}	17.47 MPa
σ_{33}^{max}	17.47 MPa

Table 5.4: Experimental tensile and compressive properties in direction 3.

Compressive tangent modulus evaluation

The mechanical properties summarized in Table 5.4 are sufficient for almost all the numerical and analytical models considered. However, the tangent modulus theory requires the so-called tangent modulus, i.e., defining the slope of the stress vs. strain curve at any load level. The exact requirement comes from the non-linear elastic FE solution, SOL 106. For consistency with the linear elastic modulus, the tangent modulus is evaluated through the identical specimens run. Ten different curves are available (one per specimen); the following algorithm has been implemented to obtain a sample representative. The longitudinal and imposed displacement, thus the axial deformation, are synchronized over time within each run, as the test features a displacement control. The stresses can then be averaged, at each sampling instant, to build a representative curve of the sample. Figure 5.4 shows the scattered trend of the tangent modulus, sampled with the central difference method at regular intervals; a 6-th degree polynomial curve well interpolates it. At very low loads, the tangent modulus gradually settles. It takes

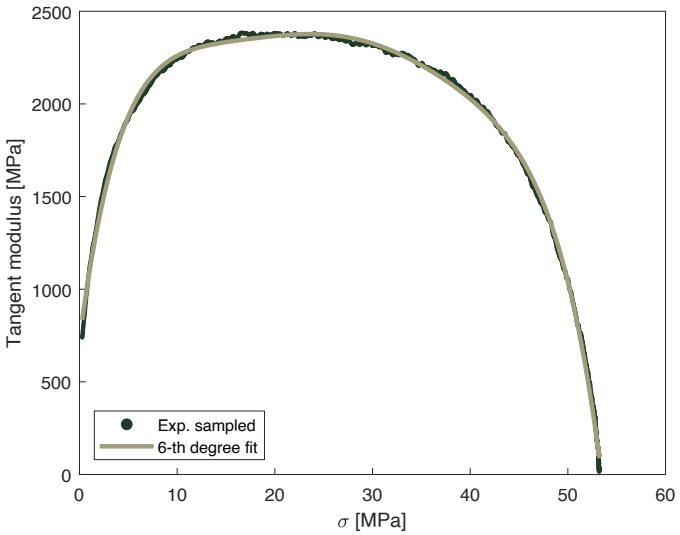

Figure 5.4: Compressive tangent modulus of 3D-printed PLA along with direction 3, based on RUN VIII specimens.

a substantially constant value starting from 10 MPa, and up to 45 MPa. It then decreases very rapidly until it reaches zero. These observations are consistent with the values discussed in Table 5.3 for the proportional limit and yield stress.

5.4.2 DIC buckling observation

As discussed in the introduction, observing buckling is possible by monitoring transverse displacements. In this regard, the DIC is very helpful because it records a map of displacements instead of a value at one (or more) specific coordinates (see LVDTs). Figures 5.5-5.7 discuss the transverse displacement distributions for three specimens; in particular, they show a map for five different stages starting from the beginning of the test. The σ_{MAX} label refers to the instant in which the maximum load has been recorded for the examined specimen. Before, the actual applied load identifies the stages; after, by the time elapsed from σ_{MAX} application. In the initial stages of compression, the transverse displacement distribution is symmetrical to the vertical axis; a simple compression occurs, which involves transversal displacements due to the Poisson effect. The shorter specimen, 20 mm, features barreling compression, and this symmetry holds in all stages of the test. The 25 and 30 mm samples also featured this behavior. The 35 mm specimen is a turning point. The last stages of the test feature a double-barreling compression, only partially noticeable as the lower and upper bulge are slightly shifted towards the front and back surface, respectively. Despite this difference, the symmetry to the vertical axis holds in all stages of the test. Finally, the last specimen, 55

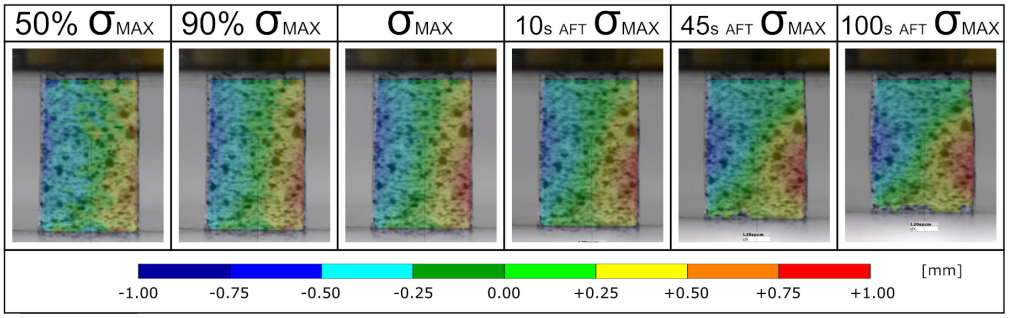

Figure 5.5: DIC maps of the transverse displacement distribution in RUN I specimen.

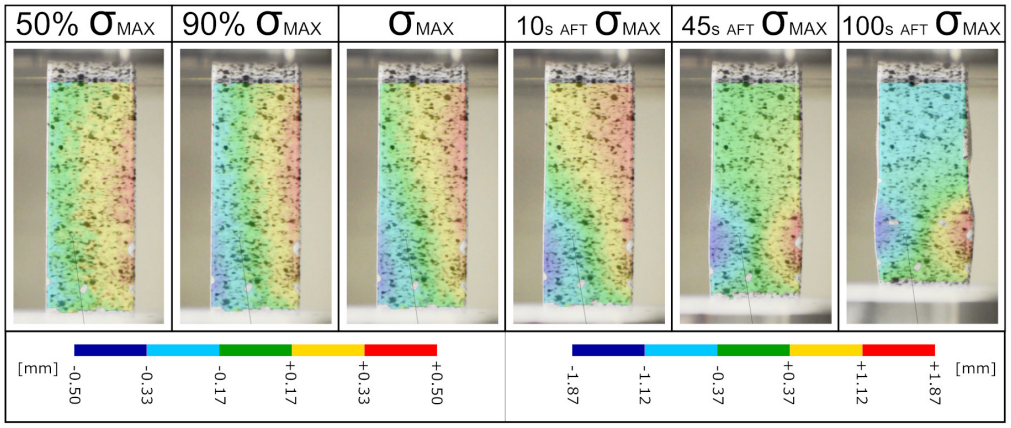

Figure 5.6: DIC maps of the transverse displacement distribution in RUN IV specimen.

mm, shows the buckling in longer coupons. As the maximum load is approached, the transverse displacements map is no longer symmetric. The classic shape of a column buckling appears in the following stages, as the highest displacement values concentrate in the middle section. Another very intuitive way to represent buckling is to plot the transverse displacement where it takes the maximum absolute value as a function of the applied load. Figures 5.8a-5.8j trace this quantity in two control points, chosen in correspondence with the right and left side of the surface monitored via DIC. To further confirm what has been discussed above, all plots are initially symmetrical. In shorter specimens, this trend continues even after the maximum load. However, in the longer samples, one of the two control points changes direction just before the maximum load and agrees to the other. However, all the graphs share the following description: the initial section features negligible transverse displacements and is therefore very steep. In the second section, the absolute value of the displacements increases very rapidly. The breaking point is

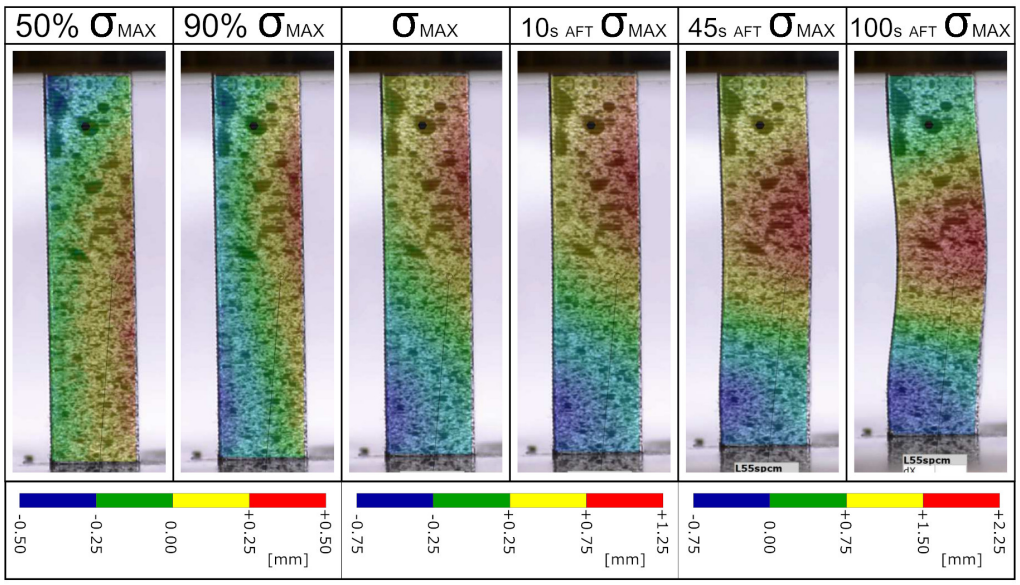

Figure 5.7: DIC maps of the transverse displacement distribution in RUN VIII specimen.

the (local) maximum load, which has already been classified as the yield stress. This note suggests plastic buckling; following the LM criterion, the yield stress of each specimen that undergoes buckling has been identified as its critical load.

5.4.3 Critical load discussion and prediction

The critical load vs. overall length is provided by Figure 5.9 for the buckled specimens only. The boxplot shows the median values (red line) and the Q1/25th and Q1/75th percentiles (horizontal blue lines) to consider the distribution of experimental results of each run. The yellow line also shows the mean value trend and indicates no substantial variability in this range of lengths, except for some anomalies in the 45 and 65 mm specimens.

Assessment of the critical loads prediction

This section is dedicated to assessing whether the numerical and analytical approaches to this event, already available for conventional materials, can be used when dealing with FFF 3D-printed parts confidently. Whether analytical or numerical, the methods require some of these mechanical characteristics: the linear modulus of elasticity, the yield stress, and the tangent modulus. Table 5.4 shows that the tensile and compressive performances of 3D-printed PLA are significantly

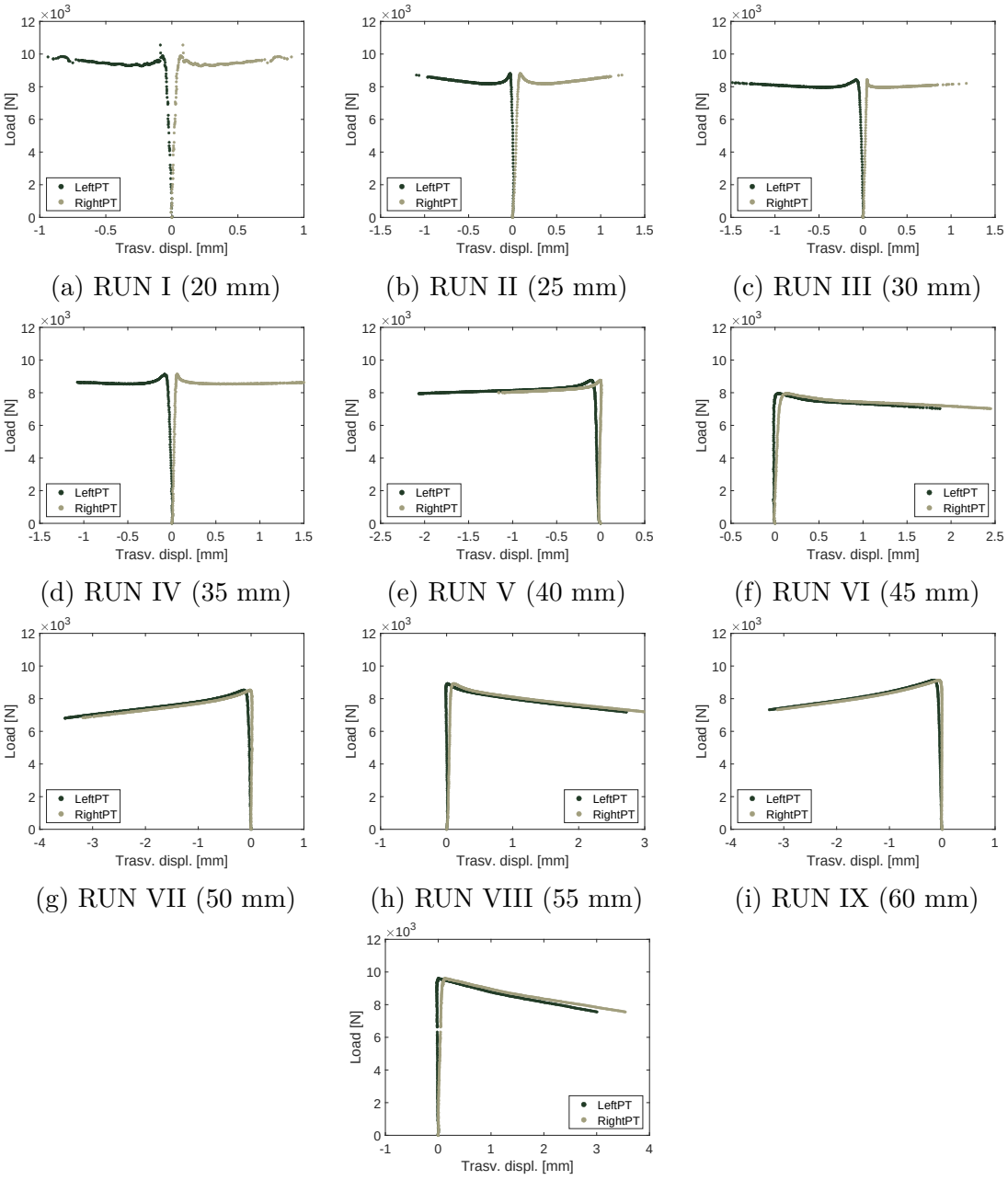

(a) RUN I (20 mm)

(b) RUN II (25 mm)

(c) RUN III (30 mm)

(d) RUN IV (35 mm)

(e) RUN V (40 mm)

(f) RUN VI (45 mm)

(g) RUN VII (50 mm)

(h) RUN VIII (55 mm)

(i) RUN IX (60 mm)

(j) RUN X (65 mm)

Figure 5.8: DIC monitoring of the transverse displacements in two control points per specimen.

different, even with the same evaluation direction. Johnson's formula and the tangent modulus theory are certainly not applicable considering the mechanical properties determined in the tensile tests as the tensile yield stress is considerably lower

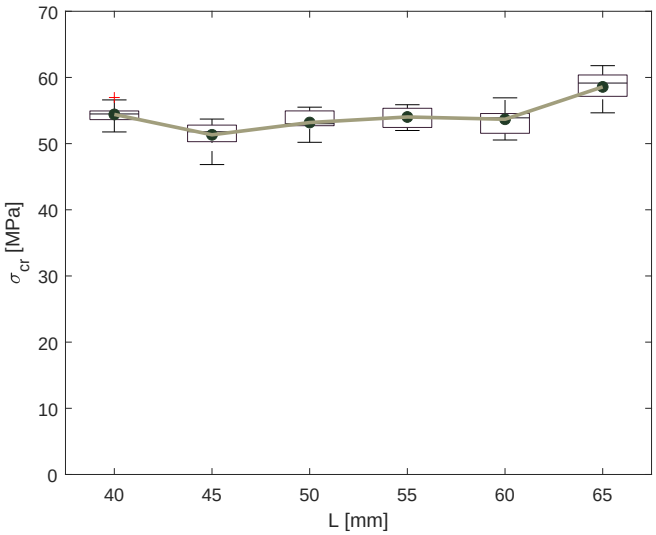

Figure 5.9: Boxplot of the critical loads per each run.

than the compressive one. Johnson's formula returns critical stress lower than the yield stress, and these values would not be compatible with the experimental evidence. Simultaneously, the tangent modulus theory would not provide any results above the tensile yield stress due to the impossibility of evaluating the modulus. Therefore these two models have been implemented with compression properties only. Through them, it is possible to calculate the limit and the transition slenderness ratios:

$$S_{lim} = \pi\sqrt{\frac{E_{33C}}{\sigma^{pro}_{33C}}} = 22.23 \quad , \quad S_{tra} = \pi\sqrt{\frac{2E_{33C}}{\sigma^{y}_{33C}}} = 29.29 \tag{5.8}$$

The results of Equation 5.8 show that all the specimens have a slenderness ratio lower than S_{lim}, therefore S_{tra}. This point raises doubts about whether the Euler formula can produce effective results: it has been considered, for reference, by integrating both the compressive and tensile stiffness modulus. The Euler and Johnson formulas can be simply applied for calculating critical stress at different slenderness ratios. The tangent modulus theory requires a different approach as the same modulus is a function of the applied load. By exploiting the relationship shown in Figure 5.4, a solution is to determine for each stress-module pair the slenderness ratio that makes that stress critical.

The predictions of the three analytical models and the experimental results are compared in Figure 5.10. From the previous reasoning, it follows that Johnson's formula and the tangent modulus theory are proposed by exploiting only the compression properties. Instead, the linear Euler model exploits both the tensile and the compressive mechanical properties. LM returns the highest values, as higher

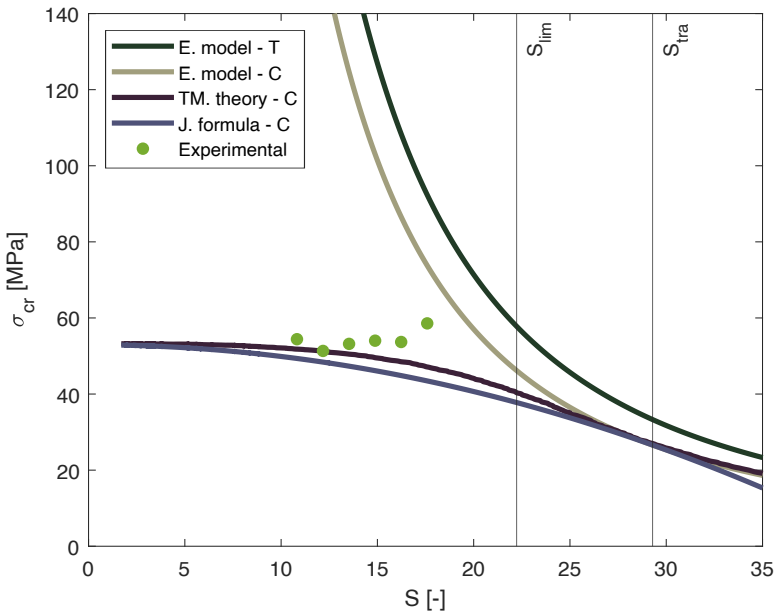

Figure 5.10: Comparison between the analytical predictions and the experimental critical stresses.

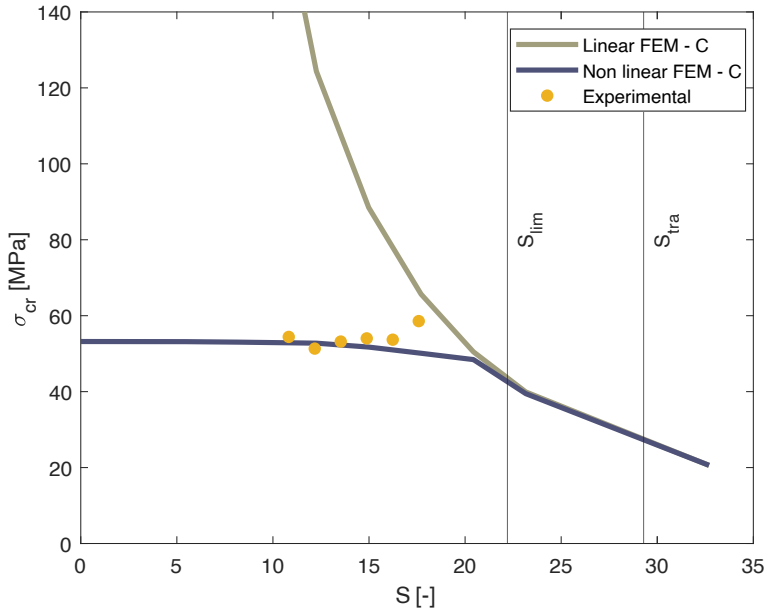

Figure 5.11: Comparison between the numerical predictions and the experimental critical stresses.

as smaller is the slenderness ratio. The curve considering the tensile modulus of elasticity ranks higher due to the experimental properties discussed in Table 5.4.

The tangent modulus theory and Johnson's formula estimates are closer to the experimental results, although these are slightly underestimated.

The predictions of the two numerical models and the experimental results are compared in Figure 5.11, instead. The linear solution, SOL 101, considers a linear elastic constitutive model defined through the experimental E_{33C}. The non-linear solution, SOL 106, considers an elastoplastic constitutive model in which the averaged compressive stress vs. strain relation of RUN VII samples is defined. SOL 101 returns the highest values; the higher, the smaller the slenderness ratio. SOL 106, instead, is very close to the experimental results.

Chapter 6

An applicative example: a 3D-printed drone

The mechanical behavior of a 3D-printed component is mildly anisotropic: the mechanical properties of PLA degrade in the transition from the filament to the finished part. It has been shown that the constitutive model of the material must reflect this behavior to predict the mechanical response of a component satisfactorily. This chapter describes an application example of the methodology deepened throughout the work. The starting point is the preliminary design of a UAV with a 3D-printed frame through FFF; already discussed in the past, this project did not consider the structure validation. The approach discussed in the characterization campaign does not allow analyzing any component. For this reason, a structural validation is proposed, limiting the study to the mechanical response of some specific components. The design proves to be adequate and measured to the surrounding conditions. Evaluating the tensile strengths in the three principal material directions allows validating the structure from the ultimate load perspective and proves to be essential.

6.1 Introduction

Shifting FFF from prototyping to production necessarily requires the mechanical design of the components, and the previous chapters proposed and validated an approach to this concern. Fused Filament Fabrication and PLA make a pair easy to access to the end-user: the technology has been cleared to the consumer market, and the material is very cheap and easy to find. Both aspects have meant that, over time, the self-production practice has rapidly spread. End users often design and produce small functional components for everyday life without a (perhaps unnecessary) evaluation of mechanical performance. In this context, a tool dedicated to designing FFF components would certainly help for a conscious design. As already

anticipated in the previous chapter, it could define the mechanical response of a FFF component starting from its printing parameters and the feedstock material properties. On the other side, the tool could suggest an optimized printing strategy according to its geometry and boundary conditions.

This chapter is dedicated to an applicative example of the results discussed to qualify their importance in the above perspective. The object of this example is PoliDrone, a multirotor Unmanned Aerial Vehicle (UAV) with customizable configurations.

6.2 PoliDrone: a 3D-printed UAV

This UAV is particularly suitable due to some features falling into the concept of customization. The patented [103] and key idea behind this project reflects its structure: it is a multirotor; however, the number of rotors and their spatial arrangement is not chosen beforehand but can be customized. At the center of the UAV is a circular structure, which houses most of the electronics; it also has an external track in the circumferential direction, with 12 anchor points. A single or a couple of rotors is installed on another element, referred to as an arm. Arms can be hooked to the track and fixed in the anchor points following a specific scheme, in a variable number between 3 and 8. The number and arrangement of the arms change the drone performances: the first point is to let the end-user choose the suitable configuration for each mission and configure the drone accordingly. Each arm contains the necessary avionics, the motor driver, and a socket: the arm is a sort of plug-and-play device. Each anchoring point features a socket: once a new element is installed and connected, the control unit automatically auto-updates. The second point is to provide the user with the electronics into self-configuring kits, leaving the user to print and assembly the structural elements. This also allows the user to count on a configuration that can evolve, even adapting to new requirements. Figure 6.1 shows a graphic rendering of the UAV in a four-arm configuration.

6.2.1 Design constraint

As anticipated, the end-user can modify the UAV configuration. This customization translates into the number of arms, i.e., both the number of engines and propellers. To this end, the UAV central structure is universal and, at the same time, compatible with each configuration; this requirement translates into a design allowing the user to make such customizations easily. To ensure modularity, it is essential that:

- the control unit design handles all configurations,

Figure 6.1: Graphic rendering of the PoliDrone UAV.

- each arm houses its electronics,
- the battery design ensures excellent autonomy in all configurations.

The maximum take-off weight (MTOW) of the UAV provides a further and strong design constraint. Drones have to comply with dedicated regulations issued by the Italian Civil Aviation Authority (ENAC) in Italy. They target drone flight operations, which are listed as a function of the drone weight. In particular, article 12 of the *Remotely piloted aerial vehicles Regulation* [104] states that:

> Remotely-piloted aircraft system (RPAS) specialized operations with remotely-piloted aircraft (RPA) with an operating take-off mass of less than or equal to 2 kg are to be considered non-critical in any operative scenario, providing that the RPA design criteria and manufacturing techniques result in harmless features that shall be verified in advance by ENAC or by an organization recognized by ENAC.

Maximum take-off weight of 2 kg brings considerable simplifications and is a further design constraint. This value includes the (possible) payloads; the ability to customize the UAV also translates in letting the user choose the payload among different items, following the specific needs. Therefore, it is of fundamental importance to limit the weight of avionics, electronics, battery, and structure. The structural weight of the drone depends on:

- the geometry of the elements,
- the material,

- the configuration (e.g., the number of arms).

The weight of avionics, electronics, battery instead depends on performance requirements and results from a more complex design.

6.2.2 The frame components

The initial design has been proposed and discussed in [105]; a first optimization of the element geometries followed in [106]. This analysis allowed an early reduction of the structural weight, even without an objective structural optimization, as the mechanical behavior of the PLA was only partially known. Furthermore, this limitation prevented the validation of their structural performances. This section briefly reviews the characteristics of the elements to assess the problem and identify some critical and eligible components for structural analysis. In the following reference will be made to the following set-ups (see Figure 6.2 for reference):

- C4A: configuration with 4 arms,
- C6A: configuration with 6 arms,
- C8A: configuration with 8 arms.

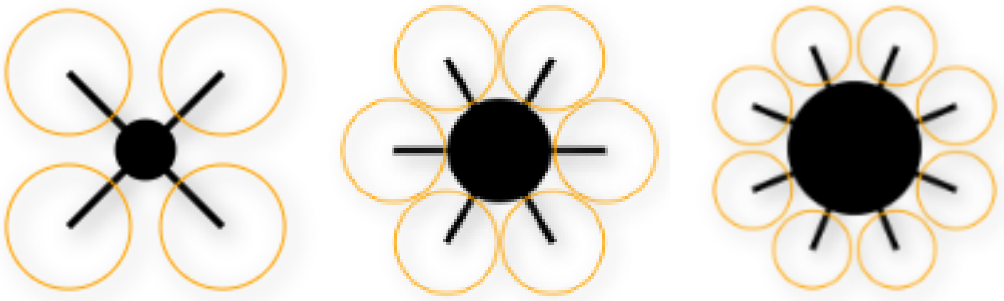

(a) C4A. (b) C6A. (c) C8A.

Figure 6.2: PoliDrone configurations considered in the preliminary design. The elements in these figures are not in scale.

Main core elements

The central/main element is designed as a circularly symmetrical object, composed of an upper and a lower plate. Both the components are externally equipped with a single track: once assembled, the two create a guide on which the supporting elements of the arms can be housed and can slide to take the position required by

the specific configuration. The radial location of each arm depends on the configuration (that is, on their number) and is pre-determined. Along with the guide and the radial direction, a certain number of numbered anchor points define all the arm locations; a guide table helps the user identify each arm position in each specific configuration. This set-up is of fundamental importance because, for each design, the flight control and management strategies rely on the relative position of the rotors, which cannot be an arbitrary choice. The two elements are shown in Figure 6.3; the upper plate features a vertical cylindrical wall, which encloses the volume necessary to install the avionics, electronics, and battery.

Figure 6.3: Graphic rendering of the central/main elements.

Arms

The arms are the key components of this project, as already discussed. Each arm is an assembly consisting of an upper, a lower, and a supporting element. The first two items define a hollow volume, once assembled, dedicated to the electronics and the ESG; they also feature anchor points to install the motors. It is a full-fledged all-in-one assembly, ready to go once connected. The supporting element guarantees the connection with the core: its front region features an open seat; the shape of its rear part adapts to the guide of the central structure. Figure 6.4 shows a graphic rendering of the arm assembly. Once assembled, the two arm elements slide into the seat, and the support settles into the rail. Two threaded cylinders housed in through holes and fastened by two nuts on the lower and upper plate surfaces make the support and the central structure integral. The two arm elements are prevented from sliding inside the support by a fastener: it acts as an anchor point and guarantees an optimal relative positioning of the propellers

Figure 6.4: Graphic rendering of the arm assembly.

in the different configurations, ensuring sufficient separation. Figure 6.5 shows an exploded view of a complete arm assembled with the core.

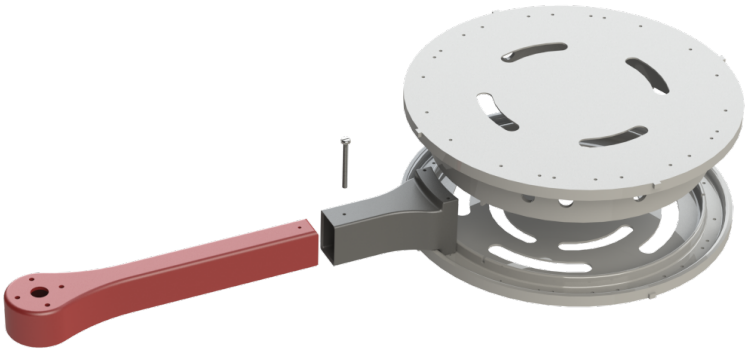

Figure 6.5: Exploded view of a complete arm assembled with the core.

Domes and landing gears

Upper and lower spherical domes enclose the core elements; these two provide an additional hollow volume to house any further electronics and the payload. They also guarantee flotation in case of a water landing. Landing gears have a trivial goal; their design ensures sufficient ground separation. They connect to the core through the circular track: their upper region adapts to the guide of the central structure, featuring an arm support-like shape.

A first assessment of the structural weight is discussed in Table 6.1; it follows the first optimization of the element geometries in [106], and consider Eryone black PLA as the material (see Table 1.1 for reference). The weights result from the CAD volume evaluation. The three configurations result in the total weights discussed in the last rows.

Individual weights			Bill of Materials		
Part no.	Description	Weight [g]	C4A	C6A	C8A
	Upper plate	108.2	1	1	1
	Bottom plate	77.7	1	1	1
	Upper arm element	16.0	4	6	8
	Bottom arm element	20.3	4	6	8
	Arm support	23.6	4	6	8
	Upper dome	72.5	1	1	1
	Bottom dome	87.0	1	1	1
	Landing gear	49.8	2	2	2
	Overall structure weight →		684 g	804 g	924 g

Table 6.1: PoliDrone frame weights assessment.

6.2.3 Preliminary design

This section discusses the preliminary set-up of the UAV and presents the selected avionics components. This discussion is fundamental to estimate the UAV flight parameters and performance to define the boundary conditions for the structural analyses. Schematically, a UAV consists of the following elements:

- frame,
- control unit,
- DC brushless motors,
- electronic speed controls (ESC),
- propellers,
- Li-Po battery.

These components are briefly discussed below; the project exploited the simulation software xcopterCalc [107]. This preliminary design has the sole purpose of defining the boundary conditions to evaluate the mechanical response of some components of the frame. It is not the purpose of this section to provide a detailed report on the

aircraft design scheme. Each component choice has cascading effects on the whole project; however, it directly defines some stakes for specific components, helping in their selection. The order of this thread follows this logic.

Propeller design

The choice of propellers depends on dimensional and efficiency parameters. A general guideline is that the bigger the propeller diameter, the more efficient it is. The frame prescribes that the helices be coplanar; the set-up (i.e., the number of arms) imposes different constraints on the maximum size: larger propellers are possible with four arms, smaller with eight. Since the smaller propellers would have been inefficient in the first set-up, different propellers have been considered in the three configurations to maintain high efficiency. Manufacturers use two parameters to classify the performances:

- trust constant, T_c, which indicates the percentage of absorbed power converted into thrust; in practice, this value is less than 1.
- power constant, P_c, which corrects the absorbed power to ideal conditions; in practice, this value is higher than 1.

The geometric parameter is a design constraint: the propellers have been selected on the market by maximizing T_c and minimizing P_c. Table 6.2 reports the datasheet of the identified models. The dimensions are in inches; the pitch to diameter ratio is less than 2/3 to avoid stall with increasing load.

Set-up	Manufacturer	Model	dia	pitch	T_c	P_c
C4A	Aeronaut	CamCarbon	$13'$	$5'$	1.07	0.99
C6A		CamCarbon	$11'$	$4.5'$	1.07	0.99
C8A		CamCarbon	$8'$	$4.5'$	1.07	0.99

Table 6.2: Aeronaut propellers datasheet.

Motor design

Brushless motors are widespread in multicopters [108]; a direct current source powers them. They have several advantages over brushed motors, including a longer life expectancy, lower inertia, and a higher rotation speed. Choosing a specific model depends on many factors. The initial screening follows some technical specifications of the UAV:

- all-up-weight,
- n° of rotors,

- frame size,
- battery-rated voltage,
- propeller diameter,
- propeller pitch,
- propeller blades.

These parameters drive the recommended ranges for three technical characteristics:

- rpm / voltage,
- minimum motor power,
- minimum ESC size.

These ranges allow refining the engine database in search of the optimal model. In this specific application, the three different set-ups (quad-, exa-, octa-copter) feature other parameters; consequently, the wizard is not unique. The all-up-weight can be set assuming that the payload saturates the total weight to the maximum value discussed in Section 6.2.1. The number of rotors, and the characteristics of the propellers, follow the previous reasoning. The frame size designates the maximum overall dimension. Table 6.3 discusses the input parameters and the results of this preliminary assessment for the three set-ups. The ranges only partially overlap,

Motor wizard			
Input parameters	C4A	C6A	C8A
all-up weight	2000 g	2000 g	2000 g
n° of rotors	4 - flat	6 - flat	8 - flat
frame size	580 mm	580 mm	580 mm
battery-rated voltage	11.1 V	11.1 V	11.1 V
propeller diameter	13′	11′	8′
propeller pitch	5′	5′	5′
propeller blades	2	2	2
Calculated optimal design ranges			
rpm / voltage [rpm/V] →	680 – 1000	740 – 1070	1090 – 1580
min. motor power [W] →	270 – 475	175 – 305	155 – 275
min ESC size [A] →	30 – 50	20 – 35	20 – 30

Table 6.3: Optimal design ranges for motor selection.

so it is not easy to find an optimal configuration for all three set-ups. Another parameter to consider is the motor weight because it increasingly influences the UAV performance moving towards the higher configurations. The choice fell on NeuMotors model 1230/5Y; its datasheet is reported in Table 6.4 for convenience.

NeuMotors model 1230/5Y	
rpm / voltage	987 KV
body length	33 mm
weight	35 g
idle current	0.5 A @ 10 V
max cont. power	250 W
resistance	0.225 Ω
torque constant	9.698 mNm/A

Table 6.4: NeuMotors model 1230/5Y datasheet.

Electronic Speed Controller design

The wizard defining the optimum motor parameters also provides a helpful indication of the ESC size in terms of continuous current. The range varies from one set-up to another, depending on the specific number of motors. However, a preliminary simulation evaluated the maximum current value in the worst condition as less than 15 A. This value has been considered to filter the components database, choosing between the lightest and the smallest models. Both the requirements are intended to contain the overall weight. The fists directly, as an ESC is required per motor; the second indirectly, as each arm is sized to house an ESC each and can be as smaller (lighter) the smaller the size of the controller. The datasheet of the selected ESC is reported in Table 6.5.

Talon 15	
input voltage	$2-4$ S
max continuous amperage	15 A
width	14.7 mm
length	27.9 mm
depth	8.1 mm
weight	7.2 g

Table 6.5: Talon 15 ESC datasheet

6.2.4 Final simulations

The xcopterCalc simulation results are reviewed in Table 6.6; they are grouped by weight and performance labels and discussed for all three configurations. These results imply a 6000 mAh battery, warning that different capacities have a different effect on weight and performance. For each set-up, the all-up-weight is indicated, which considers all the UAV elements except the payload. The maximum payload

derives from performance considerations; however, the additional payload is limited by the weight of 2000 g that the drone must undergo. Note how as the configuration

PoliDrone multicopter - Preliminary Design				
		C4A	C6A	C8A
Weights	Frame	684 g	804 g	924 g
	Drive	228 g	321 g	414 g
	Battery	426 g	426 g	426 g
	ALL-UP	1338 g	1551 g	1764 g
	Add. Payload	662 g	449 g	236 g
	Max. Payload	1140 g	1415 g	391 g
Performances	est. Range	3178 m	3343 m	3336 m
	est. rate of climb	4.4 m/s	5.1 m/s	2.8 m/s
	min. flight time	5.8 min	5.4 min	8.4 min
	mixed flight time	14.3 min	13.9 min	12.6 min
	hover flight time	20.1 min	19.6 min	15.0 min
	Trust-Weight	2.1 : 1	2.2 : 1	1.4 : 1

Table 6.6: Preliminary design of PoliDrone multicopter: weight and performance estimations.

changes, the weight of the frame and the drive varies, and this affects the payload. The most performing configuration from the perspective of maneuverability and flight time seems to be the C6A; nevertheless, it offers a lower load capacity than the C4A. At maximum load, all configurations retain a residual throttle higher than 20%; this, combined with the Trust-Weight values, guarantees good maneuverability.

6.3 Multicopter structural analysis

From the structural perspective, the multicopter frame needs to be tested to verify its feasibility, adequacy, and rigidity. Setting up a FE analysis allows evaluating these aspects. Still, it requires defining the mechanical properties of the materials, other than the geometry and boundary conditions. Up to this moment, Polidrone did not receive any numerical validation from this point of view: the anisotropy of the FFF-printed components was known, but it was not yet clear how to manage it. The heart of this research work described their mechanical behavior through the CLT approach, deriving its application from the field of composite materials. This approach confirmed that components printed with a linear infill and a 100% filling exhibit a mild orthotropic behavior. The mechanical response is similar to that obtained in the tensile tests on the feedstock filament, but

only in the bead deposition direction (referred to as direction 1). A slightly less rigid behavior has been recorded in the perpendicular one (referred to as direction 2). Outside of the $1-2$ plane behavior described by CLT, direction 3 also showed a decrease in the stiffness if compared to the filament. What is even more important is that the tensile strength differs significantly between the three directions. The implication of these results is essential: a first (not conservative) approach to the structural analysis could rely on the mechanical properties declared by the manufacturer. However, the validation tests proved they are inadequate in predicting the mechanical response, as they globally overestimate the stiffness. They are not accurate in the definition of the safety margins because they also overestimate the tensile strength. On the other hand, the feedstock filament properties deliver more satisfactory results in a first approximation but still not effective in the ultimate load perspective.

The new results of this characterization campaign allow overcome some of these limitations, but they deliver others. It is intrinsic to define a 3×3 stiffness matrix that the application field is limited to mainly two-dimensional structures. A further limitation appears while considering that the principal directions in the material reference system have a precise meaning. This approach has been validated only on two-dimensional objects parallel to the build plate. Therefore, it is not capable, at the moment, of analyzing any component. This outcome will be possible if the definition of the mechanical behavior is completed up to the 6×6 stiffness matrix. In this context, the structural validation is limited to studying the mechanical response of some specific components well suited to this definition due to their shape and boundary conditions.

6.3.1 Arm assembly analysis

The arms can be schematized as beam elements, pinned at one end and loaded from a point load on the other. They feature a rectangular and thin-walled cross-section; all the walls are 1.5 mm thick. Excluding the support, each arm is made up of two almost mirror-like elements. In both, the base surface is flat and significantly extended, which favors a print with this surface adhering to the build plate (see Figure 6.6). The predominant effect will be bending; a good printing strategy consists in arranging the filaments parallel to the longitudinal direction to exploit the higher stiffness and strength of this material direction. The support is a single component, and it can be printed similarly, with two faces parallel to the print bed. As shown in Figure 6.7: arranging the part will require designing some support elements due to the greater thickness in the right-end region and the empty socket in the central section. The effects of bending are even more important for this component, as it is located at the root, next to the constraint. Again, arranging the filaments parallel to the longitudinal direction exploits this material direction with higher stiffness and strength. Any printing with the longitudinal axis oriented

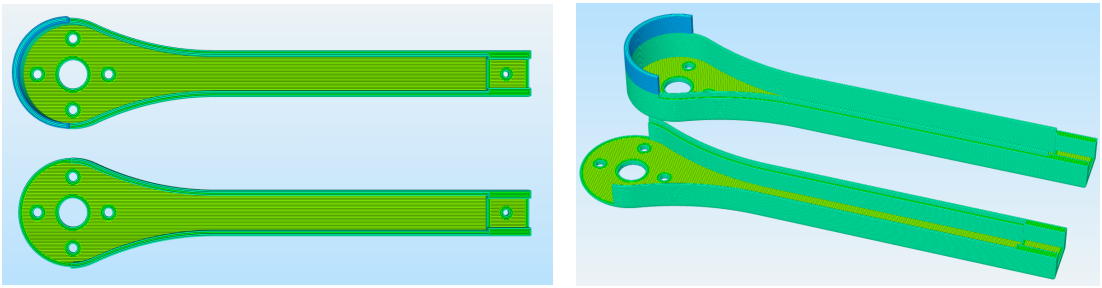

(a) Top view. (b) Side view.

Figure 6.6: FFF 3D-printing preview of the arm elements.

along with the vertical direction would limit supporting material. Still, it would be risky as the bending tensile/compression state would develop along with direction 3, which is the weaker. A severe condition has been considered to validate the stiffness

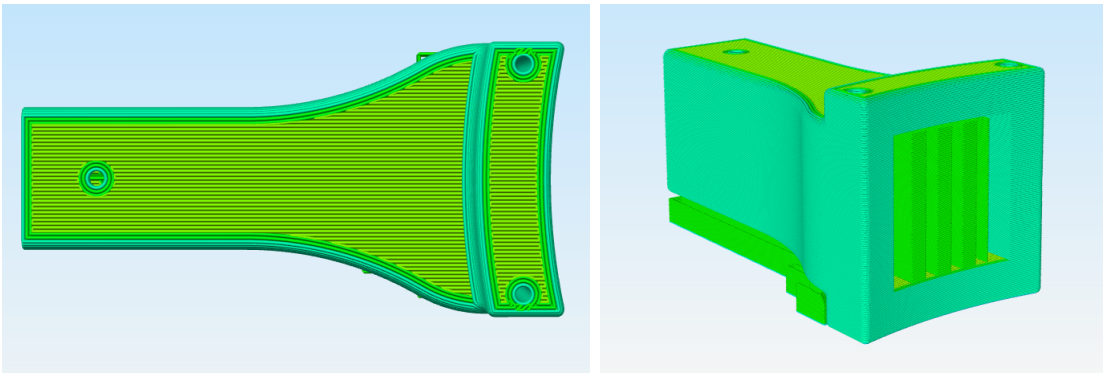

(a) Top view. (b) Side view.

Figure 6.7: FFF 3D-printing preview of the arm support.

and dimensional adequacy of these components: the UAV is at its MTOW, takes off vertically, and accelerates at maximum throttle. The vertical thrust is equally distributed; therefore, the four-arm configuration is discussed, being the worst-case.

Background information

The MTOW is 2000 g ($\approx$ 20 N), as discussed in Section 6.2.1. Preliminary design results show that the C4A set-up features a Trust-to-Weight (TtW) ratio of 2.1 : 1, which means that the engines can generate a trust 2.1 times the weight at full throttle. In this configuration, the thrust generated by the single-engine in the heaviest condition can be calculated as follows:

$$L = \frac{\text{TtW} \times \text{MTOW}}{\text{arm n}^\circ} = \frac{2.1 \times 20 \text{ N}}{4} = 10.5 \text{ N} \tag{6.1}$$

The load is transmitted from the motor metal casing to the arm at the four anchor points through threaded fittings. Once assembled, the upper and lower arm elements mate with the support and are kept in place by two bolts. The rear part of the support mates with the core rails and is held in place by two pairs of fasteners.

Geometry of the model

The geometry of the three components is modeled separately in SolidWorks and converted into a Parasolid Model Part (with .x_t extension). This export allows exchanging the model with different software not handling the proprietary CAD format (.sldprt). Before exporting to .x_t, the geometry has been simplified by removing all fillets, thus transforming all three components into hollow parallelepipeds-like, with four faces of constant thickness, orthogonal to each other. This simplification is explained below. Once imported into MSC Patran, the models could not be directly analyzed. They are still three-dimensional components, requiring a 3D element mesh and a 3D orthotropic constitutive model for material properties definition. A surrogate shell representation has been designed for each element using the *Create Midsurface* tool, as shown in Figure 6.8. The global ref-

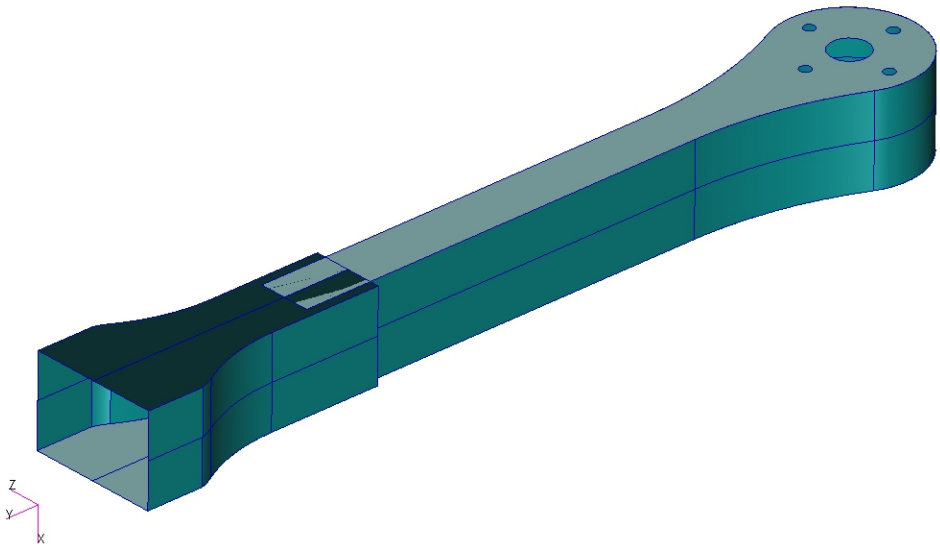

Figure 6.8: Surrogate shell representation of the arm assembly for FE analysis.

erence system is also presented: the Y axis is oriented along with the longitudinal direction, and the X points down. The shell properties definition will recover the appropriate thickness information, keeping the differences among the walls. This procedure allows a partial overlap between surfaces, noticeable in the interface region between the components, to be fixed with appropriate offsets. In the end, the native solid geometry has been replaced with a shell geometry, but this required

several steps to arrive at an accurate result. Removing the fillets facilitates this result as it allows, at least in the central region of the arm, to use only four surfaces to describe the geometry fully.

Boundary conditions

The load is applied as a "total load" and distributed equally on four annuli, concentric with the anchoring points of the motor metal casing. In the first instance, it is assumed that the fastener heads rest on an M6 washer (external diameter 12.5 mm). Regarding the constraint conditions, it is speculated that the support rear edges are pinned, which does not differ much from reality due to the fastening system (see Figure 6.9). The arm is an assembly of three components; the contact

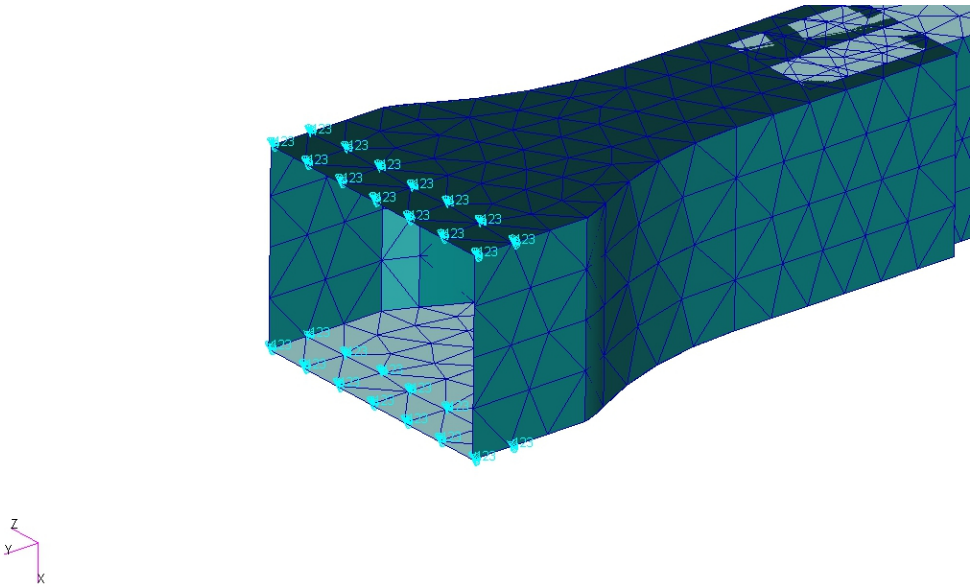

Figure 6.9: Constraint boundary conditions applied on the arm support.

relationships between the surfaces have been defined after their placement on site. An ideal adhesion is set for the upper and lower surfaces in contact between the two arm components and the support. This hypothesis does not differ much from reality due to the compression preload induced by the fasteners. On the other hand, for the lateral surfaces, a simple contact has been set, which allows the exchange of normal compressive forces between them and ensures no interpenetration but does not exclude a relative movement. The upper and lower elements of the arm will be joined later after the mesh is defined.

Mesh and properties definition

The assembly has been meshed with 2D shell elements, with Tria3 topology, using Paver mesher (see Figure 6.10). IsoMesh is non-compatible as the surfaces obtained from a solid of any shape are not isoparametric. The coarseness initially followed the Global Edge Length value calculated automatically by MSC Patran. However, the results will be discussed in terms of gradually finer meshes, allowing the solution convergence evaluation. After meshing, the equivalence tool is used to bond the superposed nodes of the different surfaces that make up each body and delete duplicates. This operation welds the upper and lower arm elements together.

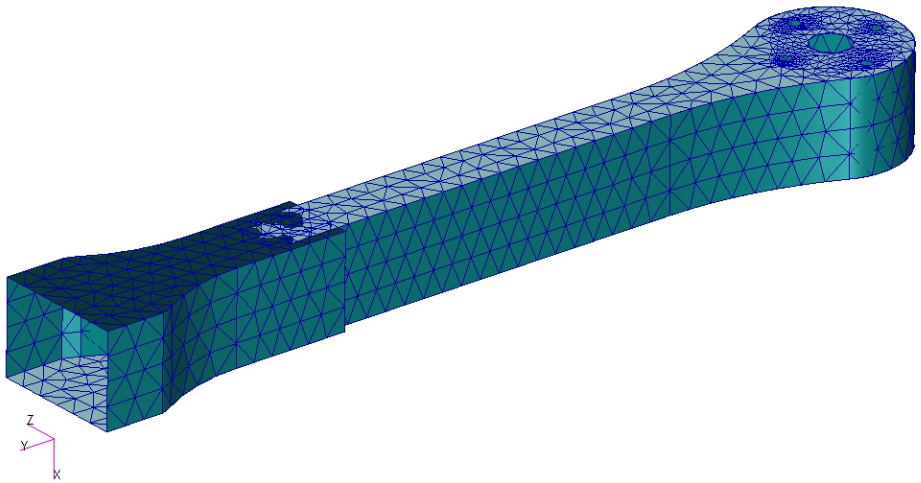

Figure 6.10: PoliDrone arm meshed with Tria3 2D shell elements.

A separate discussion concerns the element properties definition. Taking into account the manufacturing strategy shown in Figures 6.6-6.7, only the upper and lower surfaces of the assembly can enjoy the 2D orthotropic mechanical properties obtained in Chapter 3 and validated in Chapter 4. While retaining the two-dimensional nature, the vertical walls are mainly arranged on the $1-3$ plane of the material. The mechanical properties determined in direction 3 in the tensile tests discussed in Chapter 5 help handle this. The mild orthotropy found so far is further confirmed by the values defined in this direction for the tensile stiffness modulus. However, nothing can be speculated about the shear modulus G_{13}. In analogy to the terminology of FE models discussed in Chapter 4, the following constitutive models have been considered:

- **CLT(ORT)**: 2D orthotropic constitutive model for a single layer, defined considering the outputs of Chapter 3. The 5×5 stiffness matrix has been

traced back to the 3×3 stiffness matrix with appropriate penalties over the shear moduli G_{23} and G_{13}. A laminated composite has been defined, laying up layers with the real raster angle and thickness. It defines the mechanical properties of the upper and lower surfaces.

- **CLT(ISO)_D3**: 2D isotropic constitutive model, defined considering the outputs of the tensile tests performed along with direction 3, discussed in Chapter 5. The material properties have been defined through a 2D orthotropic constitutive model, appropriately tuned, to keep the kinematics unaltered. It defines the mechanical properties of the side surfaces.

Table 6.7 summarizes the parameters used to tune those two constitutive models. The references for evaluating the safety margins of the structural elements are

Constitutive models					
CLT(ORT)			CLT(ISO)_D3		
E_{11}	3008	MPa	E_{11}	2894	MPa
E_{22}	2876	MPa	E_{22}	2894	MPa
ν_{12}	0.286	-	ν_{12}	0.3	-
G_{12}	1227	MPa	G_{12}	1113	MPa
G_{23}	10^3	GPa	G_{23}	10^3	GPa
G_{31}	10^3	GPa	G_{31}	10^3	GPa

Table 6.7: Mechanical properties for FE constitutive models.

reported in Table 6.8. As a specific failure criterion for FFF components has not yet been developed, this information will help in a first assessment.

Tensile limits			
		prop. limit	ultimate stress
ORT	Dir. 1	$\sigma_{11}^{max} = 56.4$ MPa	$\sigma_{11}^{pro} = 54.0$ MPa
	Dir. 2	$\sigma_{22}^{max} = 46.2$ MPa	$\sigma_{22}^{pro} = 48.0$ MPa
	Dir. 3	$\sigma_{33}^{max} = 13.1$ MPa	$\sigma_{33}^{pro} = 17.5$ MPa
ISO	-	$\sigma_{fil}^{max} = 58.5$ MPa	-

Table 6.8: Tensile strengths in material principal directions.

Results

Figures 6.11-6.12 show the displacement map (see Figure 6.11), and the map of the axial component (Y direction) of the stress tensor (see Figures 6.12a-6.12b), both superimposed on the arm deformed shape. A double plot allows seizing the

last one from both sides. The maps of the two transverse component (X and Z directions) are also shown in Figures 6.13a-6.13b. They play a marginal role as the mechanical response of the arm is bending. The upper surface sustains compressive, while the lower tensile stresses. Both grow from the tip towards the arm root; as expected, the most stressed area is near the joint. A certain discontinuity is present in the interface area between the arm and the support; this discontinuity is different between the lateral and upper/lower surfaces due to the diverse nature of the contact. The anchor point of the motor metal casing farthest from the tip appears to be the most stressed in the analysis. However, this is mainly because the model applied load points towards the X direction, not following the arm bending, hence the rotation of the application region. Table 6.9 discusses the convergence

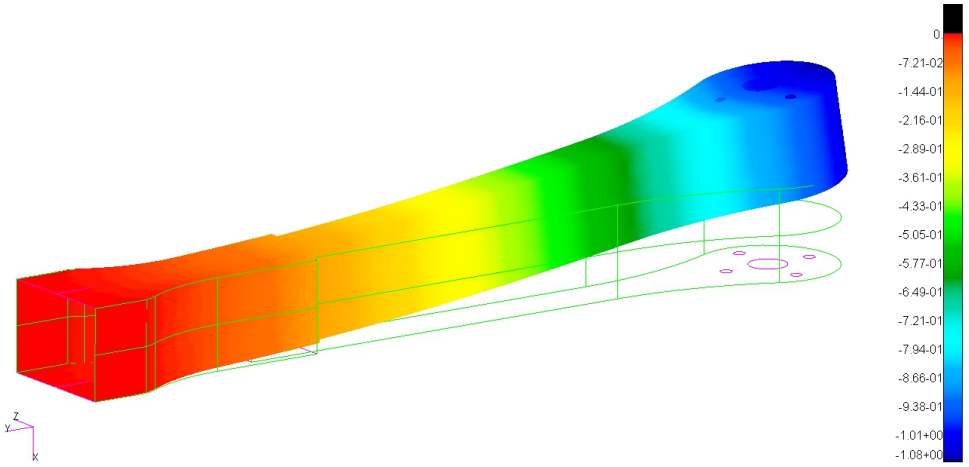

Figure 6.11: Transverse displacement map, superimposed on the arm deformed shape. The results are expressed in mm.

of the result with a gradually finer mesh. The results are expressed as a function of the Global Edge Length (GEL) and in terms of transverse displacement and maximum longitudinal stress. Apart from the initial settling of the results, denser meshes return practically coincident results; below GEL = 2 is assumed. In the material reference system, the extreme values assumed by σ_{11} are 2.08 MPa and -2.08 MPa, and they take place symmetrically over the top and the bottom surfaces of the support. Excluding the curved regions, σ_{11} coincides with σ_{yy} in the structure reference system, as all the filaments have been deposited in the axial direction. Excluding the stress concentration region of the first anchor point of the motor metal casing, the extreme values assumed by σ_{22} are 1.06 MPa and -2.38 MPa. They take place in the bottom contact region between the arm elements and the support and in the engine anchor region. σ_{22} coincides with σ_{zz} in the structure reference system, but only in the upper and lower surfaces; it is not defined for the side surfaces as it is oriented along with the thickness direction of the shell elements. The extreme values assumed by σ_{33} in material reference system are 1.27

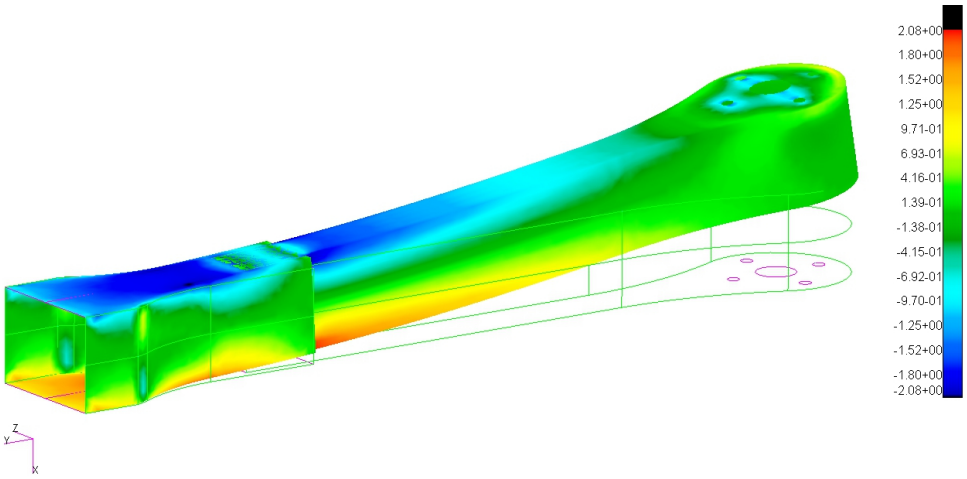

(a) Top view.

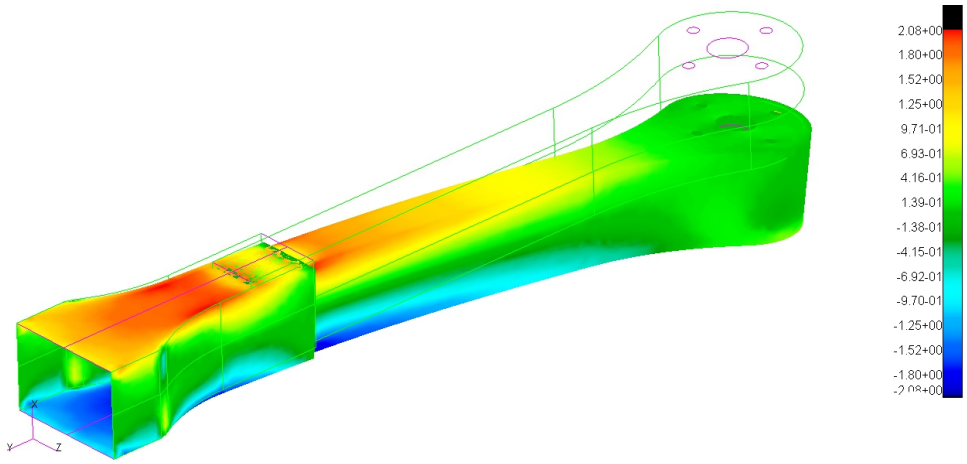

(b) Bottom view.

Figure 6.12: Axial component of the stress tensor map, superimposed on the arm deformed shape. The results are expressed in MPa.

MPa and -0.84 MPa; it defined in the side surfaces only as it is oriented along with the thickness direction of the shell elements elsewhere; there, it coincides with the σ_{zz} in the structure reference system. The ultimate values obtained are minimal, and this should not come as a surprise. The cross-section is large and offers its highest moment of inertia to the axis around which the bending occurs, although the thickness of the individual panels is limited. Despite the limited stresses, further optimization is difficult to achieve for the following reasons:

- the section is hollow to house the avionics and guarantee waterproofing in the event of a water landing,

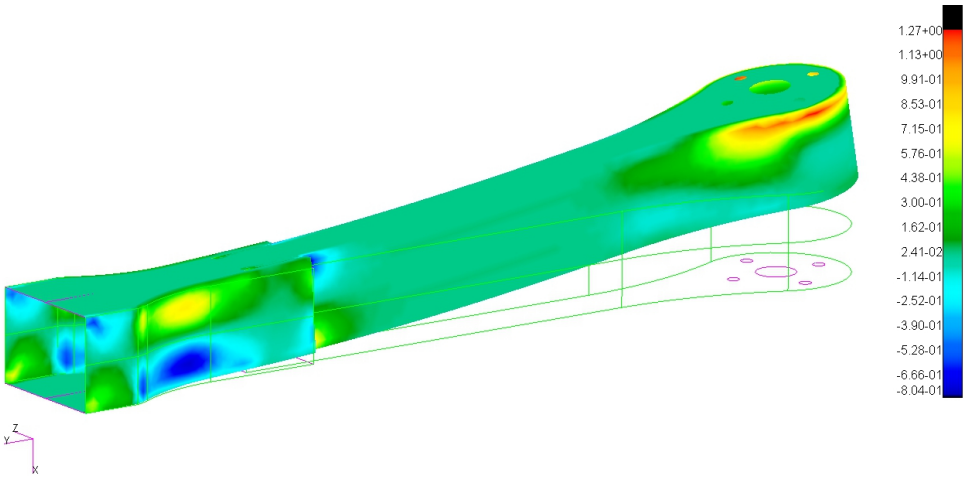

(a) x component.

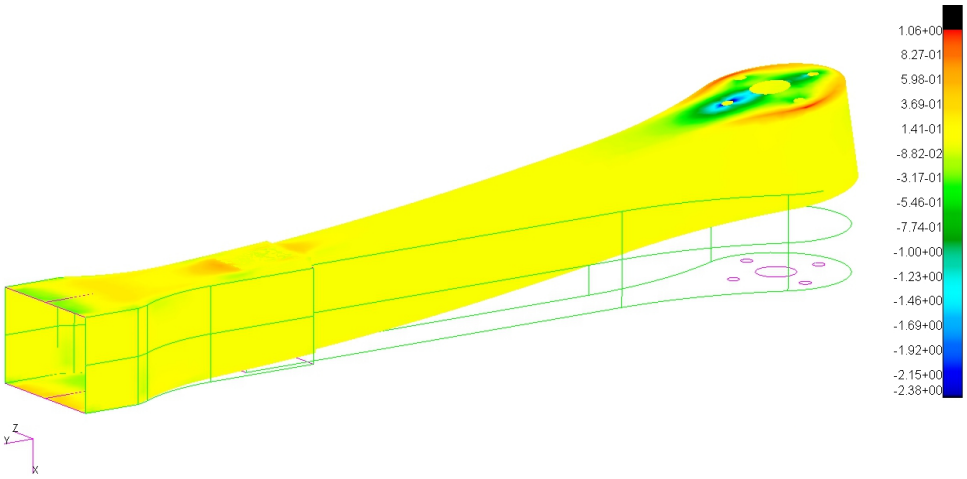

(b) z component.

Figure 6.13: Transverse components of the stress tensor map, superimposed on the arm deformed shape. The results are expressed in MPa.

- a less rigid arm would result in an increased deflection under load; this would shift the direction of application of the thrust,
- a decrease in the wall thickness would limit the impact resistance of the frame.

From a structural point of view, the frame elements analyzed in this chapter can be considered validated because the highest stresses are much lower than those recorded in the experimental campaign. At the moment, this comparison can be carried out component by component, as if they were simple and decoupled stresses. This application example highlights the lack of a failure criterion specifically designed for FFF-application, which would consider the combined action of

GEL [mm]	nodes no.	elements no.	u_{tip} [mm]	σ_y^{max} [MPa]
10	1010	1402	−1.01	1.66
7.5	1255	1712	−1.00	1.87
5	1860	2686	−1.03	1.88
4	2546	3834	−1.06	1.95
3	3825	6036	−1.07	2.03
2	7741	13130	−1.08	2.08

Table 6.9: Mesh convergence.

the different stress components, allowing defining safety margins.

Chapter 7

3D model for hygrothermal stress analysis

This chapter[1] describes an exact layer-wise 3D solution for hygrothermal mechanical analysis of multilayered structures. This reliable solution can be considered as a starting point for a dedicated tool for 3D printing optimization with a view to the mechanical response. The moisture content and temperature effects have been added to a consolidated solution for static and free vibration analysis by exploiting the exponential matrix method to solve the differential equations. The solution is validated against reference methods available in the literature and handles spherical and cylindrical shells as well as plates with a comprehensive formulation. The thermal analysis only is presented, as the hygrometric one follows the same development. In addition, consolidated results for validation are present only in the first case. It also holds for Functionally Graded Materials (FGMs), keeping open the option to consider different optimizations in the thickness direction for 3D-printed components.

7.1 Introduction

The previous chapters have shown that the anisotropic mechanical behavior of FFF printed elements can be traced back to orthotropy under specific circumstances. The validation tests of Chapter 4 shown that the mechanical response is better described by an orthotropic constitutive model than by an isotropic one, although in the preliminary simplifying CLT hypothesis. The Classical Lamination Theory has been introduced to overcome the fact that the mechanical characterization campaign is partial, as it allowed deriving only the 3×3 reduced stiffness

[1]Part of the work described in this chapter has been previously published in [109–114]

matrix. As discussed, two more shear tests and a further tensile test would be necessary to fully define the mechanical behavior. However, this method has been crucial: it made it possible to record a first preliminary confirmation of the approach faster and easier, intending to develop the mechanical characterization fully in the future. Provided that a single layer behaves in an orthotropic way, the stacking sequence with which the various layers are superimposed plays a key role. In other terms, the lamination sequence is a critical parameter in determining the mechanical response of the component by deriving the terminology from composite materials. Chapter 2 discussed that while considering the mechanical characteristics of each layer, CLT loses detail following an Equivalent Single Layer approach and extends Kirchoff classical theory from isotropic applications to laminated structures. A consequence of this simplification is that CLT loses the through-the-thickness detail. This aspect is of extreme importance in the context of FFF, as the experimental results have shown that the anisotropy in terms of tensile and shear strength is very marked. The failure estimation is also a result that cannot be yielded accurately by CLT, and this is coupled with the through-the-thickness detail. The last point is crucial: given a complete characterization campaign, it may be speculated that the anisotropy in terms of strength will be even more pronounced. A partial confirmation comes from the preliminary tensile tests in the direction perpendicular to the building plate carried out during the buckling analysis. They showed how in the third main direction in the material reference system, the polymer behaves differently.

A layer-wise evaluation of the problem is then crucial in this respect. It would also allow to include the effects of thermal and hygrometric loads in the stress analysis. Managing the thermal and hygrometric loads on polymeric components in FFF is also crucial to assess the shift from prototyping to production. Although most polymers are characterized by a low glass transition temperature [115], limiting their applications to non-critical thermal scenarios, the limited strength values can increase the specific importance of thermal effects. A hint comes from the printing defects: very often, the sudden shrinkage of a polymeric component after its forming induces delamination (i.e., the separation of overlapping layers), occurring precisely in the direction featuring the low tensile strength. Recent researches suggested that the thermal expansion coefficient of FFF processed components has the same order of magnitude as virgin PLA even with different infill percentages [116]. How this varies in the material frame of reference has yet to be evaluated. In the detail of the considered material, PLA is also a water-absorbing polymer [117, 118]. This aspect must considered: even the moisture content can induce an additional stress field, as well as a reduction in mechanical performances. It would be very convenient to develop an ad hoc tool harmonizing hygrothermal stress analyses with 3D-printed components. The output could be a tool defining the mechanical response of a FFF component starting from its printing parameters and the feedstock material properties. On the other side, the tool could suggest an

optimized printing strategy according to the thermal, hygrometric, and mechanical loads and the component geometry.

The starting point for this type of tool is a reliable solution for stress analysis. Solving the problem always results in finding the solution of the indefinite equilibrium equations, considering the boundary equilibrium conditions, geometric relations, and compatibility or congruence equations. In analyzing a three-dimensional body, the equations can be solved in a strong or weak form. The weak form solutions handle the differential equations numerically after reducing them to algebraic equations through suitable numerical techniques. However, the weak forms require validation by a strong form solution. The differential equations are solved analytically, defining the values of the unknown functions in each point of the body. The diffusion of weak forms derives from the geometry, and boundary conditions of real application components, challenging and not allowing an analytical solution. This chapter discusses an exact layer-wise 3D tool for hygrothermal-mechanical analysis of multilayered structures. This solution is based on a consolidated model proposed by Brischetto for the free vibration analysis of a wide range of multilayered isotropic and orthotropic primary structural elements [119–121]. The application field of this solution has been then expanded to the static analysis [122, 123], also including Functionally Graded Materials (FGM) in the lamination sequence [124, 125]. The thermal stress analysis and hygroscopic stress analysis have been added to this solution by exploiting some key aspects, including using the exponential matrix method for solving differential equations and the division of the structure into mathematical (i.e., fictitious) layers.

7.1.1 Geometry and reference system definition

Shells are primary structural elements. Consider the middle point of a segment with length h moving on a reference surface Ω_0. If the segment keeps perpendicular to the surface, this motion forms a shell. Two more surfaces lie in a symmetrical position to Ω_0: the upper and the lower surfaces, generated respectively by the segment upper and the lower endpoints (see Figure 7.1). Ω_0 is the locus of the points falling midway between the two external surfaces, and it takes the name of the middle surface. h is the thickness of the shell. The shape of Ω_0 determines the geometry of the shell. If Ω_0 is a flat figure (i.e., a square or a rectangle), it generates a *plate*; if it is a cylindrical surface, it generates a *cylindrical shell* or a *cylinder*; if it is a double-curved surface, it generates a *spherical shell*.

The reference system (α, β, z) is mixed-curvilinear and orthogonal to consider the four geometries in a single formulation. α and β lie on Ω_0, while z is normal to it and heads towards the upper surface; it ranges from $-h/2$ to $h/2$. In certain cases, however, it will be more convenient to use a second thickness coordinate $\tilde{z}$, ranging from 0 at the bottom to h at the top. The reference dimensions of the shell are evaluated over Ω_0 in α and β direction; they are a and b, respectively.

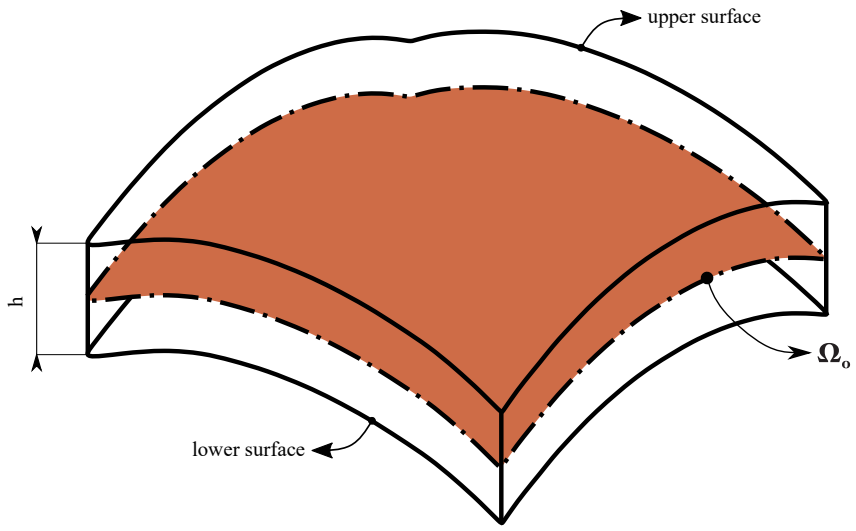

Figure 7.1: Generic definition of a shell, its reference surface and its thickness.

Still, on the middle surface, the shell radii of curvatures R_α and R_β are defined. By recalling the previous description, the *spherical shell* features both finite radii of curvature. This geometry is the more general case of all the others: when the inverse of a single curvature radius is zero, the shell degenerates into a *cylinder* or a *cylindrical shell*; when both the inverse of R_α and R_β are zero, a plate is defined. This single reference system simplifies the discussion because it works indistinctly for all geometries as long as the α and β coordinates follow the geometrical features of Ω_0 (see Figure 7.2). In this single reference system, it is convenient to define a single set of equations describing the problem.

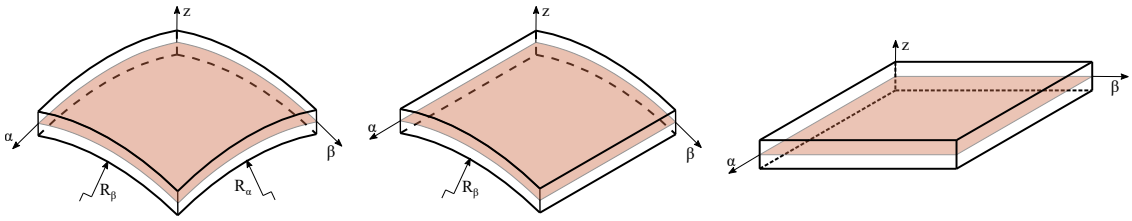

Figure 7.2: Mixed-curvilinear and orthogonal reference system, detailed for a spherical shell, a cylindrical shell, and a plate.

All the equations will consider the curvature(s) using two parametric coefficients. Their introduction simplifies the problem, grouping all the geometry into a single formulation, written for the most general case and able to degenerate to that for simpler geometries. As discussed in [126], with constant curvature radii in both

directions, those coefficients take the following form:

$$H_\alpha = \left(1+\frac{z}{R_\alpha}\right) = \left(1+\frac{\tilde{z}-h/2}{R_\alpha}\right), \quad H_\beta = \left(1+\frac{z}{R_\beta}\right) = \left(1+\frac{\tilde{z}-h/2}{R_\beta}\right), \quad H_z = 1 \tag{7.1}$$

H_α and H_β are two linear functions of the thickness coordinate; their slope decreases as the curvature radii increase. To be thorough, Equations 7.1 include H_z, which equals 1 as z is a rectilinear coordinate. The same occurs for both H_α and H_β when their curvature radii are infinite.

From now on, reference will be made to a generic shell with N physical layer. Index n will be used to label a generic layer; it varies from 1, at the bottom, to N, at the top. For classical isotropic and orthotropic materials, the mechanical, thermal, and hygrometric coefficients depend on the layer and are constant within it. Being a z function, the parametric coefficients H_α and H_β are not constant even inside each $n-th$ layer, except for the case of plates as $R_\alpha = R_\beta = \infty$, thus $H_\alpha = H_\beta = 1$.

7.2 Temperature and moisture content profile

A prerequisite for evaluating thermal and hygrometric stress distribution is knowing the temperature and moisture content distribution across the body. This solution disregards the mutual coupling between stresses and thermal/hygrometric loads and calculates temperature and moisture content separately once the boundary conditions, the materials, and the lamination scheme have been defined. Considering a general coordinate system (u_1, u_2, u_3), the temperature is a function of the space and the time, $T(u_1, u_2, u_3, t)$; its distribution follows the heat equation:

$$\frac{\partial T}{\partial t} - \alpha \nabla^2 T = 0 \tag{7.2}$$

∇^2 is the Laplace operator, α the thermal diffusivity, t the time. The moisture content also is a function of the space and time, $\phi(u_1, u_2, u_3, t)$; its distribution follows the Fick second law of diffusion:

$$\frac{\partial \phi}{\partial t} - D \nabla^2 \phi = 0 \tag{7.3}$$

D is the diffusion coefficient. Equation 7.2 and Equation 7.3 both represent a transport equation: the meaning of the field variable changes, but the mathematical formulation is identical. The solution is also the same: the same algorithm can evaluate both the temperature and the moisture content profile. Since this solution discards the mutual coupling, from now on, the formulation for the thermal analysis only is described for simplicity, warning that the hygrometric one is obtained in the same way.

7.2.1 3D solution to heat conduction problem

Consider a system of curvilinear and orthogonal coordinates (u_1, u_2, u_3); the heat conduction differential equation, in a homogeneous body, under stationary conditions, and excluding the generation of internal energy is $\nabla \boldsymbol{q}(u_1, u_2, u_3) = 0$, where ∇ is the nabla operator. Ozisik [127] specialized the heat flux divergence, re-writing it as

$$\nabla \boldsymbol{q} = \frac{1}{a}\left[\frac{\partial}{\partial u_1}\left(\frac{a}{a_1}q_1\right) + \frac{\partial}{\partial u_2}\left(\frac{a}{a_2}q_2\right) + \frac{\partial}{\partial u_3}\left(\frac{a}{a_3}q_3\right)\right] \tag{7.4}$$

The components of the heat flux in u_i directions have the following expression:

$$q_i = -k_i \frac{1}{a_i}\frac{\partial \theta}{\partial u_i} \tag{7.5}$$

k_i are the thermal conductivity coefficients, a_i the scale factors, and $\theta = T - T_0$ the over-temperature with respect to the reference value T_0. If the radii of curvature in u_i directions are constant, they have the same formulations of the parametric coefficients introduced in Equations 7.1. The product of the tree scale factors is defined as a, for conciseness. Povstenko [128] specialized the heat conduction equation in the mixed-curvilinear and orthogonal reference system (α, β, z), introduced the definition of the heat fluxes (Equation 7.5) and the parametric coefficients (Equation 7.1), leading to the following relation:

$$\frac{1}{H_\alpha H_\beta}\left[\frac{\partial}{\partial \alpha}\left(\frac{H_\alpha H_\beta}{H_\alpha}k_\alpha \frac{1}{H_\alpha}\frac{\partial \theta}{\partial \alpha}\right) + \frac{\partial}{\partial \beta}\left(\frac{H_\alpha H_\beta}{H_\beta}k_\beta \frac{1}{H_\beta}\frac{\partial \theta}{\partial \beta}\right)\right] + \frac{\partial}{\partial z}\left(k_z \frac{\partial \theta}{\partial z}\right) = 0 \tag{7.6}$$

In general, the thermal conductivity coefficients and the scale factors are not constant within a shell; for this reason the differential operators do not enclose the over-temperature θ, only. As anticipated in Section 7.1.1 the former items depend on lamination and might be constant inside each layer if classical isotropic and orthotropic materials are considered. The latter are a function of the thickness coordinate if one or both of the curvature radii are finite. The thermal conductivity coefficients might also be a function of z if Functionally Graded Materials are considered. Specializing Equation 7.6 for each physical layer would be only a partial solution: it would solve the dependence on z for classical material thermal properties only, but it would not help with the parametric coefficients in shell geometries. It wouldn't help for FGM layers anyway.

The problem can be simplified by approximating the linear dependence on z. Each $n-th$ physical layer can be divided into M_n fictitious (mathematical) layers. Given this approach, the shell now features a total number of M mathematical layers, which are given by:

$$M = \sum_{n=1}^{N} M_n \tag{7.7}$$

If each mathematical layer is thin enough (i.e., there are enough fictitious layers), both parametric coefficients can be evaluated in the layer midpoint with an excellent approximation; the same applies to the thermal properties of FGMs. The number of mathematical layers granting the convergence of the results varies from case to case and will be discussed later.

Let m be the mathematical layers index; it ranges from 1 to M. Re-writing Equation 7.6 for each $m-th$ mathematical layer, the coefficients related to the thermal properties are constant, and the parametric coefficients as well; this allows assigning the differential operators to the thermal variable only. The heat conduction differential equations becomes:

$$k_{\alpha}^{*m}\frac{\partial^2\theta}{\partial\alpha^2}+k_{\beta}^{*m}\frac{\partial^2\theta}{\partial\beta^2}+k_{z}^{*m}\frac{\partial^2\theta}{\partial z^2}=0 \tag{7.8}$$

with

$$k_{\alpha}^{*m}=\frac{k_1^m}{H_{\alpha}^2},\qquad k_{\beta}^{*m}=\frac{k_2^m}{H_{\beta}^2},\qquad k_{z}^{*m}=k_{z}^{m} \tag{7.9}$$

A closed solution is possible, assuming that temperature field has an harmonic form over Ω_0; this assumption is made in analogy to the displacement field, that will be discussed hereinafter.

$$\theta^m(\alpha,\beta,z)=\Theta^m(z)sin(\bar{\alpha}\alpha)sin(\bar{\beta}\beta) \tag{7.10}$$

Equation 7.10 introduces a further assumption: it decouples the dependence from the thickness coordinate and the surface coordinates. In each layer m, $\Theta^m(z)$ defines the temperature amplitude, and it is a function of the thickness coordinate only. The two trigonometric functions introduce two more coefficients, $\bar{\alpha}=\frac{p\pi}{a}$ and $\bar{\beta}=\frac{q\pi}{b}$, which consider the half-wave numbers p and q in α and β direction, respectively, and the mid-surface dimensions. The harmonic form of the temperature field satisfies Equation 7.8. However, it is necessary to identify an appropriate function $\Theta^m(z)$ of the thickness coordinate. An attempt function is:

$$\Theta^m(z)=\Theta_0^m exp(s^m z) \tag{7.11}$$

Θ_0^m and s^m depend on the mathematical layer. s^m is easily calculated introducing Equations 7.10-7.11 into Equation 7.8:

$$-k_{\alpha}^{m*}\bar{\alpha}^2-k_{\beta}^{m*}\bar{\beta}^2+k_{z}^{m*}s^{m2}=0 \tag{7.12}$$

from which it results:

$$s_{1/2}^{m*}=\pm\sqrt{\frac{k_{\alpha}^{m*}\bar{\alpha}^2+k_{\beta}^{m*}\bar{\beta}^2}{k_{z}^{m*}}} \tag{7.13}$$

Another form of the solution in the thickness direction, Equation 7.11, considering s_1^{m*} is:

$$\Theta^m(z) = C_1^m cosh(s_1^m \times z) + C_2^m sinh(s_1^m \times z) \tag{7.14}$$

Again, such a solution holds within a mathematical layer. Consequently, two coefficients (C_1^m, C_2^m) have to be quantified for each fictitious $m-th$ layer, which leads to an overall number of $2 \times M$ unknowns. The problem, however, is well-posed: at each interface, two continuity equations hold; both the temperature and the heat flux in z direction must be continuous:

$$\Theta_b^{m+1} = \Theta_t^m \tag{7.15}$$

$$k_z^{m+1*}\Theta_{,zb}^{m+1} = k_z^{m*}\Theta_{,zt}^m \tag{7.16}$$

m designates a generic mathematical layer, sharing an interface with the next one. b and t identify the bottom and the top of the layer and subscript $_{,z}$ expresses the partial derivative $\frac{\partial}{\partial z}$. The meaning of Equations 7.15-7.16 is trivial: the temperature at the bottom of the $m+1-th$ layer coincides with that at the top of the $m-th$; the thermal flow at the top of the $m-th$ layer coincides with that at the bottom of the $m+1-th$. Through Equation 7.14, the two conditions take the following expressions:

$$C_1^{m+1}cosh(s^{m+1}z_b^{m+1}) + C_2^{m+1}sinh(s^{m+1}z_b^{m+1}) = C_1^m cosh(s^m z_t^m) + C_2^m sinh(s^m z_t^m) \tag{7.17}$$

$$\begin{aligned} &m_z^{m+1}s_1^{m+1}C_1^{m+1}sinh(s^{m+1}z_b^{m+1}) + m_z^{m+1}s_1^{m+1}C_2^{m+1}cosh(s^{m+1}z_b^{m+1}) = \\ =&m_z^m s_1^m C_1^m sinh(s^m z_t^m) + m_z^m s_1^m C_2^m cosh(s^m z_t^m) \end{aligned} \tag{7.18}$$

z_b^{m+1} is the z coordinate of the bottom of the $m+1-th$ layer; z_t^m the top of the $m-th$ layer. It is useful to compact both the expression by replacing the terms that multiply the unknowns with four transfer coefficients. This allows expressing the coefficients C_i with $i = 1, 2$ of a layer to the those of the previous:

$$\begin{bmatrix} C_1 \\ C_2 \end{bmatrix}^{m+1} = \begin{bmatrix} T_{\Theta 1}^{m+1,m} & T_{\Theta 2}^{m+1,m} \\ T_{\Theta 3}^{m+1,m} & T_{\Theta 4}^{m+1,m} \end{bmatrix} \begin{bmatrix} C_1 \\ C_2 \end{bmatrix}^m \tag{7.19}$$

The four coefficients of the transfer matrices take the following form:

$$T_{\Theta 1}^{m+1,m} = \frac{\left(\frac{k_z^m s_1^m sinh(s^m z_t^m)}{k_z^{m+1} s_1^{m+1} cosh(s^{m+1} z_b^{m+1})} - \frac{cosh(s^m z_t^m)}{sinh(s^{m+1} z_b^{m+1})}\right)}{\left(\frac{k_z^{m+1} s_1^{m+1} sinh(s^{m+1} z_b^{m+1})}{k_z^{m+1} s_1^{m+1} cosh(s^{m+1} z_b^{m+1})} - \frac{cosh(s^{m+1} z_b^{m+1})}{sinh(s^{m+1} z_b^{m+1})}\right)} \tag{7.20}$$

$$T_{\Theta 2}^{m+1,m} = \frac{\left(\frac{k_z^m s_1^m cosh(s^m z_t^m)}{k_z^{m+1} s_1^{m+1} cosh(s^{m+1} z_b^{m+1})} - \frac{sinh(s^m z_t^m)}{sinh(s^{m+1} z_b^{m+1})}\right)}{\left(\frac{k_z^{m+1} s_1^{m+1} sinh(s^{m+1} z_b^{m+1})}{k_z^{m+1} s_1^{m+1} cosh(s^{m+1} z_b^{m+1})} - \frac{cosh(s^{m+1} z_b^{m+1})}{sinh(s^{m+1} z_b^{m+1})}\right)} \tag{7.21}$$

$$T_{\Theta 3}^{m+1,m} = \frac{\left(\frac{k_z^m s_1^m sinh(s^m z_t^m)}{k_z^{m+1} s_1^{m+1} sinh(s^{m+1} z_b^{m+1})} - \frac{cosh(s_m z_t^m)}{cosh(s^{m+1} z_b^{m+1})}\right)}{\left(\frac{k_z^{m+1} s_1^{m+1} cosh(s^{m+1} z_b^{m+1})}{k_z^{m+1} s_1^{m+1} sinh(s^{m+1} z_b^{m+1})} - \frac{sinh(s^{m+1} z_b^{m+1})}{cosh(s^{m+1} z_b^{m+1})}\right)} \tag{7.22}$$

$$T_{\Theta 4}^{m+1,m} = \frac{\left(\frac{k_z^m s_1^m cosh(s_m z_t^m)}{k_z^{m+1} s_1^{m+1} sinh(s^{m+1} z_b^{m+1})} - \frac{sinh(s^m z_t^m)}{cosh(s^{m+1} z_b^{m+1})}\right)}{\left(\frac{k_z^{m+1} s_1^{m+1} cosh(s^{m+1} z_b^{m+1})}{k_z^{m+1} s_1^{m+1} sinh(s^{m+1} z_b^{m+1})} - \frac{sinh(s^{m+1} z_b^{m+1})}{cosh(s^{m+1} z_b^{m+1})}\right)} \tag{7.23}$$

By labelling $[T_\Theta]^{(m+1,m)}$ the transfer matrix in Equation 7.19, the coefficients of the bottom ($m = 1$) and the top ($m = M$) layer can be related recursively using Equation 7.19:

$$\begin{bmatrix} C_1 \\ C_2 \end{bmatrix}^M = \left[T_\Theta\right]^{(M,M-1)} \left[T_\Theta\right]^{(M-1,M-2)} ..... \left[T_\Theta\right]^{(3,2)} \left[T_\Theta\right]^{(2,1)} \begin{bmatrix} C_1 \\ C_2 \end{bmatrix}^1 = \left[T_\Theta\right]^{(M,1)} \begin{bmatrix} C_1 \\ C_2 \end{bmatrix}^1 \tag{7.24}$$

Two equations in two variables are the basis of the system of Equation 7.24. The coefficients of both the top and the bottom layer can be calculated, adding to them the boundary conditions of the problem:

$$\begin{aligned} C_1^M &= T_{\Theta 1}^{M,1} C_1^1 + T_{\Theta 2}^{M,1} C_2^1 \\ C_2^M &= T_{\Theta 3}^{M,1} C_1^1 + T_{\Theta 4}^{M,1} C_2^1 \\ \Theta(z=0) &= C_1^1 cosh(s_1 \times 0) + C_2 sinh(s_1 \times 0) = C_1^1 \\ \Theta(z=h) &= C_1^M cosh(s_1 \times h) + C_2^M sinh(s_1 \times h) \end{aligned} \tag{7.25}$$

With the first layer coefficients, Equation 7.19 allows calculating all the remaining values subsequently, and the temperature profile is then determined. In the following, reference will be made to Θ_{3D} when considering this thermal profile.

7.2.2 1D solution to heat conduction problem

The evaluation of the thermal profile can be simplified when the thickness ratio is high enough. In a three-dimensional problem, all the three heat fluxes defined in Equation 7.5 are considered in the heat flux divergence, Equation 7.4. However, when the in-surface dimensions a and b are high if compared to h, the relative weight of the heat fluxes in directions α and β decreases. With the same assumptions of an homogeneous body under stationary conditions, the heat conduction differential equation can be simplified to:

$$\frac{\partial}{\partial z}\left(k_3^* \frac{\partial \Theta}{\partial z}\right) = 0 \tag{7.26}$$

This condition has a wide range of applications as the thermal properties of the structure are inside the brackets; their variations along the thickness direction are considered, either for a non transversely isotropic lamination, or for the use of FGM. The brackets enclose the thermal flux in z; as its derivative to the thickness direction is 0, it is constant along with it. If the heat flux is constant throughout the whole thickness of the shell, it is constant in each mathematical layer. In each fictitious layer, the coefficient of thermal conductivity is constant even for FGMs: consequently, the temperature is linear within each layer.

$$q_z^m = -k_z^m \frac{d\Theta^m}{dz} = -\frac{k^m}{h^m}(\Theta_t^m - \Theta_b^m) = constant \tag{7.27}$$

Θ_t^m and Θ_b^m stand for the top and the bottom temperature of the $m-th$ layer. The term $\frac{k^m}{h^m}$ is the thermal conductance of the $m-th$ layer; the inverse is its thermal resistance R^m. In analogy with thermal resistances, across each layer there is a $\Delta\Theta$, just as there is an electric potential gap across an electrical resistance. The overall thermal resistance coefficient can be calculated in the same way the overall electrical resistance is, in series resistance:

$$R_{eq} = \sum_{m=1}^{M} \frac{h^m}{k_z^m} \tag{7.28}$$

R_{eq} defines the equivalent thermal properties of the shell in the thickness direction as that of an equivalent single-layer. It allows calculating the heat flux along z from the temperature gap between the top and the bottom.

$$q_z = \frac{1}{R_{eq}}(\Theta_t - \Theta_b) \tag{7.29}$$

The boundary conditions define the heat flux along with the thickness direction, together with the thermal properties and the thicknesses of the layers. Since the heat flux keeps constant within each layer, and the thermal properties and thicknesses of each layer are known, it is possible to calculate the temperature at any

coordinate z backing up from one of the two external surfaces. The temperature profile is always kept linear within each layer, but its slope varies according to its thermal resistance to ensure a constant thermal flow. In the following, reference will be made to Θ_{1D} when considering this thermal profile.

The linear profile

A further simplification considers the temperature profile as linear throughout the shell thickness. It is an extreme simplification since it does not consider how the thickness acts in the physics of the problem, nor the different possible thicknesses and thermal properties in the stacking sequence. It provides good results only when a transversally isotropic thin plate is considered. In the following, reference will be made to Θ_l when considering this thermal profile.

7.3 Three-dimensional equilibrium equations for static analysis

Consider a shell with a generic stacking sequence, with N physical layers. The following differential equilibrium equations define the static problem in each $n-th$ layer:

$$H_\beta \frac{\partial \sigma^n_{\alpha\alpha}}{\partial \alpha} + H_\alpha \frac{\partial \sigma^n_{\alpha\beta}}{\partial \beta} + H_\alpha H_\beta \frac{\partial \sigma^n_{\alpha z}}{\partial z} + \left(\frac{2H_\beta}{R_\alpha} + \frac{H_\alpha}{R_\beta}\right)\sigma^n_{\alpha z} = 0, \tag{7.30}$$

$$H_\beta \frac{\partial \sigma^n_{\alpha\beta}}{\partial \alpha} + H_\alpha \frac{\partial \sigma^n_{\beta\beta}}{\partial \beta} + H_\alpha H_\beta \frac{\partial \sigma^n_{\beta z}}{\partial z} + \left(\frac{2H_\alpha}{R_\beta} + \frac{H_\beta}{R_\alpha}\right)\sigma^n_{\beta z} = 0, \tag{7.31}$$

$$H_\beta \frac{\partial \sigma^n_{\alpha z}}{\partial \alpha} + H_\alpha \frac{\partial \sigma^n_{\beta z}}{\partial \beta} + H_\alpha H_\beta \frac{\partial \sigma^n_{zz}}{\partial z} - \frac{H_\beta}{R_\alpha}\sigma^n_{\alpha\alpha} - \frac{H_\alpha}{R_\beta}\sigma^n_{\beta\beta} + \left(\frac{H_\beta}{R_\alpha} + \frac{H_\alpha}{R_\beta}\right)\sigma^n_{zz} = 0 \tag{7.32}$$

($\sigma^n_{\alpha\alpha}$, $\sigma^n_{\beta\beta}$, σ^n_{zz}, $\sigma^n_{\beta z}$, $\sigma^n_{\alpha z}$, $\sigma^n_{\alpha\beta}$) are the six stress components. Equations 7.30-7.32 cover all the geometries so far described; no assumptions has been made on the curvature radii exception made for what discussed when defining H_α and H_β: R_α and R_β are both constant. If a curvature radius equals infinite, Equations 7.30-7.32 automatically adapt to cylindrical shells and cylinders; with both the radii equal infinite, they adapt to plates.

7.3.1 The displacement, load and temperature fields

The present solution relies on a displacement-form; to this end, the constitutive equations and the geometrical relations will be defined and then introduced into Equations 7.30-7.32 to re-write them. A closed solution will be possible; however,

it is necessary to assume that the displacement field takes a bi-harmonic form in α and β directions.

$$u^n(\alpha,\beta,z) = U^n(z)cos(\bar{\alpha}\alpha)sin(\bar{\beta}\beta) \tag{7.33}$$
$$v^n(\alpha,\beta,z) = V^n(z)sin(\bar{\alpha}\alpha)cos(\bar{\beta}\beta) \tag{7.34}$$
$$w^n(\alpha,\beta,z) = W^n(z)sin(\bar{\alpha}\alpha)sin(\bar{\beta}\beta) \tag{7.35}$$

As for the temperature field, Equations 7.33-7.35 decouple the dependence from the thickness coordinate and the surface coordinates. In each layer n, $U^n(z)$, $V^n(z)$ and $W^n(z)$ define the displacements amplitude in α, β and z directions, respectively, and they are a function of the thickness coordinate only. Coefficients $\bar{\alpha}$ and $\bar{\beta}$ have been already discussed. A side effect of Equations 7.33-7.35 are the kinematic boundary conditions; the shells are simply supported, that is:

$$w = v = 0, \qquad \text{for} \quad \alpha = 0, a \tag{7.36}$$
$$w = u = 0, \qquad \text{for} \quad \beta = 0, b \tag{7.37}$$

This solution handles mechanical loads applied on the top and the bottom external surfaces only. A closed solution will be possible if they, too, have a harmonic form in α and β directions:

$$p_{\alpha t}(\alpha,\beta) = P_{\alpha t}cos(\bar{\alpha}\alpha)sin(\bar{\beta}\beta) \tag{7.38}$$
$$p_{\beta t}(\alpha,\beta) = P_{\beta t}sin(\bar{\alpha}\alpha)cos(\bar{\beta}\beta) \tag{7.39}$$
$$p_{zt}(\alpha,\beta) = P_{zt}sin(\bar{\alpha}\alpha)sin(\bar{\beta}\beta) \tag{7.40}$$
$$p_{\alpha b}(\alpha,\beta) = P_{\alpha b}cos(\bar{\alpha}\alpha)sin(\bar{\beta}\beta) \tag{7.41}$$
$$p_{\beta b}(\alpha,\beta) = P_{\beta b}sin(\bar{\alpha}\alpha)cos(\bar{\beta}\beta) \tag{7.42}$$
$$p_{zb}(\alpha,\beta) = P_{zb}sin(\bar{\alpha}\alpha)sin(\bar{\beta}\beta) \tag{7.43}$$

In Equations 7.38-7.43, the first subscript indicates the load application direction, the second the surface on which it acts. E.g., $P_{\beta t}$ is applied on the top surface, and it acts along the β direction. The analytical expression of the equations is analogous to that introduced for displacements. There is no dependence on the coordinate thickness as the load amplitudes have a defined value on the two surfaces.

This solution also handles thermal and hygroscopic loads, which are body/field loads. They induce a mechanical response when they differ from the reference conditions. The amplitude of both the fields can be imposed on the bottom and top external surfaces. In the most general case, their field keeps as a function of the thickness coordinate as the top and bottom amplitudes might differ.

7.3.2 Equilibrium equations in terms of displacements

This section introduces the constitutive equations, which express the stresses in terms of strains, and the geometrical relationships, which relate the strains to

displacement derivatives. Together, they allow to re-write Equations 7.30-7.32 in displacement form.

The linear elastic constitutive equations give the connection between the six stress components and the six strain components. The closed-form solution of Equations 7.30-7.32 can be found when considering isotropic or orthotropic materials only; the latter with an orthotropic angle equal to 0° or 90° in the structure reference system. The last requirement implies an alignment between the material and the structure reference system. Under this assumption, the relation between the stress and the strain components already discussed in Chapter 2 holds; in a mixed-curvilinear and orthogonal reference system, it reads:

$$\begin{bmatrix} \sigma^n_{\alpha\alpha} \\ \sigma^n_{\beta\beta} \\ \sigma^n_{zz} \\ \sigma^n_{\beta z} \\ \sigma^n_{\alpha z} \\ \sigma^n_{\alpha\beta} \end{bmatrix} = \begin{bmatrix} C^n_{11} & C^n_{12} & C^n_{13} & 0 & 0 & 0 \\ C^n_{12} & C^n_{22} & C^n_{23} & 0 & 0 & 0 \\ C^n_{13} & C^n_{23} & C^n_{33} & 0 & 0 & 0 \\ 0 & 0 & 0 & C^n_{44} & 0 & 0 \\ 0 & 0 & 0 & 0 & C^n_{55} & 0 \\ 0 & 0 & 0 & 0 & 0 & C^n_{66} \end{bmatrix} \begin{bmatrix} \epsilon^n_{\alpha\alpha} \\ \epsilon^n_{\beta\beta} \\ \epsilon^n_{zz} \\ \gamma^n_{\beta z} \\ \gamma^n_{\alpha z} \\ \gamma^n_{\alpha\beta} \end{bmatrix} \tag{7.44}$$

The geometrical relationships have a more complex expression than Equations 2.3 due to curvature. Furthermore, they not only relate the six strain components ($\epsilon^n_{\alpha\alpha}$, $\epsilon^n_{\beta\beta}$, ϵ^n_{zz}, $\gamma^n_{\beta z}$, $\gamma^n_{\alpha z}$, $\gamma^n_{\alpha\beta}$) and the three displacement components u^n, v^n and w^n (in α, β, z direction, respectively). They also relate the normal strains to the thermal field. If the radii of curvature are constant, they take the following simplified expression:

$$\epsilon^n_{\alpha\alpha} = \frac{1}{H_\alpha}\frac{\partial u^n}{\partial \alpha} + \frac{w^n}{H_\alpha R_\alpha} - \alpha^n_\alpha \theta^n \tag{7.45}$$

$$\epsilon^n_{\beta\beta} = \frac{1}{H_\beta}\frac{\partial v^n}{\partial \beta} + \frac{w^n}{H_\beta R_\beta} - \alpha^n_\beta \theta^n \tag{7.46}$$

$$\epsilon^n_{zz} = \frac{\partial w^n}{\partial z} - \alpha^n_z \theta^n \tag{7.47}$$

$$\gamma^n_{\beta z} = \frac{1}{H_\beta}\frac{\partial w^n}{\partial \beta} + \frac{\partial v^n}{\partial z} - \frac{v^n}{H_\beta R_\beta} \tag{7.48}$$

$$\gamma^n_{\alpha z} = \frac{1}{H_\alpha}\frac{\partial w^n}{\partial \alpha} + \frac{\partial u^n}{\partial z} - \frac{u^n}{H_\alpha R_\alpha} \tag{7.49}$$

$$\gamma^n_{\alpha\beta} = \frac{1}{H_\alpha}\frac{\partial v^n}{\partial \alpha} + \frac{1}{H_\beta}\frac{\partial u^n}{\partial \beta} \tag{7.50}$$

α^n_α, α^n_β and α^n_z are the thermal expansion coefficients of the $n-th$ layer in α, β, z directions, respectively. Equations 7.45-7.50 cover a wide application field. Furthermore, when no thermal field acts, they degenerate into static and dynamic mechanical analysis relations.

Introducing the geometrical relationships into the constitutive equations lead to an explicit link between stress and displacement components, temperature, and moisture content fields.

$$\sigma^n_{\alpha\alpha} = \frac{C^n_{11}}{H_\alpha} u^n_{,\alpha} + \frac{C^n_{11}}{H_\alpha R_\alpha} w^n + \frac{C^n_{12}}{H_\beta} v^n_{,\beta} + \frac{C^n_{12}}{H_\beta R_\beta} w^n + C^n_{13} w^n_{,z} - \lambda^n_\alpha \theta^n \ , \tag{7.51}$$

$$\sigma^n_{\beta\beta} = \frac{C^n_{12}}{H_\alpha} u^n_{,\alpha} + \frac{C^n_{12}}{H_\alpha R_\alpha} w^n + \frac{C^n_{22}}{H_\beta} v^n_{,\beta} + \frac{C^n_{22}}{H_\beta R_\beta} w^n + C^n_{23} w^n_{,z} - \lambda^n_\beta \theta^n \tag{7.52}$$

$$\sigma^n_{zz} = \frac{C^n_{13}}{H_\alpha} u^n_{,\alpha} + \frac{C^n_{13}}{H_\alpha R_\alpha} w^n + \frac{C^n_{23}}{H_\beta} v^n_{,\beta} + \frac{C^n_{23}}{H_\beta R_\beta} w^n + C^n_{33} w^n_{,z} - \lambda^n_z \theta^n \tag{7.53}$$

$$\sigma^n_{\beta z} = \frac{C^n_{44}}{H_\beta} w^n_{,\beta} + C^n_{44} v^n_{,z} - \frac{C^n_{44}}{H_\beta R_\beta} v^n \tag{7.54}$$

$$\sigma^n_{\alpha z} = \frac{C^n_{55}}{H_\alpha} w^n_{,\alpha} + C^n_{55} u^n_{,z} - \frac{C^n_{55}}{H_\alpha R_\alpha} u^n \tag{7.55}$$

$$\sigma^n_{\alpha\beta} = \frac{C^n_{66}}{H_\alpha} v^n_{,\alpha} + \frac{C^n_{66}}{H_\beta} u^n_{,\beta} \tag{7.56}$$

Subscripts $_{,\alpha}$, $_{,\beta}$ and $_{,z}$ express the partial derivatives $\frac{\partial}{\partial\alpha}$, $\frac{\partial}{\partial\beta}$ and $\frac{\partial}{\partial z}$. They are introduced to compact the equations at this point; however, this notation applies to the rest of the discussion. λ^n_α, λ^n_β, and λ^n_z combine the elastic constants with the thermal expansion coefficients:

$$\lambda^n_\alpha = C^n_{11}\alpha^n_\alpha + C^n_{12}\alpha^n_\beta + C^n_{13}\alpha^n_z \tag{7.57}$$

$$\lambda^n_\beta = C^n_{12}\alpha^n_\alpha + C^n_{22}\alpha^n_\beta + C^n_{23}\alpha^n_z \tag{7.58}$$

$$\lambda^n_z = C^n_{13}\alpha^n_\alpha + C^n_{23}\alpha^n_\beta + C^n_{33}\alpha^n_z \tag{7.59}$$

The constitutive equations in displacement form may be now introduced into the equilibrium equations. However, a further simplification comes if the harmonic form of displacements, temperature, and moisture content are introduced. These steps allow writing Equations 7.30-7.32 in terms of the amplitudes of displacement and temperature, and their appropriate derivatives in the z direction. The differential equations of equilibrium are now a function of the thickness coordinate only. For a

generic $n-th$ layer, they take the form:

$$
\begin{aligned}
&(-\frac{C_{55}^n H_\beta}{H_\alpha R_\alpha^2} - \frac{C_{55}^n}{R_\alpha R_\beta} - \bar{\alpha}^2 \frac{C_{11}^n H_\beta}{H_\alpha} - \bar{\beta}^2 \frac{C_{66}^n H_\alpha}{H_\beta}) U^n + (-\bar{\alpha}\bar{\beta} C_{12}^n - \bar{\alpha}\bar{\beta} C_{66}^n) V^n + \\
&+ (\bar{\alpha}\frac{C_{11}^n H_\beta}{H_\alpha R_\alpha} + \bar{\alpha}\frac{C_{12}^n}{R_\beta} + \bar{\alpha}\frac{C_{55}^n H_\beta}{H_\alpha R_\alpha} + \bar{\alpha}\frac{C_{55}^n}{R_\beta}) W^n + (\frac{C_{55}^n H_\beta}{R_\alpha} + \frac{C_{55}^n H_\alpha}{R_\beta}) U_{,z}^n + \\
&+ (\bar{\alpha} C_{13}^n H_\beta + \bar{\alpha} C_{55}^n H_\beta) W_{,z}^n + (C_{55}^n H_\alpha H_\beta) U_{,zz}^n - \bar{\alpha} H_\beta \lambda_\alpha \Theta^n = 0
\end{aligned}
\tag{7.60}
$$

$$
\begin{aligned}
&(-\bar{\alpha}\bar{\beta} C_{66}^n - \bar{\alpha}\bar{\beta} C_{12}^n) U^n + (-\frac{C_{44}^n H_\alpha}{H_\beta R_\beta^2} - \frac{C_{44}^n}{R_\alpha R_\beta} - \bar{\alpha}^2 \frac{C_{66}^n H_\beta}{H_\alpha} - \bar{\beta}^2 \frac{C_{22}^n H_\alpha}{H_\beta}) V^n + \\
&+ (\bar{\beta}\frac{C_{44}^n H_\alpha}{H_\beta R_\beta} + \bar{\beta}\frac{C_{44}^n}{R_\alpha} + \bar{\beta}\frac{C_{22}^n H_\alpha}{H_\beta R_\beta} + \bar{\beta}\frac{C_{12}^n}{R_\alpha}) W^n + (\frac{C_{44}^n H_\alpha}{R_\beta} + \frac{C_{44}^n H_\beta}{R_\alpha}) V_{,z}^n + \\
&+ (\bar{\beta} C_{44}^n H_\alpha + \bar{\beta} C_{23}^n H_\alpha) W_{,z}^n + (C_{44}^n H_\alpha H_\beta) V_{,zz}^n - \bar{\beta} H_\alpha \lambda_\beta \Theta^n = 0
\end{aligned}
\tag{7.61}
$$

$$
\begin{aligned}
&(\bar{\alpha}\frac{C_{55}^n H_\beta}{H_\alpha R_\alpha} - \bar{\alpha}\frac{C_{13}^n}{R_\beta} + \bar{\alpha}\frac{C_{11}^n H_\beta}{H_\alpha R_\alpha} + \bar{\alpha}\frac{C_{12}^n}{R_\beta}) U^n + (\bar{\beta}\frac{C_{44}^n H_\alpha}{H_\beta R_\beta} - \bar{\beta}\frac{C_{23}^n}{R_\alpha} + \bar{\beta}\frac{C_{22}^n H_\alpha}{H_\beta R_\beta} + \bar{\beta}\frac{C_{12}^n}{R_\alpha}) V^n + \\
&+ (\frac{C_{13}^n}{R_\alpha R_\beta} + \frac{C_{23}^n}{R_\alpha R_\beta} - \frac{C_{11}^n H_\beta}{H_\alpha R_\alpha^2} - \frac{2C_{12}^n}{R_\alpha R_\beta} - \frac{C_{22}^n H_\alpha}{H_\beta R_\beta^2} - \bar{\alpha}^2 \frac{C_{55}^n H_\beta}{H_\alpha} - \bar{\beta}^2 \frac{C_{44}^n H_\alpha}{H_\beta}) W^n + \\
&+ (-\bar{\alpha} C_{55}^n H_\beta - \bar{\alpha} C_{13}^n H_\beta) U_{,z}^n + (-\bar{\beta} C_{44}^n H_\alpha - \bar{\beta} C_{23}^n H_\alpha) V_{,z}^n + (\frac{C_{33}^n H_\beta}{R_\alpha} + \frac{C_{33}^n H_\alpha}{R_\beta}) W_{,z}^n + \\
&+ (C_{33}^n H_\alpha H_\beta) W_{,zz}^n + (\frac{H_\beta}{R_\alpha}(\lambda_\alpha - \lambda_z) + \frac{H_\alpha}{R_\beta}(\lambda_\beta - \lambda_z)) \Theta^n - H_\alpha H_\beta \lambda_z \Theta_{,z}^n = 0\,.
\end{aligned}
\tag{7.62}
$$

Mechanical and thermal coefficients feature the superscript n: they depend on the layer and, for classical isotropic and orthotropic materials, are constant within it. Despite this, the coefficients multiplying displacements and temperature amplitudes (and their derivatives in z) are not constant even inside each layer due to the parametric coefficients H_α and H_β, which are a z function. As already discussed for the temperature profile, the problem can be simplified by approximating the linear dependence on z, dividing each $n-th$ physical layer into M_n fictitious (mathematical) layers. This foresight allows dealing with a set of three differential equations per mathematical layer with constant coefficients. This approach is employed from this point onwards; therefore, in all equations, the index n (physical layer) is replaced by the index m (mathematical layer), ranging from 1 to M. The number of mathematical layers granting the convergence of the results varies from case to case and will be discussed later.

The mathematical layers in FGM problems

The subdivision of physical layers into mathematical layers is also useful for a particular set of problems. Up to this point, the formulation has taken into account classical isotropic and orthotropic materials. However, suppose one or more layers

is made up of a Functionally Graded Material (FGM): even the mechanical and thermal coefficients of Equations 7.60-7.62 are a function of z. The same reasoning discussed for the parametric coefficients holds here: if each mathematical layer is thin enough (i.e., there are enough fictitious layers), the mechanical and thermal coefficients can be evaluated in the layer midpoint with an excellent approximation.

7.4 Solution of 3D equilibrium equations

Established that the coefficients of the Equations 7.60-7.62 are constant in each mathematical layer, the notation can be simplified by labeling each block in parentheses with a coefficient name. A_s^m (s ranging from 1 to 19) are those multiplying displacements, and their derivatives; J_s^m (s ranging from 1 to 4) the temperature and its derivatives:

$$A_1^m U^m + A_2^m V^m + A_3^m W^m + A_4^m U_{,z}^m + A_5^m W_{,z}^m + A_6^m U_{,zz}^m + J_1^m \Theta^m = 0 \tag{7.63}$$

$$A_7^m U^m + A_8^m V^m + A_9^m W^m + A_{10}^m V_{,z}^m + A_{11}^m W_{,z}^m + A_{12}^m V_{,zz}^m + J_2^m \Theta^m = 0 \tag{7.64}$$

$$A_{13}^m U^m + A_{14}^m V^m + A_{15}^m W^m + A_{16}^m U_{,z}^m + A_{17}^m V_{,z}^m + A_{18}^m W_{,z}^m + A_{19}^m W_{,zz}^m + \\ + J_4^m \Theta^m + J_3^m \Theta_{,z}^m = 0 \tag{7.65}$$

Equations 7.63-7.65 are a system of second-order differential equations in the displacement amplitude U^m, V^m, and W^m. However, they also contain the temperature and its derivative to z. The temperature is a continuous function of the thickness coordinate, and its profile across z has already been calculated. The addition of three displacement identities allows handling the differential order; applying this methodology, and compacting the formulation using matrices, Equations 7.63-7.65 become:

$$\begin{bmatrix} A_6 & 0 & 0 & 0 & 0 & 0 \\ 0 & A_{12} & 0 & 0 & 0 & 0 \\ 0 & 0 & A_{19} & 0 & 0 & 0 \\ 0 & 0 & 0 & 0 & 0 & 0 \\ 0 & 0 & 0 & 0 & 0 & 0 \\ 0 & 0 & 0 & 0 & 0 & 0 \end{bmatrix}^m \begin{bmatrix} U \\ V \\ W \\ U' \\ V' \\ W' \end{bmatrix}^{'m} = \\ \begin{bmatrix} 0 & 0 & 0 & A_6 & 0 & 0 \\ 0 & 0 & 0 & 0 & A_{12} & 0 \\ 0 & 0 & 0 & 0 & 0 & A_{19} \\ -A_1 & -A_2 & -A_3 & -A_4 & 0 & -A_5 \\ -A_7 & -A_8 & -A_9 & 0 & -A_{10} & -A_{11} \\ -A_{13} & -A_{14} & -A_{15} & -A_{16} & -A_{17} & -A_{18} \end{bmatrix}^m \begin{bmatrix} U \\ V \\ W \\ U' \\ V' \\ W' \end{bmatrix}^m + \begin{bmatrix} 0 & 0 & 0 & 0 & 0 & 0 \\ 0 & 0 & 0 & 0 & 0 & 0 \\ 0 & 0 & 0 & 0 & 0 & 0 \\ -J_1 & 0 & 0 & 0 & 0 & 0 \\ -J_2 & 0 & 0 & 0 & 0 & 0 \\ -J_4 & -J_3 & 0 & 0 & 0 & 0 \end{bmatrix}^m \begin{bmatrix} \Theta \\ \Theta' \\ 0 \\ 0 \\ 0 \\ 0 \end{bmatrix}^m \tag{7.66}$$

The mathematical layer index m has been transferred to matrices and vectors to compact the equation; for the same reason, the superscript $'$ expresses a derivative to z. The matrix form of Equation 7.66 allows it to be handled as:

$$\boldsymbol{D}^m \frac{\partial \boldsymbol{U}^m}{\partial z} = \boldsymbol{A}_M^m \boldsymbol{U}^m + \boldsymbol{A}_T^m \boldsymbol{\Theta}^m \tag{7.67}$$

The unknows of the problem are in the vectorial form:

$$\boldsymbol{U}^m = \begin{bmatrix} U \\ V \\ W \\ U' \\ V' \\ W' \end{bmatrix}^m \quad , \quad \boldsymbol{\Theta}^m = \begin{bmatrix} \Theta \\ \Theta' \\ 0 \\ 0 \\ 0 \\ 0 \end{bmatrix}^m \tag{7.68}$$

By defining $\frac{\partial \boldsymbol{U}^m}{\partial z} = \boldsymbol{U}'^m$, $\boldsymbol{A}_M^{*m} = \boldsymbol{D}^{-1m} \boldsymbol{A}_M^m$, and $\boldsymbol{A}_T^{*m} = \boldsymbol{D}^{-1m} \boldsymbol{A}_T^m$, two further mathematical steps are possible:

$$\boldsymbol{U}'^m = \boldsymbol{D}^{-1m} \boldsymbol{A}_M^m \boldsymbol{U}^m + \boldsymbol{D}^{-1m} \boldsymbol{A}_T^m \boldsymbol{\Theta}^m \tag{7.69}$$

$$\boldsymbol{U}'^m = \boldsymbol{A}_M^{*m} \boldsymbol{U}^m + \boldsymbol{A}_T^{*m} \boldsymbol{\Theta}^m \tag{7.70}$$

The mathematical layers are thin enough for geometrical (and possibly materials) requirements. The temperature profile can be assumed as a linear function of the thickness coordinate inside each fictitious layer; this facilitates implementing the solution. In other terms, inside each $m-th$ layer, the temperature, and its derivative, have the following expression:

$$\begin{aligned} \Theta^m(z) &= a_\Theta^m z + b_\Theta^m \\ \Theta'^m(z) &= a_\Theta^m \end{aligned} \tag{7.71}$$

with a_Θ^m and b_Θ^m two constants defining the $m-th$ temperature profile. a_Θ^m is the temperature at the bottom of the $m-th$ layer and b_Θ^m the slope of the temperature profile within the layer. In case the 3D/1D solutions to heat conduction problem have been considered, Θ^{3D} and Θ^{1D}, the temperatures at each interface have been already calculated; the slope can be derived from the temperature gradient of the $m-th$ layer and its thickness. For the linear assumed temperature profile, Θ^a, b_Θ^m is the slope of the temperature profile across the entire shell.

Equation 7.70 is a system of first order differential equations in z; the equations are not homogeneous due to the end therm, which is a function of z. Consider a generic set of differential equations in the form

$$\frac{\mathrm{d}\vec{x}}{\mathrm{d}t} = \boldsymbol{A}\vec{x} + \vec{f}(t) \tag{7.72}$$

$\vec{x}$ is a $n \times 1$ vector, $\boldsymbol{A}$ a $n \times n$ constant coefficient matrix and $\vec{f}(t) = [f_1(t) \dots f_n(t)]^T$ a given vector function. As shown in [129, 130], a solution of Equation 7.72 is:

$$\vec{x}(t) = \mathrm{e}^{(t-t_0)\boldsymbol{A}}\vec{x}_0 + \int_{t_0}^{t} \mathrm{e}^{(t-s)\boldsymbol{A}}\vec{f}(s)ds \tag{7.73}$$

The terms of the equation with matrix $\boldsymbol{A}$ appears at the exponent take the name of *exponential matrices*; their explicit form is:

$$\mathrm{e}^{(t-t_0)\boldsymbol{A}} = \sum_{i=0}^{\infty} \frac{\boldsymbol{A}^i}{i!}(t-t_0)^i \tag{7.74}$$

$$\mathrm{e}^{(t-s)\boldsymbol{A}} = \sum_{i=0}^{\infty} \frac{\boldsymbol{A}^i}{i!}(t-s)^i \tag{7.75}$$

The index i at which the series expansion is stopped plays a role in the convergence of the solution and will be discussed later.

The last term of Equation 7.70 needs to be re-written in an explicit form to give it the form showed in Equation 7.72:

$$\boldsymbol{\Theta}^{*m} = \boldsymbol{A}_T^{*m}\boldsymbol{\Theta}^m = \begin{bmatrix} 0 & 0 & 0 & 0 & 0 & 0 \\ 0 & 0 & 0 & 0 & 0 & 0 \\ 0 & 0 & 0 & 0 & 0 & 0 \\ J_1^{*m} & 0 & 0 & 0 & 0 & 0 \\ J_2^{*m} & 0 & 0 & 0 & 0 & 0 \\ J_4^{*m} & J_3^{*m} & 0 & 0 & 0 & 0 \end{bmatrix} \begin{bmatrix} a_\Theta^m z + b_\Theta^m \\ a_\Theta^m \\ 0 \\ 0 \\ 0 \\ 0 \end{bmatrix} = \begin{bmatrix} 0 \\ 0 \\ 0 \\ J_1^{*m}(a_\Theta^m z + b_\Theta^m) \\ J_2^{*m}(a_\Theta^m z + b_\Theta^m) \\ J_4^{*m}(a_\Theta^m z + b_\Theta^m) + J_3^{*m} a_\Theta^m \end{bmatrix} \tag{7.76}$$

The Equation 7.70 can be then compacted as

$$\boldsymbol{U}'^m = \boldsymbol{A}_M^{*m}\boldsymbol{U}^m + \boldsymbol{\Theta}^{*m} \tag{7.77}$$

and, since $\boldsymbol{\Theta}^{m*}$ contains only linear functions of z, its solution is

$$\boldsymbol{U}^m(z) = \mathrm{e}^{z\boldsymbol{A}_M^{*m}}\boldsymbol{U}^k(0) + \int_0^z \mathrm{e}^{(z-s)\boldsymbol{A}_M^{*m}}\boldsymbol{\Theta}^{*m}(s)ds \tag{7.78}$$

The assumption that the temperature profile is linear in the thickness in each $m-th$ layer is not strictly necessary; however, it simplifies the implementation of this solution as all the integrals are polynomial functions of z.

7.4.1 The intra-laminae relations

Equation 7.78 establishes a link between the values of the displacement vector U_m at the bottom of the $m-th$ layer and those at a generic thickness coordinate within the same layer. With $z = h^m$, Equation 7.78 computes the components of the displacement vector at the top of the $m-th$ layer.

$$\boldsymbol{U}^m(z) = \boldsymbol{A}_M^{**m}\boldsymbol{U}^m(0) + \boldsymbol{A}_\Theta^{**m}(h^m) \tag{7.79}$$

where $\boldsymbol{A}_M^{**m} = \mathrm{e}^{z\boldsymbol{A}_M^{*m}}$ and $\boldsymbol{A}_\Theta^{**m} = \int_0^{h^m} \mathrm{e}^{(z-s)\boldsymbol{A}_M^{*m}} \boldsymbol{\Theta}^{*m}(s)ds$. Suppose no temperature gradient exists, and its value coincides with the reference one. In that case, the second term is identically zero, and the matrix $\boldsymbol{A}_M^{**m}$ gives the intra-layer relation between displacements. Whether thermal effects are being investigated, the intra-layer relation suffers the additional term, which is a punctual function of the temperature.

7.4.2 The interlaminar conditions

The intra-laminae relations can be linked together, discussing the interface requirements between adjacent layers and the external mechanical boundary conditions. From a mechanical point of view, each interface must guarantee the continuity of transverse shear and normal stresses:

$$\sigma_{zzb}^m = \sigma_{zzt}^{m-1}\,,\quad \sigma_{\alpha zb}^m = \sigma_{\alpha zt}^{m-1}\,,\quad \sigma_{\beta zb}^m = \sigma_{\beta zt}^{m-1} \tag{7.80}$$

The mechanical continuity conditions keep the same formalism as the thermal ones: the given stress must take the same value when evaluated at the bottom (b) of the $m-th$ layer and at the top (t) of the $m-1-th$ layer. The equilibrium equations are in terms of displacements and their respective derivatives; Equations 7.53-7.55 allow translating the mechanical continuity conditions into a displacement form.

$$\begin{aligned}
&-\frac{C_{13}^{m-1}}{H_{\alpha t}^{m-1}}\bar{\alpha}U_t^{m-1} + \frac{C_{13}^{m-1}}{H_{\alpha t}^{m-1}R_\alpha}W_t^{m-1} - \frac{C_{23}^{m-1}}{H_{\beta t}^{m-1}}\bar{\beta}V_t^{m-1} + \frac{C_{23}^{m-1}}{H_{\beta t}^{m-1}R_\beta}W_t^{m-1} + C_{33}^{m-1}W_t^{m-1\prime} - \\
&+\lambda_z^{m-1}\Theta_t^{m-1} = -\frac{C_{13}^{m}}{H_{\alpha b}^{m}}\bar{\alpha}U_b^{m} + \frac{C_{13}^{m}}{H_{\alpha b}^{m}R_\alpha}W_b^{m} - \frac{C_{23}^{m}}{H_{\beta b}^{m}}\bar{\beta}V_b^{m} + \frac{C_{23}^{m}}{H_{\beta b}^{m}R_\beta}W_b^{m} + C_{33}^{m}W_b^{m\prime} - \lambda_z^{m}\Theta_b^{m}
\end{aligned} \tag{7.81}$$

$$-\frac{C_{55}^{m-1}}{H_{\alpha t}^{m-1}}\bar{\alpha}W_t^{m-1} + C_{55}^{m-1}U_t^{m-1} - \frac{C_{55}^{m-1}}{H_{\alpha t}^{m-1}R_\alpha}U_t^{m-1} = -\frac{C_{55}^{m}}{H_{\alpha b}^{m}}\bar{\alpha}W_b^{m} + C_{55}^{m-1}U_b^{m} - \frac{C_{55}^{m}}{H_{\alpha b}^{m}R_\alpha}U_b^{m} \tag{7.82}$$

$$-\frac{C_{44}^{m-1}}{H_{\beta t}^{m-1}}\bar{\beta}W_t^{m-1} + C_{44}^{m-1}V_t^{m-1} - \frac{C_{44}^{m-1}}{H_{\beta t}^{m-1}R_\beta}V_t^{m-1} = -\frac{C_{44}^{m}}{H_{\beta b}^{m}}\bar{\beta}W_b^{m} + C_{44}^{m}V_b^{m\prime} - \frac{C_{44}^{m}}{H_{\beta b}^{m}R_\beta}V_b^{m} \tag{7.83}$$

A further mathematical step consists of making explicit the derivative of each displacement, evaluated at the bottom of the $m-th$ layer.

$$W_b^{m'} = \frac{1}{C_{33}^m}\left(\bar{\alpha}\frac{C_{13}^m}{H_{\alpha b}^m} - \bar{\alpha}\frac{C_{13}^{m-1}}{H_{\alpha t}^{m-1}}\right)U_t^{m-1} + \frac{1}{C_{33}^m}\left(\bar{\beta}\frac{C_{23}^m}{H_{\beta b}^m} - \bar{\beta}\frac{C_{23}^{m-1}}{H_{\beta t}^{m-1}}\right)V_t^{m-1} + \frac{1}{C_{33}^m}\left(\frac{C_{13}^{m-1}}{H_{\alpha t}^{m-1}R_\alpha} + \frac{C_{23}^{m-1}}{H_{\beta t}^{m-1}R_\beta} - \frac{C_{13}^m}{H_{\alpha b}^m R_\alpha} - \frac{C_{23}^m}{H_{\beta b}^m R_\beta}\right)W_t^{m-1} + \frac{C_{33}^{m-1}}{C_{33}^m}W_t^{m-1'} + \frac{1}{C_{33}^m}(\lambda_z^m - \lambda_z^{m-1})\Theta_t^{m-1} \tag{7.84}$$

$$U_b^{m'} = \frac{1}{C_{55}^m}\left(\bar{\alpha}\frac{C_{55}^{m-1}}{H_{\alpha t}^{m-1}} - \bar{\alpha}\frac{C_{55}^m}{H_{\alpha b}^m}\right)W_t^{m-1} + \frac{1}{C_{55}^m}\left(-\frac{C_{55}^{m-1}}{H_{\alpha t}^{m-1}R_\alpha} + \frac{C_{55}^m}{H_{\alpha t}^m R_\alpha}\right)U_t^{m-1} + \frac{C_{55}^{m-1}}{C_{55}^m}U_t^{m-1'} \tag{7.85}$$

$$V_b^{m'} = \frac{1}{C_{44}^m}\left(\bar{\beta}\frac{C_{55}^{m-1}}{H_{\beta t}^{m-1}} - \bar{\beta}\frac{C_{44}^m}{H_{\beta b}^m}\right)W_t^{m-1} + \frac{1}{C_{44}^m}\left(-\frac{C_{44}^{m-1}}{H_{\beta t}^{m-1}R_\beta} + \frac{C_{44}^m}{H_{\beta t}^m R_\beta}\right)V_t^{m-1} + \frac{C_{44}^{m-1}}{C_{44}^m}V_t^{m-1'} \tag{7.86}$$

All these relations can be compacted by assigning to each block that multiplies a displacement or its derivative a coefficient $T_s^{m-1,1}$ (with s varying from 1 to 11):

$$U_b^{m'} = T_1 U_t^{m-1} + T_2 W_t^{m-1} + T_3 U_t^{m-1'} \tag{7.87}$$

$$V_b^{m'} = T_4 V_t^{m-1} + T_5 W_t^{m-1} + T_6 V_t^{m-1'} \tag{7.88}$$

$$W_b^{m'} = T_7 U_t^{m-1} + T_8 V_t^{m-1} + T_9 W_t^{m-1} + T_{10} W_t^{m-1'} + T_{11}\Theta_t^{m-1} \tag{7.89}$$

A further condition to satisfy is congruency/continuity: all the three displacement components must take the same value when evaluated at an interface, that is at the bottom (b) of the $m-th$ layer and at the top (t) of the $m-1-th$ layer.

$$u_b^m = u_t^{m-1}\,,\quad v_b^m = v_t^{m-1}\,,\quad w_b^m = w_t^{m-1} \tag{7.90}$$

The displacement continuity conditions are written in displacement form, obviously. Together with the mechanical continuity conditions, they can be grouped into a matrix form:

$$\begin{bmatrix} U \\ V \\ W \\ U' \\ V' \\ W' \end{bmatrix}^m = \begin{bmatrix} 1 & 0 & 0 & 0 & 0 & 0 \\ 0 & 1 & 0 & 0 & 0 & 0 \\ 0 & 0 & 1 & 0 & 0 & 0 \\ T_1 & 0 & T_2 & T_3 & 0 & 0 \\ 0 & T_4 & T_5 & 0 & T_6 & 0 \\ T_7 & T_8 & T_9 & 0 & 0 & T_{10} \end{bmatrix}^{m-1,m} \begin{bmatrix} U \\ V \\ W \\ U' \\ V' \\ W' \end{bmatrix}^{m-1} + \begin{bmatrix} 0 & 0 & 0 & 0 & 0 & 0 \\ 0 & 0 & 0 & 0 & 0 & 0 \\ 0 & 0 & 0 & 0 & 0 & 0 \\ 0 & 0 & 0 & 0 & 0 & 0 \\ 0 & 0 & 0 & 0 & 0 & 0 \\ T_{11} & 0 & 0 & 0 & 0 & 0 \end{bmatrix}^{m-1,m} \begin{bmatrix} \Theta \\ \Theta' \\ 0 \\ 0 \\ 0 \\ 0 \end{bmatrix}^{m-1} \tag{7.91}$$

A further compact writing of Equation 7.91 is:

$$\boldsymbol{U}^m = \boldsymbol{T}_M^{m-1,m}\boldsymbol{U}^{m-1} + \boldsymbol{T}_\Theta^{m-1,m}\boldsymbol{\Theta}^{m-1} \tag{7.92}$$

With $M-1$ interfaces, $M-1$ mechanical and thermal transfer matrices grant the continuity conditions across the layers.

7.4.3 Boundary conditions

The kinematic and mechanical boundary conditions are here introduced. Plates and shells have simply supported edges; they can be loaded on the top and the bottom surfaces of the structure. As previously anticipated, the kinematic boundary conditions are automatically satisfied by the harmonic form assumed by the displacements. The mechanical boundary conditions are here imposed:

$$\sigma_{zz} = p_{zb}, \quad \sigma_{\alpha z} = p_{\alpha b}, \quad \sigma_{\beta z} = p_{\beta b} \quad \text{for} \quad z = -h/2 \quad or \quad \tilde{z} = 0 \tag{7.93}$$

$$\sigma_{zz} = p_{zt}, \quad \sigma_{\alpha z} = p_{\alpha t}, \quad \sigma_{\beta z} = p_{\beta t} \quad \text{for} \quad z = +h/2 \quad or \quad \tilde{z} = h \tag{7.94}$$

Equations 7.53-7.55 allow translating them into a displacement form:

$$\sigma^M_{zzt} = -\bar{\alpha}\frac{C^M_{13}}{H_{\alpha t}}U^M_t + \frac{C^M_{13}}{H_{\alpha t}R_\alpha}W^M_t - \bar{\beta}\frac{C^M_{23}}{H_{\beta t}}V^M_t + \frac{C^M_{23}}{H_{\beta t}R_\beta}W^M_t + C^M_{33}W^M_{t,z} = P^M_{zt} \tag{7.95}$$

$$\sigma^M_{\beta zt} = -\bar{\beta}\frac{C^M_{44}}{H_{\beta t}}W^M_t + C^M_{44}V^M_{t,z} - \frac{C^M_{44}}{H_{\beta t}R_\beta}V^M_t = P^M_{\beta t} \tag{7.96}$$

$$\sigma^M_{\alpha zt} = -\bar{\alpha}\frac{C^M_{55}}{H_{\alpha t}}W^M_t + C^1_{55}U^M_{t,z} - \frac{C^M_{55}}{H_{\alpha t}R_\alpha}U^M_t = P^M_{\alpha t} \tag{7.97}$$

$$\sigma^1_{zzb} = -\bar{\alpha}\frac{C^1_{13}}{H_{\alpha b}}U^1_b + \frac{C^1_{13}}{H_{\alpha b}R_\alpha}W^1_b - \bar{\beta}\frac{C^1_{23}}{H_{\beta b}}V^1_b + \frac{C^1_{23}}{H_{\beta b}R_\beta}W^1_b + C^1_{33}W^1_{b,z} = P^1_{zb} \tag{7.98}$$

$$\sigma^1_{\beta zb} = -\bar{\beta}\frac{C^1_{44}}{H_{\beta b}}W^1_b + C^1_{44}V^1_{b,z} - \frac{C^1_{44}}{H_{\beta b}R_\beta}V^1_b = P^1_{\beta b} \tag{7.99}$$

$$\sigma^1_{\alpha zb} = -\bar{\alpha}\frac{C^1_{55}}{H_{\alpha b}}W^1_b + C^1_{55}U^1_{b,z} - \frac{C^1_{55}}{H_{\alpha b}R_\alpha}U^1_b = P^1_{\alpha b} \tag{7.100}$$

With the stresses specified in terms of displacements and their derivatives, the loads applied on the top and at the bottom can be grouped in two separate vectors:

$$\boldsymbol{B^M}(h^M)\boldsymbol{U^M}(h^M) = \boldsymbol{P}^M_t\,, \tag{7.101}$$

$$\boldsymbol{B^1}(0)\boldsymbol{U^1}(0) = \boldsymbol{P}^1_b\,, \tag{7.102}$$

where

$$\boldsymbol{P}^M_t = \begin{bmatrix} P^M_{zt} \\ P^M_{\beta t} \\ P^M_{\alpha t} \end{bmatrix} \qquad \boldsymbol{P}^1_b = \begin{bmatrix} P^1_{zb} \\ P^1_{\beta b} \\ P^1_{\alpha b} \end{bmatrix} \tag{7.103}$$

$\boldsymbol{U^1}(0)$, $\boldsymbol{U^M}(h^M)$ are $\boldsymbol{U}$ vector respectively evaluated at the bottom of the whole mutilayered structure (layer 1, $\tilde{z}^1 = 0$), and at the top (layer M, $\tilde{z}^T = h_T$). Matrices $\boldsymbol{B^M}(h^M)$ and $\boldsymbol{B^1}(0)$ contain the coefficients multiplying displacement and their

derivatives in Equations 7.95-7.100. It is necessary to systematize Equations 7.101-7.102 to solve the problem; however the vector of unknowns is evaluated once at the top and once at the bottom of the shell.

Starting from $M-th$ layer, it is possible to recursively introduce Equation 7.92 into Equation 7.79 to link the displacement vector evaluated at the bottom of the first layer and the displacement vector evaluated at the top of the last layer. With zero sovra-temperature the two vectors are linked by a matrix; however, when the boundary conditions do not coincide with the reference temperature, a set of additional terms appears. Here follows an example for $M = 5$ mathematical layers:

$$\begin{aligned}
&\boldsymbol{U}_t^5 = \boldsymbol{A}_M^{**5}\boldsymbol{T}_M^{4,5}\boldsymbol{A}_M^{**4}\boldsymbol{T}_M^{3,4}\boldsymbol{A}_M^{**3}\boldsymbol{T}_M^{2,3}\boldsymbol{A}_M^{**2}\boldsymbol{T}_M^{1,2}\boldsymbol{A}_M^{**1}\boldsymbol{U}^1(0)+\\
&\boldsymbol{A}_M^{**5}\boldsymbol{T}_M^{4,5}\boldsymbol{A}_M^{**4}\boldsymbol{T}_M^{3,4}\boldsymbol{A}_M^{**3}\boldsymbol{T}_M^{2,3}\boldsymbol{A}_M^{**2}\boldsymbol{T}_M^{1,2}\boldsymbol{A}_{\Theta\,t}^{**1}+\\
&\boldsymbol{A}_M^{**5}\boldsymbol{T}_M^{4,5}\boldsymbol{A}_M^{**4}\boldsymbol{T}_M^{3,4}\boldsymbol{A}_M^{**3}\boldsymbol{T}_M^{2,3}\boldsymbol{A}_M^{**2}\boldsymbol{T}_\Theta^{1,2}\boldsymbol{\Theta}_t^1+\\
&\boldsymbol{A}_M^{**5}\boldsymbol{T}_M^{4,5}\boldsymbol{A}_M^{**4}\boldsymbol{T}_M^{3,4}\boldsymbol{A}_M^{**3}\boldsymbol{T}_M^{2,3}\boldsymbol{A}_{\Theta\,t}^{**2}+\\
&\boldsymbol{A}_M^{**5}\boldsymbol{T}_M^{4,5}\boldsymbol{A}_M^{**4}\boldsymbol{T}_M^{3,4}\boldsymbol{A}_M^{**3}\boldsymbol{T}_\Theta^{2,3}\boldsymbol{\Theta}_t^2+\\
&\boldsymbol{A}_M^{**5}\boldsymbol{T}_M^{4,5}\boldsymbol{A}_M^{**4}\boldsymbol{T}_M^{3,4}\boldsymbol{A}_{\Theta\,t}^{**3}+\\
&\boldsymbol{A}_M^{**5}\boldsymbol{T}_M^{4,5}\boldsymbol{A}_M^{**4}\boldsymbol{T}_\Theta^{3,4}\boldsymbol{\Theta}_t^3+\\
&\boldsymbol{A}_M^{**5}\boldsymbol{T}_M^{4,5}\boldsymbol{A}_{\Theta\,t}^{**4}+\\
&\boldsymbol{A}_M^{**5}\boldsymbol{T}_\Theta^{4,5}\boldsymbol{\Theta}_t^4+\\
&\boldsymbol{A}_{\Theta\,t}^{**5}
\end{aligned} \tag{7.104}$$

The first-row term of Equation 7.104 is the only one including the displacement vector evaluated at the bottom of the structure; it is the only non-zero term when the temperature is constant and equal to the reference one. It defines the 6×6 matrix $\boldsymbol{H}$ for multilayered structures:

$$\boldsymbol{H} = \boldsymbol{A}_M^{**M}\boldsymbol{T}_M^{M-1,M}\boldsymbol{A}_M^{**M} - 1\boldsymbol{T}_M^{M-2,M-1}.....\boldsymbol{A}_M^{**2}\boldsymbol{T}_M^{1,2}\boldsymbol{A}_M^{**1} \tag{7.105}$$

M terms ending with $\boldsymbol{A}_{\Theta\,t}^{**m}$ and $M-1$ ending in $\boldsymbol{\Theta}_t^m$ complete the Equation when the temperature differs from the reference conditions. The first terms are M as they explicitly contain the assumed linear profile within each layer; the latter are $M-1$ as they identify the temperature at each interface. Their sum is the 6×1 vector $\boldsymbol{H}_\Theta$. Through $\boldsymbol{H}$ and $\boldsymbol{H}_\Theta$, Equation 7.104 reads:

$$\boldsymbol{U}_t^M = \boldsymbol{H}\boldsymbol{U}^1(0) + \boldsymbol{H}_\Theta \tag{7.106}$$

Through Equation 7.106, Equation 7.101 can be rewritten in therms of $\boldsymbol{U}_b^1$:

$$\boldsymbol{B}_t^M\boldsymbol{H}\boldsymbol{U}^1(0) = \boldsymbol{P}_t^M - \boldsymbol{B}_t^M\boldsymbol{H}_\Theta \tag{7.107}$$

Equation 7.107 can now be merged with Equation 7.102:

$$\begin{bmatrix}\boldsymbol{B}_t^M\boldsymbol{H}\\ \boldsymbol{B}_b^1\end{bmatrix}\boldsymbol{U}^1(0) = \begin{bmatrix}\boldsymbol{P}_t^M - \boldsymbol{B}_t^M\boldsymbol{H}_\Theta\\ \boldsymbol{P}_b^1\end{bmatrix} \tag{7.108}$$

and, with the following definitions:

$$\boldsymbol{E} = \begin{bmatrix} \boldsymbol{B}_t^M \boldsymbol{H} \\ \boldsymbol{B}_b^1 \end{bmatrix} \quad \boldsymbol{U}^1(0) = \begin{bmatrix} U \\ V \\ W \\ U' \\ V' \\ W' \end{bmatrix}_b^1 \quad \boldsymbol{P} = \begin{bmatrix} \boldsymbol{P}_t^M - \boldsymbol{B}_t^M \boldsymbol{H}_\Theta \\ \boldsymbol{P}_b^1 \end{bmatrix} \tag{7.109}$$

Equation 7.108 reads

$$\boldsymbol{E}\boldsymbol{U}^1(0) = \boldsymbol{P} \tag{7.110}$$

$\boldsymbol{U}^1(0)$ is a vector in R^6 of the unknowns, and it contains the three displacement components and their respective derivatives evaluated at the bottom of the first layer. The vector of loads $\boldsymbol{L}$ contains 6 elements; in the first 3, the term $-\boldsymbol{B}_t^M \boldsymbol{H}_\Theta$ acts as a corrective factor of the top load vector $\boldsymbol{P}_t^M$.

Equation 7.110 covers a wide range of problems and configurations. It is valid for spherical shells with constant radii of curvature. It automatically converts into an equation for cylindrical panels and plates when one or both the radii are infinite. It can consider structures both loaded on top/bottom surfaces and subjected to a thermal load. From the results of Equation 7.110, the vector $\boldsymbol{U}$ can be calculated at any thickness coordinate through Equation 7.92 and Equation 7.79. The derivatives of the displacements with respect to the thickness coordinate are a direct solution of the problem; those with respect to α and β can be exactly calculated deriving the harmonic forms of the displacements. The stresses can now be calculated using the constitutive equations.

The whole discussion has been fully developed for the thermal stress analysis, leaving out the hygrometric stress analysis. The choice is deliberate, as the heat equation and the second law of diffusion are both transport equations with the same mathematical formulation. The 3D, 1D, and assumed linear solutions are identical, as long as the meaning of the introduced coefficients is changed by substituting the conductivity coefficients with the diffusivity ones. The introduction of the hygrometric field in the field of deformations is also similar to what is discussed in Equations 7.45-7.47, provided that the coefficients of hygrometric expansion are substituted for the coefficients of thermal expansion.

7.5 Model Assessments

This section discusses three assessments for the proposed solution model. Two parameters need to be quantified: the number M of fictitious layers and the exponential matrices expansion coefficient. This aspect already received considerations for the elastic part of the solution. In multilayered structures, with classical

isotropic and orthotropic layers, 100 fictitious layers combined with a third expansion order for the exponential matrix ensure convergence. The mathematical layers are not necessary for plates, and the convergence is always guaranteed with an expansion order equal to 12 [109, 131]. When the lamination sequence also includes FGM layers, it is necessary to introduce 300 fictitious layers to approximate the mechanical properties in the thickness direction correctly [110], ensuring the solution convergence. The comparison with established thermo-elastic solutions allows to qualify the model and to quantify those two parameters to ensure solution convergence. Section 7.2 discussed three possible methods for calculating the temperature profile in the thickness direction. All three strategies produce a temperature distribution that acts as a field load within the structure. The elastic part of the model is the same; however, a different thermal load distribution will produce a different mechanical response. To better identify the results, the following nomenclature will be used below:

- **SOL-$\boldsymbol{\theta^a}$**: these results are calculated under the hypothesis that the temperature follows a linear profile along z; θ is a function of the top and bottom temperatures only. It is an extremely simplifying hypothesis, often used in literature when the formulation could not consider the temperature distribution in the thickness direction. It does not consider the thermal properties of the individual layers nor the thicknesses.
- **SOL-$\boldsymbol{\theta^{1D}}$**: these results are calculated under the hypothesis that the heat flux is constant along z. This requires that the temperature profile is linear within each physical layer; its slope changes from one to the other due to its thermal resistivity. Therefore, this hypothesis considers the thermal properties of the individual layers; however, it discards the effects of thickness in each layer.
- **SOL-$\boldsymbol{\theta^{3D}}$**: these results are calculated by solving the heat conduction problem in 3D without any preliminary assumptions. It considers all the specificities of the problem, from thermal to geometric properties.

The results of the three assessments will validate the model, and establish that expanding the exponential matrix up to the third order, introducing 300 mathematical layers, is always sufficient to ensure solution convergence

7.5.1 Assessment 1

This solution has been assessed for plate geometry by considering the reference solution of Bhaskar et al. [132]. The authors developed a linear uncoupled thermo-elastic solution for simply supported composite laminates by assuming that a bi-sinusoidal ($m = n = 1$) sovra-temperature field evolves linearly in the thickness direction. The reference and the discussed solutions are directly comparable

only when the temperature profile is not calculated through the 3D or 1D heat conduction equations, but it is assumed to be linear. $\theta_t = +1K$ and $\theta_b = -1K$ are the sovra-temperature amplitudes imposed at the top and bottom external surfaces, respectively. A plate geometry is considered, with a three layer $0°/90°/0°$ stacking sequence; the overall thickness is equally distributed among the three. The layer mechanical and thermal properties in material reference system are reported in Table 7.1. The comparison between the reference solution is discussed in Table

Mechanical properties	Thermal properties
$E_{11}/E_{22} = 25$	$\alpha_2/\alpha_1 = 1125$
$E_{11}/E_{33} = 25$	$\alpha_3/\alpha_1 = 1125$
$G_{12}/E_{22} = 0.5$	$\kappa_1 = 36.42$ W/mK
$G_{13}/E_{22} = 0.5$	$\kappa_2 = \kappa_3 = 0.96$ W/mK
$G_{23}/E_{22} = 0.2$	
$\nu_{12} = \nu_{13} = \nu_{23} = 0.25$	

Table 7.1: Mechanical and thermal properties of Assessment 1.

7.2. Following the results discussed in [109, 131] for the elastic solution convergence, the exponential matrix is expanded to the third-order; tentative fictitious layer numbers are considered. M is an integer multiple of 3 as the number of the layers because they have the same thickness. The same parameters are used to calculate the thermal profile and to evaluate the mechanical response. The performances of the proposed solution are discussed for several thickness ratios in terms of dimensionless transverse displacement and the in-plane shear stress:

$$\bar{w} = \frac{w}{h\alpha_1(a/h)^2} \quad , \quad \bar{\sigma}_{\alpha\beta} = \frac{\sigma_{\alpha\beta}}{\alpha_1 E_{22}} \tag{7.111}$$

SOL-θ^a is in line with the reference solution already starting from $M = 102$. A greater number of mathematical layers guarantees perfect coincidence between the results. SOL-θ^{1D} give the same results; this is due to the lamination sequence. As Table 7.2 shows, regardless of the lamination angle, there is transverse isotropy; there is no difference between the two models because the thermal resistivity is the same among the three layers. SOL-θ^{3D} gives different results for thick plates, which demonstrates the importance of the relative weight of the thickness; the results approach the previous ones as the structure gets thinner. The indications discussed at specific $\bar{z}$ coordinates in Table 7.2 are further confirmed by the plots shown in Figures 7.3-7.5. The temperature profiles in a thin and a thick plate are shown in Figure 7.3. θ^a and θ^{1D} are superposed due to the transverse isotropy of the laminate. Only θ^{3D} grasps the 3D effects, which play a marginal role as the shell becomes thinner. The temperature is a field load, which affects the mechanical response in terms of displacement and stress shown in the figures. SOL-θ^a and SOL-θ^{1D} give coincident results, insufficiently thorough when the plate is thick.

a/h	2	10	50	100	2	10	50	100
	$\bar{w}(\tilde{z}=h)$				$\bar{\sigma}_{\alpha\beta}(\tilde{z}=0)$			
Ref.SOL[132]	96.79	17.39	10.50	10.26	269.3	76.29	51.41	50.53
	$M=102$							
SOL-θ^a	97.02	17.39	10.50	10.26	269.3	76.29	51.41	50.53
SOL-θ^{1D}	97.02	17.39	10.50	10.26	269.3	76.29	51.41	50.53
SOL-θ^{3D}	49.06	16.40	10.47	10.25	143.0	71.96	51.27	50.50
	$M=210$							
SOL-θ^a	96.82	17.39	10.50	10.26	269.3	76.29	51.41	50.53
SOL-θ^{1D}	96.82	17.39	10.50	10.26	269.3	76.29	51.41	50.53
SOL-θ^{3D}	48.88	16.39	10.47	10.25	142.9	71.96	51.27	50.50
	$M=300$							
SOL-θ^a	96.80	17.39	10.50	10.26	269.3	76.29	51.41	50.53
SOL-θ^{1D}	96.80	17.39	10.50	10.26	269.3	76.29	51.41	50.53
SOL-θ^{3D}	48.87	16.39	10.47	10.25	142.9	71.96	51.27	50.50

Table 7.2: Thermo-mechanical assessment for plate geometry; the reference solution is the linear uncoupled thermo-elastic model in [132]. The exponential matrix is expanded to the third-order; tentative fictitious layer numbers are considered.

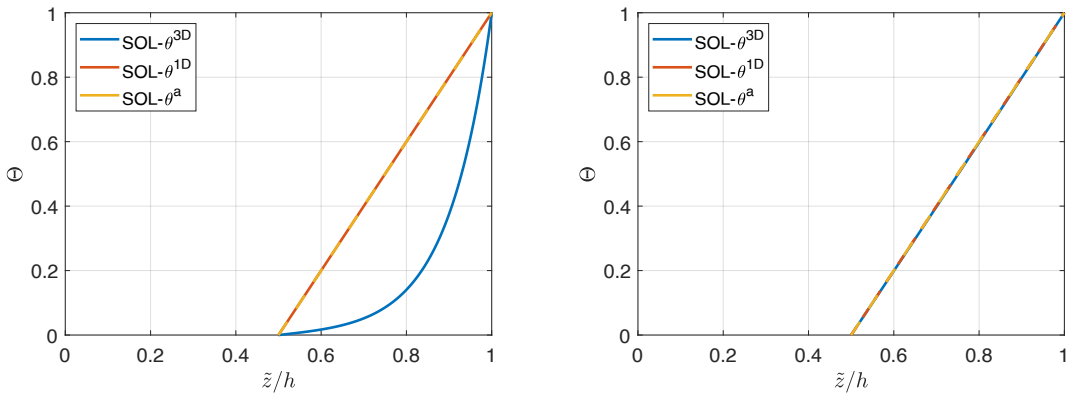

(a) $a/h=2$ (b) $a/h=50$

Figure 7.3: First assessment: temperature profiles along with the thickness direction for two different thickness ratios.

7.5.2 Assessment 2

This solution has been assessed for shell geometry, and 3D-calculated thermal profile, by considering the reference solution of Brischetto and Carrera [133]. The authors developed a fully coupled layer-wise thermo-elastic solution, in which the

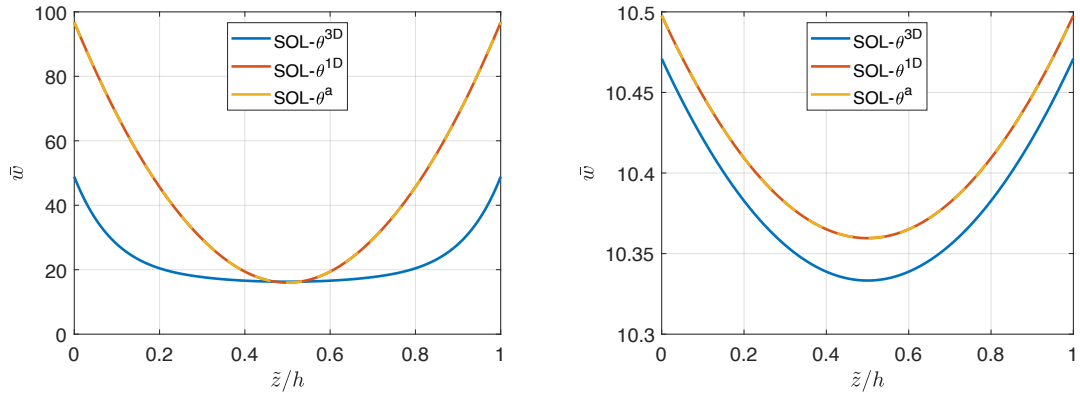

(a) $a/h = 2$ (b) $a/h = 50$

Figure 7.4: First assessment: dimensionless displacement component $\bar{w}$ profiles along with the thickness direction for two different thickness ratios.

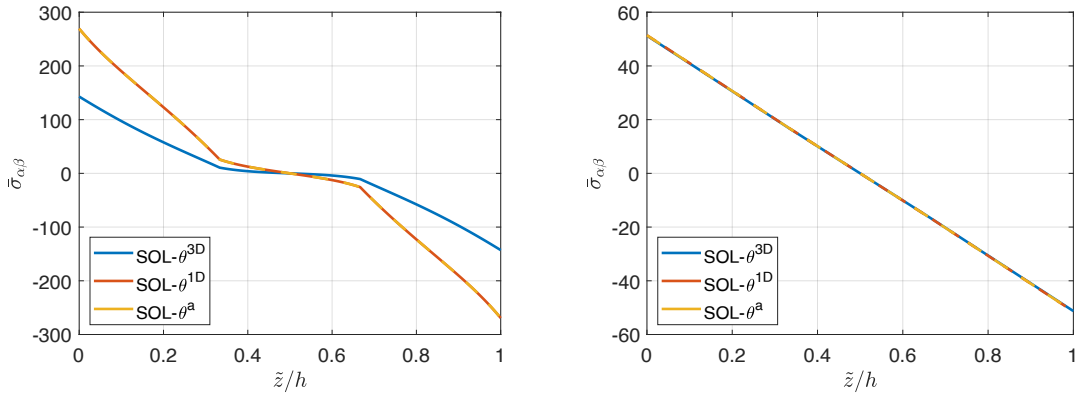

(a) $a/h = 2$ (b) $a/h = 50$

Figure 7.5: First assessment: dimensionless stress component $\bar{\sigma}_{\alpha\beta}$ profiles along with the thickness direction for two different thickness ratios.

thermal load can be assumed as linear, or calculated as a primary variable. Consequently, the reference and the discussed solutions are directly comparable in both cases. $\theta_t = +1K$ and $\theta_b = 0K$ are the sovra-temperature amplitudes imposed at the top and bottom external surfaces, respectively. A cylindrical shell is considered, and the dimensions are set as follows: the radii of curvature are $R_\alpha = 10$ m and $R_\beta = \infty$, and dimensions $a = \frac{\pi}{3} R_\alpha$ and $b = 1$ m. The stacking sequence includes an Aluminium (Al2024) and a Titanium Alloy (Ti22), as bottom and top layer, respectively. The layer mechanical and thermal properties properties are reported in Table 7.3. The comparison between the reference solution is discussed in Table 7.4. In analogy with the previous assessment, the exponential matrix is expanded

Mechanical properties	Thermal properties
Aluminium (Al2024)	
$E = 73$ GPa	$\alpha = 25 * 10^{-6}$ 1/K
$\nu = 0.3$	$\kappa = 130$ W/mK
Titanium Alloy (Ti22)	
$E = 110$ GPa	$\alpha = 8.6 * 10^{-6}$ 1/K
$\nu = 0.32$	$\kappa = 21.9$ W/mK

Table 7.3: Mechanical and thermal properties of Assessment 2.

to the third-order; tentative fictitious layer numbers are considered. M is a even number because the two layers have the same thickness. The same parameters are used to calculate the thermal profile and to evaluate the mechanical response. The performances of the proposed solution are discussed in terms of transverse and in-plane displacement, w and u; several thickness ratios are considered.

R_α/h	5	10	50	100	5	10	50	100
	$w(\tilde{z} = h/2)$ mm				$u(\tilde{z} = h)$ $[10^{-1}]$ mm			
Ref.(θ^a)[133]	0.007	0.0011	0.0048	0.0117	-0.0052	-0.0045	-0.0035	-0.0033
Ref.(θ^{3D})[133]	0.002	0.0010	0.0060	0.0129	-0.0031	-0.0031	-0.0027	-0.0023
				$M = 100$				
SOL-θ^a	0.007	0.0011	0.0048	0.0117	-0.0053	-0.0045	-0.0035	-0.0033
SOL-θ^{1D}	0.002	0.0010	0.0060	0.0129	-0.0046	-0.0037	-0.0027	-0.0023
SOL-θ^{3D}	0.002	0.0010	0.0060	0.0129	-0.0031	-0.0031	-0.0027	-0.0023
				$M = 200$				
SOL-θ^a	0.007	0.0011	0.0048	0.0117	-0.0052	-0.0045	-0.0035	-0.0033
SOL-θ^{1D}	0.002	0.0010	0.0060	0.0129	-0.0046	-0.0037	-0.0027	-0.0023
SOL-θ^{3D}	0.002	0.0010	0.0060	0.0129	-0.0031	-0.0031	-0.0027	-0.0023
				$M = 300$				
SOL-θ^a	0.007	0.0011	0.0048	0.0117	-0.0052	-0.0045	-0.0035	-0.0033
SOL-θ^{1D}	0.002	0.0010	0.0060	0.0129	-0.0046	-0.0037	-0.0027	-0.0023
SOL-θ^{3D}	0.002	0.0010	0.0060	0.0129	-0.0031	-0.0031	-0.0027	-0.0023

Table 7.4: Thermo-mechanical assessment for shell geometry, and 3D-calculated thermal profile; the reference solution is the fully coupled layer-wise thermo-elastic solution in [133]. The exponential matrix is expanded to the third-order; tentative fictitious layer numbers are considered.

As in the previous assessment, SOL-θ^a is in line with the reference solution considering an assumed temperature profile, already starting from $M = 100$. A greater

number of mathematical layers guarantees perfect coincidence between the results. SOL-θ^{3D} coincides with the reference solution considering the temperature as a primary variable, already starting from $M = 100$. SOL-θ^{1D} differs from SOL-θ^{3D} for thick plates, as the thickness effect gets an higher relative weight. It also differs from SOL-θ^{a} as it considers the effect of the lamination. Table 7.4 evaluates the

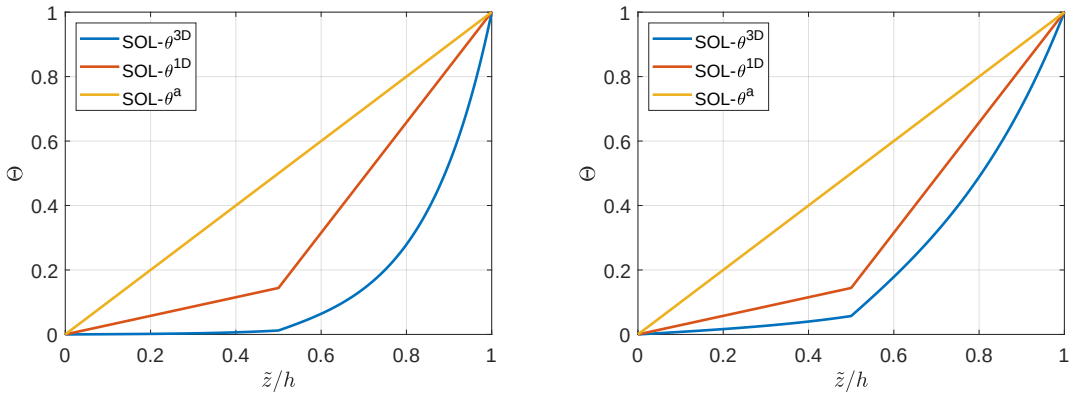

(a) $R_\alpha/h = 5$ (b) $R_\alpha/h = 10$

Figure 7.6: Second assessment: temperature profiles along with the thickness direction for two different thickness ratios.

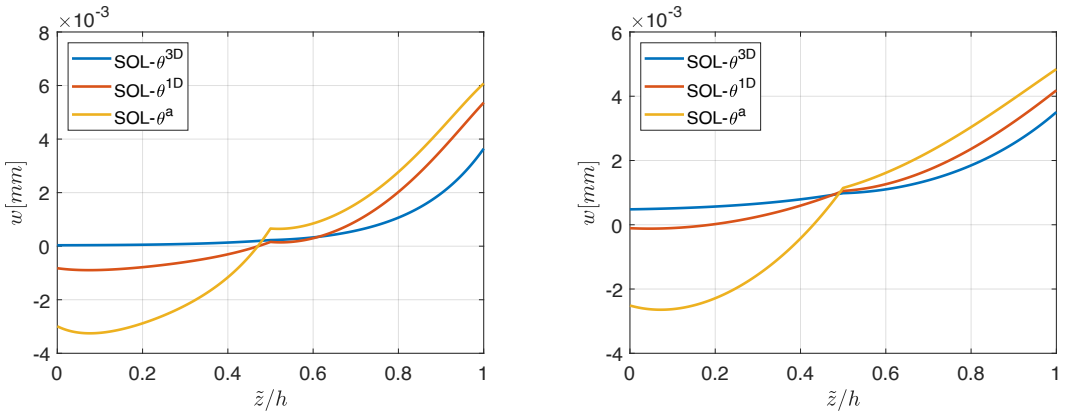

(a) $R_\alpha/h = 5$ (b) $R_\alpha/h = 10$

Figure 7.7: Second assessment: displacement component w profiles along with the thickness direction for two different thickness ratios.

displacement components w and u at specific $\bar{z}$ coordinates. Those indications are further confirmed by the plots shown in Figures 7.6-7.8. Figure 7.6 compares the temperature profiles of two shells with different thickness ratios. In both cases, the

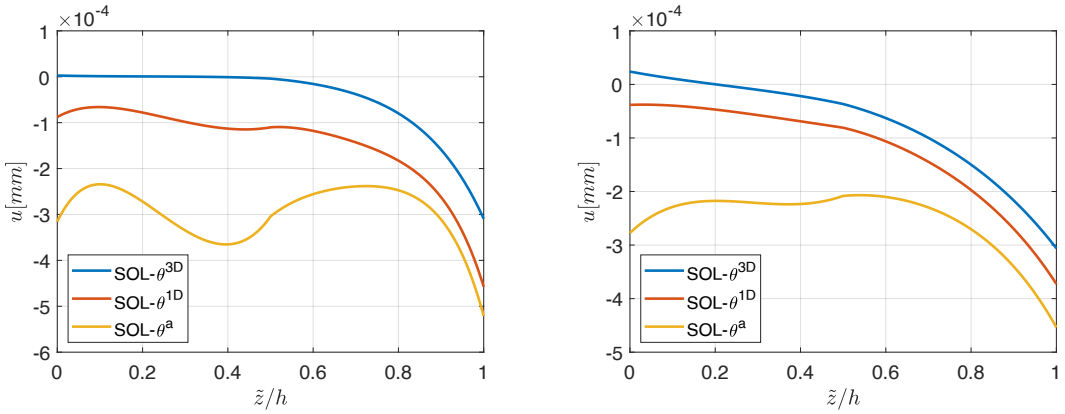

(a) $R_\alpha/h = 5$ (b) $R_\alpha/h = 10$

Figure 7.8: Second assessment: displacement component u profiles along with the thickness direction for two different thickness ratios.

θ^a temperature profile is very far from those calculated by solving the heat conduction equation. The θ^{1D} and θ^{3D} profiles grasp the different thermal properties of the two layers; they get closer as the shell becomes thinner and, the effect of thickness plays a marginal role, and a one-dimensional equation well approximates the problem. Since the temperature is a field load, this affects the mechanical response in terms of displacement shown in the figures. SOL-θ^a is very distant from the real behavior of the structure; SOL-θ^{1D} gives a more accurate estimate the thinner the shell.

7.5.3 Assessment 3

This solution has been assessed for Functionally Graded Materials applications by considering the reference solution of Reddy and Cheng [134]. The authors revealed an asymptotic method for the thermal stress analysis of FGM plates; the temperature profile along the thickness direction also is calculated with this approach. A direct comparison between the reference solution and SOL-θ^{3D} can be attempted. $\theta_t = +1K$ and $\theta_b = 0K$ are the sovra-temperature amplitudes imposed at the top and bottom external surfaces, respectively. A square plate is the considered geometry, with different thickness ratios. This model assumes a single FGM layer; the mechanical properties are estimated through the Mori-Tanaka approach [135] from those of the constituents: Zirconia, the ceramic phase, and Monel, the metallic phase. Table 7.5 reports the respective mechanical and thermal properties, the first expressed as a bulk modulus function. The mechanical and thermal properties vary along with the thickness direction; this assessment assumes that the

Mechanical properties	Thermal properties
Monel (70Ni-30Cu)	
$K^m = 227.25$ GPa	$\alpha^m = 15 * 10^{-6}$ 1/K
$G^m = 65.55$ GPa	$\kappa^m = 25$ W/mK
Zirconia	
$K^c = 125.83$ GPa	$\alpha^c = 10 * 10^{-6}$ 1/K
$G^c 58.077$ GPa	$\kappa^c = 2.09$ W/mK

Table 7.5: Mechanical and thermal properties of Assessment 3.

volume fraction of the ceramic phase is a power function of the thickness coordinate:

$$V_f^c = \left(\frac{z}{h}\right)^p \tag{7.112}$$

The law varies according to the exponent. However, its formulation makes the FGM layer metallic at the bottom ($z = 0$, $V_f^c = 0$) and ceramic at the top ($z = h$, $V_f^c = 1$). In the Mori-Tanaka formulation, the volume fraction of one of the two constituents determines the mechanical properties for different thickness coordinates. Equations 7.113-7.114 report the estimates of the bulk modulus K and of the shear modulus G:

$$\frac{K - K^m}{K^c - K^m} = \frac{V_f^c}{1 + (1 - V_f^c)\frac{K^c - K^m}{K_m + \frac{4}{3}G^m}} \tag{7.113}$$

$$\frac{G - G^m}{G^c - G^m} = \frac{V_f^c}{1 + (1 - V_f^c)\frac{G^c - G^m}{G^m + \frac{4}{3}f^m}}, \quad f^m = \frac{G^m(9K^m + 8G^m)}{6(K^m + 2G^m)} \tag{7.114}$$

Equations 7.115-7.116 report the estimates of the thermal conduction κ and heat expansion α coefficients:

$$\frac{\kappa - \kappa^m}{\kappa^c - \kappa^m} = \frac{V_f^c}{1 + (1 - V_f^c)\frac{\kappa^c - \kappa^m}{3\kappa^m}} \tag{7.115}$$

$$\frac{\alpha - \alpha^m}{\alpha^c - \alpha^m} = \frac{\frac{1}{K} - \frac{1}{K^m}}{\frac{1}{K^c} - \frac{1}{K^m}} \tag{7.116}$$

Following the elastic solution convergence requirements discussed in [110], the exponential matrix is expanded to the third-order; the assessment considers tentative fictitious layer numbers. The same parameters are used to calculate the thermal profile and to evaluate the mechanical response. Table 7.6 discusses the performances of the proposed solution in terms of dimensionless transverse displacement w and transverse stress σ_{zz} for several thickness ratios.

SOL-θ^{3D} results only are directly comparable with the reference solution; there is a practical coincidence with the reference results when 300 fictitious layers are

a/h	4	10	50	4	10	50
	$\bar{w}(\tilde{z}=h)$			$\bar{\sigma}_{zz}(\tilde{z}=h/2)$		
Ref.SOL(θ^{3D})[134]	3.043	6.021	2.853	6.217	1.015	0.04067
	$M=100$					
SOL-θ^{a}	4.284	7.733	3.593	-19.57	-2.392	-0.08990
SOL-θ^{1D}	3.208	6.066	2.854	2.581	0.9173	0.04060
SOL-θ^{3D}	3.043	6.022	2.853	6.231	1.017	0.04076
	$M=200$					
SOL-θ^{a}	4.284	7.732	3.593	-19.57	-2.392	-0.08991
SOL-θ^{1D}	3.207	6.064	2.853	2.575	0.9161	0.04055
SOL-θ^{3D}	3.042	6.020	2.853	6.223	1.016	0.04071
	$M=300$					
SOL-θ^{a}	4.284	7.732	3.593	-19.60	-2.393	-0.08991
SOL-θ^{1D}	3.207	6.063	2.853	2.573	0.9158	0.04054
SOL-θ^{3D}	3.042	6.019	2.853	6.221	1.016	0.04070

Table 7.6: Thermo-mechanical assessment for FGM applications, and 3D-calculated thermal profile; the reference solution is the asymptotic method for the thermal stress analysis in [134]. The exponential matrix is expanded to the third-order; tentative fictitious layer numbers are considered.

considered. The other two models provide different results because, as discussed, they leave out some effects. SOL-θ^{1D} is still quite close to the previous model and tends to coincide with it as the thickness decreases. On the other hand, SOL-θ^{a}; the linear temperature profile is, therefore, an unacceptable assumption for FGM-embedding structures. Table 7.6 evaluates the dimensionless displacement $\bar{w}$ and and stress $\bar{\sigma}_{zz}$ components at specific $\bar{z}$ coordinates. Those indications are further confirmed by the plots shown in Figures 7.9-7.11. The comparison between the temperature profiles of a thin and a moderately thick plates is presented in Figure 7.9. In both cases, the θ^{a} temperature profile does not grasp the change of the thermal properties along the thickness direction, and it is very far from those calculated by solving the heat conduction equation. Both the θ^{1D} and θ^{3D} grasp the FGM law, get closer as the shell becomes thinner, the effect of thickness plays a marginal role, and a one-dimensional equation well approximates the problem. Since the temperature is a field load, this affects the mechanical response. SOL-θ^{a} is very distant from the real behavior of the structure; SOL-θ^{1D} gives a more accurate estimate the thinner the shell.

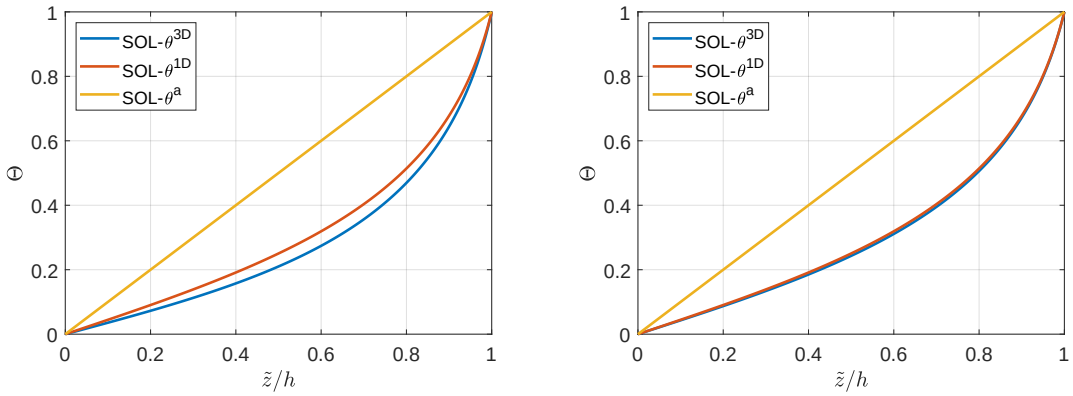

(a) $a/h = 4$ (b) $a/h = 10$

Figure 7.9: Third assessment: temperature profiles along with the thickness direction for two different thickness ratios.

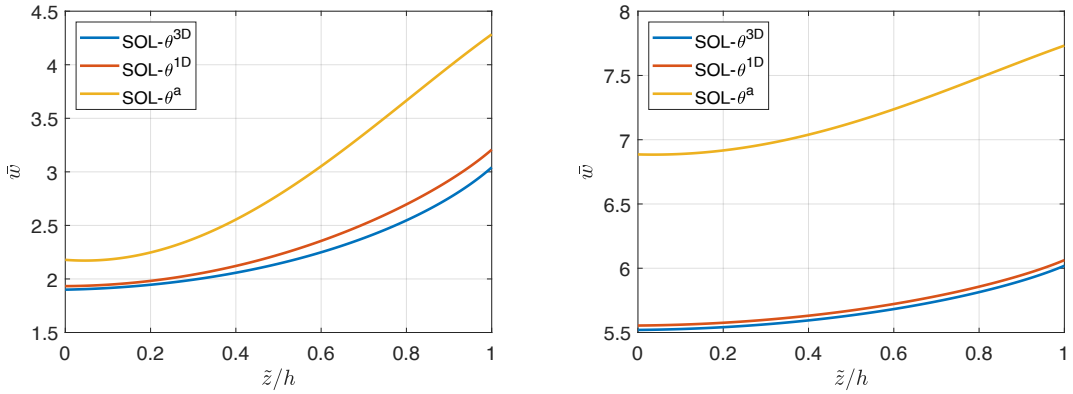

(a) $a/h = 4$ (b) $a/h = 10$

Figure 7.10: Third assessment: dimensionless displacement component $\bar{w}$ profiles along with the thickness direction for two different thickness ratios.

7.5.4 Conclusions

Following the assessments this model for hygro-thermal stress analysis can be considered as validated. The formal treatment of the problem, and the assessments, have been proposed for the thermal case only. However, the moisture content field is governed by the same mathematical relationships, and its effect can be studied identically. The elastic part of the model is derived from a previously established elastic exact solution. By exploiting the exponential matrix method already implemented to resolve the indefinite equilibrium equations, the thermal (and hygrometric) loads have been transformed into a corrective load of a (possible) external

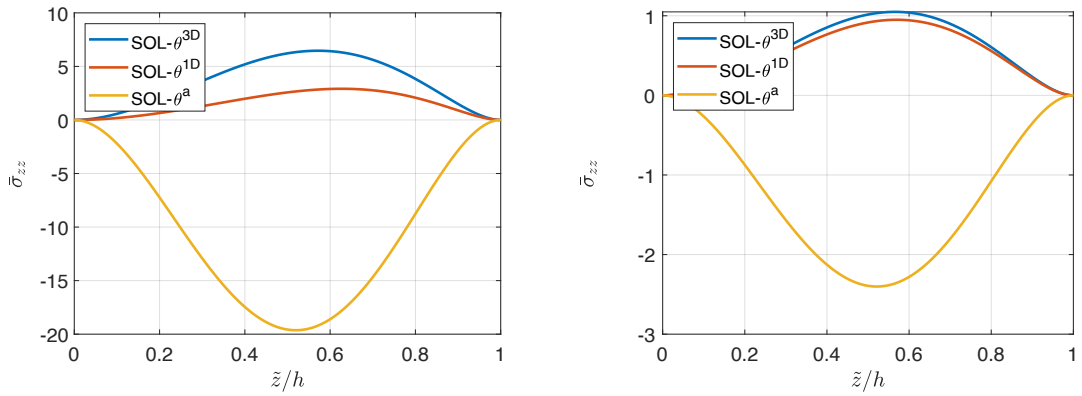

(a) $a/h = 4$ (b) $a/h = 10$

Figure 7.11: Third assessment: dimensionless stress component $\bar{\sigma}_{zz}$ profiles along with the thickness direction for two different thickness ratios.

mechanical load. This model provides an exact solution to the problem, as it explicitly solves the governing equations. Still, it analyzes simple problems in terms of geometry, boundary conditions, and variables fields. As such, it can be used to validate numerical solutions, not burdened by such strong assumptions. Depending on the formulation, numerical solutions calculate the distribution of temperature and moisture content in different ways. For this reason, the 3D heat conduction (and moisture content diffusion) equations have been considered, along with their simplified one-dimensional version. To be thorough, the assumed-linear temperature profile has also been considered. The results proposed in the assessments demonstrate how a validated elastic model is not sufficient if the thermal profile is not evaluated correctly. Assuming Θ^a as a profile involves a considerable loss of detail, negligible only for transversely isotropic and very thin structures. On the other hand, Θ^{1D} provides a good approximation even with complex laminations when the thickness of the structure is not excessive.

Chapter 8

Conclusions

8.1 Work outline and concluding remarks

This thesis aims to improve the mechanical behavior understanding of additively manufactured FFF parts to define a constitutive model. This point is of fundamental importance to define compliance with the performance criteria of the designed items, and to qualify the transition of technology from prototyping to the production of functional components. Three different perspectives run through the dissertation in its entirety, intertwining and complementing each other: theoretical, numerical, and experimental approaches.

Chapter 1 introduces the problem, presenting the Fused Filament Fabrication technology, the material, and printer used throughout the research work. It provides an outline of the operating principles and the main process parameters, also discussing the path from CAD model to a real component. It establishes a technical vocabulary for future references and introduces the themes of anisotropy and lack of standardization.

Chapter 2 aims to define a coherent approach to FFF-printed components to determine a constitutive model. In this context, the dissertation retraces the micromechanics, and macromechanics approaches already present in the literature, discussing the lack of predictive models applicable to finished components and validated with actual boundary conditions. Quasi-solid elements with a linear infill seem to underline an (at least geometric) similarity with unidirectional composites. By drawing a parallel and emphasizing the crucial distinctions, the chapter proposes describing the mechanical behavior through the Classical Lamination Theory. In this regard, it retraces the theory to frame the characteristics of future characterization tests.

Chapter 3 describes the mechanical characterization process conducted with a view to CLT. The aim is to fill the absence of standardized test methods for FFF 3D-printed components. Once established the unsuitability of the test methods adopted for conventionally processed polymers, the dissertation proposes a set-up similar

to that used in the case of composite materials. It is a new and unconsolidated approach; consequently, a set of DoEs is presented to design the tab geometry, ensuring a uniform load introduction into the specimens. Once the tensile and shear tests have been completed, it provides the elastic coefficients necessary to define the 2D orthotropic material stiffness matrix. The main findings of this chapter can be summarized as follows:

- Parts produced via FFF have an anisotropic behavior; this behavior can be traced back to a simpler and mild orthotropy if the print features a linear and 100% infill.
- As a consequence of the previous point, the mechanical properties differ according to the evaluation direction. Along the filament deposition direction (direction 1), the stiffness modulus is slightly lower than the one observed in the feedstock filament. In the two directions perpendicular to it (direction 2, in the printing plane, and direction 3 outside the printing plane), a slight decrease in the stiffness modulus is observed, in the same order of magnitude (about 4%).
- Of considerable importance is the variability found in the tensile strengths. The difference found with the feedstock filament values is minimal in direction 1 (56 MPa, -3.5% to the reference value). However, it considerably increases when considering direction 2 (46.2 MPa, -20%) and becomes critical when considering direction 3 (17.5 MPa, -70%).

Chapter 4 aims to check whether CLT can actually describe the mechanical behavior of FFF-printed parts if tuned with the mechanical properties previously determined. To this end, the dissertation discusses a three-point bending test and bending/bending-torsion tests on a cantilever beam with a point load at the tip. The outcome of tests is simulated through 2D FE models, tuned with three different constitutive models, to allow comparison. The first considers the 2D orthotropic properties, the second the measured isotropic properties of the feedstock filament, and the third the properties reported by the manufacturer. The dissertation shows that:

- The mechanical response prediction of thin components, predominantly arranged in the $1-2$ plane, is excellent when the model is tuned with 2D orthotropic mechanical properties following the CLT approach. More significant inconsistencies arise if an isotropic constitutive model is considered. If the feedstock filament determines the isotropic properties, the errors can be considered as acceptable, as they are less than 8%. The filament datasheet properties must always be verified to establish that they reflect the filament and not its precursors.

Chapter 5 proposes a preliminary evaluation of the compression properties of FFF-printed parts. This aspect has received little attention, but its assessment is of fundamental importance for discussing a future failure criterion and considering buckling phenomena. In this context, the dissertation examines that:

- The mechanical properties in compression can differ from those in tension; this has been experimentally verified for direction 3. In this context, the difference is considerable and must be considered, especially when dealing with bucking phenomena. A reasonable estimate of the critical loads can be obtained using isotropic constitutive models. Still, these must reflect the mechanical properties in compression to return consistent results.

Chapter 6 discusses an application example. The newly validated approach and its mechanical properties are used to verify the structural behavior of some simple frame elements of a 3D-printed UAV. This application is limited to the mechanical response of some specific components due to their geometry and mesostructure. This highlights the importance of developing the characterization up to the complete definition of the 3D orthotropic matrix.

Chapter 7 proposes the starting point of a dedicated tool for 3D printing optimization: an exact layer-wise 3D solution for hygrothermal mechanical analysis of multilayered structures. This need arises from the differences found in terms of modulus of elasticity and especially tensile strength, requiring a layer-wise evaluation of the mechanical response of FFF parts. The stress tensor components must be carefully evaluated in the material reference system to validate the structural performance of a functional element. In the perspective of an ad-hoc tool for structural assessment of polymeric 3D-printed components, the effects of thermal and hygrometric loads must be evaluated because they play a significant role due to the limited mechanical performances of polymers. Reference methods from the consolidated literature validate the solution. The ability to manage different ways of calculating temperature and moisture content profiles allows the following consideration: significant differences arise in the mechanical performance with a simplified and not explicitly calculated profiles, as temperature and moisture content act as field loads.

The dissertation also consists of three appendices, which complement the work. Appendix B discusses that:

- The displacement ad strain monitoring on polymeric samples can be successfully accomplished with a non-contact system, the Digital Image Correlation. Compared to traditional contact systems, this avoids any mutual influence between the specimen and the transducer. Contact instruments locally alter the field of deformations in components with a low stiffness modulus. In the PLA case, this effect is confirmed, despite limited, but it would increase its importance in less rigid configurations.

Appendix A examines the tensile properties of the feedstock filament to provide a benchmark and assess the details of the material datasheet. In this context, it proposes two set-ups, overcoming the absence of a standardized procedure. Appendix C reports all the experimental results per specimen. Appendix D details the 2D drawings of the supports designed in the research activity framework for different experimental tests.

8.2 Future work

This dissertation is part of an ambitious long-term goal: an ad-hoc tool dedicated to structural analysis and optimization of 3D-printed components. It traces this path by proposing and validating a simplified approach; the results pave the way for future research, including:

- To extend the mechanical characterization campaign to define a 3D orthotropic constitutive model.
- To validate this constitutive model through more general tests from the geometric and boundary conditions perspectives.
- To extend the compression properties evaluation to the two remaining principal material directions.
- To define and validate a failure criterion.
- To explain the link between the feedstock filament properties and the finished part ones.
- To implement these results in an analytical tool, necessary to validate future numerical tools.

Appendix A

Tensile test over PLA filament

A set of tensile tests has been performed on the a PLA filament to characterize its mechanical properties before the 3D printing process took place. These tests aimed to provide a benchmark for the mechanical properties of the printed components, assessing the details discussed in the feedstock material datasheet. Provided that no standardized test method exists for tensile properties determination on polymeric filaments for FFF applications, two experimental set-ups are proposed. Similar applications in other fields inspire the first set-up; the tensile strength is determined, but not the elastic modulus due to difficulties in monitoring the tensile strains. A second set-up with an innovative gripping system is then proposed.

A.1 Introduction

The technical data sheets accompanying commercial-grade filaments often indicate some mechanical properties. The filament production process can be simplified as follows: natural raw PLA pellets are dried, mixed with selected additives (the colored pigments, for example), brought to temperature, and extruded in the form of a filament. As also anticipated in Table 1.1, the considered filament reports in its data-sheet the following indication:

$$E^{RAW} = 3950\text{MPa} \qquad \text{via ASTM D638} \tag{A.1}$$

ASTM D638 is the standard test method for tensile properties determination in polymers, providing a dog-bone specimen for tensile properties determination. This rules out that the mechanical properties have been determined directly from the filament. Despite this exclusion, it is not clear whether the assessment considered:

- the polymer processed via FFF, and if so, with which printing parameters;
- PLA pellets cast into a mold, and if so, at what stage concerning drying and additives addition.

A preliminary assessment of PLA mechanical properties before the FFF process has been necessary due to these uncertainties. Two different filament lots have been considered to quantify the mechanical properties scatter over different batches, with the same color, manufacturer, and compound:

- Filament A, manufactured in 2019, and used in all mechanical tests included in this word.
- Filament B, manufactured in 2020.

In the following, a large number of specimens, and two different set-ups, will be considered. Figure A.1 illustrates the nomenclature used for their identification to facilitate the reading and referring to the results.

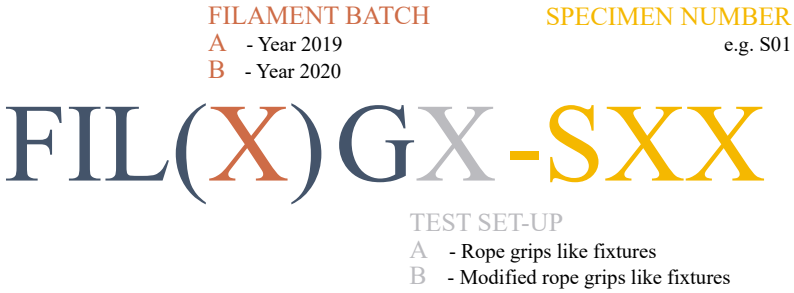

Figure A.1: Nomenclature definition for filament specimens.

No standard test method for polymeric 3D-printable filaments exists until now; reference has been made to standardized tensile tests in analogous evaluations, which involve threads, twines, ropes, and wires to get guidance. Excluding all set-ups dedicated to metallic materials, a starting point can be considered the Standard Test Methods for Tensile Testing of Aramid Yarns, issued by ASTM under the designation D7269 [136]. The set-ups required by other regulations, such as, for example, ASTM C1557 [137], are ineffective due to the diameter of the filament: in that case, the specimens are expected to have a maximum transverse dimension of 0.25 mm, while FFF filament is 1.75 mm in diameter. In these fields, the specimen is in the form of a yarn or a cord. *Rope grips* are used for tensile load application; an example is shown in Figure A.2a. The yarn is wound around a drum one or more times, depending on the geometry of the specific grip; one end is secured into a vise fixture, one goes towards the other grip. The friction between the string and the drum plays a key role, and string winding increases the frictional area. The target is to avoid specimen slippage or failure due to stress concentrations into the vise. Those grips (i.e., the drum diameter) are designed considering the estimated maximum load carried out by the string before failure. A modified version of rope grips are the so-called *bollard grips*[1]; the scope is the same. The string is wrapped

[1]In harbors, bollards are thick and solid columns used for rope wrapping in boat anchoring.

(a) Rope grip (b) Bollar grip

Figure A.2: Instron rope and bollard grips. Copyright © 2014 Illinois Tool Works Inc. All rights reserved.

around the bollard; one end is secured into a vise fixture, one goes towards the other grip. The bollard diameter depends on the specimen estimated strength; the higher, the larger the diameter [138].

A.2 Filament strength determination

These fixtures are a niche device and were not available among the laboratory equipment. Figure 3.2 already showed the standard fixture for tensile tests onboard the MTS QTest Elite. The operation is simple: the two plates get closer and tighten a flat item by operating the handles. In contact with the item, the two inner sides of the plates are provided with a knurled surface to prevent slipping. Note that a socket is present between the plates and the fixture body, already used in Chapter 3 to house the tensile specimens alignment support. An adapter has been specifically designed to turn the standard tensile test into a rope grips-like fixture.

A.2.1 Design of rope-grips like fixture

Figure A.3a shows an exploded view of the assembly. The adapter is positioned into the socket of the fixture body. Figure A.4 shows better its geometry. It is a 3D-printed PLA element, characterized by two horizontal flat surfaces, over which the two metallic plates can slide; between the two, a higher element stands, characterized by a rounded pocket. This pocket is the seat for a metallic disk. The pocket radius is the same as the metallic disk; needless to say, this element

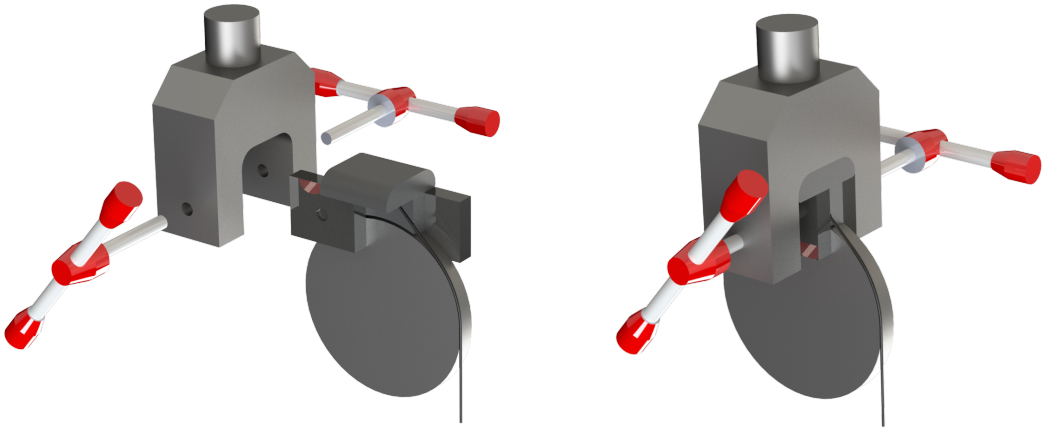

(a) Exploded view (b) Compact view

Figure A.3: Rope grips-like fixture assembly.

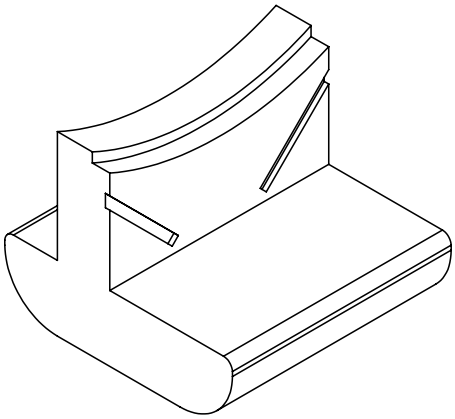

Figure A.4: Geometry of the rope grips-like fixture adapter.

supports the disk, preventing its translations during the assembly. Once tightened, the two plates act as a constraint for the disk, making the components a solid group. To allow the filament to be wrapped with a certain number of winding onto the disk, an appropriate clearance has been designed into the disk support; given the disk thickness and the filament diameter, a maximum number of 3 winding are possible. A vise fixture for the filament ends has been designed as a socket facing one metallic plate, characterized by a lower thickness than the filament diameter. In this way, once the two metallic plates are tightened, the specimen end is also clamped. The description is valid for both the top and the lower fixture; to keep the filament parallel to the load application direction, the top and the bottom fixture are anti-symmetric so that the filament exits both on the same side.

A.2.2 Test set-up

The number of winding is an initial design parameter. A preliminary set of tensile tests have been performed with different windings to evaluate any influence and derive the optimal configuration. All the tensile tests are in displacement control, with the upper grip moving away from the lower one at 5 mm/min. This testing speed has been selected for coherence with the general practices for tensile tests in polymers. During each test, the machine control system sampled the applied load and the imposed displacement at a frequency of 5 Hz. Figure A.5 shows the

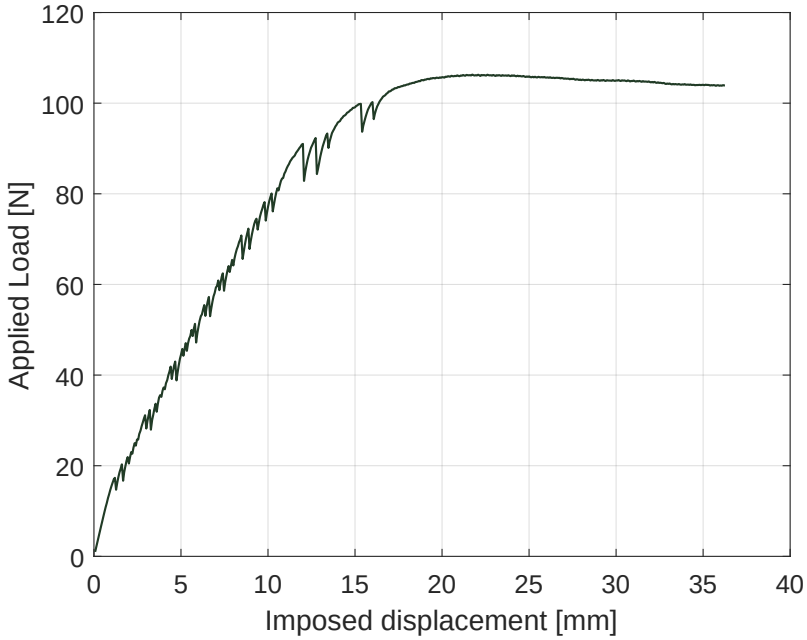

Figure A.5: Preliminary tensile test on PLA filament; two-windings configuration.

applied load vs. imposed displacement curve obtained for a representative filament in the 2 windings configuration. The trend is evident; the curve evolves with a linear relationship between the two variables, followed by a wide non-linear (and plastic) deformation region. However, the curve features several and frequent oscillations: those singularities manifested when the filament sections winded on the cylindrical plate slipped forward in the direction of the filament under tension. On the other end, the zero-winding configuration led to a smoother relation between the two variables, as shown in Figure A.6. No slippage took place, failures occurred in the region between the two circular plates, and no necking of the filament seemed to be induced close to the clamp. Plus, the preliminary specimens sustained higher loads than those in nonzero-winding configurations. So this suggests that no stress-concentration occurred. The applied load vs. imposed displacement curve features an initial behavior, which corresponds to filament line-up with the load application

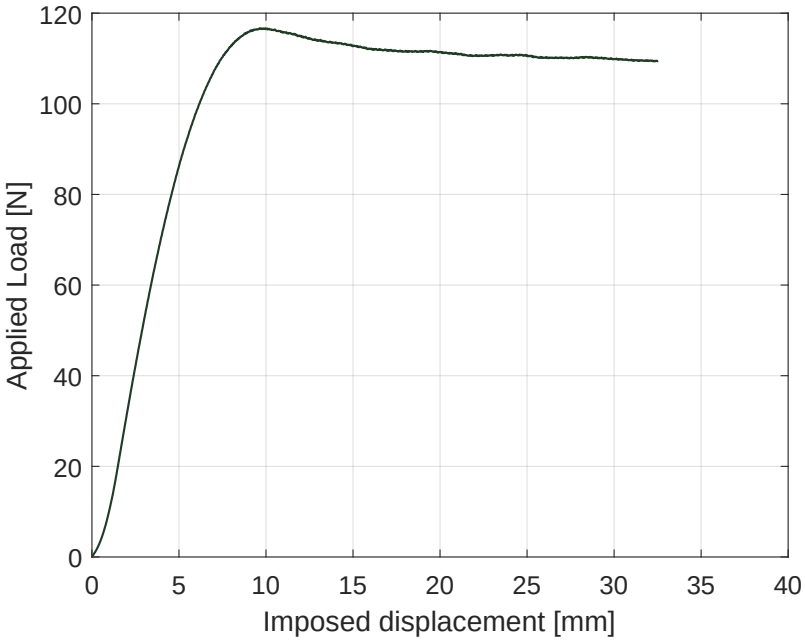

Figure A.6: Preliminary tensile test on PLA filament; zero-windings configuration.

direction, a linear behavior, and a wide plastic deformation region at an almost constant load. With this set-up in mind, concerns arose on how to determine the tensile properties. The stress σ_{fil} derives from the applied load L, divided for the initial cross-section of the filament A_{fil_0} (see Equation A.2); the tensile strength is its maximum recorded value.

$$\sigma_{fil} = \frac{L}{A_{fil_0}} \tag{A.2}$$

The stress vs. strain necessarily requires evaluating the tensile strain; this is also a pre-requisite for quantifying the stiffness modulus of the filament. Contact transducers are challenging to apply here given the transverse dimensions of the filament and its shape; for the same reason, non-contact systems (e.g., DIC) experienced difficulties in correlating such a thin body. A solution could come from the classical definition of strain, the ratio between elongation and initial length; however, the filament free length is not very useful, as it varies during the test. The sections of the specimen in contact with the metallic discs undergo a stress state, too: as the load increases, they move towards the free length.

A.2.3 Results and discussion

This first experimental campaign, therefore, stops at the load vs. displacement relation (see Figures A.7a-A.7b) and at the tensile strengths σ_{fil}^{max}, whose values

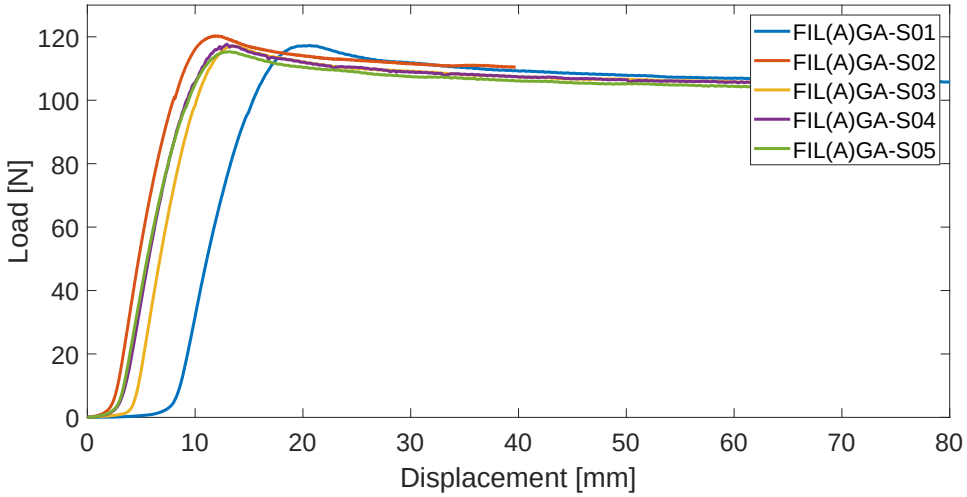

(a) FIL(A) sample.

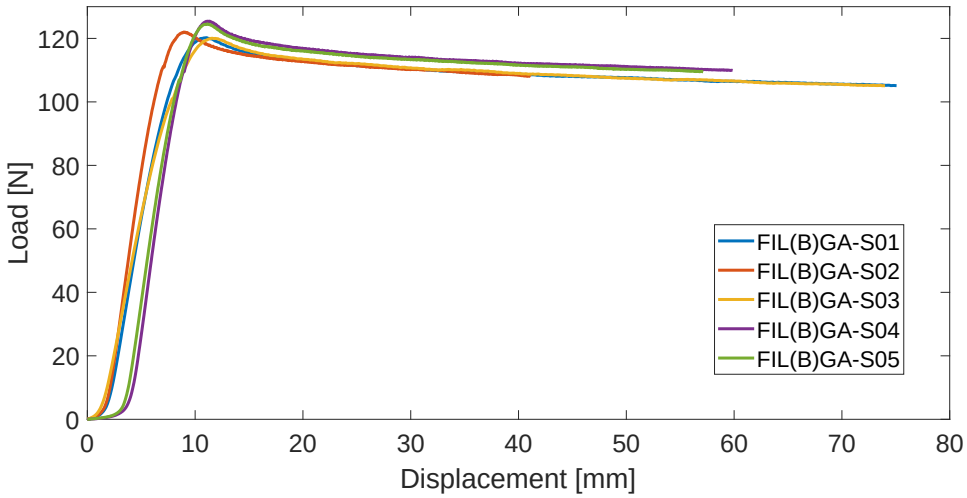

(b) FIL(B) sample.

Figure A.7: Filament strength determination: applied load vs. imposed displacement curves for FIL(A) and FIL(B) samples.

Table A.1 summarizes. A total number of 5 specimens has been considered; their diameters d^{fil} have been measured with a digital caliper before the test took place. The results in terms of PLA filament strength turned out to be in line with the raw material value reported in Table 1.1, even if a bit lower. This underlines the importance of this preliminary assessment. Also, note the small difference between the 2020 batch filament, FIL(B), and 2019 one, FIL(A), showing a little variability between samples of the same manufacturer. It is not clear, at this stage, whether

Filament A			Filament B		
	d_{fil} [mm]	σ_{fil}^{max} [MPa]		d_{fil} [mm]	σ_{fil}^{max} [MPa]
FIL(A)GA-S01	1.60	58.35	FIL(B)GA-S01	1.60	59.85
FIL(A)GA-S02	1.60	59.88	FIL(B)GA-S02	1.60	60.70
FIL(A)GA-S03	1.60	58.25	FIL(B)GA-S03	1.60	59.75
FIL(A)GA-S04	1.60	58.55	FIL(B)GA-S04	1.60	62.40
FIL(A)GA-S05	1.60	57.38	FIL(B)GA-S05	1.60	61.96
FIL(A) sample			FIL(B) sample		
mean	1.60	58.48	mean	1.60	60.94
st.dev	–	0.81	st.dev	–	1.08

Table A.1: Filament strength determinations: mechanical results obtained using the rope-grips like fixtures.

this variability depends on the aging of the sample.

A.3 Filament modulus determination

The rope grips-like did not allow the strains to be monitored, thus preventing the elastic modulus quantification. This section proposes and validates modified grips and a dedicated set-up designed to deal with a confident measuring of the free length through which the strains can be evaluated.

A.3.1 Design of the new grips

The idea behind this modified gripping system is still to design an adapter to turn the standard tensile test into a rope grips-like fixture, however, by changing the load transmission mode to prevent the specimen from slipping. Figure A.8b shows an exploded view of the assembly. The adapter is made of two parts, here too positioned into the socket of the fixture body. Figure A.8b better shows their geometry. Once assembled, two elements feature a slot that evolves with the same radius of curvature of the metallic disc. The cross-section of such slot develops following an inclined plane, inducing a gradual constraint. Observe Figure A.9: the filament portion facing downwards undergoes tensile tests as a similar device supports it at the bottom. The filament evolves along with the slot; the sideway filament does not participate in the test. The cross-section dimensions induce a perfect constraint sideways. Instead, the downward exit section induces only a slight compression of the filament, which limits its sliding. If the filament does not slip during the test, it is possible to measure the initial length L_0 at instant zero and use it for strain calculation.

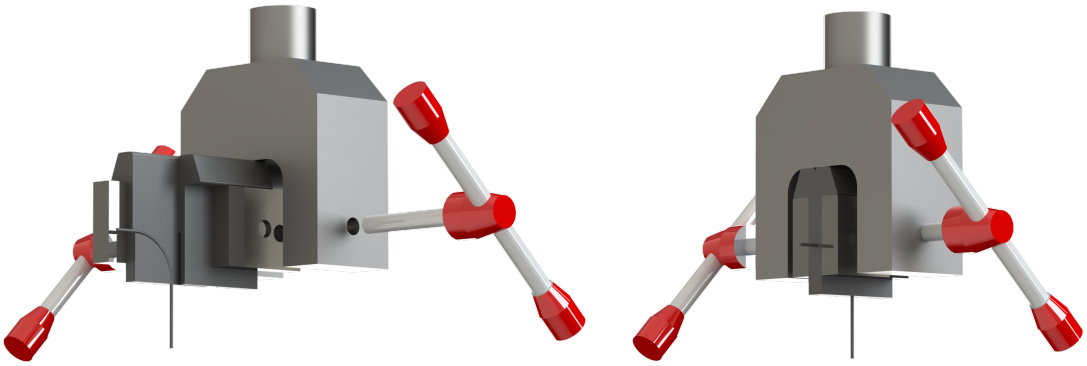

(a) Exploded view (b) Compact view

Figure A.8: Modified rope grips-like fixture assembly.

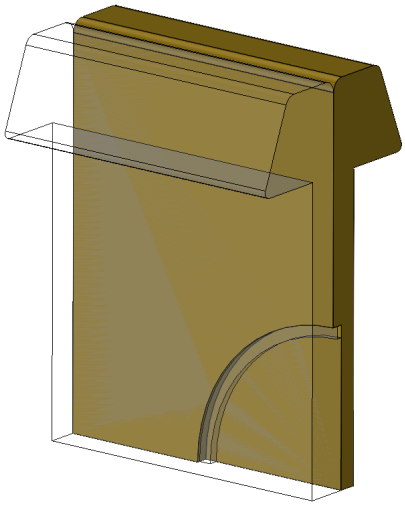

Figure A.9: Geometry of the modified rope grips-like fixture adapter.

A.3.2 Test set-up

A total number of 10 specimens has been tested per filament sample. The filament needs to be perfectly straight to measure its length; as the filament positioning is manual, following procedure has been implemented to ensure this requirement.

- 250 mm long specimens have been obtained from FIL(A) and FIL(B) spools. This value represents the overall length, not the actual length that undergoes tensile loading, due to the end constraints and manual positioning;
- each specimen is installed into the grips, respecting its curvature due to previous storage into spools;

Filament A			Filament B		
	l_0 [mm]	d_{fil} [mm]		l_0 [mm]	d_{fil} [mm]
FIL(A)GB-S01	226	1.60	FIL(B)GB-S01	198	1.60
FIL(A)GB-S02	224	1.60	FIL(B)GB-S02	200	1.60
FIL(A)GB-S03	219	1.60	FIL(B)GB-S03	202	1.60
FIL(A)GB-S04	218	1.60	FIL(B)GB-S04	202	1.60
FIL(A)GB-S05	220	1.60	FIL(B)GB-S05	204	1.60
FIL(A)GB-S06	219	1.60	FIL(B)GB-S06	207	1.60
FIL(A)GB-S07	220	1.60	FIL(B)GB-S07	208	1.60
FIL(A)GB-S08	222	1.60	FIL(B)GB-S08	210	1.60
FIL(A)GB-S09	220	1.60	FIL(B)GB-S09	214	1.60
FIL(A)GB-S10	212	1.60	FIL(B)GB-S10	216	1.60
FIL(A) sample			FIL(B) sample		
mean	222	1.60	mean	206	1.60
st.dev	5.06	–	st.dev	5.66	–

Table A.2: Filament modulus determinations: geometrical dimensions of the specimens.

- a pre-load $P = 20$ N is applied before the test takes place; in this way, the filament takes a straight shape, abandons the initial curvature, and results wholly aligned with the load application direction;
- the filament initial length l_0 and diameter d_{fil} are measured (see Table A.2);
- the testing machine moves at a constant displacement speed of 5 mm/min.

During the test, the machine control system measured the applied load and the imposed displacement. The tensile stress σ_{fil} has been calculated with Equation A.2, considering the preload P into the load L. The tensile strain has been calculated through Equation A.3.

$$\epsilon_{fil} = \frac{\Delta L}{l_0} \tag{A.3}$$

A.3.3 Results and discussion

Figure A.10 shows the preliminary stress vs. strain curves for both the samples, allowing some considerations.

- All the specimens show the classic and initial linear elastic behavior. Before the maximum load, there is a noticeable non-linear deformation region. Once the highest stress is exceeded, the specimens fail; however, there is a

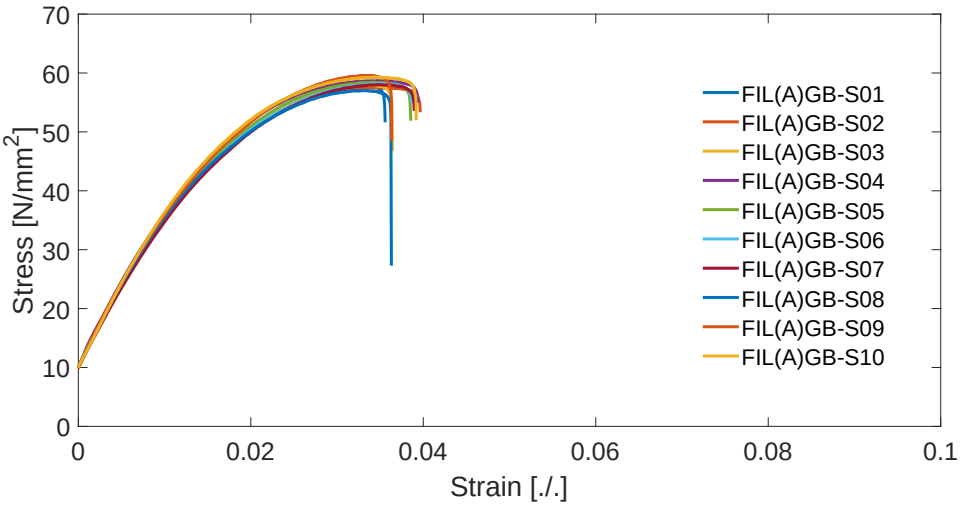

(a) FIL(A) sample.

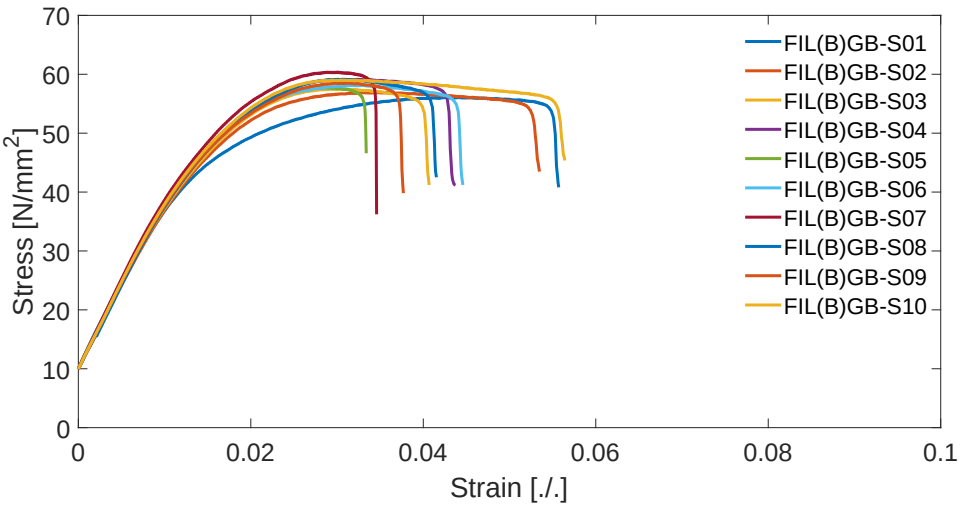

(b) FIL(B) sample.

Figure A.10: Filament modulus determination: preliminary stress vs. strain curves for FIL(A) and FIL(B) samples.

fair amount of variability. FIL(A) samples failed suddenly, FIL(B) coupons showed a more or less pronounced plastic region.

- All curves start at non-zero stress. This comes from the strain measuring, which started from the preload stress.

The second issue can be addressed by calculating the angular coefficient of the linear section and offsetting the curves to start from the origin. The angular coefficient

is none other than the stiffness modulus. This approach is not unusual but present in all the standard test methods for mechanical characterization, expecting a linear relationship between two variables. All of them discuss that the initial part of the experimental curve is a toe region, not representing the mechanical behavior of the material. It must be offset, considering the slope of the linear section. Therefore, this set-up disregards a small amount of the stress vs. strain relation; however, this region features very low tensile loads, corresponding to where the toe region is expected to occur.

The elastic modulus has been calculated through a set of linear regressions on intervals of gradually increasing size. The iteration stop when the new linear regression coefficient differs from the mean of the previously calculated value by more than 5%. The offsetted curves are given in Figures A.11a-A.11b; together with the tensile strengths, they are summarized in Table A.3.

Filament A			Filament B		
	σ_{fil}^{max} [MPa]	E_{fil} [MPa]		σ_{fil}^{max} [MPa]	E_{fil} [MPa]
FIL(A)GB-S01	58.02	3195	FIL(B)GB-S01	56.32	3181
FIL(A)GB-S02	57.75	3004	FIL(B)GB-S02	57.27	2927
FIL(A)GB-S03	58.09	3425	FIL(B)GB-S03	57.84	3198
FIL(A)GB-S04	58.90	3592	FIL(B)GB-S04	59.32	2962
FIL(A)GB-S05	58.52	3476	FIL(B)GB-S05	57.96	3272
FIL(A)GB-S06	58.45	2998	FIL(B)GB-S06	58.41	3081
FIL(A)GB-S07	58.23	3024	FIL(B)GB-S07	60.38	3343
FIL(A)GB-S08	57.08	3021	FIL(B)GB-S08	59.32	2925
FIL(A)GB-S09	59.67	3327	FIL(B)GB-S09	58.79	3020
FIL(A)GB-S10	59.44	3235	FIL(B)GB-S10	59.32	3025
FIL(A) sample			FIL(B) sample		
mean	58.42	3196	mean	58.49	3093
st.dev	0.73	208	st.dev	1.12	140

Table A.3: Filament modulus determinations: mechanical results obtained following the modified rope grips-like fixtures.

Comparing the results obtained in terms of tensile strength with those reported in Table A.1: they are coincident for FIL(A) sample and coherent (even if slightly lower) for FIL(B) sample. The mechanical behavior certainly differs, as demonstrated by the absence of an extensive plastic deformation region. However, using the comparison in terms of tensile strength as a benchmark, it can be inferred that no excessive stress concentration occurs due to the proposed fixtures, at least until the applied stress reaches the tensile strength. It can be further speculated that this set-up is suitable for studying the mechanical behavior of FFF filaments only up

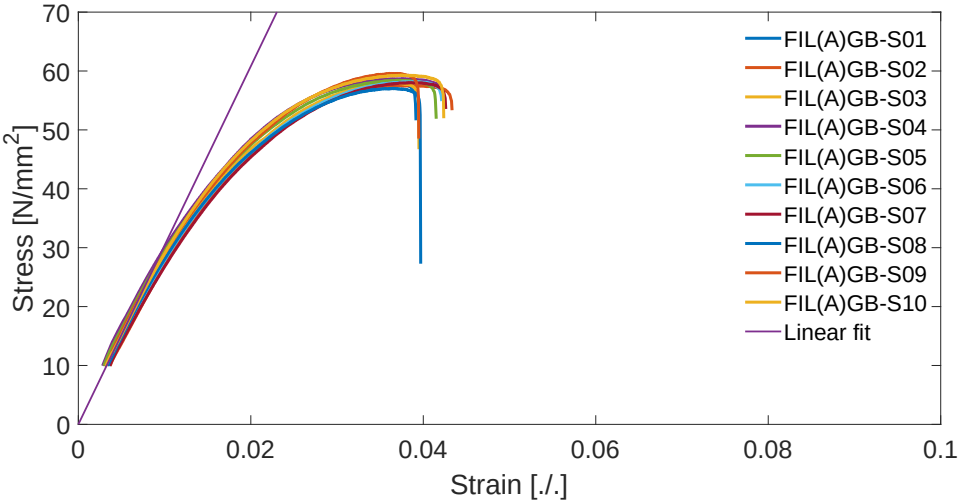

(a) FIL(A) sample.

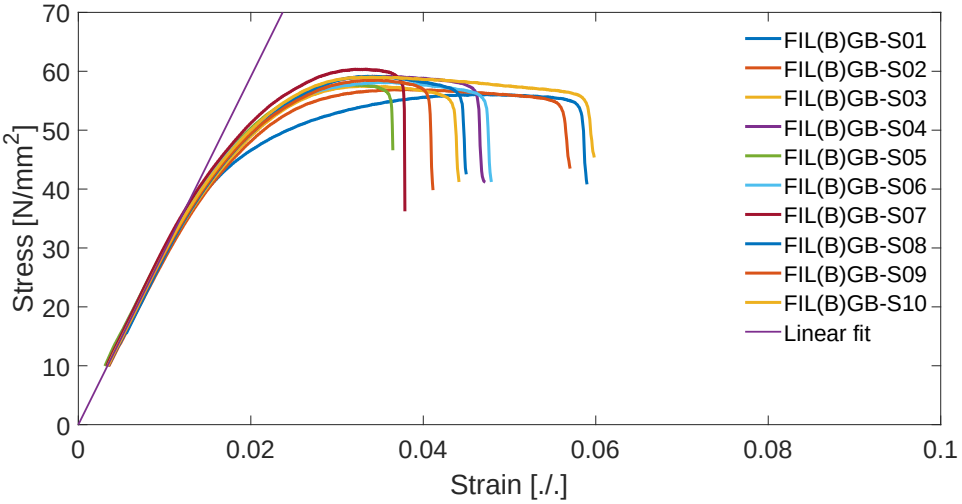

(b) FIL(B) sample.

Figure A.11: Filament modulus determination: offsetted stress vs. strain curves for FIL(A) and FIL(B) samples.

to tensile strength as it does not allow exploring the entire deformation field. Note the average values of the stiffness modulus. For both samples, they are considerably lower than stated in the datasheet. Taking $E^{RAW} = 3950$ MPa as a reference, filament A recorded a lower stiffness modulus of -19%, while B of -20%. Again, a slight difference is present between the results obtained from the two filaments, showing a little variability between samples of the same manufacturer.

Appendix B

Digital Image Correlation

The entire work relies on an extensive mechanical test campaign: tensile, compressive, and bending tests are discussed throughout the thesis. Except in special cases, all these tests require external monitoring of displacements and deformations induced by the boundary conditions. Since a material with a low stiffness modulus has been considered, initial concerns arose about the technique to be considered. As this appendix will discuss, evidence shows that in-contact instruments can affect the mechanical response of polymeric specimens. Digital Image Correlation (DIC) proved to be the most suitable candidate, as it is a non-contact optical-numerical method for displacements-measuring and deformations-calculation with a simple and low-cost set-up. This appendix[1] gives an overview of the technique and quantifies the effects of a strain-gauge installation on a polymeric specimen to qualify the choice.

B.1 Introduction

The overall work of this research project relied on a heterogeneous group of mechanical tests. Some of them are meant to determine certain mechanical properties; others study a particular mechanical phenomenon; others still serve as validation tests. The complete study of these tests requires evaluating the effects induced by the boundary conditions in terms of displacements and deformations. More specifically, the following overview retraces each test indicating which quantities to monitor.

Tensile tests, described and dealt within Chapter 3. These tests are used to determine some elastic constants to define the 3×3 stiffness matrix. The specimen has a constant rectangular cross-section along its entire longitudinal axis. Its front

[1]Part of the work described in this appendix has been previously published in [139]

surface should be monitored to determine longitudinal and transverse strains. The first one allows evaluating the tensile stiffness modulus in the load application direction; the latter is used to quantify the Poisson ratio.

Shear tests, described and dealt within Chapter 3. These tests are used to determine the shear modulus G_{12} to complete the 3×3 stiffness matrix. The specimen has a constant rectangular cross-section along its entire longitudinal axis. Its front surface should be monitored to determine longitudinal and transverse strains to calculate the shear strain and then evaluate the shear modulus.

Bending/torsion and bending tests, described and dealt within Chapter 4. These tests validate that the mechanical response of 3D-printed PLA could be described through the 3×3 reduced stiffness matrix. In three-point bending tests, the testing machine directly measures the centerline deflection. In studying the bending of a cantilever beam with constant cross-section and a point load at the tip, the end deflection must be measured externally. In studying the bending-torsion of the same beam, it is also necessary to measure the deflection gradient in the transverse direction to consider the section out-of-plane warping.

Compressive tests, described and dealt within Chapter 5. These tests are used to evaluate the out-of-plane compressive properties and to study the buckling phenomenon. The specimen has a constant square cross-section. The longitudinal strain serves to determine the elastic modulus in compression. The transverse displacements are used to monitor the occurrence of buckling.

Tensile tests on FFF filament, described and dealt with in Appendix A. Due to its small cross-sectional size, direct monitoring of axial deformation is complex. For this reason, the grips have been modified to precisely define the initial length of the specimen and calculate the strain from the displacement sampled by the testing machine.

The case studies are very heterogeneous. In some cases, measuring the strains in two directions perpendicular to each other is required. Other tests require measuring one or more displacements in a single direction. In others, a strain and a displacement in two different directions need simultaneous monitoring. It is vital to select techniques allowing precise measuring.

The literature provides many points of interest, discussing instruments that contemplate surface contact and others that carry out remote monitoring [140]. Strain Gauges (SGs) are commonly used to measure deformations [141]; however, it is a matter of concern that their installation might alter the strain field, especially in materials with a low stiffness modulus [142]. The impact of this point must be quantified and taken into consideration to avoid tainting the results. Clip-on extensometers offer an alternative; however, there are two difficulties to be addressed. They are provided with a pair of teeth perpendicular to the measurement direction. When the strains in two orthogonal directions have to be quantified, only bi-axial

extensomenters can be used, not always available among laboratory instruments. The second point is related to the indentation effects that the teeth can produce on soft materials. Embedded Fiber Bragg Grating can be used in plastics [143]. Their influence on the mechanical response of materials is nil; however, they have to be installed inside the component to be monitored during its manufacturing, following dedicated processing [144]. A solution to these problems is remote monitoring systems, such as DIC, video extensometers [58], or laser extensometers. These instruments stay at a distance from the specimen, observing its surface [145]. The disadvantage of these approaches is that the surface must be in view, requiring some distance, and stationary. DIC is extremely interesting for two respects. It directly determines the displacements and calculates the strains from them, providing a complete solution for all analysis cases discussed above. This guarantees homogeneity in the results because all the measurements exploit the same instrument; through this approach, different instruments for deformations and displacements are unnecessary, simplifying the calibration procedure. Furthermore, the set-up is straightforward: dedicated systems exist, but 2D DIC can also rely on DSLR cameras associated with a dedicated post-processor.

B.2 The Digital Image Correlation

The concepts behind DIC can be traced back to the early 1970s [146]; already in 1975, researchers discussed improved algorithms able to conjugate images with a different timestamp to correlate a displacement that took place between the two [147]. Shortly after [148], DIC started to be used in experimental stress analysis. The idea is simple: given a *reference image* of an object at rest (still/undeformed), and a set of *current images* obtained in subsequent instants, a comparison is made to detect and measure the displacements (if any) [149]. Digital images are processed, making this method extremely flexible and applicable to a wide range of scales, allowing very accurate analyses in any well-lit environment. All DIC algorithms track the grey distributions over the surface to be correlated; consequently, the only set-up that needs to be performed (object-side) is surface preparation. The grey distribution takes place at pixel-scale; as a consequence, the accuracy of this method directly depends on the acquisition systems. One could distinguish among 2D DIC (single camera), in which flat surfaces are correlated, and 3D DIC (stereo camera), in which non-flat surfaces or out-of-plane movements are studied. In the following, the basic principles of 2D DIC systems are discussed, together with the algorithms. The open source 2D DIC program *Ncorr* running on MATLAB, developed at Georgia Institute of Technology [150] has been considered. This tool has been validated for low-cost 2D DIC solid mechanics application [151].

B.2.1 Algorithm principles

The algorithm carries out a comparison between the current images, showing the body deforming (or moving), and the reference images, aimed to correlate the displacements and derive a strain field. In the first step, the operator is prompted to highlight the so-called *Region of Interest* (ROI), representing the 2D surface area to be correlated; this step is always performed on the reference image, as it depicts the initial condition. The software splits the ROI in a certain number of *facets* or *subsets*, which usually takes a circular or a square shape. The subsets are spaced, for computational reason. The software evaluates the gray distributions inside each facet and goes searching them through the current images. Similar grays distributions in different facets might lead the algorithm to confuse them; this is why the surface should feature a random gray pattern at a sufficiently low scale. Subset dimension is a critical parameter of the correlation process, as it substantially affects the accuracy of the measurements; in Ncorr it is referred to as *RG DIC Radius*. Any DIC software prompts the user to set this dimension:

- larger subsets are preferable when the main target is the displacements; as they are more easily recognizable by the algorithm;
- smaller subsets are preferable when the strains are the main target. They are described through a first- or second-order polynomial; increasing the size of the subsets, that is, reducing their number, leads to a loss in the details and a smoothing effect.

As discussed in Chapter 1, a black PLA has been used throughout this work; a white spry easily allowed to obtain the required pattern before each test took place.

Displacement field measurement

With the ROI split into subsets, the algorithm tries to localize the central point of each of them in all the current images. This step is performed by evaluating the so-called *Correlation Coefficient* between the current subset and the subsets of the current images and looking for its maximum value [149]. Several criteria might be used; Ncorr 2D takes advantage of the so-called *Normalized Sum of Squared Difference* (NSSD); the correlation coefficient C_{NSSD} is calculated in the way expressed by Equation B.1.

$$C_{NSSD} = \sum_{i=-M}^{M} \sum_{j=-M}^{M} \left[\frac{f(x_i, y_i)}{\bar{f}} - \frac{g(x_i, y_i)}{\bar{g}} \right]^2 \tag{B.1}$$

$f(x_i, y_i)$ and $g(x_i, y_i)$ respectively measures the gray values in the reference and in the current image; $\bar{f}$ and $\bar{g}$ are the average values in the subset. Given a single facet, the correlation coefficients for any point in the current image are calculated; the

maximum gives the facet position in the actual current image. This calculation is just an estimate, as it fails to derive the exact position of points of finite dimensions. An interpolation with biquintic splines is performed, to which an iterative non-linear optimization follows. Several algorithms share this procedure; however, the analysis would be very heavy from the computational point of view if performed for all the subsets. Ncorr implements a simplification; the operator places one or more *seeds* over the ROI, representing some point(s) of reference. Once the seed(s) has(have) been located into the current images, an initial estimate of the subset four vertices position is obtained. The procedure continues from these points and lasts until the ROI displacements have been completely calculated. This process is advantageous from the computational point of view and solid. More than one seed can be positioned; this splits the ROI into a certain number of sub-domains, in which the analysis takes place in parallel, further speeding up the calculation.

At the end of this phase, the displacement field is expressed into pixels. A conversion factor is necessary to convert the displacements into a coherent unit of measurement. A user-friendly tool allows setting the linear dimension of an edge over a calibration image. Ideally, the linear dimensions of the specimen edges are known accurately; a line is drawn over a selected edge, and its dimension is set. The software then converts the pixels to mm and scales the results. Due to perspective and shadows, the edge boundaries are not always detectable with precision. A graph paper sheet has been positioned next to the specimen in a co-planar way with respect to the monitoring surface. The grid edges are more easily detectable, and the dimensions of the grid are known precisely. In this respect, it is compulsory that the camera keeps immobile and at a predetermined distance from the surface for all the test. Any lens shift or any displacement of the specimen in the direction perpendicular to that of the focal plane would change the respective distances and invalidate the scale factor.

Strain field calculation

After the displacement field has been measured per each frame, all DIC systems allow evaluating the strain field of the surface. The displacements undergo numerical derivation, but their field is usually very noisy. To overcome this, Ncorr performs a local least square interpolation of the displacements into square surfaces of $2M + 1$ pixels per side. The strains are then calculated in the central points of

the squares using the Green-Lagrange expressions of Equation B.2.

$$\begin{aligned}
\epsilon_{xx} &= \frac{1}{2}\left[2\frac{\partial u}{\partial x} + \left(\frac{\partial u}{\partial x}\right)^2 + \left(\frac{\partial v}{\partial x}\right)^2\right] \\
\epsilon_{xy} &= \frac{1}{2}\left(\frac{\partial u}{\partial y} + \frac{\partial v}{\partial x} + \frac{\partial u}{\partial x}\frac{\partial v}{\partial y} + \frac{\partial v}{\partial x}\frac{\partial u}{\partial y}\right) \\
\epsilon_{yy} &= \frac{1}{2}\left[2\frac{\partial v}{\partial y} + \left(\frac{\partial v}{\partial y}\right)^2 + \left(\frac{\partial u}{\partial y}\right)^2\right]
\end{aligned} \tag{B.2}$$

B.2.2 Main issues

DIC is an easy and effective instrument; as with any technique, it has limitations and issues whose impact has been extensively studied over time. The phenomenons that might negatively affect data collection need to be evaluated and avoided. This subsection discusses the main issues taken into account in set-up evaluation and preliminary validation.

Surface pattern

DIC measurements are considerably dependent on the surface pattern. As previously discussed, the gray distribution has to be as random as possible for the subset to be identified; the gray distribution also affects the choice of facet dimensions. This concern is difficult to parameterize; it is difficult to attribute a numerical value to the gray distribution, assessing its effectiveness. Ncorr evaluates the correlation coefficient and counts how many iterations are required to locate a subset. When these exceed a threshold value, likely, the gray distribution does not have a suitable pattern. A spray from a certain distance usually allows to obtain a sufficiently random pattern; however, this parameter is definitely linked to a trial and error process.

Out-of-plane motion or misalignment

2D DIC inspects a planar surface; this means that the instrument focal plane and the correlating surface should be parallel and at a fixed distance. Those requirements are sometimes difficult to be maintained all the tests long. Leaving aside the reciprocal positioning between the instrument and the surface, unavoidable movements in the out-of-plane direction may happen due to the load case. Even in the case of a plane stress state, eccentricities might occur in load application; even if that were not the case, out-of-plane motions manifest by the Poisson effect. This effect is amplified if the sensor and the specimen are very close, as those displacements take a greater percentage weight. This concern implies that 2D DIC must necessarily be restricted to applications in which the motion or deformation

occurs within a plane, and reducing the relative weight of transverse displacements with geometric considerations.

Lens distortion

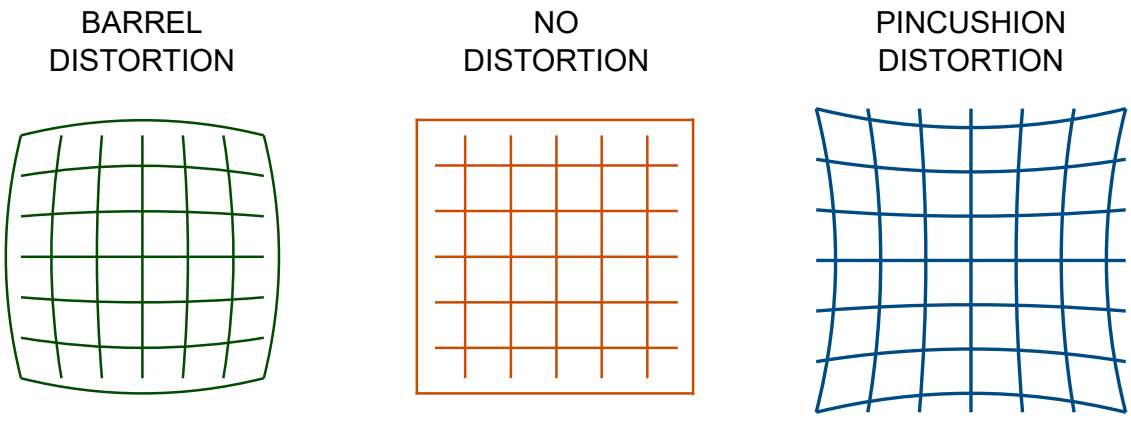

Figure B.1: Barrell distortion and pincushion distortion in an image.

Optical distortion is a defect that shows objects with a different shape or in a different position with respect to reality. It occurs when the straight lines in a scene do not correspond to straight lines in the image. Distortions are a form of optical aberration, which might follow several patterns. In photography, they are due to the optical lenses, which are not flat: their curvature and geometry induce radially symmetric distortions, typically the *barrel distortion* and the *pincushion distortion*. In Figure B.1 both are presented. In barrel, distortion takes place when magnification decreases while one moves away from the optical axis. In pincushion, distortion magnification decreases once one gets closer to the optical axis. This concern is linked to geometrical and known characteristics of the optics; consequently, it can be studied in advance and taken into account, making a preliminary evaluation of the distortion parameters [152, 153].

B.2.3 DIC set-up

Almost all the tensile, compressive, and flexural tests presented in this work have been performed using a simple 2D DIC system as a monitoring device. This was possible as a plane surface has been identified in all the specimens and monitored during the test. Its behavior has been video-recorded with a DSLR Nikon D3500 camera, with Nikkor 18-55mm f/3.5-5.6G DX VR AF-P optics. In all tests, the load application direction is a certainty imposed by the (calibrated) testing machine in tensile and compression tests, or imposed by the force of gravity in bending/torsion and bending test. The grid of the camera reference system has been aligned through

manual levels. The DSLR camera has been operated a little before the beginning of the test to let the vibrations dissipate. Once the test ends, all the frames are extracted from the video and imported into Ncorr. This camera records video at 30 FPS (Frames Per Second); however, not all the frames have been considered. The acquisition frequency has been lowered, following some considerations:

- Displacements and strains need to be synced over time with other mechanical variables sampled by different devices (i.e., the applied load sampled by the testing machine). Consequently, the acquisition frequency needed to be aligned between the concurring instruments/techniques;
- at 30 FPS, adjacent frames are at 1/30 s, which is a minimal time. As all the mechanical tests look for quasi-static loading, small displacements occurred between adjacent frames, with an order of magnitude similar to that of the noise oscillations;
- reducing the frames to analyze reduces the processing time.

The first step is to synchronize the video with the data sampled by the testing machine. The details depend upon the test and are discussed in the respective chapters; the general procedure followed these steps:

- the operator performs the correlation using a tentative frame as a reference image;
- the first frame in which the displacement maps show concordant direction with the load application direction is assumed as instant 1 of the test. The frame preceding it is set as the reference image, against which the displacements of the following ones (the current images) are calculated.

All the correlations benefit from a multi-thread computer; four seeds split the ROI into four sectors to be analyzed simultaneously. Once the correlation ended, the displacement calibration proceeded as previously discussed.

Optics distortion quantification

The (possible) image distortion took immediate center stage. Figure B.2 shows a cross-section view of the DSLR optics. Lenses vary from 18 to 55 mm, with different curvatures and thicknesses; each lens induces a different distortion effect of the image. In this respect, a review article of the optics [154] quantified the effect for each of them, discussing that the 18 mm lens led to a barrel-type distortion of 4.3%, which dropped to 3.0% with the 24 mm lens. A pillow distortion, instead, was found while using the 55 mm lens. The total absence of optical distortion characterized the images taken with the 35 mm lens. If confirmed, no distortion correction would be needed. The following test has been designed to assess the set-up and verify the

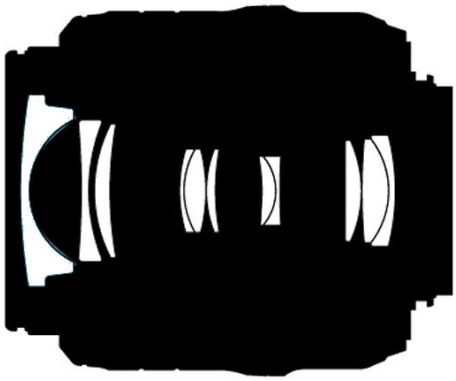

Figure B.2: Cross section view of Nikkor 18-55mm f/3.5-5.6G DX VR AF-P optics.

absence of distortion effects. The test consists of the displacements correlation of an object moving at a constant speed in the focal plane. The component has a flat surface, and it moves through the entire focal plane at a constant translation speed of 10 mm/min. The MTS QTest testing machine ensures the translation speed, as its upper grip is used to impress the movement. The surface does not have a great extent in the transverse direction; however, it develops in the region occupied by the specimens in tensile, compression, and bending tests.

Figures B.3-B.4 show the transverse displacements map at instant $t_1 = 15$ s and $t_2 = 30$ s, respectively; both images show the same scale, so they are easily comparable. Table B.1 summarizes the correlation parameters, the software default values already validated in [150] have been considered. Table B.2 lists the results of the two reference frames.

DIC Parameters			
RG-DIC Radius	43	Subset spacing	3
Diffnorm cutoff	10^{-6}	Iteration cutoff	50
Threads	4		

Table B.1: DIC default parameters in Ncorr.

Displacements are evenly distributed on the surface. The averaged displacement amplitude coincides with the expectations for the considered instant. Further confirmation comes from Figure B.5 showing the transverse displacement sampled in the central point of the surface and in the end-right region over time. The displacement vs. time relation is perfectly linear in both cases; their slope coincides with

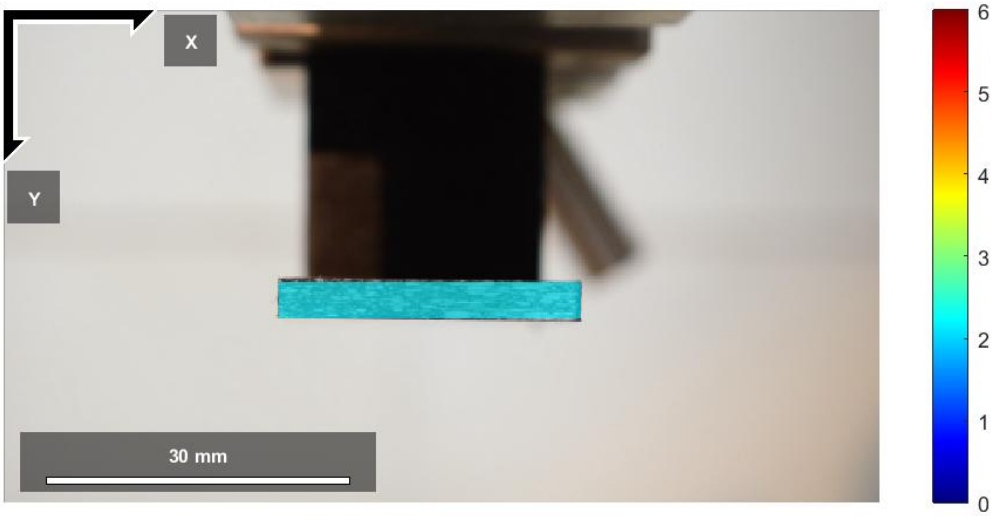

Figure B.3: Optics distortion quantification: displacements map at $t_1 = 15$ s of the preliminary test. The color scale is in mm.

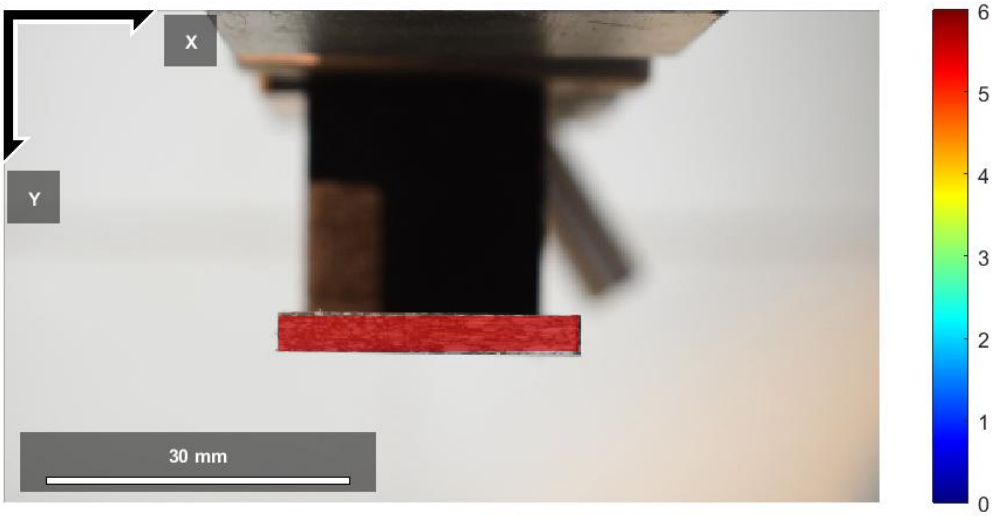

Figure B.4: Optics distortion quantification: displacements map at $t_1 = 30$ s of the preliminary test. The color scale is in mm.

the imposed displacement speed. No distortion took place during the translation; this validated both the set-up and the absence of optical aberration, at least in the central region of the optics.

DIC Results		
	Frame 450	Frame 900
Timestamp	$t_1 = 15$ s	$t_2 = 30$ s
Corr. coeff. cutoff	0.1092	0.1281
Max	2.50 mm	5.01 mm
Min	2.48 mm	5.00 mm
Median	2.49 mm	5.01 mm
Unitx/pixel	0.045084	

Table B.2: Optics distortion quantification: DIC results at instant $t_1 = 15$ s and $t_2 = 30$ s.

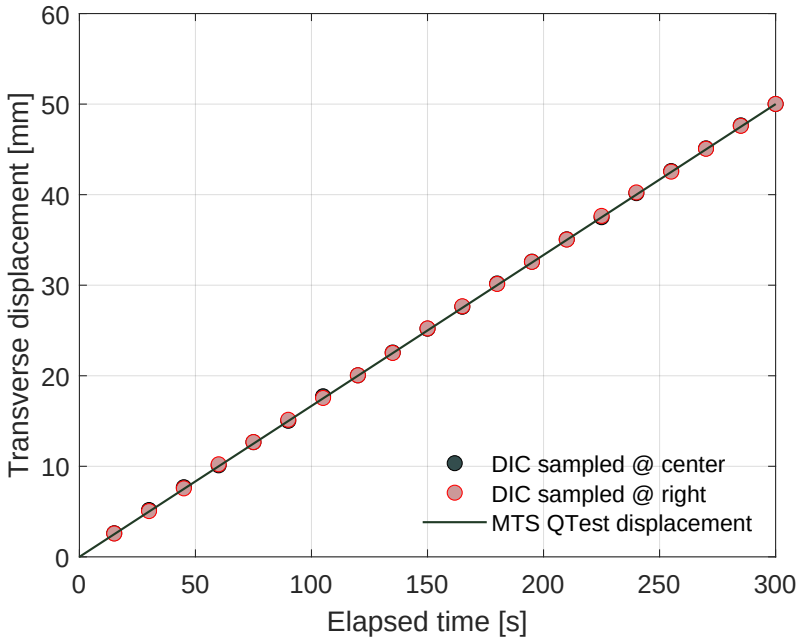

Figure B.5: Optics distortion quantification: displacements recorded on a simple translation test.

B.3 DIC strains in experimental tests

Digital Image Correlation presents a significant difference compared to conventional measuring instruments, as it allows to have a displacement/deformation map. DIC provides a large number of displacements/strains at the specified sampling rate, as each subset is a measurement point. Tools such as strain gauges, LVDT, and extensometers, on the other hand, provide a measurement only in the region they are applied to by sampling a single displacement/strain over time. This

DIC peculiarity is undoubtedly advantageous in many cases; think of monitoring two or more points on the same surface, sample displacements, and deformations simultaneously and in two orthogonal directions, with the same instrument. However, in other cases, it requires an adjustment to comply with established standard procedures.

Taking as a reference the standard test method to determine tensile properties in composites (see Chapter 3), the set-up requires the transducers to be positioned symmetrically about the mid-span, mid-width location. The literature discusses set-ups with:

- a single transducer symmetrically placed about the mid-span, mid-width location over the front surface of the coupon;
- a pair of transducers symmetrically placed about the mid-span, mid-width location over the front surface of the coupon;
- a triple of transducers, adding a transducer on the rear surface to the pair discussed in the previous point.

The location requirements depend on the stress/strain field, more uniform in the central area than near the edges. Adding multiple transducers is meant to monitor and offset bending in width and thickness directions, which might be due to eccentricities in the applied load or specimen misalignment. In the second and third set-up, averaging the strains allows compensating for misalignment but still provides a single sample over time. In mechanical characterization, the construction of the stress vs. strain curves requires a single sampling of the strain. How to behave in the case of DIC?

The following discussion relies on tensile tests; however, it can be easily extended to shear tests on $\pm 45°$ laminated specimens and to compression tests. The tensile test is designed to induce a constant and uniform stress/strain distribution in the gage section of the specimen until the material linear elastic behavior holds. This assumption may not be valid for high loads and in the plastic deformation region, especially when necking occurs. The DIC ROI coincides with the specimen gage section; therefore, it is rectangular, with m subsets in the transverse and n in the longitudinal directions. The overall number of subsets may show small variations from specimen to specimen even within the same sample as the ROI sizing is manual. A simple script has been implemented to evaluate the longitudinal distribution of the axial displacements. The grid of measurement points comprises $n \times m$ subsets, aligned with each other in m columns and n rows. For each column, the script evaluates the Pearson correlation coefficient between the displacements and the longitudinal coordinate. When this is on the order of 1, displacements follow a linear equation, whose first derivative to that transverse coordinate is the axial strain. Figure B.6 shows the longitudinal displacements map for a representative tensile specimen. Frame by frame, the script averages the strains obtained

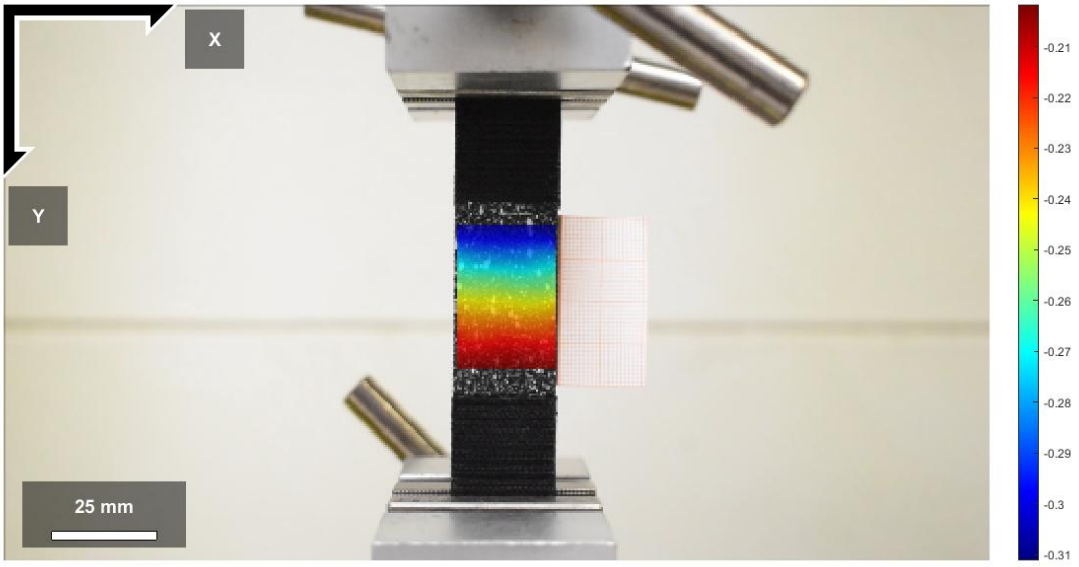

Figure B.6: Longitudinal displacements distributions for a tensile specimen, obtained via DIC. The color scale is in mm.

from each "column" and compares this value with the average value on the ROI calculated by Ncorr. The trend over time of these two mean values is shown in Figure B.7. They coincide for a good part, then diverge. When the mean Pearson

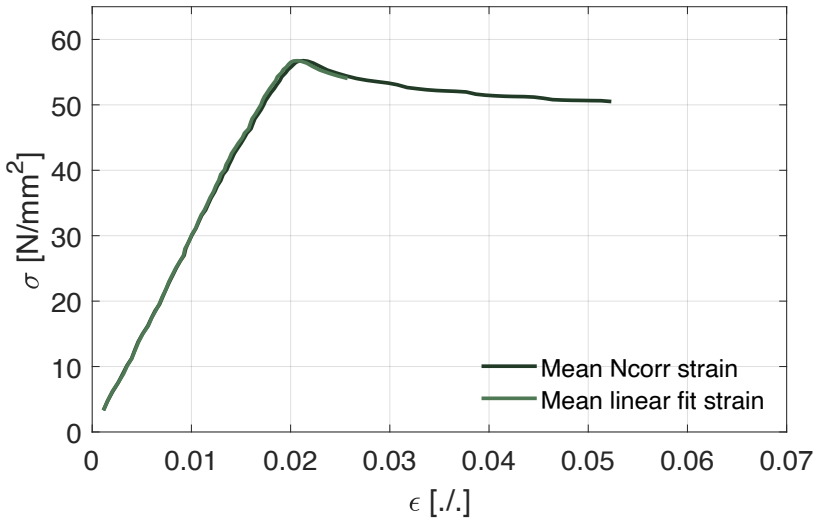

Figure B.7: Mean Ncorr strain vs. mean linear fit strain for a tensile specimen.

coefficient is no longer high, the first curve is no longer defined. The reason is easily explained: the displacements are no longer linear in the longitudinal direction starting from a certain load level; this usually coincides with necking. A similar issue occurs when using strain gauges, as at high strains it is common for them to delaminate.

The first procedure can be seen as an extension of the strain gauges set-up involving the installation of two strain gauges: it is like having m transducers, each arranged along the entire length of the ROI. However, there is no practical difference in the results with the second procedure, as soon as the material behaves linearly. Therefore, all the stress vs. strain relations discussed in this thesis consider the mean subset strains per frame. This approach made it possible to trace the plastic deformation, even if partially. When it is excessive, the surface pattern is no longer correlated by the software and the curve breaks off.

B.4 Strain gauge reinforcement effect

In the Introduction it has been mentioned that in-contact instruments might affect the mechanical response of polymeric specimens. This argument can be extended in general to materials with low stiffness modulus. This section is devoted to quantify this effect, sometimes tangible also with transducers specifically designed for polymers, to qualify the choice of the DIC. This analysis focuses on strain gauges. These transducers are still used today in numerous applications; the principle is simple: a conductor wire shows a variation in electrical resistance when undergoing a mechanical load [155]. This effect has a limited amplitude, so in the transducer, the electric wire follows a specific grid accentuating its impact along the measuring direction. The metal grid thickness is in the order of 50 μm, too thin to be handled and used on its own. A polymeric backing film encloses the electrical wires, which makes the transducer a heterogeneous component, in which two constituents of different nature coexist. The conductive grid is made of Constantan, the backing film of Polyimide (PI); their mechanical properties are reported in Table B.3. As part of this preliminary evaluation, a strain gauge specifically de-

	Constantan [156]	Polyimide [157]
Elastic Modulus	$E^{const} = 165$ GPa	$E^{pi} = 2.5$ GPa
Poisson ratio	$\nu^{const} = 0.3$	$\nu^{pi} = 0.34$
Shear Modulus	$G^{const} = 63.5$ GPa	$G^{pi} = 0.93$ GPa

Table B.3: Strain gauges phases: mechanical properties.

signed for low stiffness modulus materials has been considered; Table B.4 reports its data-sheet. Beatty [159] and Ajovalasit [160, 161] proposed two analytical models

GFLAB-3-350-70-1LJCT-F			
L_{sg}	Gauge length	3	mm
W_{sg}	Gauge width	2.9	mm
L_{sg}^{O}	Overall length	9.5	mm
W_{sg}^{O}	Overall width	5	mm
t_{sg}^{O}	Overall thickness	0.5	mm
t_{sg}^{m}	Metallic foil thickness	0.05	mm
R	Resistance	350	Ω
	Objective material	ABS	-

Table B.4: Tokyo Measuring Instruments Laboratory strain gauge datasheet [158].

that estimate the local reinforcement effect induced by a strain gauge. In Beatty's model, the local reinforcement effect depends on two coefficients, geometric and mechanical, of mutual influence between the strain-gauge and the substrate.

$$\alpha = \frac{4t_{sg}^{O}}{L_{sg}^{O}} \frac{E^{sg}}{E^{s}} \tag{B.3}$$

$$\beta = \frac{t_a}{L_{sg}^{O}} \frac{E^{s}}{G^{a}} \alpha \tag{B.4}$$

The mechanics is described in terms of the elastic modulus of the substrate E^s and that of the strain gauge E^{sg}. The shear modulus of the adhesive layer G^a and its thickness t_a also become part of this model. Assuming a perfect bond, they can be excluded by setting ∞ and 0, respectively. The two coefficients enter Equation B.5, which expresses the reinforcement effect as the ratio between the transducer strain ϵ' and the actual substrate strain ϵ.

$$\frac{\epsilon'}{\epsilon} = 1 - r\alpha - s\beta \tag{B.5}$$

The two additional coefficients r and s are meant to consider the length of the measuring grid of the strain gauge L_g. Ajovalasit has discussed a similar expression. In the hypothesis of perfect adhesion, the strain gauge reinforcement effect on a flat surface with semi-infinite dimensions, an estimate is given by:

$$\frac{\epsilon'}{\epsilon} = 1 - \frac{t_{sg}^{O}}{L_{sg}^{O}} \frac{E_{sg}}{E_s} \phi\left(\frac{L_{sg}^{O}}{t_{sg}^{O}}, \frac{L_g}{t_{sg}^{O}}\right) \tag{B.6}$$

However, both the models require an estimate of the mechanical properties of the sensor.

Strain-gauge mechanical properties estimation

Homogenization can provide a possible solution: it is possible to estimate the equivalent mechanical properties drawing an analogy to composite materials and evaluating the volume fraction of the two constituents. Figure B.8a shows the metal grid of the strain gauge under consideration. The metal wires develop along the

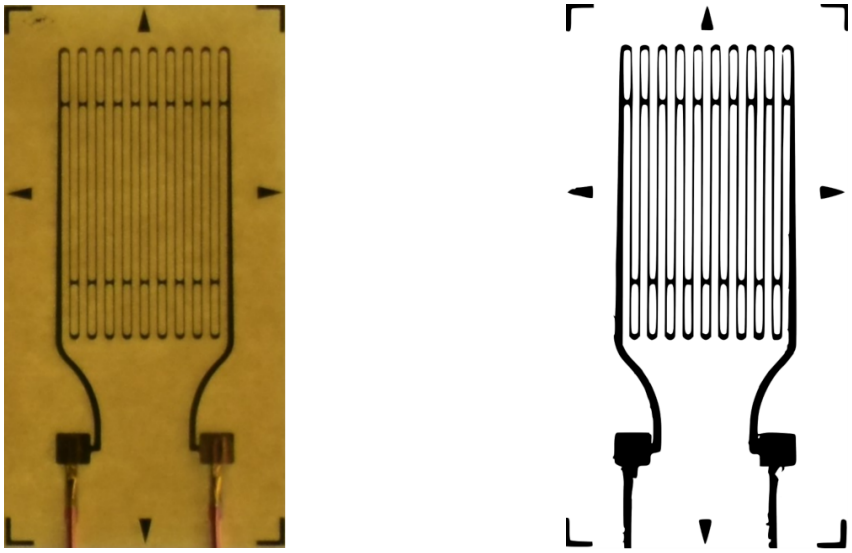

(a) Actual image. (b) Vectors internal path.

Figure B.8: Strain gauge front view.

measurement direction, thus coinciding with the load application one. Along with it, the upper-bound modulus of elasticity of the strain-gauge E^{sg} can be calculated as:

$$E^{sg} = V_f^{const} * E^{const} + V_f^{pi} * E^{pi} \tag{B.7}$$

similar reasoning applies to the Poisson ratio ν^{sg}:

$$\nu^{sg} = V_f^{const} * \nu^{const} + V_f^{pi} * \nu^{pi} \tag{B.8}$$

Therefore, the mechanical properties of the transducer depend on the individual properties of the two constituents (E^{const}, E^{pi}, ν^{const}, and ν^{pi}) and their volumic fraction V_f^{const} and V_f^{pi}. The estimate of the volume fraction can be obtained from the frontal view of the transducer through the following steps:

1. the image is cut flush with the edges of the strain gauge and imported into a vector graphics software;

2. the boundaries of the metal grid are well distinguishable in the background to be reproduced through the edge detection tool, an image processing technique. The paths obtained are shown in Figure B.8b; this allows having net boundaries.

3. a Matlab tool quantifies the percentage surface occupied by the black paths.

In the front view, the metal grid occupies 12.67% of the surface. However, the strain gauge datasheet reports that constantan occupies one-tenth of the total thickness, which leads to a volumetric percentage $V_f = 1.267\%$. Following this result and taking into consideration the strain-gauge mechanical and geometrical properties previously discussed (see Tables B.3-B.4), Equations B.7-B.8 lead to the following estimates:

$$E^{sg} = 4.46GPa, \qquad \nu^{sg} = 0.34 \tag{B.9}$$

The magnitude of the reinforcement effect strictly depends on the mechanical properties of the substrate, as shown by Beatty and Ajovalasit models. The next subsection discusses a small experimental campaign to quantify them and experimentally verify the analytical estimates.

Strain-gauge reinforcement quantification

Single grid strain gauges are designed to measure strain in a specific direction. For this reason, a tensile test is the best suitable way to evaluate its functioning, as the geometry of the specimen and the boundary conditions aim to induce a uniform and uniaxial stress/strain field. A tensile test allows using the apparent modulus of elasticity as a benchmark parameter; this enables understanding the phenomenon better as it directly quantifies the stiffness [161]. The reinforcing effect can be quantified if the strain-gauge is paired with another strain-measuring technique. The DIC has been considered a benchmark. For consistency, FFF 3D-printed rectangular and flat specimens have been considered, following the set-up discussed in Chapter 3. All considerations in terms of specimen and tab geometry, and test characteristics are also valid here. $[\pm 45°]$ specimens have been considered. The experimental campaign considered a total number of eight specimens, divided into two runs of 4. The samples undergo the same tensile test, with the following differences:

- **Run(I)** specimens. " stands for Instrumented; a single strain gauge has been bonded to them, potentially affecting their mechanical response. DIC also monitored those coupons.
- **Run(F)** specimens. F Stands for Free; these specimens undergo tensile tests monitored via DIC only, incurring in no influence by any measuring device.

Figures B.9-B.10 show the failure modes of Run(F) and Run(I) specimens, respectively. All the specimens failed within the gage region. The results of the fourth specimen of Run(I) have been disregarded as it slipped during the experiment; furthermore, its strain gauge delaminated, as shown in Figure B.10. As in all the tests described in Chapter 3, the tensile stress has been derived by dividing

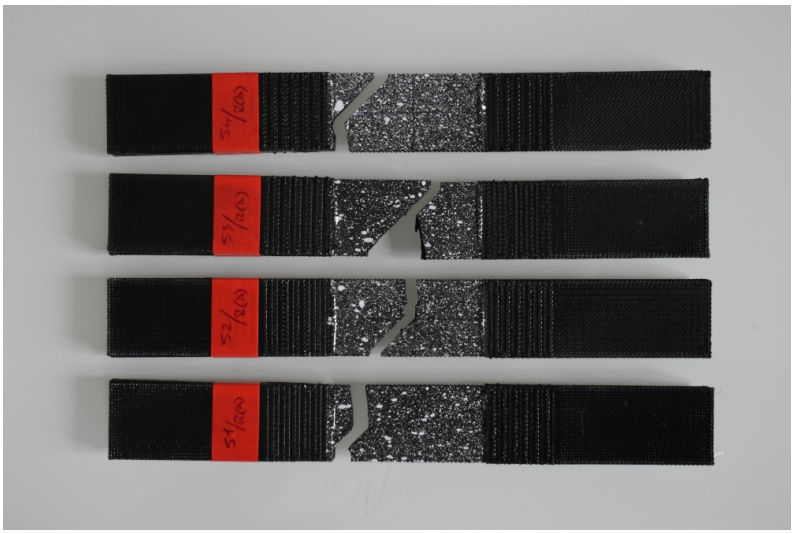

Figure B.9: Failure modes of Run(F) specimens.

Figure B.10: Failure modes of Run(I) specimens.

the load applied by the testing machine by the original cross-sectional dimension of the specimen. For the Run(I) coupons, the SG strain derived directly from the transducer measurement; for both runs, the DIC strain calculation followed the procedure discussed in Section B.3. The stress/strain sampling has been conducted at 5 Hz. Once synced over time, the apparent modulus of elasticity has been quantified through a set of linear regressions on intervals of gradually increasing size. The iteration stops when the new linear regression coefficient differs from the mean of the previously calculated value by more than 5%. The results are shown in Table B.5. Two columns list Run(I) results because two strain measurements have been

Run(F)		Run(I)		
	E^F_{DIC} (via DIC) [MPa]		E^I_{DIC} (via DIC) [MPa]	E^I_{SG} (via SG) [MPa]
F1	3427	I1	3308	3362
F2	3354	I2	3395	3429
F3	3294	I3	3355	3448
F4	3358			
mean	3358	mean	3353	3413
st.dev	55	st.dev	44	45

Table B.5: Apparent moduli of elasticity for Run(F) and Run(I) specimens.

performed; consequently, two modules per specimen have been calculated. Note that there is no known difference between E^F_{DIC} and E^I_{DIC}, which implies that the strain gauges application did not induce any substantial influence on the overall behavior of the specimen. The standard deviation also assumes a similar value between the two distributions, which compensates for the small sample size. Their averaged value, $E_{DIC} = 3355$ MPa, has been identified as the actual modulus of elasticity of the 3D-printed PLA under these conditions. Run(I) specimens showed stiffer behavior when monitored by SGs. The difference is not very large, +1.80% in percentage, which can be attributed to the local reinforcement effect under investigation. This value is compatible with the Beatty and Ajovalasit estimates, which can be obtained from Equations B.5-B.6, using $E_{DIC} = 3355$ MPa as the substrate stiffness modulus and $E^{sg} = 4.46$ GPa as an estimate of the strain gauge stiffness modulus. The results are reported in Table B.6.

SG local reinforcing effect		
Experimental	Beatty	Ajovalasit
+1.80%	+2.00%	+1.99%

Table B.6: Evaluation of the local reinforcing effect: experimental vs. analytical results.

Although small, the effect appears to be confirmed. The result is an important warning, as the percentage value is bound to increase in the presence of even less rigid configurations.

Appendix C

Collection of all experimental results

This appendix reports all the individual experimental results, that were reported in aggregate form throughout the thesis. They are grouped by test typology and are preceded by a brief description.

C.1 Tensile tests

This section reports all the results of the tensile tests. Tables and graphs are grouped depending on the test they refer to.

C.1.1 Design of Experiments

This sub-section contains the results of the Design of Experiments used to design the tabs for tensile tests according to ASTM D3039. For each DoE a summary table has been reported, with the parameters of each specimen, and the individual load vs. displacement curves.

Tensile specimens loaded in direction 1: first DoE

SPECIMEN	DoE factors			Cross-section		DoE param.	
	t_{tab}	α_{tab}	v_{test}	W	T	σ_{max}	y_{fail}
	[mm]		[mm/min]	[mm]	[mm]	[MPa]	[%]
TSD1(DoE1)-S01	0.5	5°	0.5	24.94	2.98	49.72	-
TSD1(DoE1)-S02	0.5	10°	2.0	24.99	2.97	53.16	-
TSD1(DoE1)-S03	0.5	20°	3.5	24.95	3.02	53.12	-
TSD1(DoE1)-S04	0.5	90°	5.0	24.93	2.98	55.79	-
TSD1(DoE1)-S05	1.0	5°	2.0	24.96	3.00	56.21	-
TSD1(DoE1)-S06	1.0	10°	0.5	25.00	2.98	53.80	-
TSD1(DoE1)-S07	1.0	20°	5.0	24.97	3.00	58.85	-
TSD1(DoE1)-S08	1.0	90°	3.5	24.94	3.02	56.79	-
TSD1(DoE1)-S09	1.5	5°	3.5	24.95	2.95	58.07	-
TSD1(DoE1)-S10	1.5	10°	5.0	24.95	3.01	59.04	-
TSD1(DoE1)-S11	1.5	20°	0.5	24.94	2.97	53.47	-
TSD1(DoE1)-S12	1.5	90°	2.0	25.05	2.98	56.09	-
TSD1(DoE1)-S13	2.0	5°	5.0	24.99	3.00	62.28	-
TSD1(DoE1)-S14	2.0	10°	3.5	24.95	2.98	58.97	-
TSD1(DoE1)-S15	2.0	20°	2.0	24.95	3.00	54.64	-
TSD1(DoE1)-S16	2.0	90°	0.5	24.95	3.01	54.96	-

Table C.1: Tab design of tensile specimens, direction 1. Parameters and results of the first DoE.

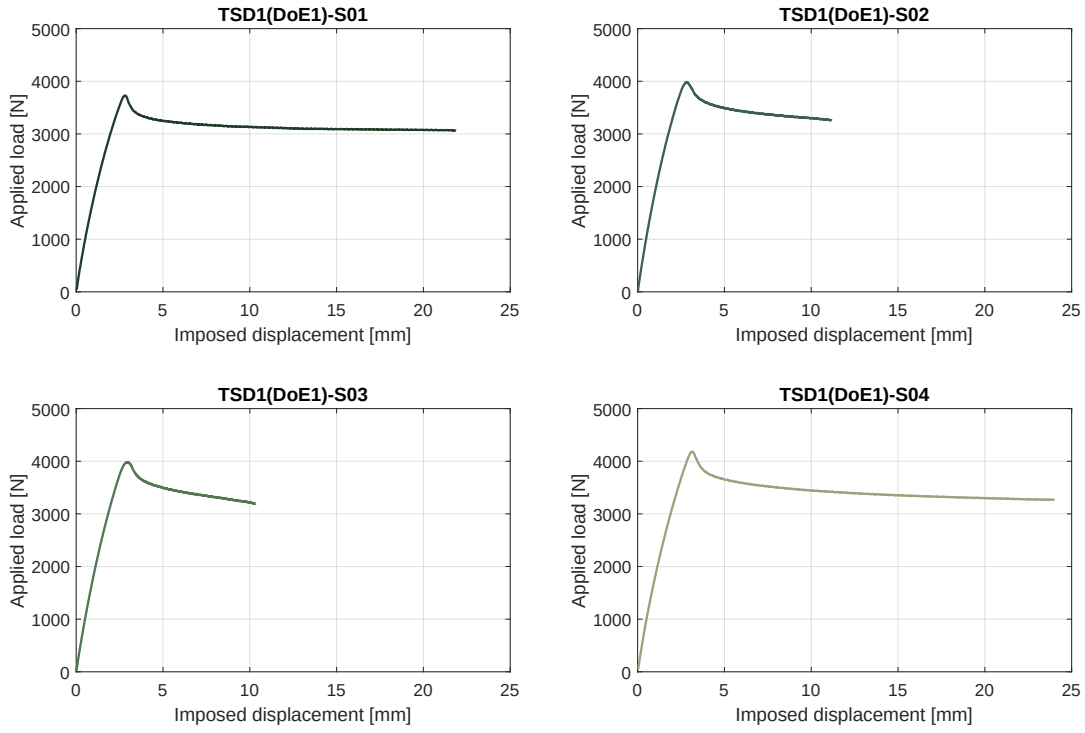

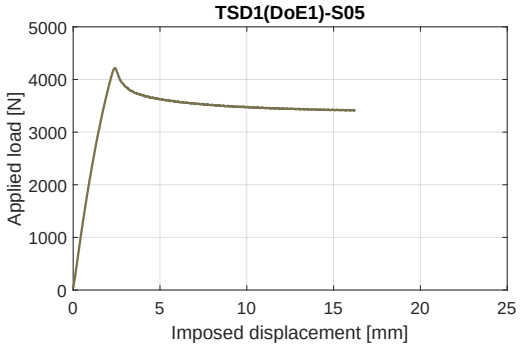
TSD1(DoE1)-S05
Applied load [N]
Imposed displacement [mm]

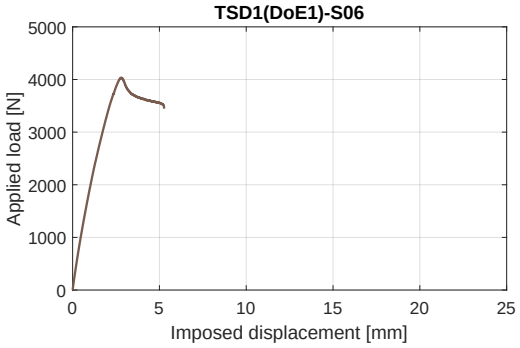
TSD1(DoE1)-S06
Applied load [N]
Imposed displacement [mm]

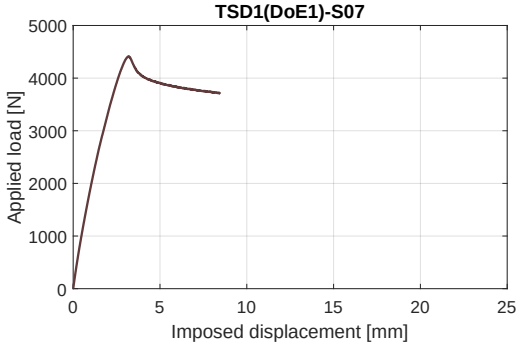
TSD1(DoE1)-S07
Applied load [N]
Imposed displacement [mm]

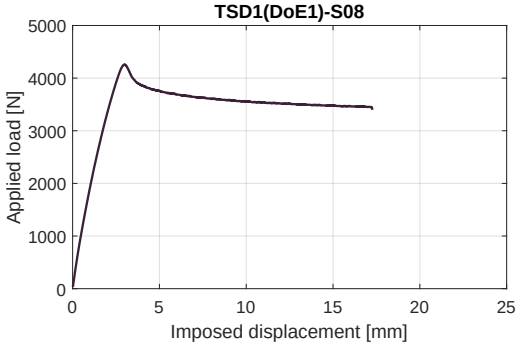
TSD1(DoE1)-S08
Applied load [N]
Imposed displacement [mm]

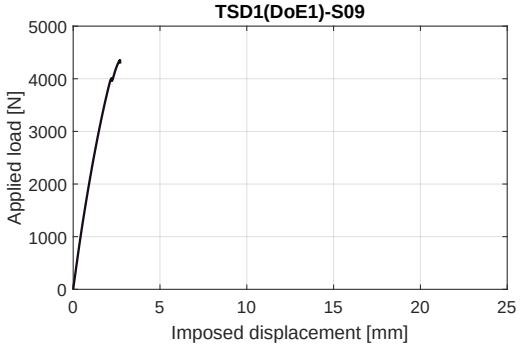
TSD1(DoE1)-S09
Applied load [N]
Imposed displacement [mm]

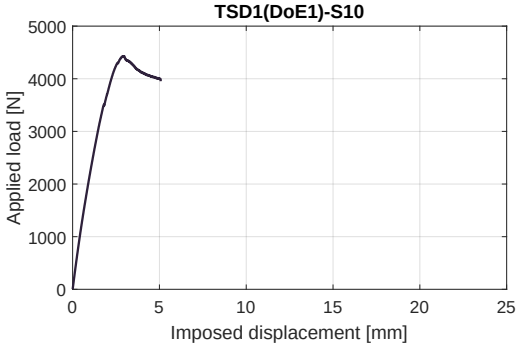
TSD1(DoE1)-S10
Applied load [N]
Imposed displacement [mm]

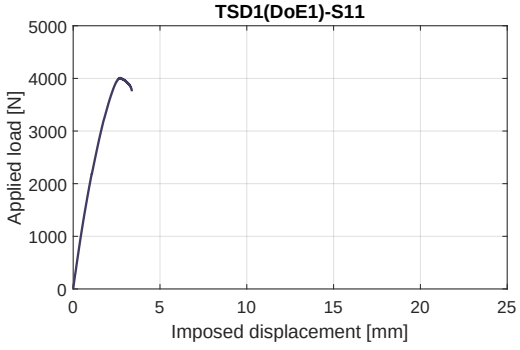
TSD1(DoE1)-S11
Applied load [N]
Imposed displacement [mm]

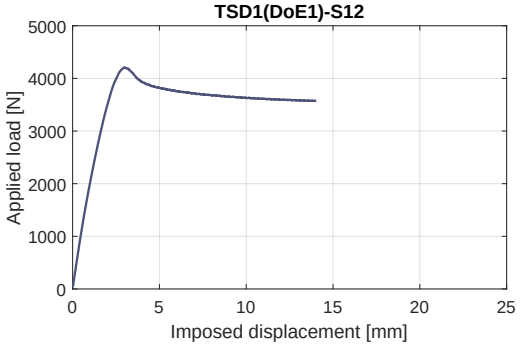
TSD1(DoE1)-S12
Applied load [N]
Imposed displacement [mm]

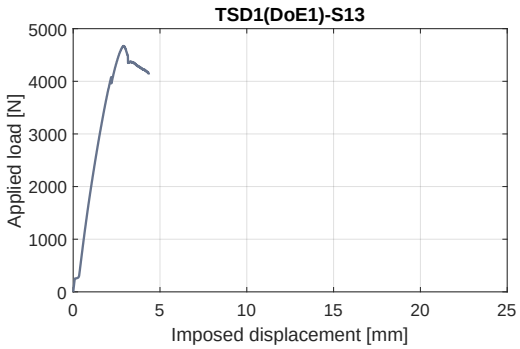
TSD1(DoE1)-S13
Applied load [N]
Imposed displacement [mm]
0
1000
2000
3000
4000
5000
0
5
10
15
20
25

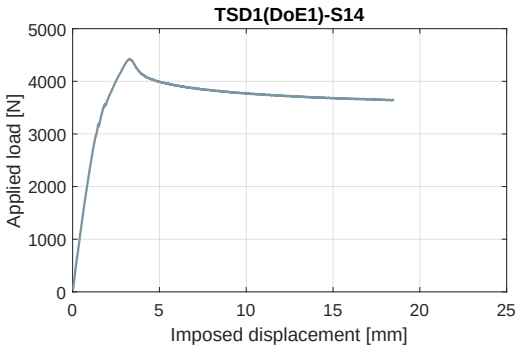
TSD1(DoE1)-S14
Applied load [N]
Imposed displacement [mm]
0
1000
2000
3000
4000
5000
0
5
10
15
20
25

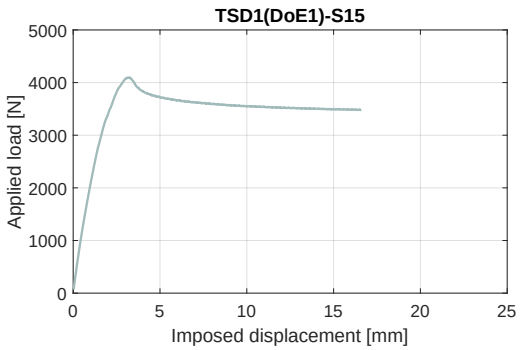
TSD1(DoE1)-S15
Applied load [N]
Imposed displacement [mm]
0
1000
2000
3000
4000
5000
0
5
10
15
20
25

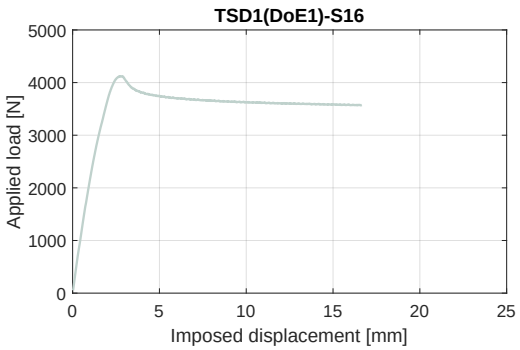
TSD1(DoE1)-S16
Applied load [N]
Imposed displacement [mm]
0
1000
2000
3000
4000
5000
0
5
10
15
20
25

Tensile specimens loaded in direction 1: second DoE

SPECIMEN	DoE factors		Cross-section		DoE param.	
	t_{tab}	α_{tab}	W	T	σ_{max}	y_{fail}
	[mm]		[mm]	[mm]	[MPa]	[%]
TSD1(DoE2)-S01	0.5	5°	24.94	2.98	51.21	-
TSD1(DoE2)-S02	0.5	10°	24.99	2.97	54.48	-
TSD1(DoE2)-S03	0.5	20°	24.95	3.02	56.71	-
TSD1(DoE2)-S04	0.5	90°	24.93	2.98	57.12	-
TSD1(DoE2)-S05	1.0	5°	24.96	3.00	57.13	-
TSD1(DoE2)-S06	1.0	10°	25.00	2.98	53.33	-
TSD1(DoE2)-S07	1.0	20°	24.97	3.00	56.77	-
TSD1(DoE2)-S08	1.0	90°	24.94	3.02	56.08	-
TSD1(DoE2)-S09	1.5	5°	24.95	2.95	58.29	-
TSD1(DoE2)-S10	1.5	10°	24.95	3.01	57.09	-
TSD1(DoE2)-S11	1.5	20°	24.94	2.97	52.20	-
TSD1(DoE2)-S12	1.5	90°	25.05	2.98	54.85	-
TSD1(DoE2)-S13	2.0	5°	24.99	3.00	60.40	-
TSD1(DoE2)-S14	2.0	10°	24.95	2.98	56.92	-
TSD1(DoE2)-S15	2.0	20°	24.95	3.00	54.71	-
TSD1(DoE2)-S16	2.0	90°	24.95	3.01	51.61	-

Table C.2: Tab design of tensile specimens, direction 1. Parameters and results of the second DoE.

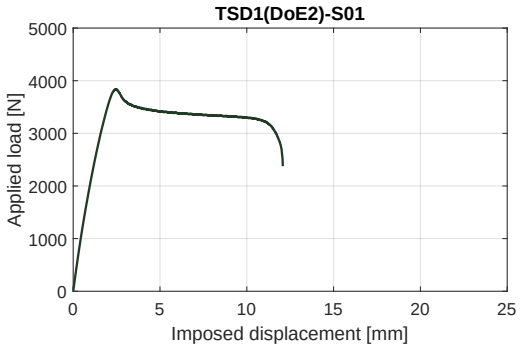

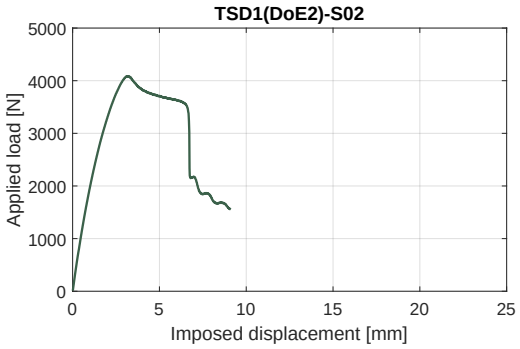

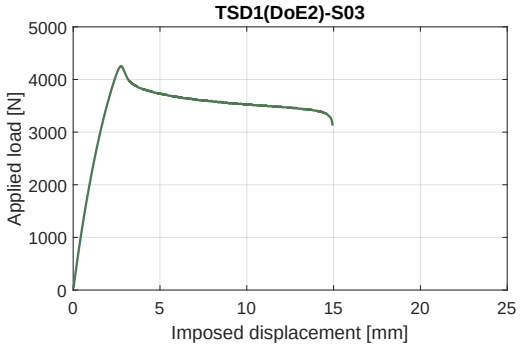
TSD1(DoE2)-S03
Applied load [N]
Imposed displacement [mm]

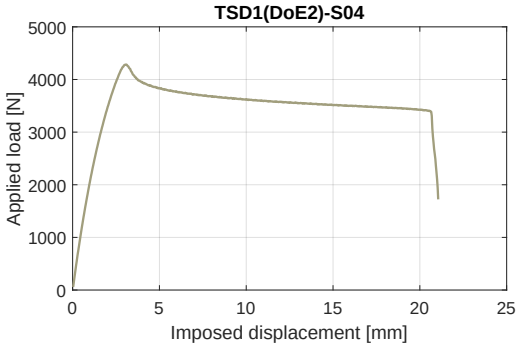
TSD1(DoE2)-S04
Applied load [N]
Imposed displacement [mm]

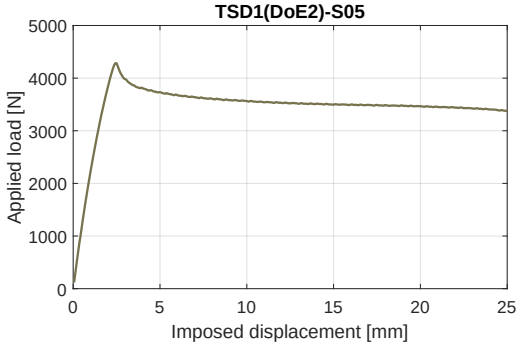
TSD1(DoE2)-S05
Applied load [N]
Imposed displacement [mm]

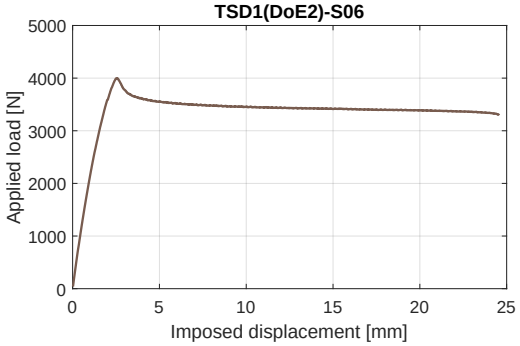
TSD1(DoE2)-S06
Applied load [N]
Imposed displacement [mm]

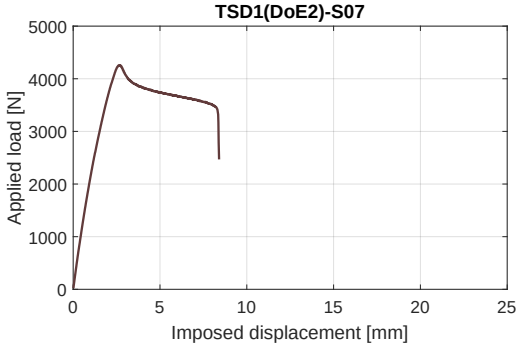
TSD1(DoE2)-S07
Applied load [N]
Imposed displacement [mm]

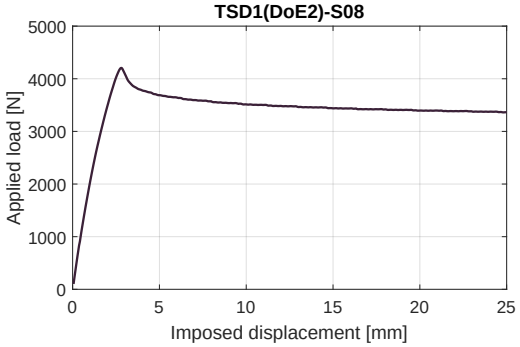
TSD1(DoE2)-S08
Applied load [N]
Imposed displacement [mm]

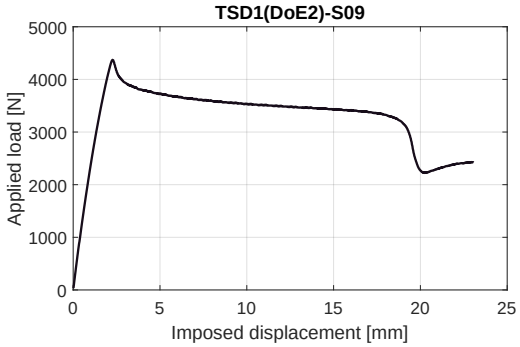
TSD1(DoE2)-S09
Applied load [N]
Imposed displacement [mm]

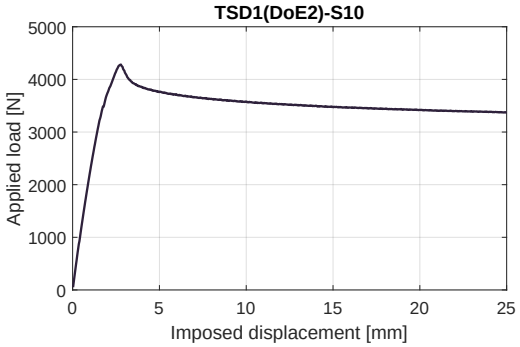
TSD1(DoE2)-S10
Applied load [N]
Imposed displacement [mm]

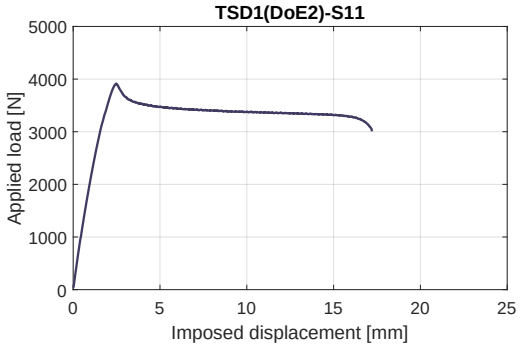
TSD1(DoE2)-S11
Applied load [N]
Imposed displacement [mm]
0
1000
2000
3000
4000
5000
0
5
10
15
20
25

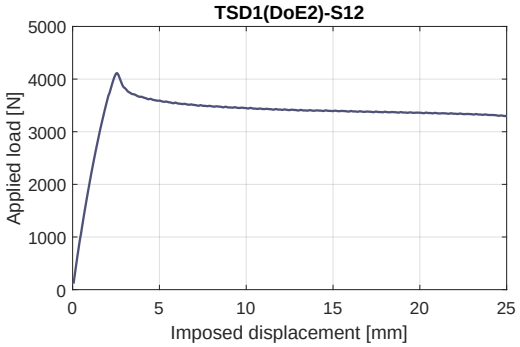
TSD1(DoE2)-S12
Applied load [N]
Imposed displacement [mm]
0
1000
2000
3000
4000
5000
0
5
10
15
20
25

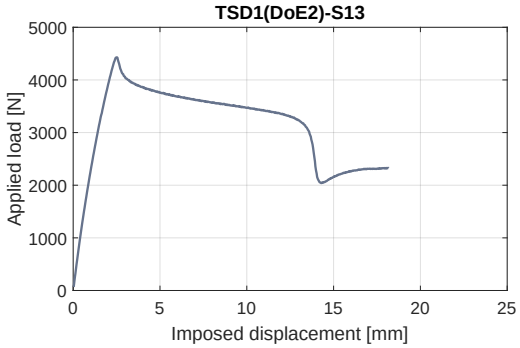
TSD1(DoE2)-S13
Applied load [N]
Imposed displacement [mm]
0
1000
2000
3000
4000
5000
0
5
10
15
20
25

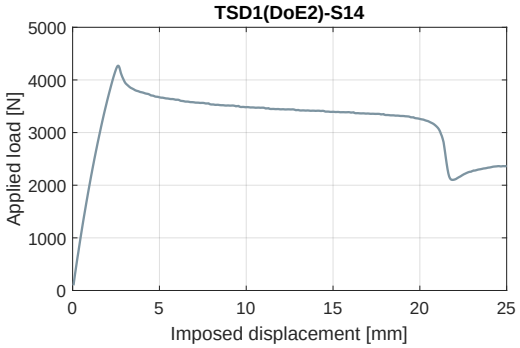
TSD1(DoE2)-S14
Applied load [N]
Imposed displacement [mm]
0
1000
2000
3000
4000
5000
0
5
10
15
20
25

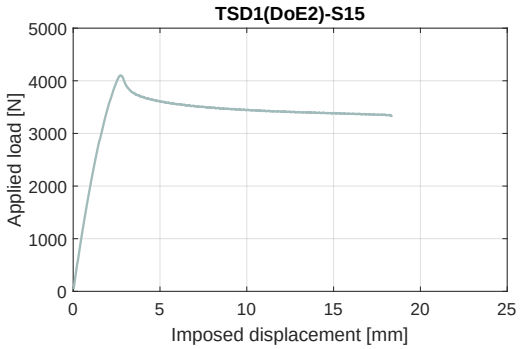
TSD1(DoE2)-S15
Applied load [N]
Imposed displacement [mm]
0
1000
2000
3000
4000
5000
0
5
10
15
20
25

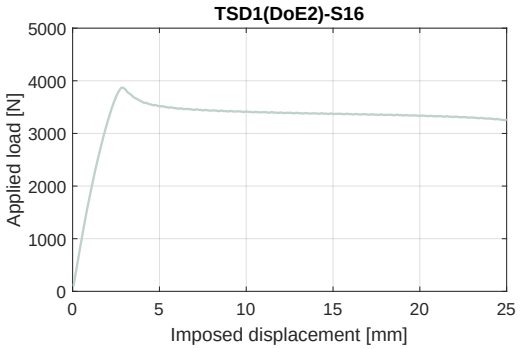
TSD1(DoE2)-S16
Applied load [N]
Imposed displacement [mm]
0
1000
2000
3000
4000
5000
0
5
10
15
20
25

Tensile specimens loaded in direction 2: first DoE

SPECIMEN	DoE factors		Cross-section		DoE param.	
	t_{tab}	α_{tab}	W	T	σ_{max}	y_{fail}
	[mm]		[mm]	[mm]	[MPa]	[%]
TSD2(DoE1)-S01	0.5	5°	24.94	2.98	40.18	7.6
TSD2(DoE1)-S02	0.5	10°	24.99	2.97	41.36	20.2
TSD2(DoE1)-S03	0.5	20°	24.95	3.02	44.44	37.8
TSD2(DoE1)-S04	0.5	90°	24.93	2.98	43.96	31.1
TSD2(DoE1)-S05	1.0	5°	24.96	3.00	43.21	32.8
TSD2(DoE1)-S06	1.0	10°	25.00	2.98	40.03	30.5
TSD2(DoE1)-S07	1.0	20°	24.97	3.00	44.53	39.1
TSD2(DoE1)-S08	1.0	90°	24.94	3.02	43.34	34.4
TSD2(DoE1)-S09	1.5	5°	24.95	2.95	42.90	0.0
TSD2(DoE1)-S10	1.5	10°	24.95	3.01	39.16	2.7
TSD2(DoE1)-S11	1.5	20°	24.94	2.97	39.93	36.7
TSD2(DoE1)-S12	1.5	90°	25.05	2.98	41.51	28.9
TSD2(DoE1)-S13	2.0	5°	24.99	3.00	44.67	6.8
TSD2(DoE1)-S14	2.0	10°	24.95	2.98	44.60	13.4
TSD2(DoE1)-S15	2.0	20°	24.95	3.00	41.75	6.3
TSD2(DoE1)-S16	2.0	90°	24.95	3.01	36.22	0.0

Table C.3: Tab design of tensile specimens, direction 2. Parameters and results of the first DoE.

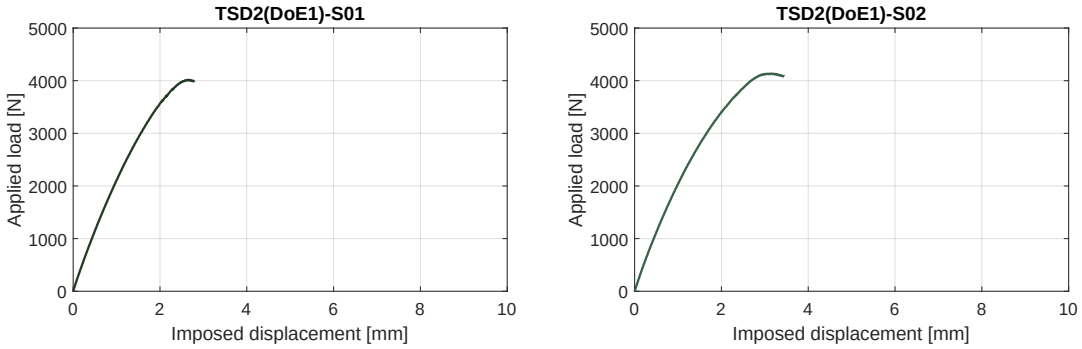

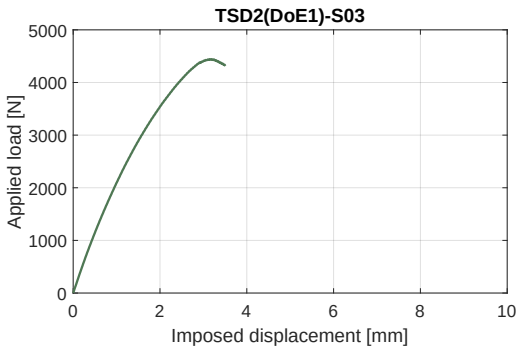
TSD2(DoE1)-S03
Applied load [N]
Imposed displacement [mm]

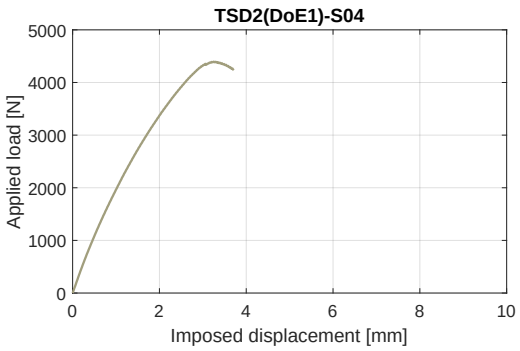
TSD2(DoE1)-S04
Applied load [N]
Imposed displacement [mm]

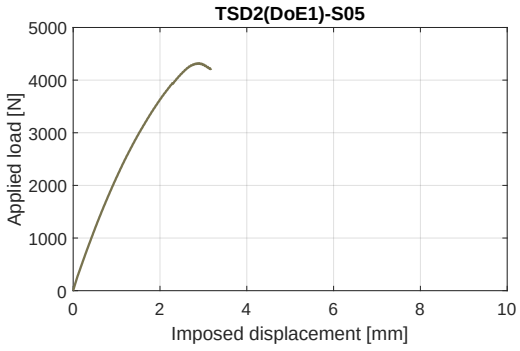
TSD2(DoE1)-S05
Applied load [N]
Imposed displacement [mm]

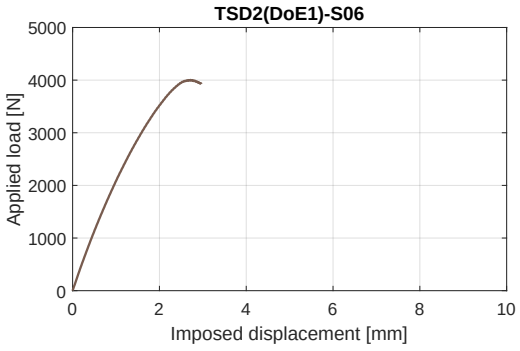
TSD2(DoE1)-S06
Applied load [N]
Imposed displacement [mm]

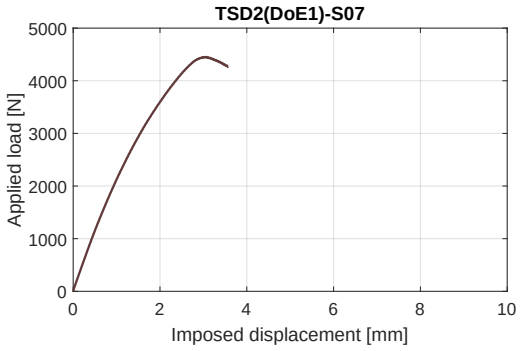
TSD2(DoE1)-S07
Applied load [N]
Imposed displacement [mm]

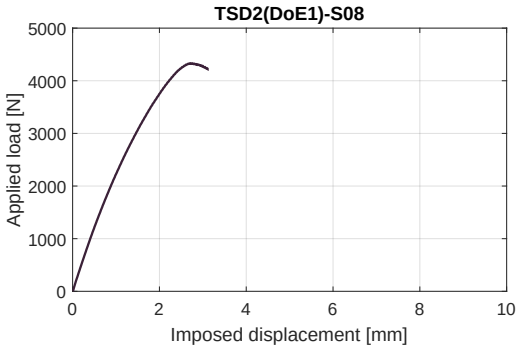
TSD2(DoE1)-S08
Applied load [N]
Imposed displacement [mm]

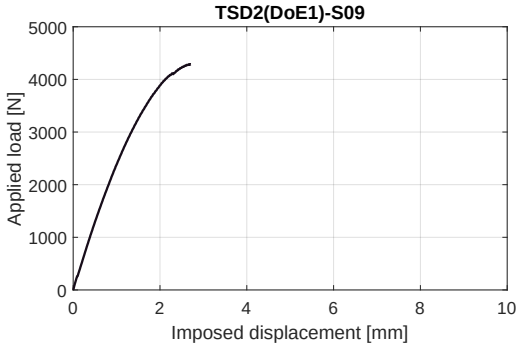
TSD2(DoE1)-S09
Applied load [N]
Imposed displacement [mm]

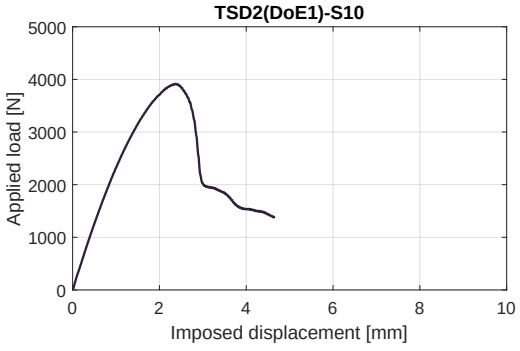
TSD2(DoE1)-S10
Applied load [N]
Imposed displacement [mm]

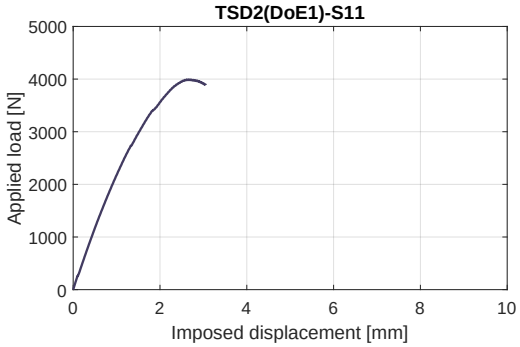
TSD2(DoE1)-S11
Applied load [N]
Imposed displacement [mm]
0
1000
2000
3000
4000
5000
0
2
4
6
8
10

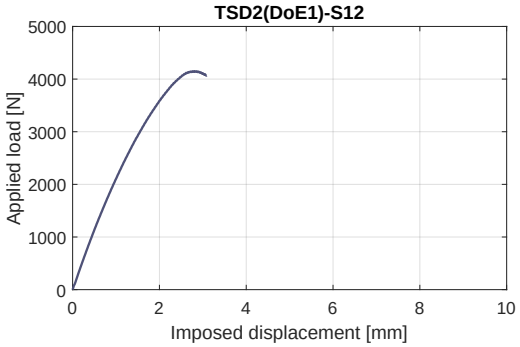
TSD2(DoE1)-S12
Applied load [N]
Imposed displacement [mm]
0
1000
2000
3000
4000
5000
0
2
4
6
8
10

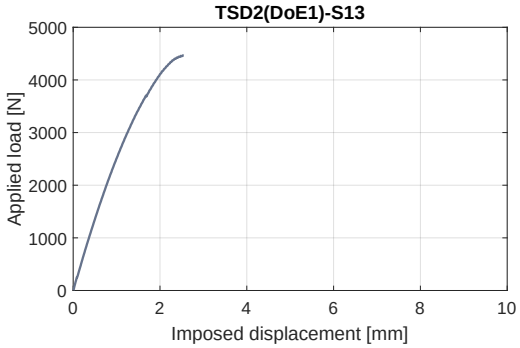
TSD2(DoE1)-S13
Applied load [N]
Imposed displacement [mm]
0
1000
2000
3000
4000
5000
0
2
4
6
8
10

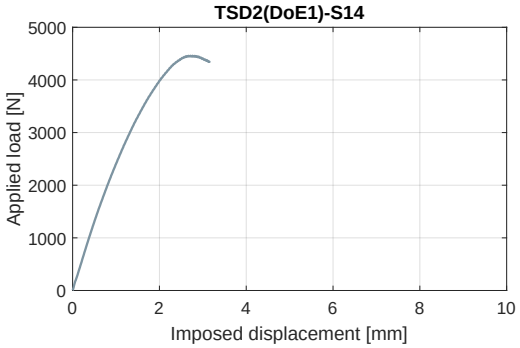
TSD2(DoE1)-S14
Applied load [N]
Imposed displacement [mm]
0
1000
2000
3000
4000
5000
0
2
4
6
8
10

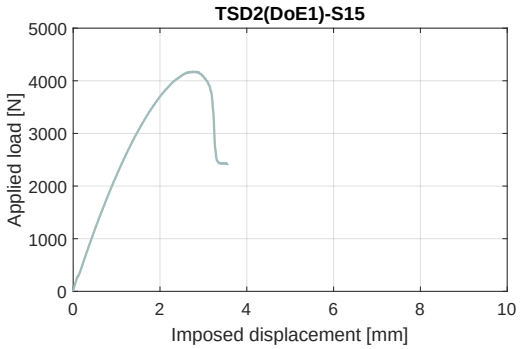
TSD2(DoE1)-S15
Applied load [N]
Imposed displacement [mm]
0
1000
2000
3000
4000
5000
0
2
4
6
8
10

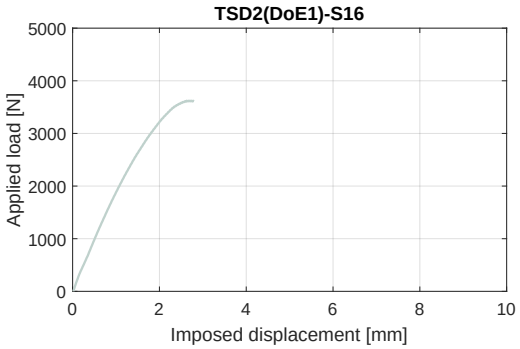
TSD2(DoE1)-S16
Applied load [N]
Imposed displacement [mm]
0
1000
2000
3000
4000
5000
0
2
4
6
8
10

Tensile specimens loaded in direction 2: second DoE

SPECIMEN	DoE factors		Cross-section		DoE param.	
	t_{tab}	α_{tab}	W	T	σ_{max}	y_{fail}
	[mm]		[mm]	[mm]	[MPa]	[%]
TSD2(DoE2)-S01	0.5	5°	24.94	2.98	45.91	2.5
TSD2(DoE2)-S02	0.5	10°	24.99	2.97	48.38	3.6
TSD2(DoE2)-S03	0.5	20°	24.95	3.02	46.05	14.3
TSD2(DoE2)-S04	0.5	90°	24.93	2.98	47.36	0.0
TSD2(DoE2)-S05	1.0	5°	24.96	3.00	50.16	0.0
TSD2(DoE2)-S06	1.0	10°	25.00	2.98	47.10	28.0
TSD2(DoE2)-S07	1.0	20°	24.97	3.00	48.28	32.0
TSD2(DoE2)-S08	1.0	90°	24.94	3.02	48.20	32.2
TSD2(DoE2)-S09	1.5	5°	24.95	2.95	49.86	9.0
TSD2(DoE2)-S10	1.5	10°	24.95	3.01	44.59	2.7
TSD2(DoE2)-S11	1.5	20°	24.94	2.97	48.42	29.4
TSD2(DoE2)-S12	1.5	90°	25.05	2.98	46.72	0.0
TSD2(DoE2)-S13	2.0	5°	24.99	3.00	49.75	11.3
TSD2(DoE2)-S14	2.0	10°	24.95	2.98	47.78	4.5
TSD2(DoE2)-S15	2.0	20°	24.95	3.00	47.23	1.3
TSD2(DoE2)-S16	2.0	90°	24.95	3.01	48.71	1.1

Table C.4: Tab design of tensile specimens, direction 2. Parameters and results of the second DoE.

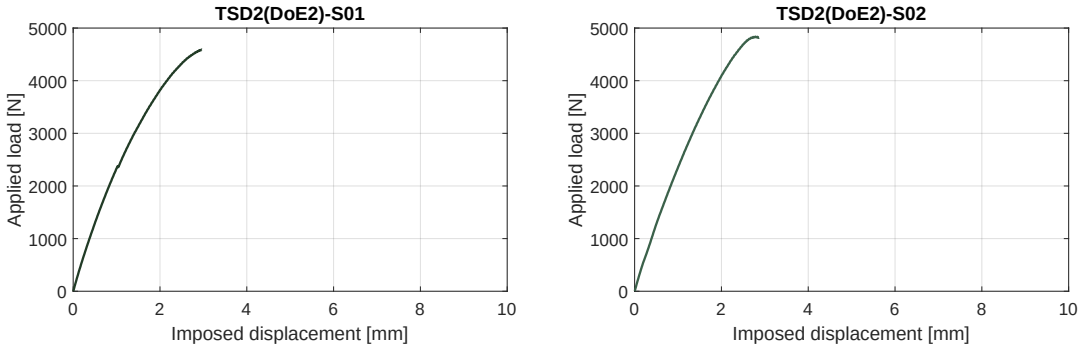

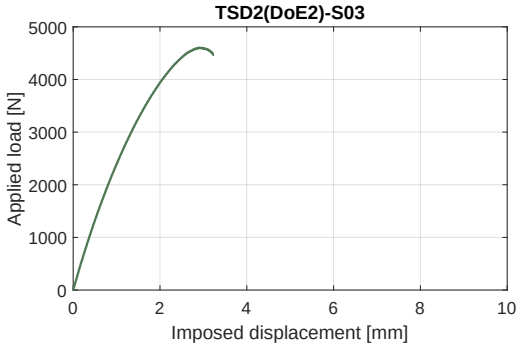
TSD2(DoE2)-S03
Applied load [N]
Imposed displacement [mm]
0
1000
2000
3000
4000
5000
0
2
4
6
8
10

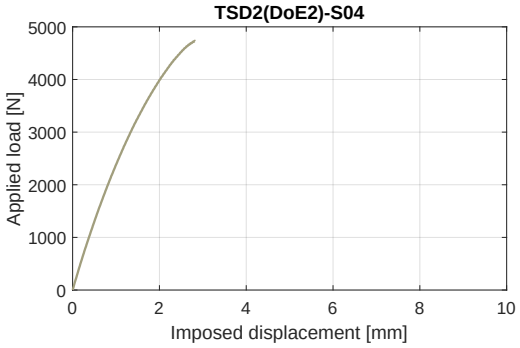
TSD2(DoE2)-S04
Applied load [N]
Imposed displacement [mm]
0
1000
2000
3000
4000
5000
0
2
4
6
8
10

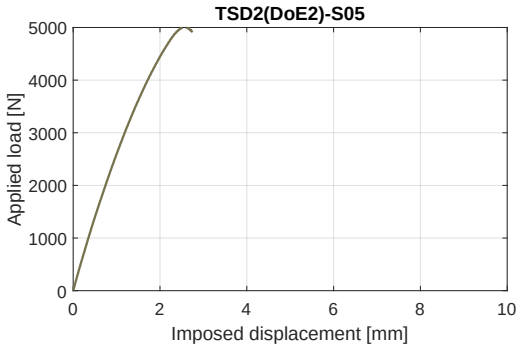
TSD2(DoE2)-S05
Applied load [N]
Imposed displacement [mm]
0
1000
2000
3000
4000
5000
0
2
4
6
8
10

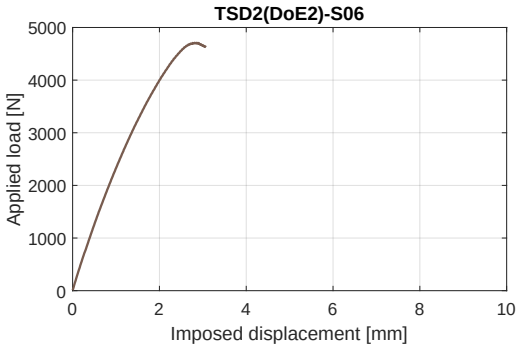
TSD2(DoE2)-S06
Applied load [N]
Imposed displacement [mm]
0
1000
2000
3000
4000
5000
0
2
4
6
8
10

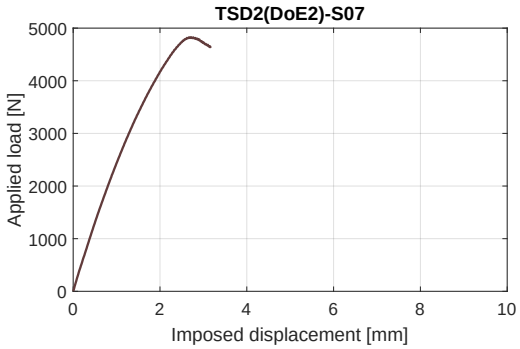
TSD2(DoE2)-S07
Applied load [N]
Imposed displacement [mm]
0
1000
2000
3000
4000
5000
0
2
4
6
8
10

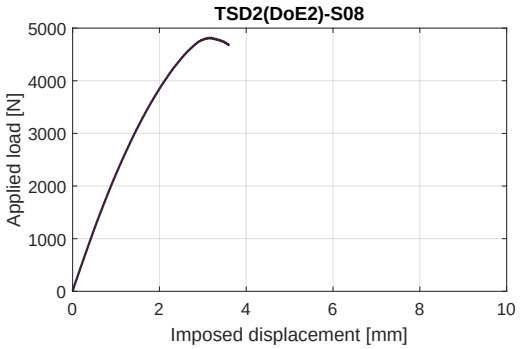
TSD2(DoE2)-S08
Applied load [N]
Imposed displacement [mm]
0
1000
2000
3000
4000
5000
0
2
4
6
8
10

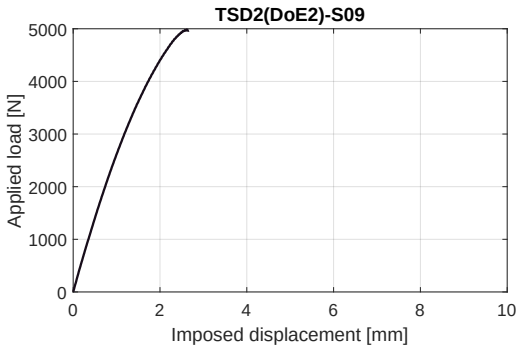
TSD2(DoE2)-S09
Applied load [N]
Imposed displacement [mm]
0
1000
2000
3000
4000
5000
0
2
4
6
8
10

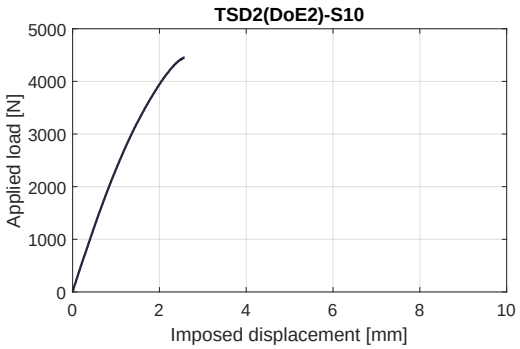
TSD2(DoE2)-S10
Applied load [N]
Imposed displacement [mm]
0
1000
2000
3000
4000
5000
0
2
4
6
8
10

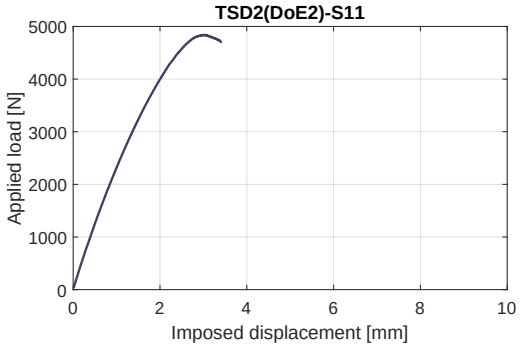
TSD2(DoE2)-S11
Applied load [N]
Imposed displacement [mm]
0
1000
2000
3000
4000
5000
0
2
4
6
8
10

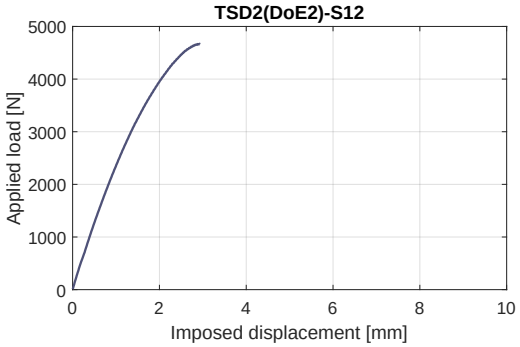
TSD2(DoE2)-S12
Applied load [N]
Imposed displacement [mm]
0
1000
2000
3000
4000
5000
0
2
4
6
8
10

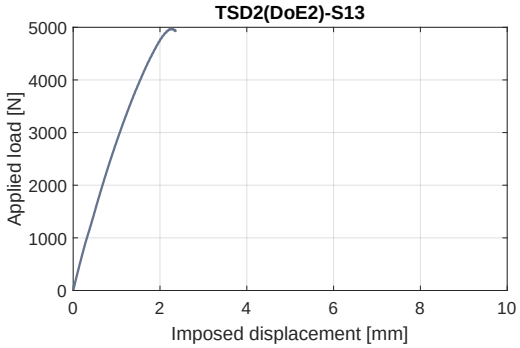
TSD2(DoE2)-S13
Applied load [N]
Imposed displacement [mm]
0
1000
2000
3000
4000
5000
0
2
4
6
8
10

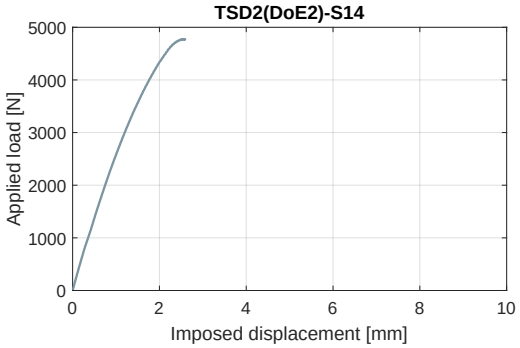
TSD2(DoE2)-S14
Applied load [N]
Imposed displacement [mm]
0
1000
2000
3000
4000
5000
0
2
4
6
8
10

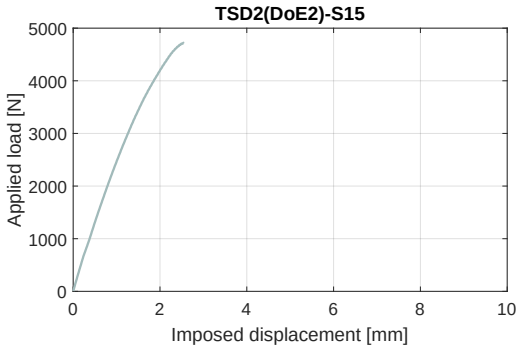
TSD2(DoE2)-S15
Applied load [N]
Imposed displacement [mm]
0
1000
2000
3000
4000
5000
0
2
4
6
8
10

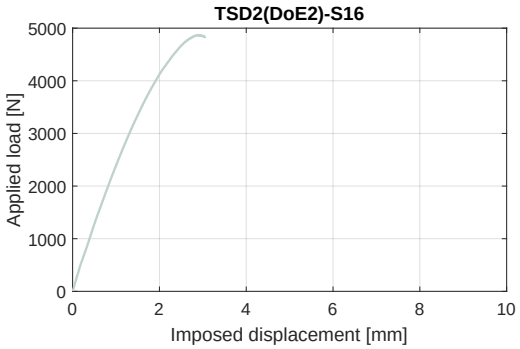
TSD2(DoE2)-S16
Applied load [N]
Imposed displacement [mm]
0
1000
2000
3000
4000
5000
0
2
4
6
8
10

C.1.2 Actual Tests

This sub-section contains the results of the actual tensile tests, performed with the designed tab geometry, and following the standard test method ASTM D3039. A summary table has been reported, and the individual load vs. displacement curves.

Tensile specimens loaded in direction 1

SPECIMEN	Cross-section		Mechanical analysis			
	W	T	E_{11}	σ_{11}^{max}	σ_{11}^{pro}	ν_{12}
	[mm]	[mm]	[MPa]	[MPa]	[MPa]	[-]
TSD1-S01	24.91	2.96	3007	56.18	53.36	0.288
TSD1-S02	24.99	3.04	3094	55.83	51.72	0.303
TSD1-S03	24.99	3.02	3029	56.99	54.33	0.269
TSD1-S04	25.00	3.04	2920	56.75	55.39	0.274
TSD1-S05	25.00	3.01	2987	56.26	51.81	0.277
TSD1-S06	24.92	2.97	2944	56.00	54.31	0.275
TSD1-S07	24.94	2.98	3037	56.41	56.41	0.297
TSD1-S08	24.91	2.97	2867	56.64	54.30	0.269
TSD1-S09	24.92	2.99	3183	56.44	54.31	0.321
TSD1 Sample						
mean	24.95	3.00	**3008**	**56.39**	**53.99**	**0.286**
st.dev	0.041	0.031	94.51	0.368	1.522	0.018

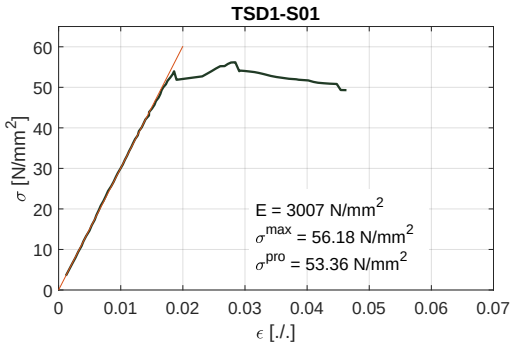

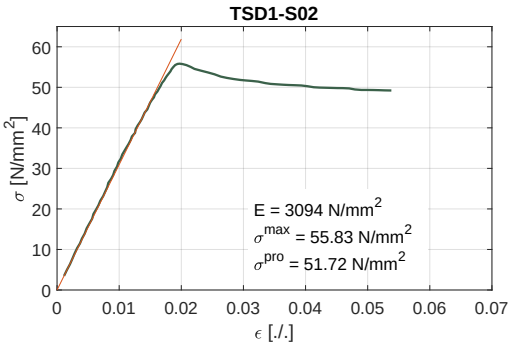

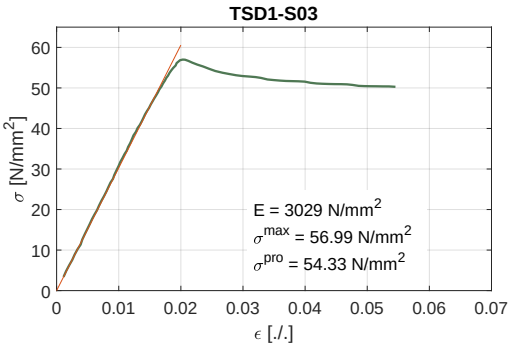
TSD1-S03
E = 3029 N/mm2
σmax = 56.99 N/mm2
σpro = 54.33 N/mm2
σ [N/mm2]
ϵ [./.]

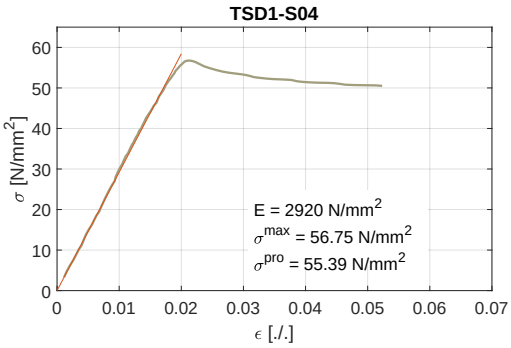
TSD1-S04
E = 2920 N/mm2
σmax = 56.75 N/mm2
σpro = 55.39 N/mm2
σ [N/mm2]
ϵ [./.]

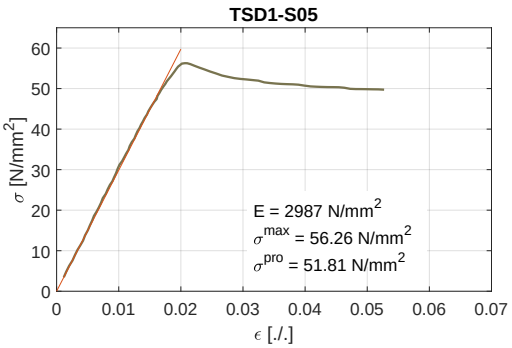
TSD1-S05
E = 2987 N/mm2
σmax = 56.26 N/mm2
σpro = 51.81 N/mm2
σ [N/mm2]
ϵ [./.]

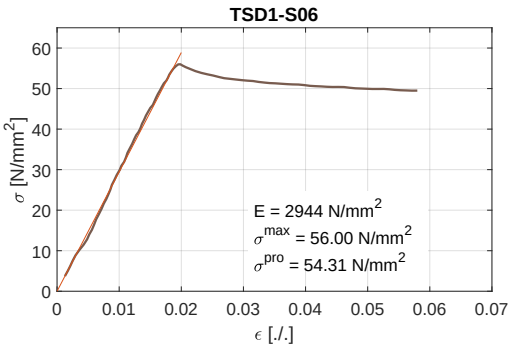
TSD1-S06
E = 2944 N/mm2
σmax = 56.00 N/mm2
σpro = 54.31 N/mm2
σ [N/mm2]
ϵ [./.]

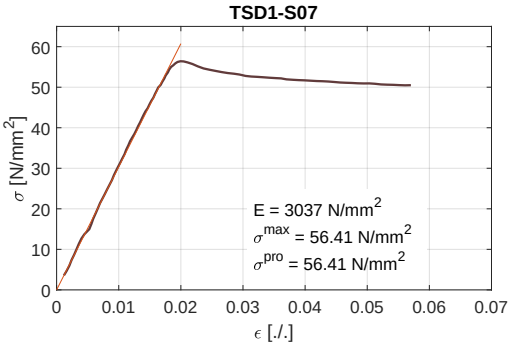
TSD1-S07
E = 3037 N/mm2
σmax = 56.41 N/mm2
σpro = 56.41 N/mm2
σ [N/mm2]
ϵ [./.]

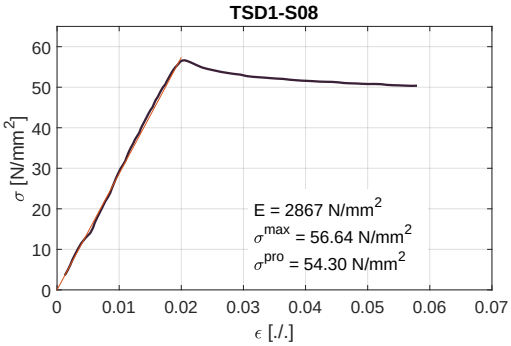
TSD1-S08
E = 2867 N/mm2
σmax = 56.64 N/mm2
σpro = 54.30 N/mm2
σ [N/mm2]
ϵ [./.]

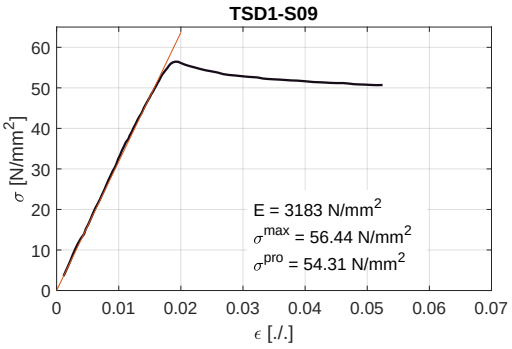
TSD1-S09
E = 3183 N/mm2
σmax = 56.44 N/mm2
σpro = 54.31 N/mm2
σ [N/mm2]
ϵ [./.]

Tensile specimens loaded in direction 2

SPECIMEN	Cross-section		Mechanical analysis			
	W	T	E_{22}	σ_{22}^{max}	σ_{22}^{pro}	ν_{23}
	[mm]	[mm]	[MPa]	[MPa]	[MPa]	[-]
TSD2-S01	24.84	4.12	2863	49.03	47.74	0.282
TSD2-S02	24.83	4.13	2783	49.03	46.24	0.233
TSD2-S03	24.82	4.14	2902	46.79	46.60	0.265
TSD2-S04	24.85	4.14	2905	49.10	46.22	0.289
TSD2-S05	24.83	4.12	2866	47.66	47.16	0.252
TSD2-S06	24.82	4.15	2840	47.90	47.31	0.249
TSD2-S07	24.83	4.13	2902	48.01	43.88	0.286
TSD2-S08	24.83	4.16	2821	49.36	46.47	0.262
TSD2-S09	24.78	4.13	2950	44.03	43.54	0.259
TSD2-S10	24.81	4.16	2926	49.50	47.00	0.292
TSD2 Sample						
mean	24.82	4.14	**2876**	**48.04**	**46.22**	**0.267**
st.dev	0.019	0.015	50.97	1.659	1.409	0.020

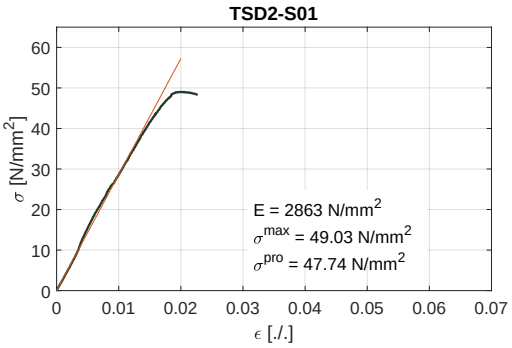

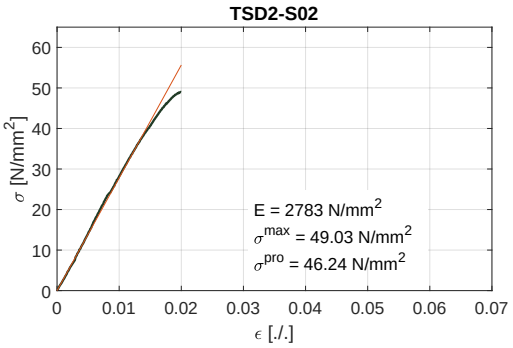

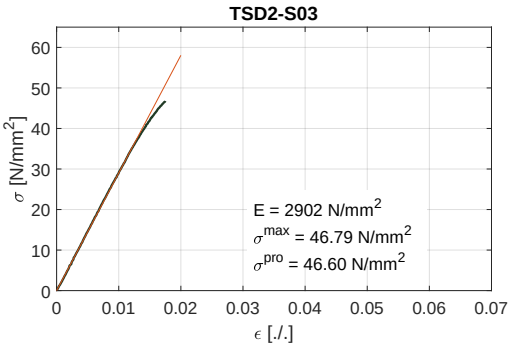
TSD2-S03
E = 2902 N/mm2
σmax = 46.79 N/mm2
σpro = 46.60 N/mm2
σ [N/mm2]
ϵ [./.]

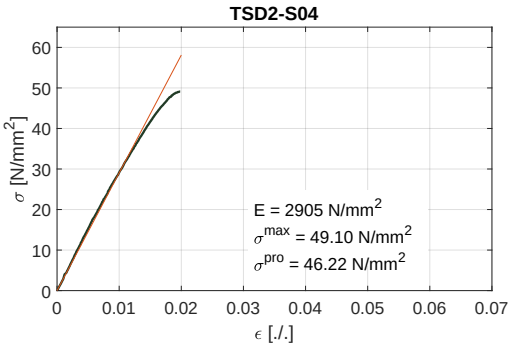
TSD2-S04
E = 2905 N/mm2
σmax = 49.10 N/mm2
σpro = 46.22 N/mm2
σ [N/mm2]
ϵ [./.]

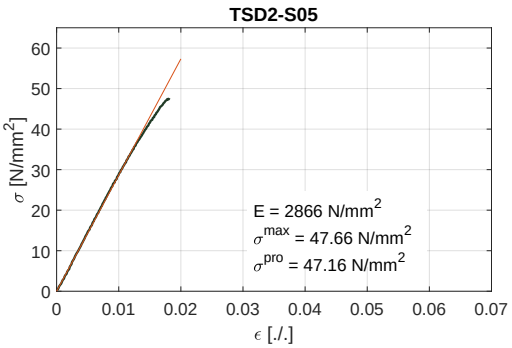
TSD2-S05
E = 2866 N/mm2
σmax = 47.66 N/mm2
σpro = 47.16 N/mm2
σ [N/mm2]
ϵ [./.]

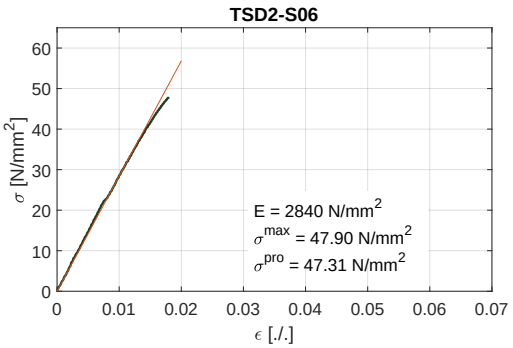
TSD2-S06
E = 2840 N/mm2
σmax = 47.90 N/mm2
σpro = 47.31 N/mm2
σ [N/mm2]
ϵ [./.]

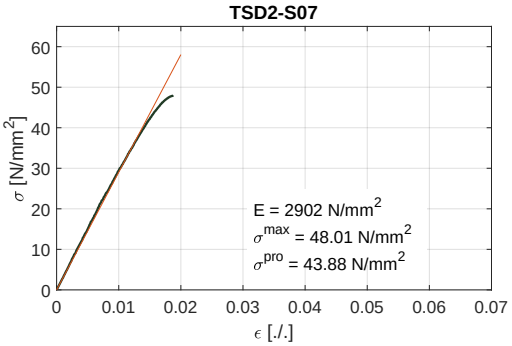
TSD2-S07
E = 2902 N/mm2
σmax = 48.01 N/mm2
σpro = 43.88 N/mm2
σ [N/mm2]
ϵ [./.]

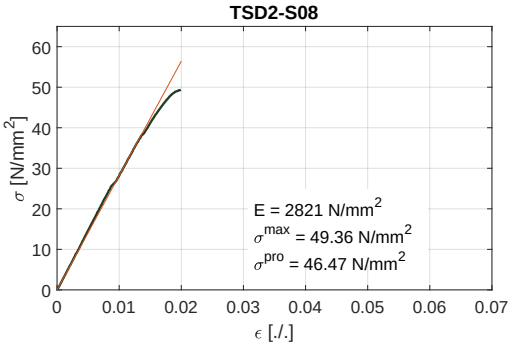
TSD2-S08
E = 2821 N/mm2
σmax = 49.36 N/mm2
σpro = 46.47 N/mm2
σ [N/mm2]
ϵ [./.]

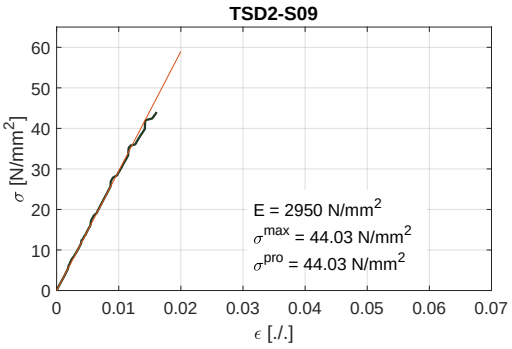
TSD2-S09
E = 2950 N/mm2
σmax = 44.03 N/mm2
σpro = 44.03 N/mm2
σ [N/mm2]
ϵ [./.]

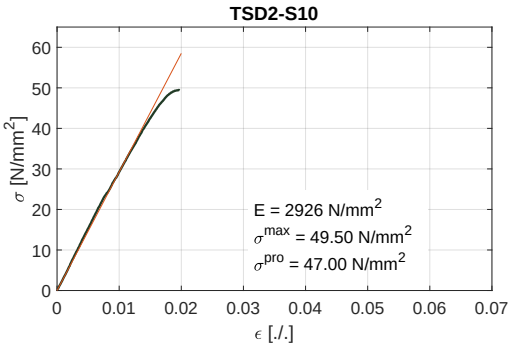
TSD2-S10
E = 2926 N/mm2
σmax = 49.50 N/mm2
σpro = 47.00 N/mm2
σ [N/mm2]
ϵ [./.]

C.2 Shear tests

This section reports all the results of the shear tests. Tables and graphs are grouped depending on the test they refer to.

C.2.1 Design of Experiments

This sub-section contains the results of the Design of Experiments used to design the tabs for shear tests according to ASTM D3039/D3518. For each DoE a summary table has been reported, with the parameters of each specimen, and the individual load vs. displacement curves.

In-plane shear specimens: first DoE

SPECIMEN	DoE factors		Cross-section		DoE param.	
	t_{tab} [mm]	α_{tab}	W [mm]	T [mm]	σ_{max} [MPa]	y_{fail} [%]
SSD12(DoE1)-S01	0.5	5°	24.94	2.98	57.93	–
SSD12(DoE1)-S02	0.5	10°	24.99	2.97	58.53	–
SSD12(DoE1)-S03	0.5	20°	24.95	3.02	57.63	–
SSD12(DoE1)-S04	0.5	90°	24.93	2.98	52.72	–
SSD12(DoE1)-S05	1.0	5°	24.96	3.00	56.95	–
SSD12(DoE1)-S06	1.0	10°	25.00	2.98	57.91	–
SSD12(DoE1)-S07	1.0	20°	24.97	3.00	58.85	–
SSD12(DoE1)-S08	1.0	90°	24.94	3.02	58.33	–
SSD12(DoE1)-S09	1.5	5°	24.95	2.95	60.35	–
SSD12(DoE1)-S10	1.5	10°	24.95	3.01	58.69	–
SSD12(DoE1)-S11	1.5	20°	24.94	2.97	58.17	–
SSD12(DoE1)-S12	1.5	90°	25.05	2.98	58.11	–
SSD12(DoE1)-S13	2.0	5°	24.99	3.00	61.55	–
SSD12(DoE1)-S14	2.0	10°	24.95	2.98	60.00	–
SSD12(DoE1)-S15	2.0	20°	24.95	3.00	59.35	–
SSD12(DoE1)-S16	2.0	90°	24.95	3.01	60.24	–

Table C.5: Tab design of in-plane shear specimens. Parameters and results of the first DoE.

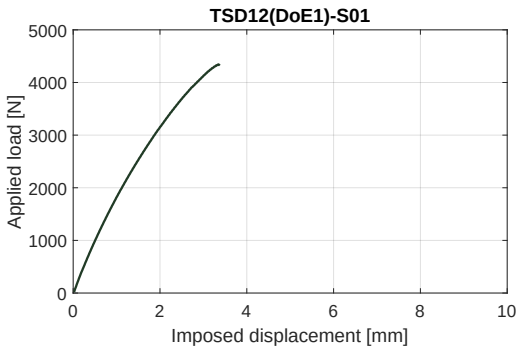
TSD12(DoE1)-S01
Applied load [N]
Imposed displacement [mm]

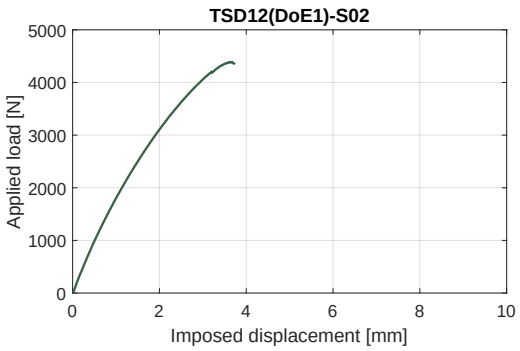
TSD12(DoE1)-S02
Applied load [N]
Imposed displacement [mm]

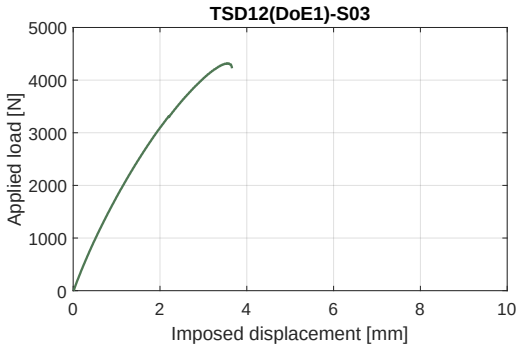
TSD12(DoE1)-S03
Applied load [N]
Imposed displacement [mm]

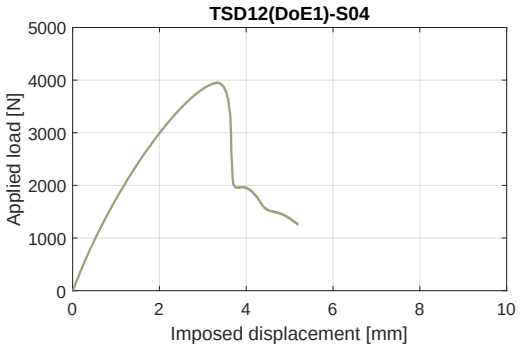
TSD12(DoE1)-S04
Applied load [N]
Imposed displacement [mm]

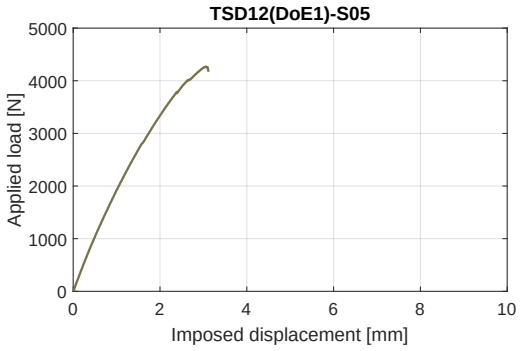
TSD12(DoE1)-S05
Applied load [N]
Imposed displacement [mm]

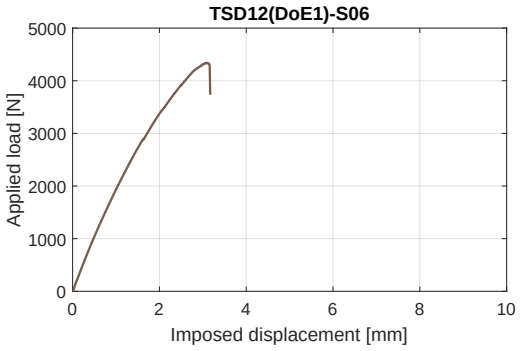
TSD12(DoE1)-S06
Applied load [N]
Imposed displacement [mm]

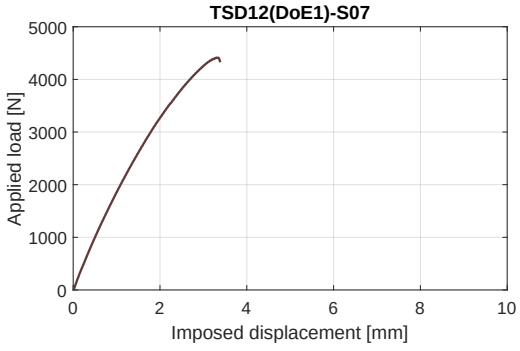
TSD12(DoE1)-S07
Applied load [N]
Imposed displacement [mm]

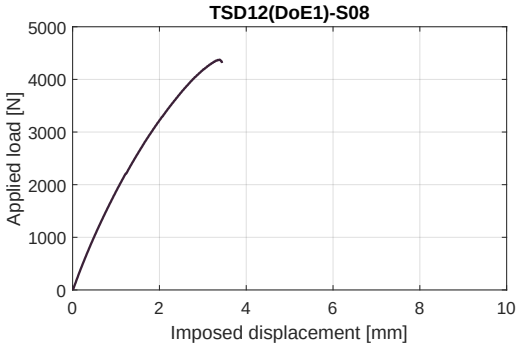
TSD12(DoE1)-S08
Applied load [N]
Imposed displacement [mm]

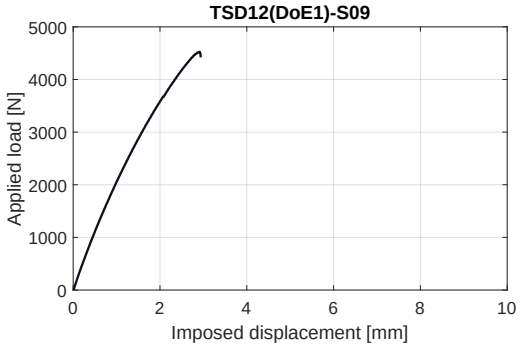
TSD12(DoE1)-S09
Applied load [N]
Imposed displacement [mm]

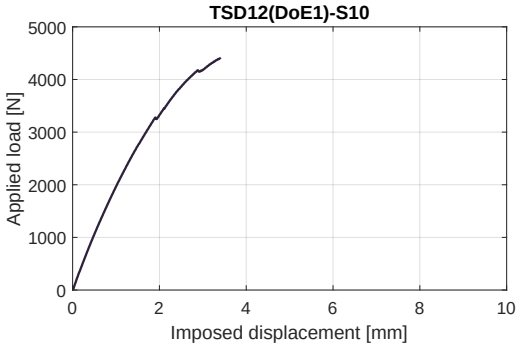
TSD12(DoE1)-S10
Applied load [N]
Imposed displacement [mm]

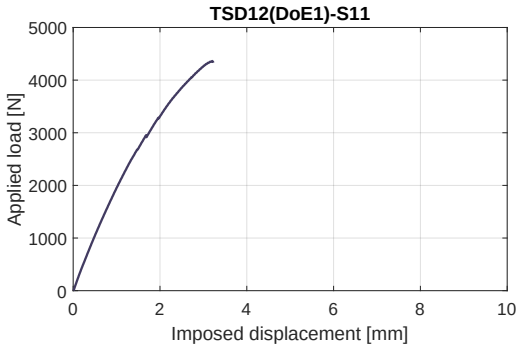
TSD12(DoE1)-S11
Applied load [N]
Imposed displacement [mm]

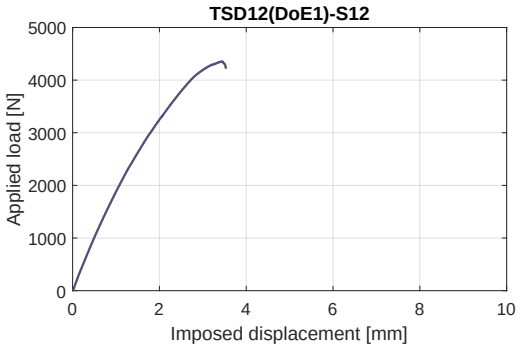
TSD12(DoE1)-S12
Applied load [N]
Imposed displacement [mm]

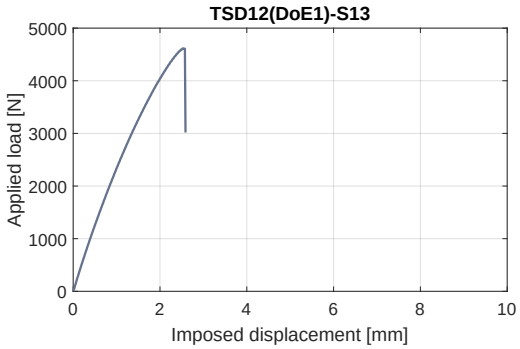
TSD12(DoE1)-S13
Applied load [N]
Imposed displacement [mm]

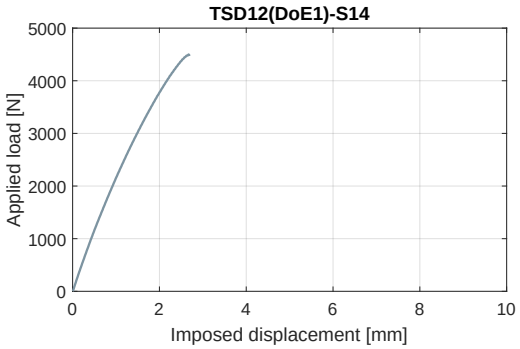
TSD12(DoE1)-S14
Applied load [N]
Imposed displacement [mm]

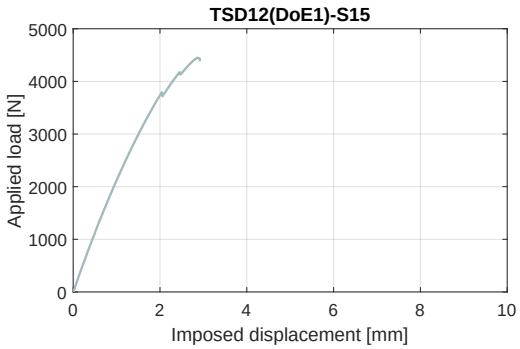
TSD12(DoE1)-S15
Applied load [N]
Imposed displacement [mm]

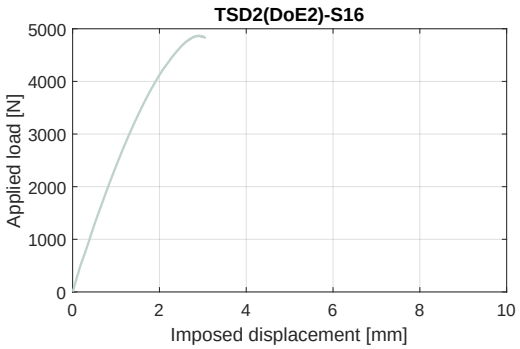
TSD2(DoE2)-S16
Applied load [N]
Imposed displacement [mm]

In-plane shear specimens: second DoE

SPECIMEN	DoE factors		Cross-section		DoE param.	
	t_{tab}	α_{tab}	W	T	σ_{max}	y_{fail}
	[mm]		[mm]	[mm]	[MPa]	[%]
SSD12(DoE2)-S01	0.5	5°	24.94	2.98	61.11	–
SSD12(DoE2)-S02	0.5	10°	24.99	2.97	56.77	–
SSD12(DoE2)-S03	0.5	20°	24.95	3.02	55.83	–
SSD12(DoE2)-S04	0.5	90°	24.93	2.98	51.77	–
SSD12(DoE2)-S05	1.0	5°	24.96	3.00	61.69	–
SSD12(DoE2)-S06	1.0	10°	25.00	2.98	60.93	–
SSD12(DoE2)-S07	1.0	20°	24.97	3.00	59.83	–
SSD12(DoE2)-S08	1.0	90°	24.94	3.02	52.67	–
SSD12(DoE2)-S09	1.5	5°	24.95	2.95	60.99	–
SSD12(DoE2)-S10	1.5	10°	24.95	3.01	60.80	–
SSD12(DoE2)-S11	1.5	20°	24.94	2.97	55.20	–
SSD12(DoE2)-S12	1.5	90°	25.05	2.98	59.53	–
SSD12(DoE2)-S13	2.0	5°	24.99	3.00	61.33	–
SSD12(DoE2)-S14	2.0	10°	24.95	2.98	61.35	–
SSD12(DoE2)-S15	2.0	20°	24.95	3.00	58.63	–
SSD12(DoE2)-S16	2.0	90°	24.95	3.01	60.93	–

Table C.6: Tab design of in-plane shear specimens. Parameters and results of the second DoE.

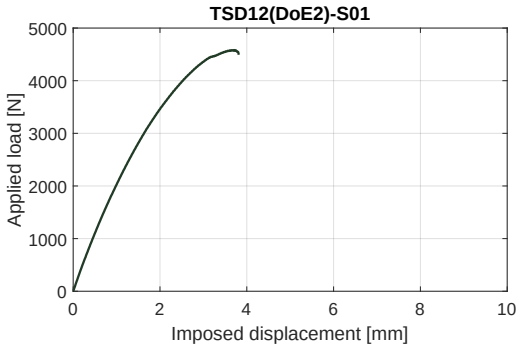

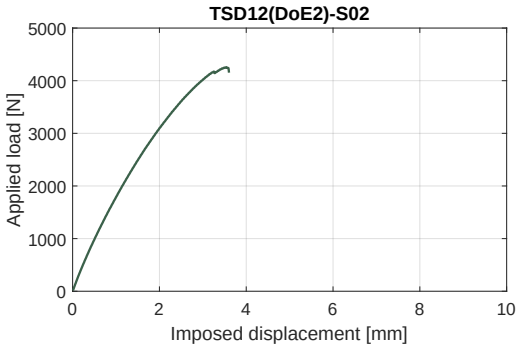

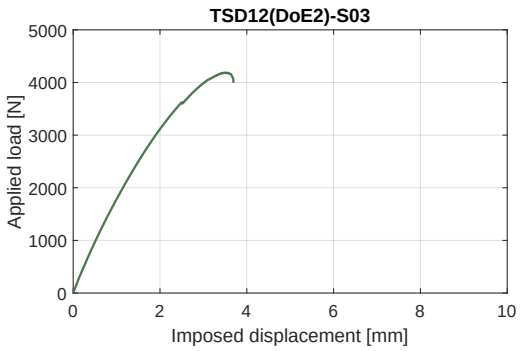
TSD12(DoE2)-S03
Applied load [N]
Imposed displacement [mm]
0
1000
2000
3000
4000
5000
0
2
4
6
8
10

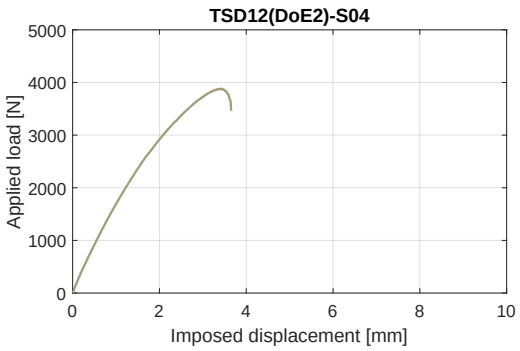
TSD12(DoE2)-S04
Applied load [N]
Imposed displacement [mm]
0
1000
2000
3000
4000
5000
0
2
4
6
8
10

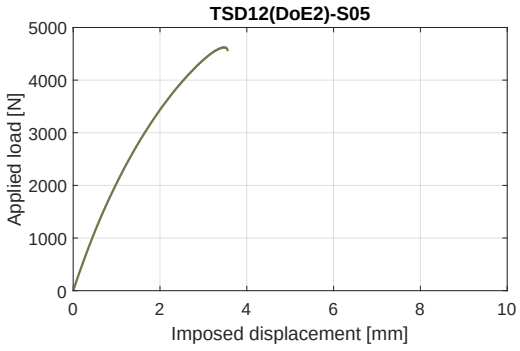
TSD12(DoE2)-S05
Applied load [N]
Imposed displacement [mm]
0
1000
2000
3000
4000
5000
0
2
4
6
8
10

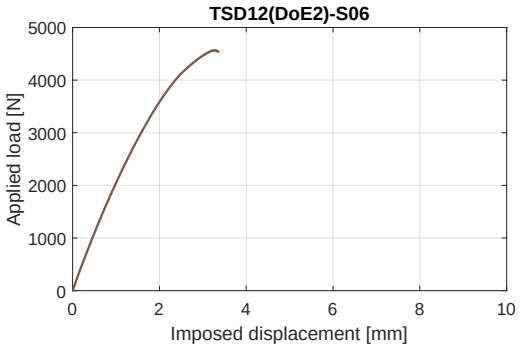
TSD12(DoE2)-S06
Applied load [N]
Imposed displacement [mm]
0
1000
2000
3000
4000
5000
0
2
4
6
8
10

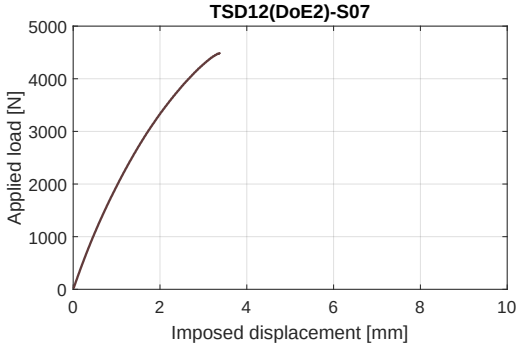
TSD12(DoE2)-S07
Applied load [N]
Imposed displacement [mm]
0
1000
2000
3000
4000
5000
0
2
4
6
8
10

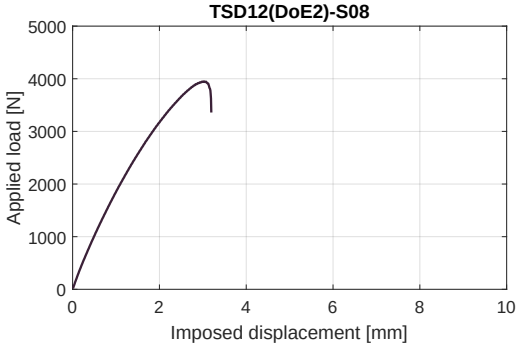
TSD12(DoE2)-S08
Applied load [N]
Imposed displacement [mm]
0
1000
2000
3000
4000
5000
0
2
4
6
8
10

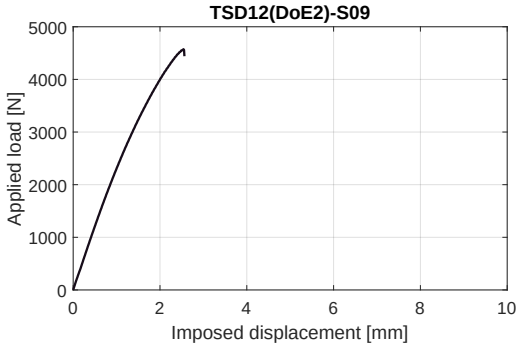
TSD12(DoE2)-S09
Applied load [N]
Imposed displacement [mm]
0
1000
2000
3000
4000
5000
0
2
4
6
8
10

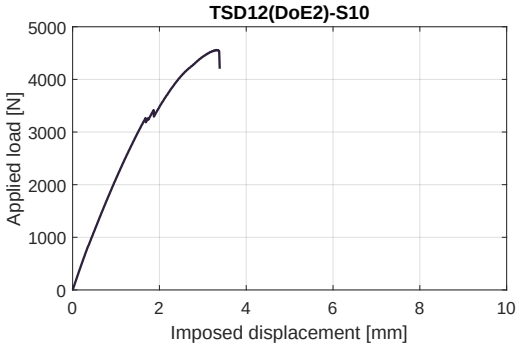
TSD12(DoE2)-S10
Applied load [N]
Imposed displacement [mm]
0
1000
2000
3000
4000
5000
0
2
4
6
8
10

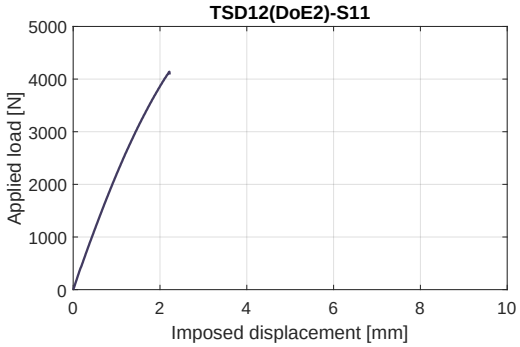
TSD12(DoE2)-S11
Applied load [N]
Imposed displacement [mm]

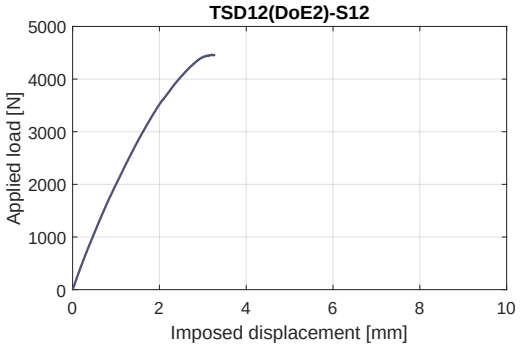
TSD12(DoE2)-S12
Applied load [N]
Imposed displacement [mm]

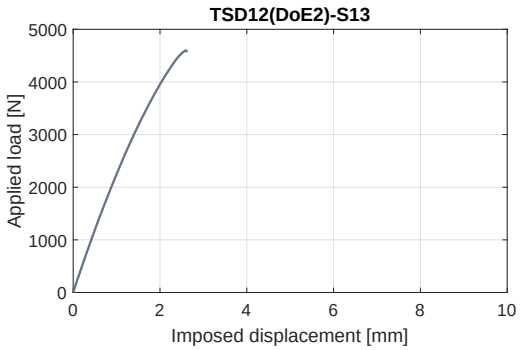
TSD12(DoE2)-S13
Applied load [N]
Imposed displacement [mm]

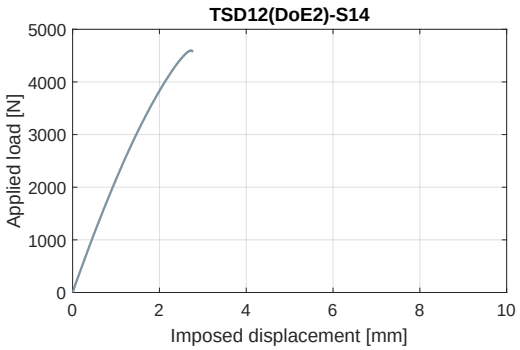
TSD12(DoE2)-S14
Applied load [N]
Imposed displacement [mm]

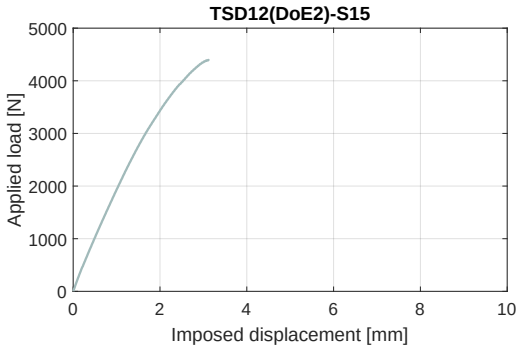
TSD12(DoE2)-S15
Applied load [N]
Imposed displacement [mm]

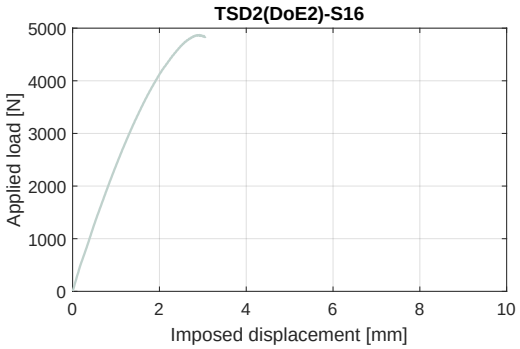
TSD2(DoE2)-S16
Applied load [N]
Imposed displacement [mm]

C.2.2 Actual Tests

This sub-section contains the results of the actual shear tests, performed with the designed tab geometry, and following the standard test method ASTM D3039/D3518. A summary table has been reported, and the individual load vs. displacement curves.

Shear specimens

SPECIMEN	Cross-section		Mechanical analysis	
	W	T	G_{12}	τ_{12}^{max}
	[mm]	[mm]	[MPa]	[MPa]
SSD12-S01	24.92	2.96	1232	30.63
SSD12-S02	24.93	2.94	1228	30.63
SSD12-S03	24.84	2.96	1240	30.30
SSD12-S04	24.89	2.94	1233	30.40
SSD12-S05	24.90	2.96	1213	30.65
SSD12-S06	24.89	2.96	1237	30.61
SSD12-S07	24.84	2.96	1230	31.12
SSD12-S08	24.89	2.96	1232	30.63
SSD12-S09	24.83	2.95	1206	30.77
SSD12-S10	24.86	2.95	1220	30.34
SSD12 Sample				
mean	24.88	2.95	**1227**	**30.61**
st.dev	0.038	0.008	10.81	0.236

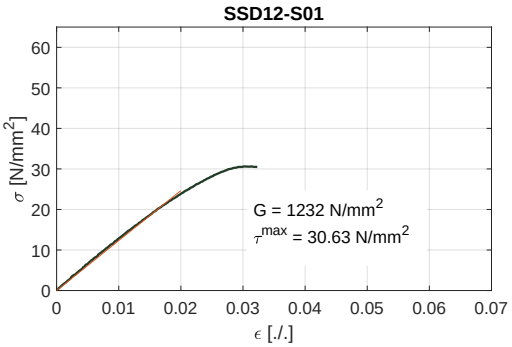

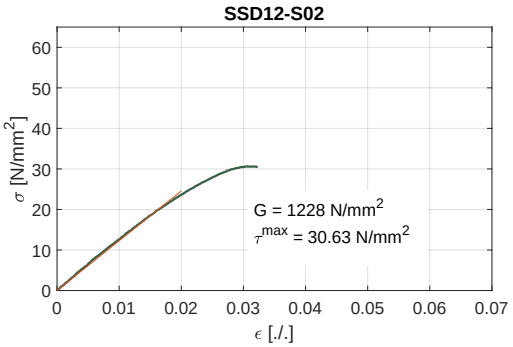

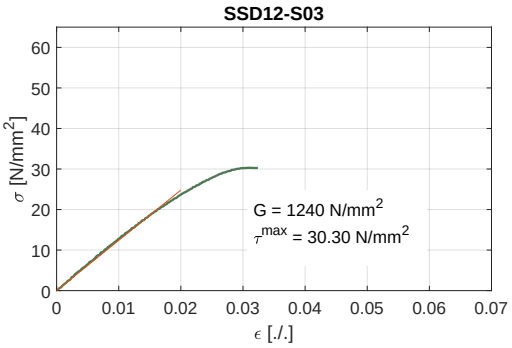
SSD12-S03
G = 1240 N/mm2
τmax = 30.30 N/mm2
σ [N/mm2]
ϵ [./.]

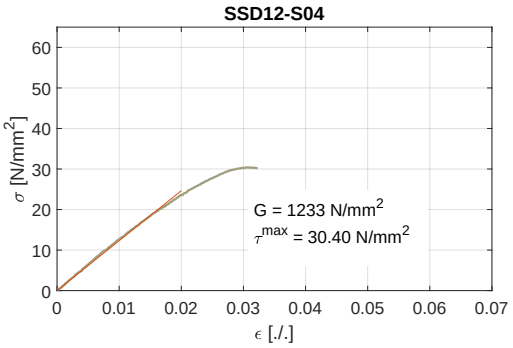
SSD12-S04
G = 1233 N/mm2
τmax = 30.40 N/mm2
σ [N/mm2]
ϵ [./.]

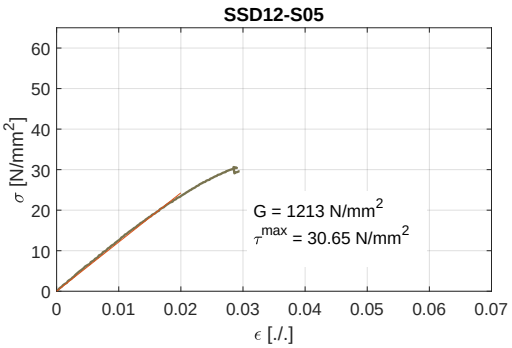
SSD12-S05
G = 1213 N/mm2
τmax = 30.65 N/mm2
σ [N/mm2]
ϵ [./.]

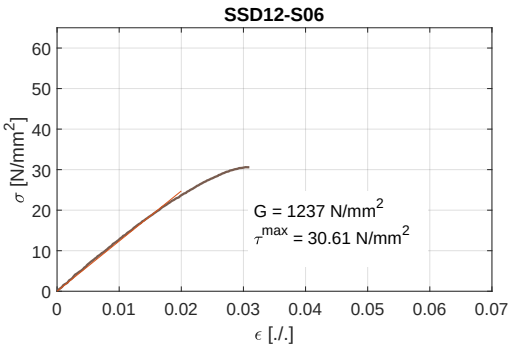
SSD12-S06
G = 1237 N/mm2
τmax = 30.61 N/mm2
σ [N/mm2]
ϵ [./.]

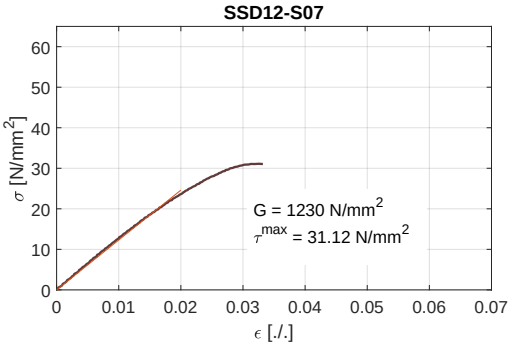
SSD12-S07
G = 1230 N/mm2
τmax = 31.12 N/mm2
σ [N/mm2]
ϵ [./.]

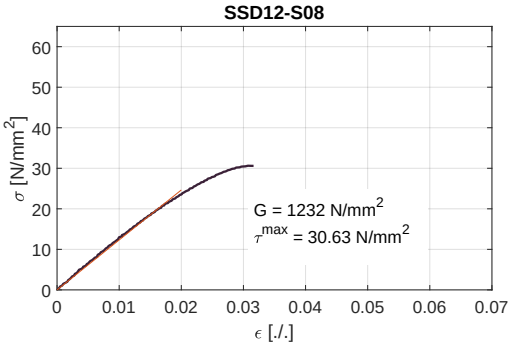
SSD12-S08
G = 1232 N/mm2
τmax = 30.63 N/mm2
σ [N/mm2]
ϵ [./.]

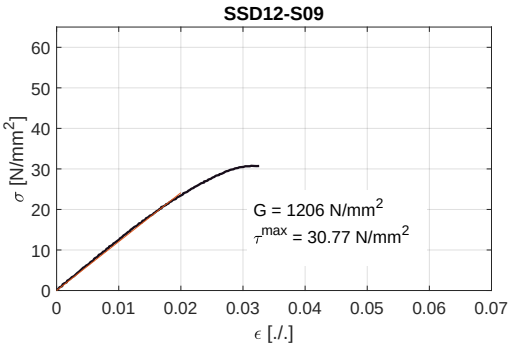
SSD12-S09
G = 1206 N/mm2
τmax = 30.77 N/mm2
σ [N/mm2]
ϵ [./.]

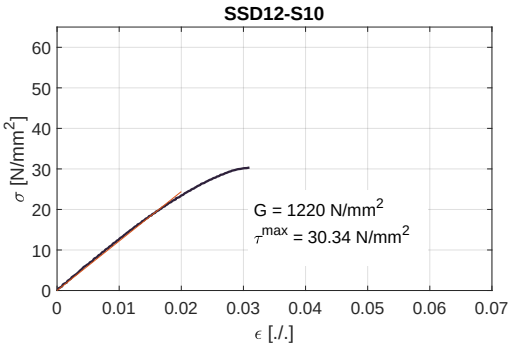
SSD12-S10
G = 1220 N/mm2
τmax = 30.34 N/mm2
σ [N/mm2]
ϵ [./.]

C.3 Validation tests

This section reports all the results of the validation tests. Tables and graphs are grouped depending on the test they refer to.

C.3.1 Three-point bending tests

This sub-section contains the results of the three-point bending tests used to validate the orthotropic behavior of 3D-printed PLA and the capabilities of CLT to predict its mechanical response. For each specimen configuration a summary table has been reported, with the parameters of each specimen, and the individual load vs. displacement curves.

[0°] three-point bending specimens

SPECIMEN	Cross-section W [mm]	T [mm]	Mechanical analysis G_{12} [MPa]	τ_{12}^{max} [MPa]
3PBD1-S01	24.92	2.96	1232	30.63
3PBD1-S02	24.93	2.94	1228	30.63
3PBD1-S03	24.84	2.96	1240	30.30
3PBD1-S04	24.89	2.94	1233	30.40
3PBD1-S05	24.90	2.96	1213	30.65
3PBD1-S06	24.89	2.96	1237	30.61
3PBD1 Sample				
mean	24.88	2.95	**1227**	**30.61**
st.dev	0.038	0.008	10.81	0.236

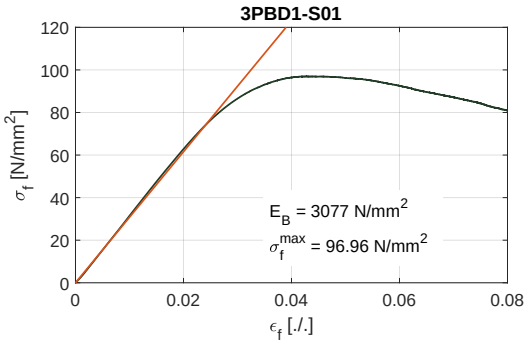

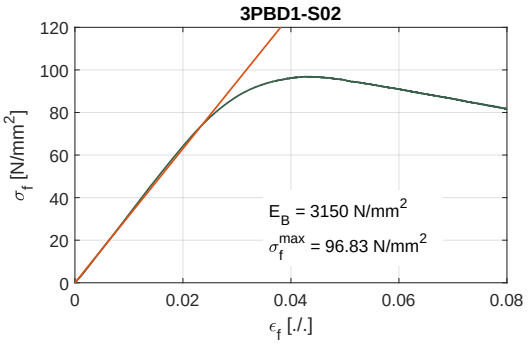

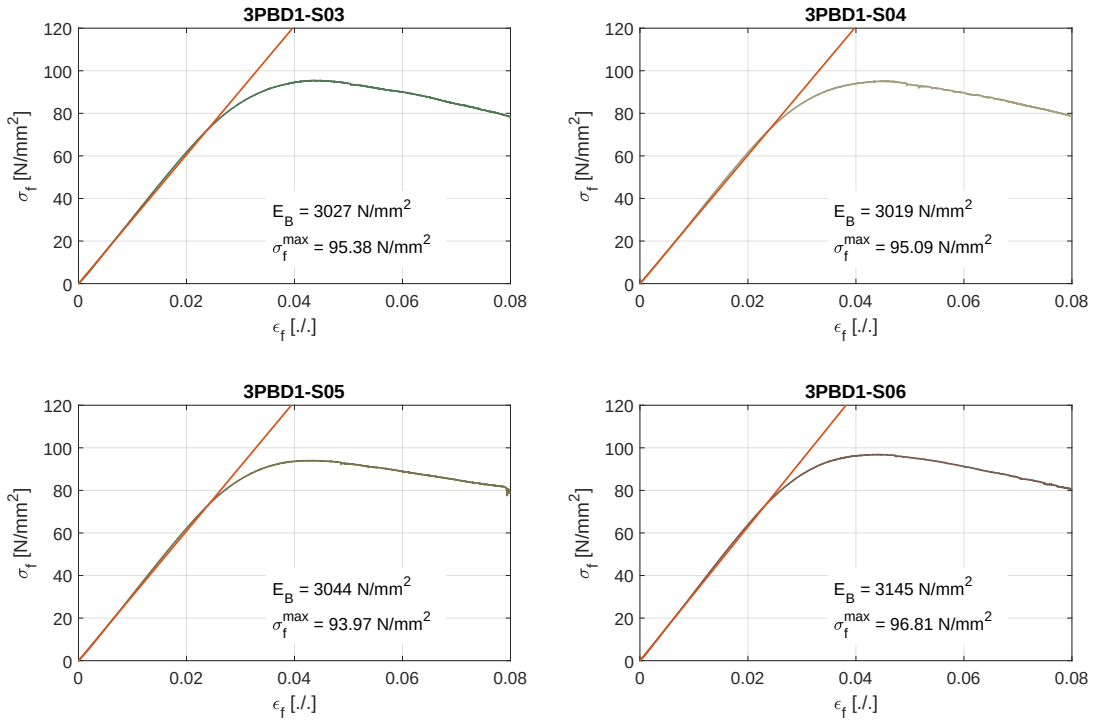

$[90°]$ three-point bending specimens

SPECIMEN	Cross-section W [mm]	T [mm]	Mechanical analysis G_{12} [MPa]	τ_{12}^{max} [MPa]
3PBD2-S01	24.92	2.96	1232	30.63
3PBD2-S02	24.93	2.94	1228	30.63
3PBD2-S03	24.84	2.96	1240	30.30
3PBD2-S04	24.89	2.94	1233	30.40
3PBD2-S05	24.90	2.96	1213	30.65
3PBD2-S06	24.89	2.96	1237	30.61
3PBD2 Sample				
mean	24.88	2.95	**1227**	**30.61**
st.dev	0.038	0.008	10.81	0.236

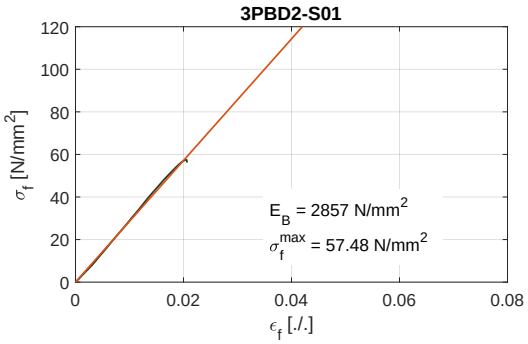

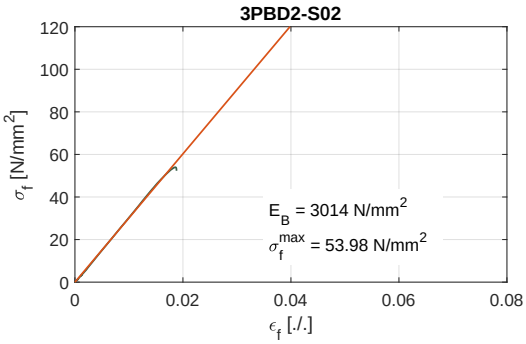

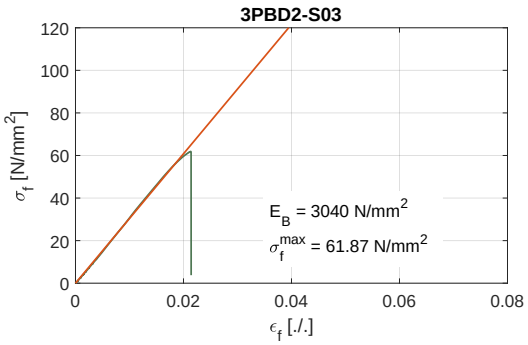

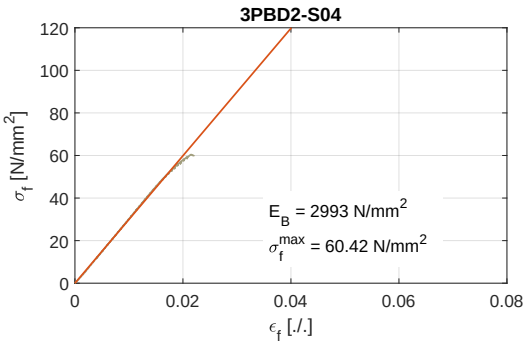

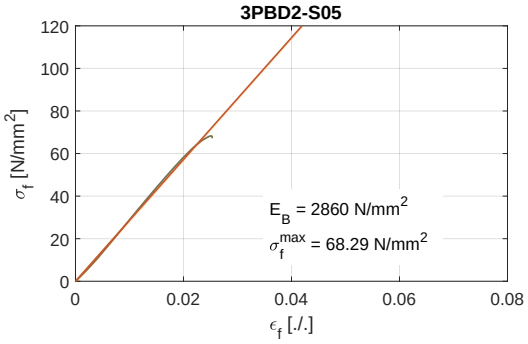

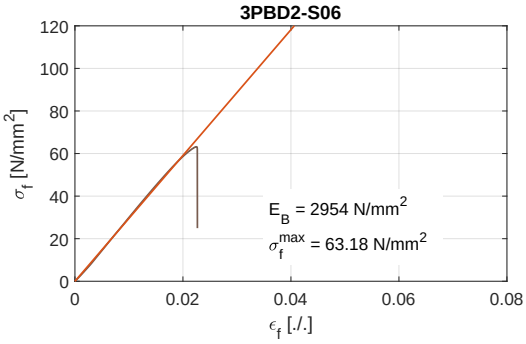

$[+45°/-45°]$ three-point bending specimens

SPECIMEN	Cross-section W [mm]	T [mm]	Mechanical analysis G_{12} [MPa]	τ_{12}^{max} [MPa]
3PBD12-S01	24.92	2.96	1232	30.63
3PBD12-S02	24.93	2.94	1228	30.63
3PBD12-S03	24.84	2.96	1240	30.30
3PBD12-S04	24.89	2.94	1233	30.40
3PBD12-S05	24.90	2.96	1213	30.65
3PBD12-S06	24.89	2.96	1237	30.61
3PBD12 Sample				
mean	24.88	2.95	**1227**	**30.61**
st.dev	0.038	0.008	10.81	0.236

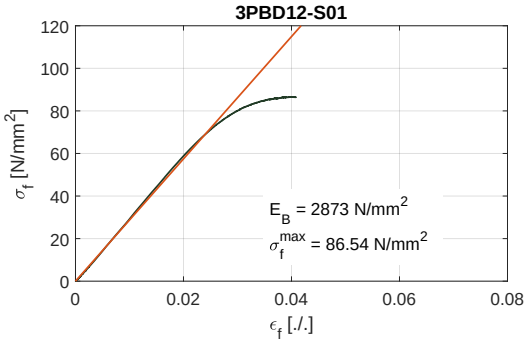

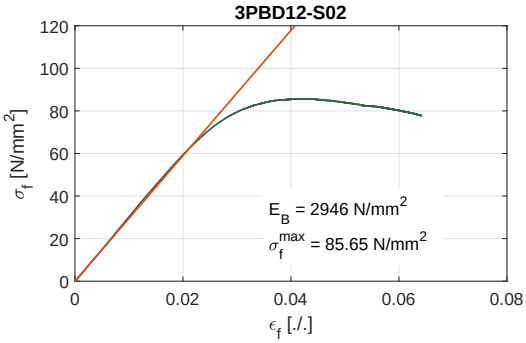

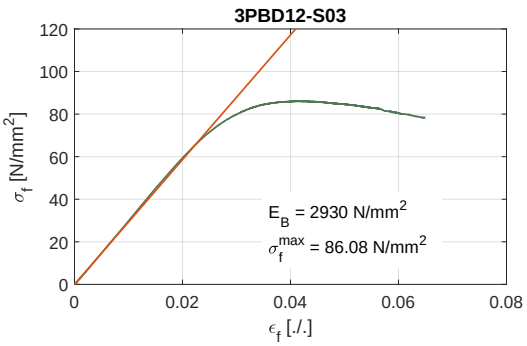
3PBD12-S03
E_B = 2930 N/mm^2
σ_f^{max} = 86.08 N/mm^2
σ_f [N/mm^2]
ϵ_f [./.]

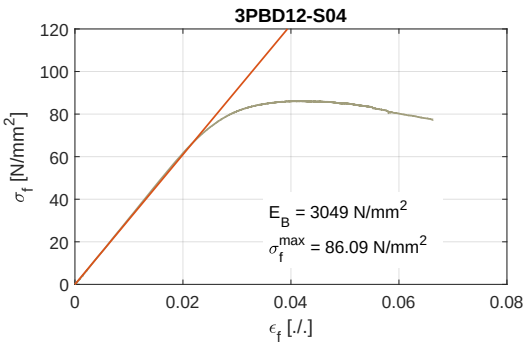
3PBD12-S04
E_B = 3049 N/mm^2
σ_f^{max} = 86.09 N/mm^2
σ_f [N/mm^2]
ϵ_f [./.]

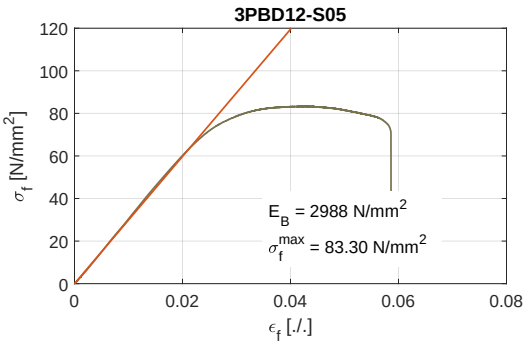
3PBD12-S05
E_B = 2988 N/mm^2
σ_f^{max} = 83.30 N/mm^2
σ_f [N/mm^2]
ϵ_f [./.]

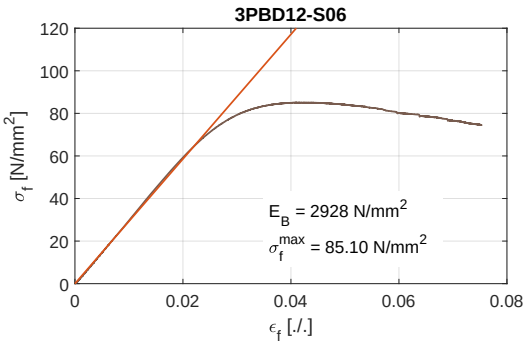
3PBD12-S06
E_B = 2928 N/mm^2
σ_f^{max} = 85.10 N/mm^2
σ_f [N/mm^2]
ϵ_f [./.]

Appendix D

2D drawings of the designed supports

This appendix reports the 2D drawing of the supports designed in this research activity framework for different experimental tests. All the components have been designed through academic-licensed CAD software SolidWorks.

All the drawings obey the ISO format and follow the first angle projection method. All dimensions are in mm.

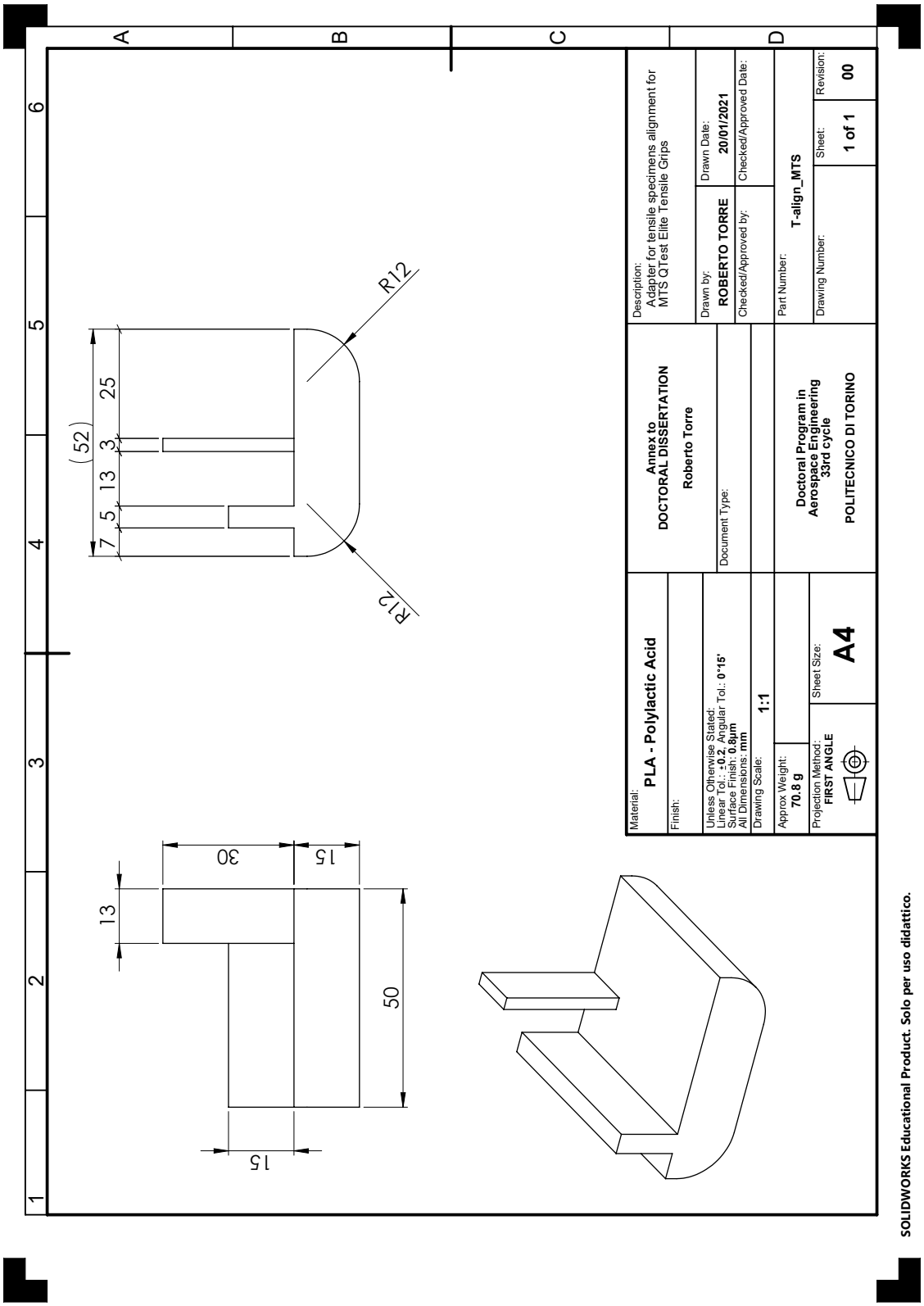
A
B
C
D
1
2
3
4
5
6
R12
R12
(52)
7
5
13
3
25
30
15
13
50
15
Material:
PLA - Polylactic Acid
Finish:
Unless Otherwise Stated:
Linear Tol.: ±0.2, Angular Tol.: 0°15'
Surface Finish: 0.8µm
All Dimensions: mm
Drawing Scale: 1:1
Approx Weight:
70.8 g
Projection Method:
FIRST ANGLE
Sheet Size:
A4
Annex to
DOCTORAL DISSERTATION
Roberto Torre
Document Type:
Doctoral Program in
Aerospace Engineering
33rd cycle
POLITECNICO DI TORINO
Description:
Adapter for tensile specimens alignment for
MTS QTest Elite Tensile Grips
Drawn by:
ROBERTO TORRE
Checked/Approved by:
Drawn Date:
20/01/2021
Checked/Approved Date:
Part Number:
T-align_MTS
Drawing Number:
Sheet:
1 of 1
Revision:
00
SOLIDWORKS Educational Product. Solo per uso didattico.

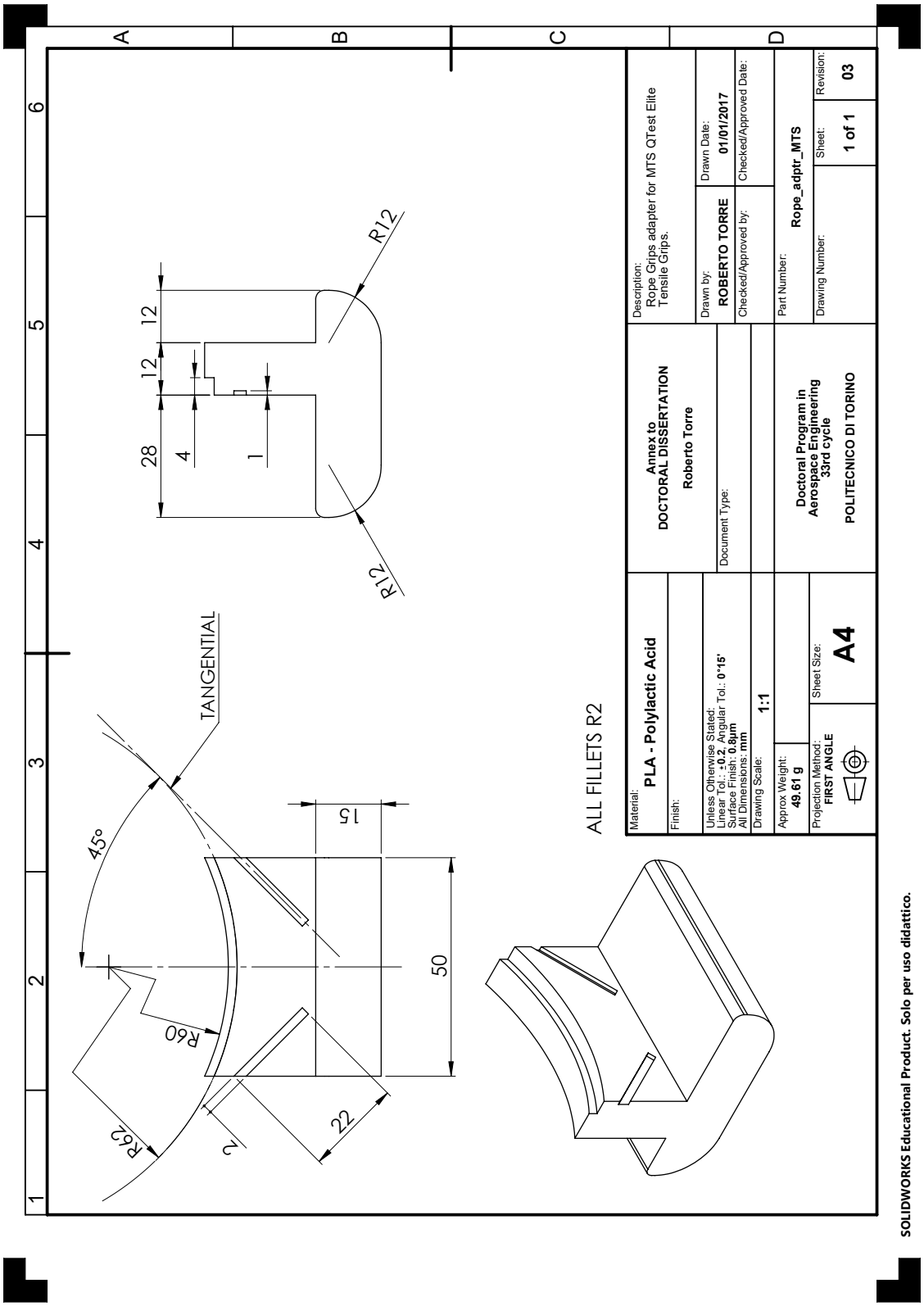
A
B
C
D
1
2
3
4
5
6
R12
R12
12
12
28
4
1
TANGENTIAL
45°
R60
R62
2
22
15
50
ALL FILLETS R2
Material:
PLA - Polylactic Acid
Finish:
Unless Otherwise Stated:
Linear Tol.: ±0.2, Angular Tol.: 0°15'
Surface Finish: 0.8µm
All Dimensions: mm
Drawing Scale: 1:1
Approx Weight: 49.61 g
Projection Method: FIRST ANGLE
Sheet Size: A4
Annex to
DOCTORAL DISSERTATION
Roberto Torre
Document Type:
Doctoral Program in
Aerospace Engineering
33rd cycle
POLITECNICO DI TORINO
Description:
Rope Grips adapter for MTS QTest Elite
Tensile Grips.
Drawn by: ROBERTO TORRE
Drawn Date: 01/01/2017
Checked/Approved by:
Checked/Approved Date:
Part Number: Rope_adptr_MTS
Drawing Number:
Sheet: 1 of 1
Revision: 03
SOLIDWORKS Educational Product. Solo per uso didattico.

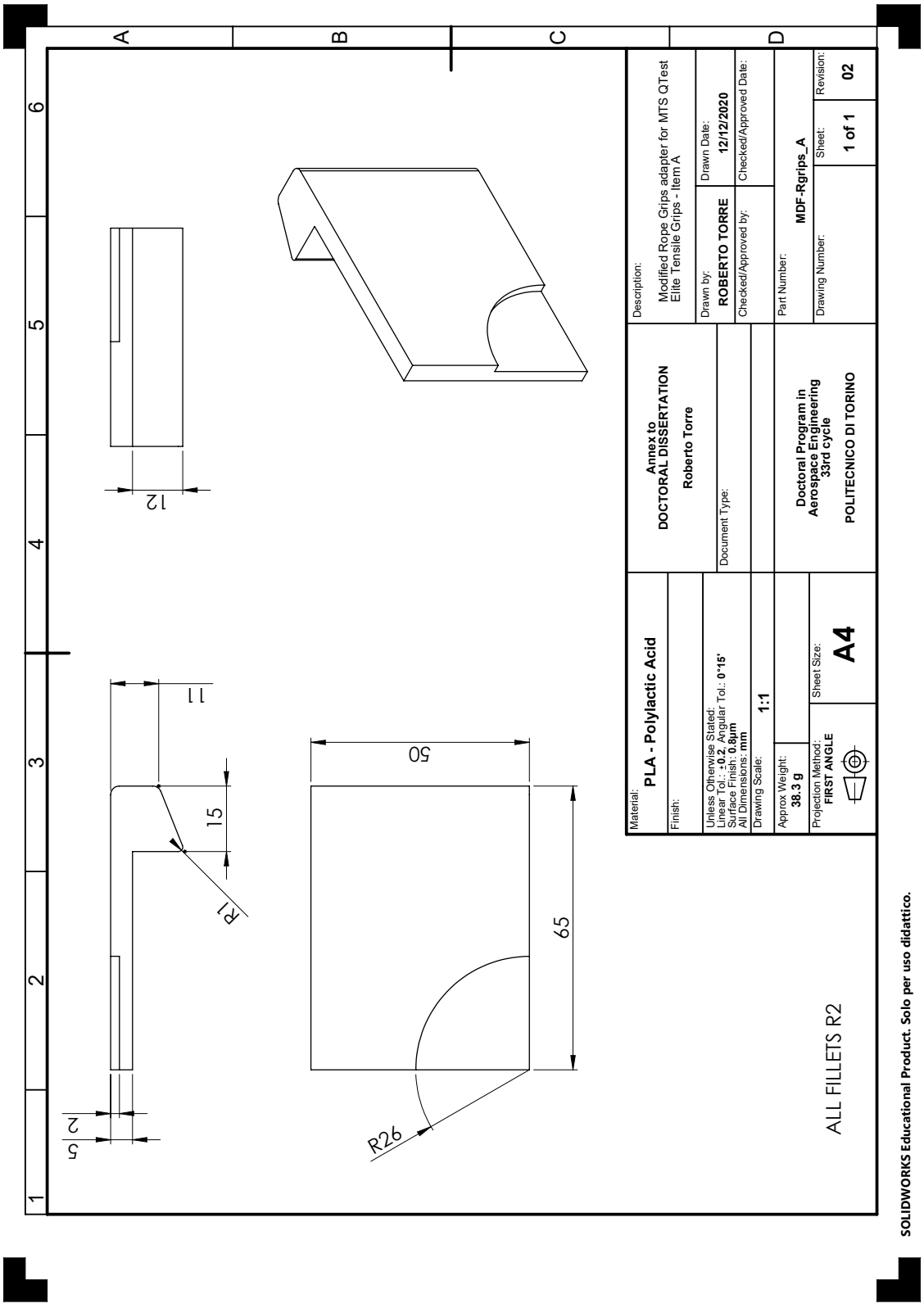
A
B
C
D
1
2
3
4
5
6
12
11
15
R1
5
2
50
65
R26
ALL FILLETS R2
Material:
PLA - Polylactic Acid
Finish:
Unless Otherwise Stated:
Linear Tol.: ±0.2, Angular Tol.: 0°15'
Surface Finish: 0.8µm
All Dimensions: mm
Drawing Scale: 1:1
Approx Weight: 38.3 g
Projection Method: FIRST ANGLE
Sheet Size: A4
Annex to
DOCTORAL DISSERTATION
Roberto Torre
Document Type:
Doctoral Program in
Aerospace Engineering
33rd cycle
POLITECNICO DI TORINO
Description:
Modified Rope Grips adapter for MTS QTest
Elite Tensile Grips - Item A
Drawn by: ROBERTO TORRE
Drawn Date: 12/12/2020
Checked/Approved by:
Checked/Approved Date:
Part Number: MDF-Rgrips_A
Drawing Number:
Sheet: 1 of 1
Revision: 02
SOLIDWORKS Educational Product. Solo per uso didattico.

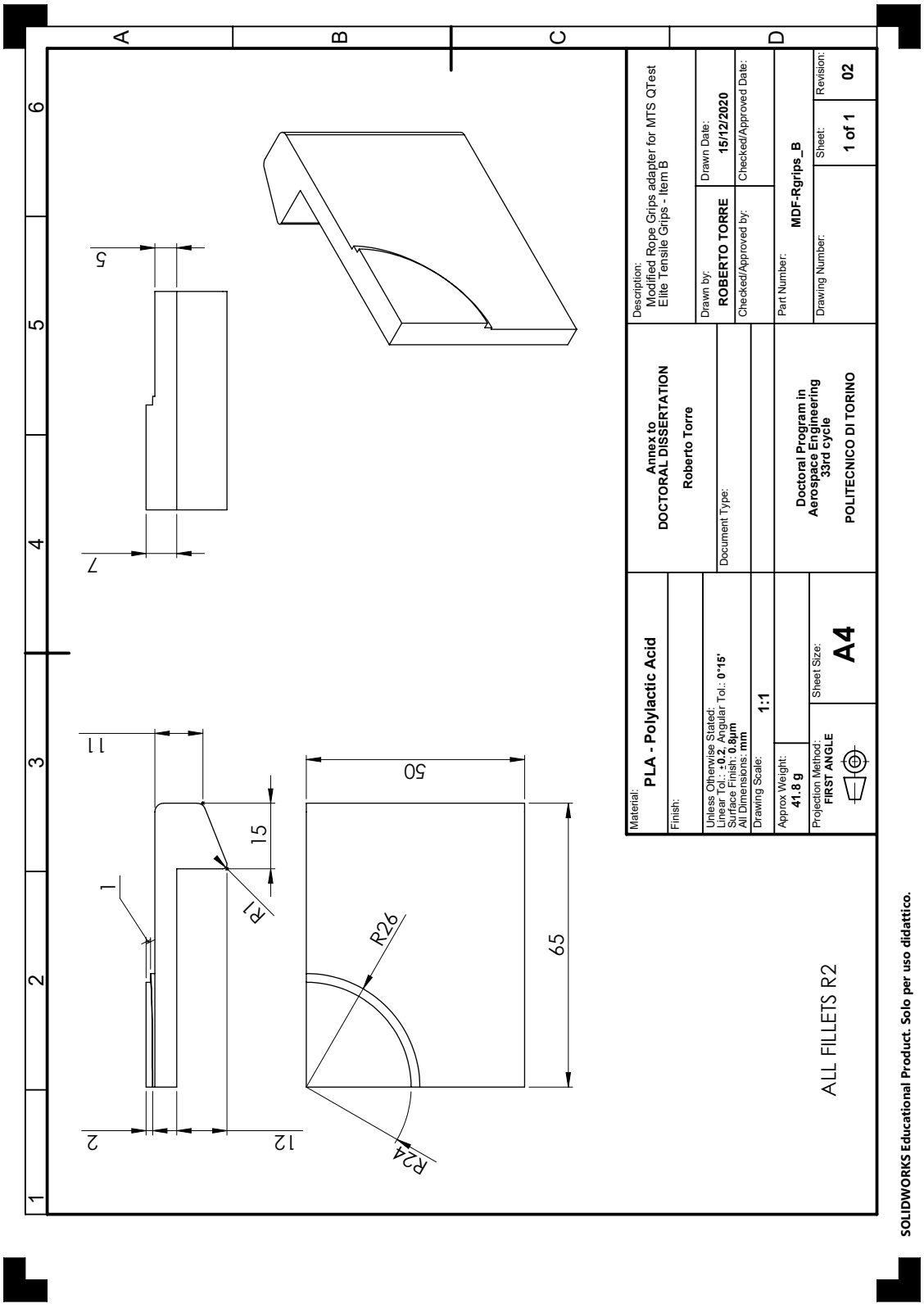
A
B
C
D
1
2
3
4
5
6
5
7
11
15
1
R1
2
12
50
R26
65
R24
ALL FILLETS R2
Material:
PLA - Polylactic Acid
Finish:
Unless Otherwise Stated:
Linear Tol.: ±0.2, Angular Tol.: 0°15'
Surface Finish: 0.8µm
All Dimensions: mm
Drawing Scale: 1:1
Approx Weight: 41.8 g
Projection Method: FIRST ANGLE
Sheet Size: A4
Annex to
DOCTORAL DISSERTATION
Roberto Torre
Document Type:
Doctoral Program in
Aerospace Engineering
33rd cycle
POLITECNICO DI TORINO
Description:
Modified Rope Grips adapter for MTS QTest
Elite Tensile Grips - Item B
Drawn by: ROBERTO TORRE
Drawn Date: 15/12/2020
Checked/Approved by:
Checked/Approved Date:
Part Number: MDF-Rgrips_B
Drawing Number:
Sheet: 1 of 1
Revision: 02
SOLIDWORKS Educational Product. Solo per uso didattico.

Bibliography

[1] Wong K.V. and Hernandez A. "A Review of Additive Manufacturing." In: *ISRN Mechanical Engineering* (2012). DOI: 10.5402/2012/208760.

[2] ASTM - American Society for Testing and Materials. *D3039 - Standard Terminology for Additive Manufacturing*. 2015.

[3] A. Gebhardt. *Understanding Additive Manufacturing*. Hanser.

[4] J.P. Kruth, M.C. Leu, and T. Nakagawa. "Progress in additive manufacturing and rapid prototyping." In: *CIRP Annals* 47.2 (1998), pp. 525–540. DOI: 10.1016/S0007-8506(07)63240-5.

[5] Y. Li et al. "Bending and stretching of certain types of heterogeneous aeolotropic elastic plates." In: *International Journal of Production Research* 55.5 (2017), pp. 1498–1515. DOI: 10.1080/00207543.2016.1231433.

[6] C.K. Chua, K.F. Leong, and C.S. Lim. *Rapid Prototyping: Principles and Applications*. Singapore: World Scientific, 2003. ISBN: 9789812381170.

[7] Inc. Stratasys. *Patent:US005121329 - Apparatus and method for creating three-dimensional objects*. United States Patent and Trademark Office, 1989. URL: https://pdfpiw.uspto.gov/.piw?Docid=05121329.

[8] think3D. *Overview of various FDM 3D Printer nozzles*. Accessed in October 2020. URL: https://www.think3d.in/comparison-of-various-3d-printer-nozzles/.

[9] V. Mazzanti, L. Malagutti, and F. Mollica. "FDM 3D Printing of Polymers Containing Natural Fillers: A Review of their Mechanical Properties". In: *Polymers* 11.7 (2019), pp. 1–22. DOI: 10.3390/polym11071094.

[10] J. Triyono et al. "The effect of nozzle hole diameter of 3D printing on porosity and tensile strength parts using polylactic acid material". In: *Open Engineering* 10.1 (2020), pp. 762–768. DOI: 10.1515/eng-2020-0083.

[11] O.A. Mohamed, S.H. Masood, and J.L Bhowmik. "Optimization of fused deposition modeling process parameters: a review of current research and future prospects". In: *Journal of Materials Processing Technology* 3 (2015), pp. 42–53. DOI: 10.1007/s40436-014-0097-7.

[12] 3dprinterly. *Which Layer Height is Best for 3D Printing?* Accessed in October 2020. URL: https://3dprinterly.com/which-layer-height-is-best-for-3d-printing/.

[13] All3DP. *Direct Drive vs Bowden Extruder Setup: The Differences*. Accessed in October 2020. URL: https://all3dp.com/2/direct-vs-bowden-extruder-technology-shootout/.

[14] NEMA - National Electrical Manufacturers Association. *ICS 16 Standard Publication: Motion/Position control motors, Controls and Feedback Devices*. 2001.

[15] J-B. Wang, J-S. Yin, and L. Yu. "The Design of Automatic Silk Material Replacement Device on 3D Printers Based on FDM Technology". In: *Proceedings of the 2017 3rd International Forum on Energy, Environment Science and Materials* (Nov. 25–26, 2017). Shenzhen, China, 2017.

[16] L. Fang et al. "Effects of Environmental Temperature and Humidity on the Geometry and Strength of Polycarbonate Specimens Prepared by Fused Filament Fabrication". In: *Open Engineering* 13 (2020), pp. 1–16. DOI: 10.3390/ma13194414.

[17] 3dgence. *Key differences: industrial VS desktop 3D printers*. Accessed in October 2020. URL: https://3dgence.com/3dnews/industrial-3d-printers/.

[18] All3DP. *3D Printer Bed Adhesion: All You Need To Know*. Accessed in October 2020. URL: https://all3dp.com/2/3d-printer-bed-adhesion-all-you-need-to-know/.

[19] C.K. Chua, G.K.J. Gan, and M. Tong. "Interface between CAD and Rapid Prototyping systems. Part 1: A study of existing interfaces". In: *The International Journal of Advanced Manufacturing Technology* 13 (1997), pp. 566–570. DOI: 10.1007/BF01176300.

[20] T.L. Leirmo, O. Semeniuta, and K. Martinsen. "Tolerancing from STL data: A Legacy Challenge". In: *Procedia CIRP* 92 (2020), pp. 218–223. DOI: 10.1016/j.procir.2020.05.180.

[21] Simplify3D. *Professional 3D Printing Software*. Accessed in October 2019. URL: https://www.simplify3d.com/.

[22] RepRap.org. *G-Code*. Accessed in September 2019. URL: https://reprap.org/wiki/G-code.

[23] B. Caulfield, P.E. McHugh, and S. Lohfeld. "Dependence of mechanical properties of polyamide components on build parameters in the SLS process". In: *Journal of Materials Processing Technology* 182 (2007), pp. 477–488. DOI: 10.1016/j.jmatprotec.2006.09.007.

[24] J.M.G. Cowie and V. Arrighi. *Polymers. Chemistry and Physics of Modern Materials*. Taylor & Francis, 2007. ISBN: 9780429125546.

[25] C. Duty et al. "What makes a material printable? A viscoelastic model for extrusion-based 3D printing of polymers". In: *Journal of Manufacturing Processes* 35 (2018), pp. 526–537. DOI: 10.1016/j.jmapro.2018.08.008.

[26] A.P. Valerga et al. "Influence of PLA Filament Conditions on Characteristics of FDM Parts". In: *Materials* 11 (2018). DOI: 10.3390/ma11081322.

[27] W. Liu et al. "Fabrication of PLA Filaments and its Printable Performance". In: *5th Annual International Conference on Material Science and Engineering (ICMSE2017)*. Xiamen, China, 2017.

[28] M. Moradi et al. "The synergic effects of FDM 3D printing parameters on mechanical behaviors of bronze Poly Lactic Acid composites". In: *Journal of Composites Science* 4.1 (2020). DOI: 10.3390/jcs4010017.

[29] Shenzhen Eryone Technology. *Eryone Galaxy PLA - Data Sheet*. https://cdn-3d.niceshops.com/upload/file/Glitter_PLA_Filament[2].pdf. 2019.

[30] H.R. Dana et al. "Polymer additive manufacturing of ABS structure: Influence of printing direction on mechanical properties". In: *Journal of Manufacturing Processes* 44 (2019). DOI: 10.1016/j.jmapro.2019.06.015.

[31] V. Harshitha and S. S. Rao. "Design and analysis of ISO standard bolt and nut in FDM 3D printer using PLA and ABS materials". In: *Materials Today: Proceedings* 19.part 2 (). DOI: 10.1016/j.matpr.2019.07.737.

[32] M. Lay et al. "Comparison of physical and mechanical properties of PLA, ABS and Nylon 6 fabricated using fused deposition modeling and injection molding". In: *Composites Part B* 176 (). DOI: 10.1016/j.compositesb.2019.107341.

[33] G.M. Swallowe. *Mechanical Properties and Testing of Polymers. Polymer Science and Technology Series*. Springer, 1999. DOI: 10.1007/978-94-015-9231-4_52.

[34] J.F. Rodríguez, J.P. Thomas, and J.E. Renaud. "Mechanical behavior of acrylonitrile butadiene styrene (ABS) fused deposition materials. Experimental investigation." In: *Rapid Prototyping Journal* 7.3 (2001). DOI: 10.1108/13552540110395547.

[35] ASTM - American Society for Testing and Materials. *D3039 - Standard Test Method for Tensile Properties of Polymer Matrix Composite Materials*. 2010.

[36] S.H. Ahn et al. "Anisotropic material properties of fused deposition modeling ABS". In: *Rapid Prototyping Journal* 8.4 (2002). DOI: 10.1108/13552540210441166.

[37] R.J. Zaldivar et al. "Influence of processing and orientation print effects on the mechanical and thermal behavior of 3D-Printed ULTEM®9085 Material." In: *Additive Manufacturing* 13 (2017). DOI: 10.1016/j.addma.2016.11.007.

[38] I. Durgun and R. Ertan. "Experimental investigation of FDM process for improvement of mechanical properties and production cost". In: *Rapid Prototyping Journal* 20.3 (2014). DOI: 10.1108/rpj-10-2012-0091.

[39] A. W. Gebisa and H. G. Lemu. "Influence of 3D Printing FDM Process Parameters on Tensile Property of ULTEM 9085". In: *14th Global Congress of Manufacturing and Management (GCMM-2018). Procedia Manufacturing 30*. Elsevier, 2019, pp. 331–338. DOI: 10.1016/j.promfg.2019.02.047.

[40] B. Wittbrodt and J.M. Pearce. "The effects of PLA color on material properties of 3-D printed components." In: *Additive Manufacturing* 8 (2015), pp. 110–116. DOI: 10.1016/j.addma.2015.09.006.

[41] B.M. Tymrak, M. Kreiger, and J.M. Pearce. "Mechanical properties of components fabricated with open-source 3-D printers under realistic environmental conditions." In: *Materials& Design* 58 (2014), pp. 242–246. DOI: 10.1016/j.matdes.2014.02.038.

[42] E. Carlier et al. "Investigation of the parameters used in fused deposition modeling of poly (lactic acid) to optimize 3D printing sessions". In: *International Journal of Pharmaceutics* 565 (2019). DOI: 10.1016/j.ijpharm.2019.05.008.

[43] M.S. Uddin et al. "Evaluating Mechanical Properties and Failure Mechanisms of Fused Deposition Modeling Acrylonitrile Butadiene Styrene Parts." In: *Journal of Manufacturing Science and Engineering* 139.8 (2017), pp. 242–246. DOI: 10.1115/1.4036713.

[44] C.A. Griffiths et al. "Effect of build parameters on processing efficiency and material performance in fused deposition modelling." In: *The Second CIRP Conference on Biomanufacturing* 49 (2016), pp. 28–32. DOI: 10.1016/j.procir.2015.07.024.

[45] N.A. Bin Sukindar et al. "Analysis on the impact process parameters on tensile strength using 3d printer repetier-host software". In: *Journal of Engineering and Applied Sciences* (2017).

[46] E. Cuan-Urquizo et al. "Characterization of the Mechanical Properties of FFF Structures and Materials: A Review on the Experimental, Computational and Theoretical Approaches." In: *Materials* 12 (2019). DOI: 10.3390/ma12060895.

[47] A. Rodríguez-Panes, J. Claver, and A.M. Camach. "The Influence of Manufacturing Parameters on the Mechanical Behaviour of PLA and ABS Pieces Manufactured by FDM: A Comparative Analysis." In: *Materials* 11 (2018). DOI: 10.3390/ma11081333.

[48] A.K. Sood, R.K. Ohdar, and S.S. Mahapatra. "Experimental investigation and empirical modelling of FDM process for compressive strength improvement". In: *Journal of Advanced Research* 8 (2012). DOI: 10.1016/j.jare.2011.05.001.

[49] G.C. Onwubolu and F. Rayegani. "Characterization and Optimization of Mechanical Properties of ABS Parts Manufactured by the Fused Deposition Modelling Process". In: *International Journal of Manufacturing Engineering* (2014). DOI: 10.1155/2014/598531.

[50] M.S. Hossain et al. "Improving tensile mechanical properties of FDM-manufactured specimens via modifying build parameters". In: *Annual international solid freeform fabrication symposium*. ISSN: 1053-2153. 2013.

[51] M.S. Hossain et al. "Improved Mechanical Properties of Fused Deposition Modeling-Manufactured Parts Through Build Parameter Modifications." In: *Polymer Testing* 136.6 (2014). DOI: 10.1115/1.4028538.

[52] J. Plott, X. Tian, and A.J. Shih. "Voids and tensile properties in extrusion-based additive manufacturing of moisture-cured silicone elastomer". In: *Additive Manufacturing* 22 (2018), pp. 606–617. DOI: 10.1016/j.addma.2018.06.010.

[53] J. R. C. Dizon et al. "Mechanical characterization of 3D-printed polymers". In: *Additive Manufacturing* 20 (2018). DOI: 10.1016/j.addma.2017.12.002.

[54] J.J. Laureto and J.M. Pearce. "Anisotropic mechanical property variance between ASTM D638-14 type i and type iv fused filament fabricated specimens." In: *Polymer Testing* 68 (2018), pp. 294–301. DOI: 10.1016/j.polymertesting.2018.04.029.

[55] A.R. Torrado and D.A. Roberson. "Failure Analysis and Anisotropy Evaluation of 3D-Printed Tensile Test Specimens of Different Geometries and Print Raster Patterns." In: *Journal of Failure Analysis and Prevention* 16.1 (2016), pp. 154–166. DOI: 10.1007/s11668-016-0067-4.

[56] F. Ning et al. "Additive manufacturing of carbon fiber reinforced thermoplastic composites using fused deposition modeling." In: *Composites Part B: Engineering* 80 (2015). DOI: 10.1016/j.compositesb.2015.06.013.

[57] J. Justo et al. "Characterization of 3D printed long fibre reinforced composites." In: *Composites Structures* 185 (2018). DOI: 10.1016/j.compstruct.2017.11.052.

[58] X. Tian et al. "Interface and performance of 3D printed continuous carbon fiber reinforced PLA composites." In: *Composites Part A: Applied Science and Manufacturing* 88 (2016). DOI: 10.1016/j.compositesa.2016.05.032.

[59] X. Tian et al. "Rapid prototyping of continuous carbon fiber reinforced polylactic acid composites by 3D printing." In: *Journal of Materials Processing Technology* 238 (2016). DOI: 10.1016/j.jmatprotec.2016.07.025.

[60] B. Brenken et al. "Fused filament fabrication of fiber-reinforced polymers: A review." In: *Additive Manufacturing* 21 (2018). DOI: 10.1016/j.addma.2018.01.002.

[61] J.M. Chacón et al. "Additive manufacturing of continuous fibre reinforced thermoplastic composites using fused deposition modelling: Effect of process parameters on mechanical properties." In: *Composites Science and Technology* 181 (2019). DOI: 10.1016/j.compscitech.2019.107688.

[62] A. El Moumen, M. Tarfaoui, and K. Lafdi. "Additive manufacturing of polymer composites: Processing and modeling approaches". In: *Composites Part B* 171 (2019). DOI: 10.1016/j.compositesb.2019.04.029.

[63] X. Wang et al. "3D printing of polymer matrix composites: A review and prospective". In: *Composites Part B* 110 (2017). DOI: 10.1016/j.compositesb.2016.11.034.

[64] S.A. Raj, E. Muthukumaran, and K. Jayakrishna. "A Case Study of 3D Printed PLA and its Mechanical Properties". In: *International Conference on Materials Manufacturing and Modelling (ICMMM - 2017). Materials Today: Proceedings 5(5)*. Elsevier, 2018, pp. 11219–11226. DOI: 10.1016/j.matpr.2018.01.146.

[65] M.A. Salim, Z.H. Termiti, and A. M. Saad. "Mechanical Properties on ABS/PLA Materials for Geospatial Imaging Printed Product using 3D Printer Technology". In: *Reference Module in Materials Science and Materials Engineering* (2019). DOI: 10.1016/B978-0-12-803581-8.11357-8.

[66] M.D. Monzón et al. "Standardization in additive manufacturing: activities carried out by international organizations and projects. The International Journal of Advanced Manufacturing Technology". In: *The International Journal of Advanced Manufacturing Technology* 76 (2014). DOI: 10.1007/s00170-014-6334-1.

[67] D. Kazmer. "Three-Dimensional Printing of Plastics. Applied Plastics Engineering Handbook". In: *The International Journal of Advanced Manufacturing Technology* (2017). DOI: 10.1016/b978-0-323-39040-8.00029-8.

[68] T. Letcher, B. Rankouhi, and S. Javadpour. "Experimental study of mechanical properties of additively manufactured ABS plastic as a function of layer parameters". In: *Proceedings of the ASME 2015 International Mechanical Engineering Congress and Exposition* (Nov. 13–19, 2015). Houston, Texas, USA, 2015.

[69] D. Croccolo, M. De Agostinis, and G. Olmi. "Experimental characterization and analytical modelling of the mechanical behaviour of fused deposition processed parts made of ABS-M30." In: *Computational Materials Science* 79 (2013), pp. 506–518. DOI: doi:10.1016/j.commatsci.2013.06.041.

[70] E. Cuan-Urquizo, S. Yang, and A. Bhaskar. "Mechanical characterization of additively manufactured material having lattice microstrutture." In: *Materials Science and Engineering* 74 (2015), pp. 1–8. DOI: 10.1088/1757-899X/74/1/012004.

[71] ASTM - American Society for Testing and Materials. *D638 - Standard Test Method for Tensile Properties of Plastics*. 2014.

[72] A.M. Forster. *Materials Testing Standards for Additive Manufacturing of Polymer Materials: State of the Art and Standards Applicability*. NIST, 2015. DOI: 10.6028/NIST.IR.8059.

[73] R.J. Young. "Strength and toughness". In: *Comprehensive Polymer Science and Supplements*. Ed. by G. Allen and J.C. Bevington. London: Elsevier, 1989. Chap. 15, pp. 511–532. DOI: 10.1016/B978-0-08-096701-1.00052-5.

[74] U. W. Gedde and M.S. Hedenqvist. *Fundamental Polymer Science*. Springer, 2019.

[75] M. Dawoud, I. Taha, and S.J. Ebeid. "Mechanical behaviour of ABS: an experimental study using FDM and injection moulding techniques." In: *Journal of Manufacturing Processes* 21 (2016), pp. 39–45. DOI: 10.1016/j.jmapro.2015.11.002.

[76] J. Martínez et al. "Comparative between FEM models for FDM parts and their approach to a real mechanical behaviour." In: *Procedia Engineering* 63 (2013), pp. 878–884. DOI: 10.1016/j.proeng.2013.08.230.

[77] M. Montero et al. "Material characterization of fused deposition modeling (FDM) ABS by designed experiments". In: *Proceedings of Rapid Prototyping and Manufacturing Conference* (May 14–17, 2001). Cincinnati, Ohio, 2001, pp. 1–21.

[78] J.H. Yang, Z. Zhao, and S.H. Park. "Evaluation of directional mechanical properties of 3D printed polymer parts". In: *Proceedings of 15th International Conference on Control, Automation and Systems (ICCAS)* (Oct. 13–16, 2015). Busan, South Korea, 2015, pp. 1952–1954. DOI: 10.1016/j.proeng.2013.08.230.

[79] P.K. Gurrala and S.P. Regalla. "Part strength evolution with bonding between filaments in fused deposition modelling." In: *Virtual and Physical Prototyping* 9.3 (2014), pp. 141–149. DOI: 10.1080/17452759.2014.913400.

[80] J. Frenkel. "Viscous flow of crystalline bodies under the action of surface tension." In: *Journal of Physics* 9 (1945), pp. 385–395.

[81] C. Bellehumeur et al. "Modeling of bond formation between polymer filaments in the fused deposition modeling process." In: *Journal of Manufacturing Processes* 6.2 (2004), pp. 170–178. DOI: 10.1016/S1526-6125(04)70071-7.

[82] F.P. Gerstle. *Composites. Encyclopedia of Polymer Science and Engineering.* Wiley, 1991.

[83] L. Li et al. "Composite modeling and analysis for fabrication of FDM prototypes with locally controlled properties." In: *Journal of Manufacturing Processes* 4.2 (2002), pp. 252–264. DOI: 10.1016/s1526-6125(02)70139-4.

[84] K.K. Chawla. "Macromechanics of Composites". In: *Composite Materials.* New York: Springer-Verlag, 1998. DOI: 10.1007/978-1-4757-2966-5.

[85] D.W.A. Rees. "Anistropic elasticity". In: *Mechanics of Elastic Solids.* London: World Scientific Publishing, 2018. DOI: 10.1142/9781786346179_0008.

[86] E. Reissner and Y. Stavsky. "Bending and stretching of certain types of heterogeneous aeolotropic elastic plates." In: *Journal of Applied Mechanics* 28.3 (1961), pp. 402–408. DOI: 10.1115/1.3641719.

[87] C.W. Bert. "Classical Lamination Theory". In: *Manual on experimental methods for mechanical testing of composites.* Ed. by R.L. Pendleton. London: Elsevier Applied Science, 1989. Chap. II B, pp. 11–16. DOI: 10.1007/978-94-009-1129-1_3.

[88] C. Casavola et al. "Orthotropic mechanical properties of fused deposition modelling parts described by classical laminate theory." In: *Materials & Design* 90 (2016), pp. 453–458. DOI: 10.1016/j.matdes.2015.11.009.

[89] D.O. Adams and Adams D.F. "Tabbing guide for composite test specimens". In: Washington: Federal Aviation Administration, 2002.

[90] ASTM - American Society for Testing and Materials. *D143 - Standard Test Method for Standard Test Method for Shear Modulus at Room Temperature.* 2013.

[91] ASTM - American Society for Testing and Materials. *D3518 - SStandard Test Method for In-Plane Shear Response of Polymer Matrix Composite Materials by Tensile Test of a +- 45° Laminate*. 2001.

[92] ASTM - American Society for Testing and Materials. *D790 - Standard Test Methods for Flexural Properties of Unreinforced and Reinforced Plastics and Electrical Insulating Materials*. 2017.

[93] S. Brischetto and R. Torre. "Buckling in FDM 3D printed PLA elements: a DIC-assisted experimental investigation". In: *Proceedings of ICMSN 2020 - 4th International Conference on Materials Sciences and Nanomaterials* (July 8–10, 2020). Cambridge, United Kingdom, 2020.

[94] R. Torre and S. Brischetto. "Buckling developed in 3D printed PLA cuboidal samples under compression: analytical, numerical and experimental investigations". In: *Additive Manufacturing* 38 (2021), pp. 1–14. DOI: 10.1016/j.addma.2020.101790.

[95] S. Szczepanik and P. Bednarczyk. "Bending and compression properties of ABS and PET structural materials printed using FFF technology". In: *Journal of Casting & Materials Engineering* 1.2 (2017), pp. 39–42. DOI: 10.7494/jcme.2017.1.2.39.

[96] T.F. Abbas, F.M. Othman, and H.B. Ali. "Effect of infill parameter on compression properties in FFF process". In: *International Journal of Engineering Research and Application* 7.10 (2017), pp. 16–19. DOI: 10.9790/9622-0710021619.

[97] S. Kotsmid and P. Beno. "Experimental Determination of the Beam Buckling Load". In: (2018).

[98] M. He et al. "Experimental investigations on mechanical properties and column buckling behavior of structural bamboo". In: *The Structural Design of Tall and Special Buildings* 24.7 (2015), pp. 491–503. DOI: 10.1002/tal.1176.

[99] J. Ye, I. Hajirasouliha, and Becque I. "Experimental investigation of local-flexural interactive buckling of cold-formed steel channel columns". In: *Thin-Walled Structures* 125 (2018), pp. 245–258. DOI: 10.1016/j.tws.2018.01.020.

[100] S. Ziolkowski A. andImielowski. "Buckling and post-buckling behaviour of prismatic aluminium columns submitted to a series of compressive loads". In: *Experimental Mechanics* 51 (2011), pp. 1335–1345. DOI: 10.1007/s11340-010-9455-y.

[101] ASTM - American Society for Testing and Materials. *D695 - SStandard Test Method for Compressive Properties of Rigid Plastics*. 2015.

[102] R.M. Jones. "Buckling of Bars, Plates and Shells". In: Virginia, USA: Bull Ridge Publishing, 2006.

[103] S. Brischetto, A. Ciano, and A. Raviola. *A multipurpose modular drone with adjustable arms*. Patent no. ITUB20155341A1. 2017.

[104] ENAC - Italian Civil Aviation Authority. *Remotely Piloted Aerial Vehicles Regulation*. 2018.

[105] S. Brischetto, A. Ciano, and C.G. Ferro. "A multipurpose modular drone with adjustable arms produced via the FDM additive manufacturing process". In: *Curved and Layered Structures* 3.1 (2016), pp. 202–213. DOI: 10.1515/cls-2016-0016.

[106] Roberto Torre. "Mechanical characterization of ABS and preliminary design for a 3D printed UAV produced via FDM". MA thesis. Politecnico di Torino, July 2016.

[107] Solution for All Markus Muller. *xcopterCalc - Multicopter calculator*. Accessed in January 2021. URL: https://www.ecalc.ch/.

[108] V.R.L. Medeiros et al. "A novel approach for brushless DC motors characterization in drones based on chaos". In: *Drones* 2.14 (2018), pp. 1–11. DOI: 10.3390/drones2020014.

[109] S. Brischetto and R. Torre. "Convergence investigation for the exponential matrix and mathematical layers in the static analysis of multilayered composite structures". In: *Journal of Composites Science* 1.2 (2017), pp. 1–15. DOI: 10.3390/jcs1020019.

[110] S. Brischetto and R. Torre. "Effects of order of expansion for the exponential matrix and number of mathematical layers in the exact 3D static analysis of functionally graded plates and shells". In: *Applied Sciences* 8.1 (2018), pp. 1–17. DOI: 10.3390/app8010110.

[111] S. Brischetto and R. Torre. "Thermo-elastic analysis of multilayered plates and shells based on 1D and 3D heat conduction problems". In: *Composite Structures* 206 (2018), pp. 326–353. DOI: 10.1016/j.compstruct.2018.08.042.

[112] S. Brischetto and R. Torre. "3D shell model for the thermo-mechanical analysis of FGM structures via imposed and calculated temperature profiles". In: *Aerospace Science and Technology* 85 (2019), pp. 125–149. DOI: 10.1016/j.ast.2018.12.011.

[113] S. Brischetto and R. Torre. "A 3D shell model for the thermal and hygroscopic stress analysis of composite and sandwich structures". In: *Proceedings of ICCS23 - 23rd International Conference on Composite Structures* (Sept. 1–4, 2020). Porto, Portugal, 2020.

[114] S. Brischetto and R. Torre. "3D hygro-thermo-elastic analysis of functionally graded material plates and shells". In: *Proceedings of ECCOMAS 2020 - 14th World Congress in Computational Mechanics* (Jan. 11–15, 2021). Virtual congress, 2021.

[115] M. Rahman, N.R. Schott, and L.K. Sadhu. "Glass transition of ABS in 3D printing". In: (2016).

[116] A.J.. Botean. "Thermal expansion coefficient determination of polylactic acid using digital image correlation". In: (2018). DOI: 10.1051/e3sconf/20183201007.

[117] G.H. Yew et al. "Water absorption and enzymatic degradation of poly(lactic acid)/rice starch composites". In: *Polymer Degradation and Stability* 90.3 (2005), pp. 488–500. DOI: 10.1016/j.polymdegradstab.2005.04.006.

[118] J. V. Ecker et al. "Mechanical properties and water absorption behaviour of PLA and PLA/wood composites prepared by 3D printing and injection moulding". In: *Rapid Prototyping Journal* 25.4 (2019), pp. 672–678. DOI: doi:10.1108/rpj-06-2018-0149.

[119] S. Brischetto. "Exact elasticity solution for natural frequencies of functionally graded simply-supported structures". In: *Computer Modeling in Engineering and Sciences* 95.3 (2013), pp. 391–430. DOI: 10.3970/cmes.2013.095.391.

[120] S. Brischetto. "An exact 3D solution for free vibrations of multilayered cross-ply composite and sandwich plates and shells". In: *International Journal of Applied Mechanics* 6.6 (2014), pp. 1–42. DOI: 10.1142/S1758825114500768.

[121] S. Brischetto. "Curvature approximation effects in the free vibration analysis of functionally graded shells". In: *International Journal of Applied Mechanics* 8.6 (2017), pp. 1–33. DOI: 10.1142/S1758825116500794.

[122] S. Brischetto. "Exact three-dimensional static analysis of single- and multi-layered plates and shells". In: *Composites Part B: Engineering* 119 (2017), pp. 230–252. DOI: 10.1016/j.compositesb.2017.03.010.

[123] S. Brischetto. "A closed-form 3D shell solution for multilayered structures subjected to different load combinations". In: *Aerospace Science and Technology* 70 (2017), pp. 29–46. DOI: 10.1016/j.ast.2017.07.040.

[124] S. Brischetto. "A general exact elastic shell solution for bending analysis of functionally graded structures". In: *Composite Stuctures* 175 (2017), pp. 70–85. DOI: 10.1016/j.compstruct.2017.04.002.

[125] S. Brischetto. "A 3D layer-wise model for the correct imposition of transverse shear/normal load conditions in FGM shells". In: *International Journal of Mechanical Sciences* 136 (2018), pp. 50–66. DOI: 10.1016/j.ijmecsci.2017.12.013.

[126] A.W. Leissa. "Vibration of Shells". In: *NASA SP-288*. Washington D.C., USA, 1973.

[127] M.N. Ozisik. "Heat Conduction". In: New York, USA: John Wiley & Sons, Inc., 1933.

[128] Y. Povstenko. "Fractional thermoelasticity". In: Switzerland: Springer, 2015.

[129] P.M. Morse. "Methods of theoretical physics". In: USA: McGraw-Hill, 1953.

[130] G.B. Arfken and H.J. Weber. "Mathematical methods for physicists". In: San Diego, USA: Elsevier Academic Press, 2005.

[131] S. Brischetto. "Convergence analysis of the exponential matrix method for the solution of 3D equilibrium equations for free vibration analysis of plates and shells". In: *Composites Part B: Engineering* 98 (2016), pp. 453–471. DOI: 10.1016/j.compositesb.2016.05.047.

[132] K. Bhaskar, T.K. Varadan, and J.S.M. Ali. "Thermoelastic solutions for orthotropic and anisotropic composite laminates". In: *Composites Part B: Engineering* 27.5 (1996), pp. 415–420. DOI: 10.1016/1359-8368(96)00005-40.

[133] S. Brischetto and E. Carrera. "Coupled thermo-mechanical analysis of one-layered and multilayered isotropic and composite shells". In: *Computer modeling in engineering & Sciences* 56.3 (2010), pp. 249–302. DOI: 10.3970/cmes.2010.056.249.

[134] J. Reddy and Z.Q. Cheng. "Three-dimensional thermomechanical deformations of functionally graded rectangular plates". In: *European Journal of Mechanics - A/Solids* 20.5 (2001), pp. 841–855. DOI: 10.1016/s0997-7538(01)01174-3.

[135] T. Mori and K. Tanaka. "Average stress in matrix and average elastic energy of materials with misfitting inclusions". In: *Acta Metallurgica* 21.5 (1973), pp. 571–574. DOI: 10.1016/0001-6160(73)90064-3.

[136] ASTM - American Society for Testing and Materials. *D7269 - Standard Test Methods for Tensile Testing of Aramid Yarns*. 2020.

[137] ASTM - American Society for Testing and Materials. *C1557 - Standard Test Method for Tensile Strength and Young's Modulus of Fibers*. 2020.

[138] The Universal Grip Company. *Bollard Grips for Tensile Testing*. https://www.universalgripco.com/bollard-grips. 2019.

[139] R. Torre and S. Brischetto. "Reinforcing Effect of Strain Gauges on 3D Printed Polymers: An Experimental Investigation". In: *American Journal of Engineering and Applied Sciences* 14.1 (2021), pp. 7–24. DOI: 10.3844/ajeassp.2021.7.24.

[140] M. Arena and M. Viscardi. "Strain state detection in composite structures: review and new challenges". In: *Journal of Composites Sciences* 2.2020 (4), pp. 1–35. DOI: 10.3390/jcs4020060.

[141] A.S. Kobayashi. "Handbook on Experimental Mechanics". In: New York: Springer, 1987.

[142] MS. Zike and L.P Mikkelsen. "Correction of gauge factor for strain gauges used in polymer composite testing". In: *Experimental Mechanics* 54 (2014), pp. 393–403. DOI: 10.1007/s11340-013-9813-7.

[143] G. Pereira, M. McGugan, and L.P. Mikkelsen. "Method for independent strain and temperature measurement in polymeric tensile test specimen using embedded FBG". In: *Polymer Testing* 50 (2016), pp. 125–134. DOI: 10.1016/j.polymertesting.2016.01.005.

[144] H. Montazerian et al. "Integrated sensors in advanced composites: a critical review". In: *Critical Reviews in Solid State and Materials Sciences* 3.2020 (45), pp. 187–238. DOI: 10.1080/10408436.2019.1588705.

[145] M. Jerabek, Z. Major, and R.W. Lang. "Strain determination of polymeric materials using digital image correlation". In: *Polymer Testing* 29.3 (2010), pp. 407–416. DOI: 10.1016/j.polymertesting.2010.01.005.

[146] P.E. Anuta. "Spatial Registration of Multispectral and Multitemporal Digital Imagery Using Fast Fourier Transform Techniques". In: *IEEE Transactions on Geoscience Electronics* 8.4 (1970). DOI: 10.1109/TGE.1970.271435.

[147] T.J. Keating, P.R. Wolf, and F.L. Scarpace. "An improved method of digital image correlation". In: *Presented at the Annual Convention of the American Society of Photogrammetry*. Vol. 41. 8. ISSN: 0099-1112. American Society of Photogrammetry. 1975.

[148] Peters W.H. and W.F. Ranson. "Digital Imaging Techniques In Experimental Stress Analysis". In: *Optical Engineering* 21.3 (1982). DOI: 10.1117/12.7972925.

[149] B. Pan et al. "Two-dimensional digital image correlation for in-plane displacement and strain measurement: a review". In: *Measurement Science and Technology* 20.6 (2009). DOI: 10.1088/0957-0233/20/6/062001.

[150] J. Blaber, B. Adair, and A. Antoniou. "Ncorr: Open-source 2D Digital Image Correlation Matlab software." In: *Experimental Mechanics* 55 (2015), pp. 1105–1122. DOI: 10.1007/s11340-015-0009-1.

[151] R. Harilal and M. Ramji. "Adaptation of open source 2D DIC software Ncorr for solid mechanics applications". In: (2014). DOI: 10.13140/2.1.4994.1442.

[152] S. Yoneyama et al. "Lens distortion correction for digital image correlation by measuring rigid body displacement". In: *Optical Engineering* 45.2 (2006). DOI: 10.1117/1.2168411.

[153] S. Yoneyama et al. "In-Plane Displacement Measurement Using Digital Image Correlation with Lens Distortion Correction". In: *JSME International Journal Series A Solid Mechanics and Material Engineering* 49.3 (2006). DOI: 10.1299/jsmea.49.458.

[154] V. Bacovsky. *Review of Nikon 18-55mm f/3.5-5.6G DX optics*. https://photographylife.com/reviews/nikon-18-55mm-dx-vr-af-p/2. Accessed on October 1, 2020. Photograpylife. 2020.

[155] K. Hoffmann. "An Introduction to Measurements using Strain Gages". In: Darmstadt, Germany: Hottinger Baldwin Messtechnikn, 1989.

[156] Wrought Materials. *Copper-Nickel Alloys - Cu Ni44 Mn1*. https://copperalliance.eu/uploads/2018/03/cuni44mn1.pdf. 1972.

[157] Dupont. *Kapton Polyimide Film General Specifications*. http://www.dupont.com/kapton/general/H-38479-4.pdf. 2020.

[158] Tokyo Measuring Instruments Laboratory. *Strain Gauges GFseries - Data Sheet*. https://tml.jp/eng/documents/strain_gauge/GFseries.pdf. 2018.

[159] M.F. Beatty and S.W. Chewning. "Numerical analysis of the reinforcement effect of a strain gage applied to a soft material". In: *International Journal of Engineering Science* 17.7 (1979), pp. 907–915. DOI: 10.1016/0020-7225(79)90019-3.

[160] A. Ajovalasit and B. Zuccarello. "Local reinforcement effect of a strain gauge installation on low modulus materials". In: *The Journal of Strain Analysis for Engineering Design* 40.7 (2005), pp. 643–653. DOI: 10.1243/030932405X3089.

[161] A. Ajovalasit et al. "Stiffness and reinforcement effect of electrical resistance strain gauges". In: *Strain* 43.4 (2007), pp. 299–305. DOI: 10.1111/j.1475-1305.2007.00354.x.

[162] J. Slotwinski and S. Moylan. *Applicability of Existing Materials Testing Standards for Additive Manufacturing Materials*. NIST, 2014. DOI: 10.6028/NIST.IR.8005.

[163] A. Bellini and S. Güçeri. "Mechanical characterization of parts fabricated using fused deposition modeling". In: *Rapid Prototyping Journal* 9 (2003), pp. 252–264. DOI: 10.1108/13552540310489631.

[164] Joachim R. Braasch Hubert W. Schreier and Michael A. Sutton. "Systematic errors in digital image correlation caused by intensity interpolation". In: *Optical Engineering* 39.11 (2000). DOI: 10.1117/1.1314593.

[165] P. Kulkarni and D. Dutta. "Deposition Strategies and Resulting Part Stiffnesses in Fused Deposition Modeling." In: *Journal of Manufacturing Science and Engineering* 121.1 (1999). DOI: 10.1115/1.2830582.

[166] L. C. Magalhães, N. Volpato, and M. A. Luersen. "Evaluation of stiffness and strength in fused deposition sandwich specimens." In: *Journal of the Brazilian Society of Mechanical Sciences and Engineering* 36.3 (2013), pp. 449–459. DOI: 10.1007/s40430-013-0111-1.

[167] C. W. Ziemian, R. D. Ziemian, and K. V. Haile. "Characterization of stiffness degradation caused by fatigue damage of additive manufactured parts." In: *Materials & Design* 109 (2016), pp. 209–218. DOI: 10.1016/j.matdes.2016.07.080.

[168] B. Huang and S. Singamneni. "Raster angle mechanics in fused deposition modelling". In: *Journal of Composite Materials* 49.3 (2014), pp. 363–383. DOI: 10.1177/0021998313519153.

[169] B. Huang and S. Singamneni. "Adaptive slicing and speed- and time-dependent consolidation mechanisms in fused deposition modeling." In: *Journal of Engineering Manufacture* 228.1 (2013), pp. 111–126. DOI: 10.1177/0954405413497474.

[170] C.W. Bert. "Anisotropic-material behavior". In: *Manual on experimental methods for mechanical testing of composites*. Ed. by R.L. Pendleton. London: Elsevier Applied Science, 1989. Chap. II A, pp. 5–10. DOI: 10.1007/978-94-009-1129-1_2.

[171] L. Tian, L. Yu, and B. Pan. "Accuracy enhancement of a video extensometer by real-time error compensation". In: *Optics and Lasers in Engineering* 110 (2018), pp. 272–278. DOI: 10.1016/j.optlaseng.2018.06.010.

[172] S. Brischetto and R. Torre. "3D thermal stress analysis in functionally graded plates and shells". In: *Proceedings of IWCMM28 - 28th International Workshop on Computational Mechanics of Materials* (Sept. 10–12, 2018). Glasgow, UK, 2018.

This Ph.D. thesis has been typeset by means of the TEX-system facilities. The typesetting engine was pdfLATEX. The document class was `toptesi`, by Claudio Beccari, with option `tipotesi=scudo`. This class is available in every up-to-date and complete TEX-system installation.